Experimental and Numerical Investigation into the Energy Conversion Process in Single and Multi Chamber Oscillating Water Column Wave Energy Converters

Simeon Doyle

Submitted for the degree of Doctor of Philosophy
at Lancaster University.

May 2021

In collaboration with Waves2Watts Ltd.

This project was supported by the Centre for Global Eco-Innovation
and is part financed by the European Regional Development Fund.

European Union
European Regional
Development Fund

Declaration

I declare that the work in this thesis has been done by myself and has not been submitted elsewhere for the award of any other degree.

Signed: Simeon Doyle

Date: 21.05.2021

Abstract

Ocean waves are an immense energy resource at our doorstep that we are yet to truly harness. Harvesting of such a complex form of energy in the harshest environments gives wave energy conversion very unique challenges requiring continual innovation toward creating a more competitive contributor to the renewable energy mix. Innovations should not only benefit the wave energy sector but other technological applications by providing attractive novel synergetic deployment opportunities.

This thesis presents an innovative solution to the issue of high wave energy costs. Research is based on a particular category of Wave Energy Converters (WECs) - the Multi-Oscillating Water Columns (M-OWCs) with focus on a unique technology, the Waves2Watts (W2W) device. The first phase involves concept verification through experimental modelling and the subsequent phase focuses on additional aspects of M-OWC technology, more specifically as an integrated breakwater. This project is novel in its methodology through the pragmatic approach of modelling each aspect of the W2W evolution with predecessors serving as benchmarks. This includes modelling several different WEC models with three different Power Take-Off systems enabling fair cross comparison for each evolutionary step toward the final M-OWC breakwater concept, which displays 36.1% efficiency in irregular waves. Both pneumatic and wave tank numerical modelling supports conclusions and provides additional insight into behaviour. The M-OWC concept generates greater power than the singular OWC benchmark by a factor equal to the number of OWCs. Furthermore, the additional width of the M-OWC, even at suboptimal chamber spacings shows better capture efficiency. These results reveal the potential of the final W2W Modular M-OWC breakwater WEC through the scalability of its power. The benefits of such a concept is anticipated to significantly reduce wave energy costs through increased capacity and novel integration fulfilling two roles – wave energy absorption and coastal protection.

Keywords

Wave Energy Converter; Oscillating Water Column; Ocean Energy; Renewable Energy; Experimental Research; Computational Fluid Dynamics.

Dedication

I dedicate this thesis to my wife for her endless support and patience, and my parents for the opportunities they have given me and their belief that I would always succeed.

'Parvis imbutus tentabis grandia tutus'.

Acknowledgements

I am extremely grateful to have been given the opportunity to undertake this PhD research project and would like to acknowledge all who were part of the journey.

Firstly, my main academic supervisor Professor George Aggidis; I greatly appreciate all of the unwavering and unconditional support you have provided throughout. Second academic supervisor Dr Suzanna Ilic, who offered a tremendous level of support and complimented the project perfectly. I am also grateful to my regular appraisal reviewers Dr Jianqiao Ye and Dr Stephen Quayle for providing helpful and constructive feedback as well as giving me confidence in my work.

My gratitude goes to my industrial supervisors and sponsors, the three directors of Waves2Watts: Adam Kyffin, Will Kyffin and Colin Vicars. Thank you for the opportunity of this PhD and welcoming me as part of the team. Your presence at many update meetings, remaining fully engaged and supportive at every step was invaluable.

This project would not be possible without the team at the Centre of Global Eco-Innovation who funded the project, managed all the laborious administrative demands of such a project and provided support at the drop of a hat.

Of course, the PhD experience would not be the same without my fellow colleagues around going through the same peaks and troughs. I thoroughly appreciate all of the support offered by my friends and colleagues of the Lancaster University Renewable Energy Group: Dr Sean Petley, Dr Andrew Morrall, Federico Atene, Jainil Shah, Neil Barker and Andrea Sanvito. Last but certainly not least, the D floor office of the engineering department always had a great atmosphere thanks to the friendly faces of these colleagues and friends: Mohamed Abdelraouf, Athanasios Papageorgou, Simon Vecten and Tomas Pereira.

List of Publications and Outputs

List of Journal Publications:

- **Doyle.S**, Aggidis.G.A., *'Development of multi-oscillating water columns as wave energy converters'*, Renewable and Sustainable Energy Reviews, Vol. 107, 2019

- **Doyle.S**, Aggidis.G.A., *'Experimental investigation and performance comparison of a single OWC, array and M-OWC'*, Renewable Energy 2020, Vol. 168, 2021

- **Doyle.S**, Aggidis.G.A., *'Advancement of Oscillating Water Column Wave Energy Technologies through Integrated Applications and Alternative Systems'*, International Journal of Energy and Power Engineering, Vol. 14, No. 12, 2020

- **Doyle.S**, Aggidis.G.A.,*'Experimental investigation into Unidirectional and Bidirectional airflow PTO systems in M-OWCs as an integrated breakwater concept'*, Renewable Energy (under review)

List of Conference Publications:

- **Doyle.S**, Aggidis.G.A., 'Investigation into multi-oscillating water column wave energy converters and a novel concept' in the book of proceedings of the RENEW 2018 Conference entitled 'Advances in Renewable Energies Offshore 2019'

Further Outputs:

- Paper presentation at RENEW 2018, The 3rd International Conference on Renewable Energies Offshore (Lisbon, Portugal)
- Presentation at the Lancaster University Renewable Energy Group forum (24/04/2018) entitled *'State-of-the-art OWC wave energy converters and the W2W device'*
- Presentation at the Post Graduate Conference 2018 entitled *'State-of-the-art OWC wave energy converters and the W2W device'* - 3rd prize in the relevant year category
- Centre of Global Eco-Innovation Annual Report 2018.
- Presentation at the Post Graduate Conference 2019 entitled *'The evolution of M-OWC wave energy converters and W2W concept verification modelling'* - 2nd prize in the relevant year category
- Centre of Global Eco-Innovation Annual Report 2019.
- Presentation at the Lancaster University Renewable Energy Group forum (26/02/2019) entitled *'The evolution M-OWC wave energy converters'*
- Presentation at the Lancaster University Renewable Energy Group forum (31/01/2020) entitled *'Experimental investigation and comparison into different types of M-OWC wave energy converters'*

Contents

Declaration **I**

Abstract **II**

Keywords **II**

Dedication **III**

Acknowledgements **IV**

Outputs **V**

List of Figures **XX**

List of Tables **XXI**

Nomenclature **XXII**

Acronyms XXII

Symbols XXIV

1 Introduction **1**

Ocean Wave Energy 1

Brief History 1

Current Status 2

Background and Motivation 6

The Waves2Watts Wave Energy Converter 7

Technology Development Assessment for WECs 11
Aims and Objectives of Research 13
Thesis Structure and Overview 15

2 Literature Review **17**
Ocean Wave Theory 17
Wave Generation and Propagation 17
Regular and Irregular Waves 21
Wave Energy Converter Technology 23
Classifications 23
Energy Conversion 25
Oscillating Water Column Development 26
Origins 26
Devices and Development 26
Evolution of the standard single chamber OWC 28
Hydrodynamic Challenges and Survivability 30
The Multi-Oscillating Water Column Concept 33
Breakwater Integrations and Synergies 40
Power Take-Off 43
Numerical Modelling 51
Relevant Computational Fluid Dynamics Theory 52
CFD for Wave Energy Applications 58
Numerical Modelling of OWCs 61
Summary and Discussion 65

3 Design of Experiments and Methodology **72**
Experimental Wave Tank Facility and Setup 72
Wave Tank and Equipment 72
Wave Generation 74
Sea State Scaling 77
Analysis Methodology 81

Post-Processing and Data Analysis 81
Hydraulic Power 83
Empirical Flow Rate and Pneumatic Power 83
Power Comparisons 85
Reflection and Energy Balance Analysis 86
Physical Model Design 88
General Model Setup 89
Phase 1 Hydrodynamic Modelling 89
Phase 1 Pneumatic Model and OWC Scaling 90
Phase 2 Tank Setup and Geometry 94
OWC Array Model 95
M-OWC Bidirectional Model 96
Breakwater Modelling 97
Unidirectional PTO Models 98

4 Phase 1: Waves2Watts Concept Verification 103
Introduction and Research Approach 103
Hydrodynamics 103
Pneumatics 107
Results and Discussion 108
Hydrodynamics 108
Pneumatics 112
Discussion and Conclusions 120
Summary 120
Additional Modelling Behind the Scenes 121

5 Phase 2: Array and Modular M-OWC Modelling 123
Introduction to Waves2Watts Phase 2 123
Results 126
Power Take-Off Damping 126
OWC Chamber Spacing 131

Cross Model Performance Comparison 133
Conclusions 137

6 Phase 2: M-OWC Breakwater and PTO Modelling 139
Introduction 139
Research Approach 140
Results and Discussion 141
The M-OWC Bidirectional 141
The M-OWC Breakwater Effect 145
Unidirectional Models 146
Single Unidirectional PTO 146
Twin Unidirectional PTO 148
Operational Losses 149
Four Model Cross Comparison 151
Induced Reflection 151
Capture Width Performance 152
Energy Balance Analysis 153
Conclusions 158

7 Numerical Modelling of M-OWC Concepts 160
Introduction 160
Premise 160
Numerical Code and Computing Resources 161
Design of CFD Models and Methodology 161
Model Geometry and Numerical Grid 162
Solver, Computational Resources and Post-processing 163
Verification and Validation 163
Pneumatic System Model 164
Full Numerical Wave Tank Model 169
Pneumatic Model Simulations Results and Analysis 177
Mesh Independence and Validation 177

Pneumatic CFD Model Comparison 180
Numerical Wave Tank Results and Analysis 186
Verification and Validation 186
Model Comparison 191
Discussion 199
Pneumatic Modelling 199
Numerical Wave Tank Simulations 200

8 Conclusions and Discussion 202
Summary of Conclusions 202
Phase 1: W2W Concept Verification 202
Phase 2: W2W as a MOWC Breakwater 204
Numerical Modelling 205
Discussion 208
Project Outcome 208
Recommendations for Future Work 209

References 213

Appendix A Methodology Support 230

Appendix B EMEC Wave Data and Runs 237

Appendix C Tank Reflection Characteristics 240

Appendix D Phase 2 Model Reflection Full Results 241

Appendix E Irregular Wave Generation 245

List of Figures

1.1 Breakdown and description of the components that make up the Levelised Cost of Energy (LCOE) metric [12] 5
1.2 Map illustration of the estimated theoretical global annual mean wave power resource [25] 6
1.3 An illustration of the basic Oscillating Water Colum concept and operation in its most general form [37] 8
1.4 An annotated version of the original design sketch of the W2W concept from the patent forming the starting point of this project [35] 10
1.5 The generalised Technology Readiness Levels scale for the technological development of wave energy converters [42] 12
1.6 Technology Readiness and Performance Levels plotted against required funding and the cost of energy [12] 13

2.1 Wave energy spectrum illustrating the range of different wave types across all frequencies with their respective disturbing and restoring forces and relative energy levels [46] 18
2.2 Characteristics and properties of water waves and illustration of deep and intermediate water waves in the XZ plane 19
2.3 Identification of wave theories for linear and non-linear waves according to terms of relative water depth and relative wave height [12] 21
2.4 The different wave regime categories illustrated by plots of the free surface in the time domain [49] 22
2.5 Diagram illustrating the different orientations of wave energy converters with respect to the incident wave direction 24
2.6 The paths toward wave energy conversion based on the different conversion stages for different WEC types (adapted from [55]) 25
2.7 Illustraion of the concept of an OWC array as an M-OWC 34
2.8 Illustration of the Segmented M-OWC Concept 34
2.9 Illustration of the Modular M-OWC Concept 35
2.10 Photographs and Models of Multi-Oscillation Water Column devices and concepts Seabreath (a) [109], Wave Mill (b) [113], KNSWING (c) [119], LEANCON (d) [56] and Stellenbosch (e) [126] 39
2.11 The classifications of PTO systems for OWC concept based WECs [42] 44

2.12 Geometry and illustrations of the main self-rectifying turbines for OWC applications: the Wells (a), Denniss-Auld (b) and impulse turbine (c) [25] 46
2.13 Example of five blade horizontal axis Savonius geometry for PTO in OWC applications [196] 47
2.14 Wave energy numerical modelling methods comparison on a scale of computational costs and fidelity [210] 52
2.15 Flow regimes and sub-layers of the boundary layer in the simple case of flow over a flat plate [212] 55

3.1 Detailed schematic of dimensioned LUREG wave tank with wave generation and absorption features, and operation equipment setup . . . 73
3.2 Wave tank maximum wave amplitude achievable and paddle angle required are plotted against wave frequency conveying the limitations in wave generation using paddles [238] 75
3.3 Time series of significant wave height and Zero-crossing period from Billia Croo over one year sampled every 30 minutes provided by EMEC 78
3.4 Full scale wave matrix showing number of occurrences for values of zero-crossing wave period and significant wave heights over the one year of history data 78
3.5 Wave occurrence distribution and illustration refinement method by highlighting the top 80 most frequent waves and the chosen 28 waves on full scale (left) and model scale (right) plots 79
3.6 Overview of OWC first stage energy conversion detailing sub-stages and associated quantities 88
3.7 The LUREG wave tank facility dimensions and setup of the experimental model, support structures and water level gauges for the Phase 1 experiments 89
3.8 OWC model geometry for the Phase 1 hydrodynamics experiments . 90
3.9 Plan view of the Phase 2 OWC Geometry (1:50) with relevant dimensions, and positioning of orifices and transducers 92
3.10 Physical 1:50 scale two chamber W2W model for Phase 1 pneumatic experiments with inlet and intermediate flap valves, and outlet orifice plate 94
3.11 Setup of the LUREG wave tank for the first block of Phase 2 M-OWC experiments for modelling M-OWCs in terminator configuration with adjustable OWC spacing 95
3.12 Setup of the LUREG wave tank with the details and dimensions of the wave probe layout, model positioning and support structures. 95
3.13 Example picture of the OWC array M-OWC model in situ at the LUREG wave tank with zero spacing 96
3.14 Annotated renders of the 1:50 design and layout of the OWC array (left) and M-OWC (right) models 97

3.15 In situ M-OWC bidirectional model with centred outlet (left) and M-OWC bidirectional breakwater model with blocking structure between OWC chambers (right) 98
3.16 In situ airflow rectifying unidirectional M-OWC breakwater models with single PTO system (left) and unidirectional M-OWC breakwater models with Twin PTO system (right) 99
3.17 Illustration of exhale and inhale processes for single turbine PTO systems 100
3.18 Illustration of exhale and inhale processes for twin turbine PTO systems 100

4.1 Illustration of intended hydrodynamic interaction sequence of the Waves2Watts concept as described in patent 104
4.2 Conditions and thresholds for slosh mode (a) and pitch stability (b) against the testing wave frequency range and relevant WEC dimensions 106
4.3 Hydrodynamic response time series for three different example relative wavelengths from all internal level gauges (ILG_{1-3}) and external gauge counterparts (WG_{1-3}) for wave frequencies f_{wave}=0.8, 0.92 and 1.2 Hz at a wave height of H=0.1 m 108
4.4 An example and illustration of an OWC operating in piston and sloshing modes with large $\lambda_{rel} = 6.454\,m$ and small relative wavelengths $\lambda_{rel} = 2.868\,m$, respectively 109
4.5 First chamber internal RAOs plotted against wave frequency range $f_{wave} = 0.8$–$1.4\,Hz$ for a constant wave height of $H_{wave} = 0.06$–$0.1\,m$. 111
4.6 First chamber internal RAO plotted against wave steepness for representative frequencies $f_{wave} = 0.8, 0.92$ and $1\,Hz$ with a wave height range of $H_{wave} =$ 112
4.7 Orifice damping plot showing internal free surface displacement RAOs from the ILG_1 of the new single OWC geometry to be used from this point on for Phase 2 modelling, plotted against a frequency range of $f_{wave} = 0.8$–$1.1\,Hz$, at a constant representative wave height of $H_{wave} = 0.08\,m$ and a range of orifice plates $O = 1, \,, 1.5\,, 2\,and\,2.5\%$ 113
4.8 Internal free surface levels (ILG_{1and2}) and internal chamber air pressure (p_{OWC1-2}) time series data plotted for OWC1 (1^{st} stage) (top) and OWC2 (2nd stage) (bottom), for the two chamber W2W attenuator model. Plotted for a representative frequency of $f_{wave} = 1\,Hz$ and wave height $H_{wave} = 0.08\,m$ 114
4.9 Internal OWC air pressure (p_{OWC1-2}) time series for OWC1 (1^{st} stage) and OWC2 (2^{nd} stage) for the two chamber W2W attenuator model for a representative frequency of $f_{wave} = 1\,Hz$ and wave height $H_{wave} = 0.08\,m$ 115
4.10 Internal OWC net air pressure (p_{NET1-2}) and internal free surface RAOs (ILG_{1-2}) for OWC1 (1^{st} stage) and OWC2 (2^{nd} stage) the two chamber W2W attenuator model for a frequency range of $f_{wave} = 0.96$–$1.04\,Hz$ and a representative wave height $H_{wave} = 0.08\,m$ 117

4.11 Internal OWC air pressure bar plot illustrating the drop between 1^{st} and 2^{nd} stages of the two chamber W2W attenuator model compared against the singular OWC for a frequency range of $f_{wave} = 0.96$–$1.04\,Hz$ and a representative wave height $H_{wave} = 0.08\,m$ 118
4.12 Representative calculated pneumatic power time series comparison between the singular OWC and the W2W M-OWC attenuator concept a representative frequency of $f_{wave} = 1\,Hz$ and wave height $H_{wave} = 0.08\,m$ 119

5.1 Example of a time series plot (at $f_{wave} = 1\,Hz$) of internal water level, external wave height and power history obtained from the single OWC experiments 127
5.2 Internal displacement RAOs for the open lid single OWC over a frequency range of $f_{wave} = 0.8$–$1.14\,Hz$ for heights $H_{wave} = 0.06,\ 0.07,\ 0.08\,m$ 128
5.3 Internal displacement RAO results from the single OWC orifice tests through a frequency range of $f_{wave} = 0.8$–$1.1\,Hz$ and a wave height of $H_{wave} = 0.08\,m$, with an orifice range $O = 1 - 3\%$ with for 100% plotted to represent zero damping 129
5.4 Normalised values of average maximum exhale pressures (left) and net pressures (right) from the single OWC for the orifice plate range $O = 1 - 3\%$ over the frequency range of $f_{wave} = 0.8$–$1.1\,Hz$ and wave height $H_{wave} = 0.08\,m$ 130
5.5 Internal displacement RAOs and normalised values of average maximum exhale pressures from the M-OWC model for an orifice plate range $O = 3.5 - 6\%$, over a frequency range of $f_{wave} = 0.8$–$1.1\,Hz$ and wave height $H_{wave} = 0.08\,m$ 131
5.6 Normalised values of mean power generated by the single OWC, the OWC array and M-OWC model with over a chamber spacing range of $a = 0-3$, for a frequency of $f_{wave} = 1\,Hz$ and wave height $H_{wave} = 0.08\,m$ 132
5.7 Average (left) and average peak values (right) for the effective and total capture width values plotted as a function of wave frequency for the single OWC, the OWC array and M-OWC models over a frequency range of $f_{wave} = 0.92$–$1.1\,Hz$ and wave height $H_{wave} = 0.08\,m$ 134
5.8 Average (bottom) and average peak (top) values for the effective (left) and total (right) capture width values for the single OWC, the OWC array and M-OWC models plotted against a chamber spacing range of $a = 0-3$, for a frequency of $f_{wave} = 1\,Hz$ and wave height $H_{wave} = 0.08\,m$ 135
5.9 Normalised values for average peak and average airflow, and average peak and mean power for the equivalent of three single OWCs, the OWC array and M-OWC models for the representative wave frequency of $f_{wave} = 1\,Hz$ and wave height $H_{wave} = 0.08\,m$ 136

6.1 Internal displacement RAOs and normalised net pressure plot for orifice plate damping test with the altered Outlet of the M-OWC Bidirectional for all regular wave run frequencies and a wave heights plotted as a function of wave steepness 142

6.2 Normalised power plot against an OWC spacing range of $a = 0 - 3$ for the altered outlet M-OWC bidirectional configuration for representative frequencies of $f_{wave} = 0.96, 1 and 1.04\,Hz$ and height $H_{wave} = 0.08\,m$. 143
6.3 Characteristic average reflection for the M-OWC Bidirectional model plotted against a frequency range of $f_{wave} = 0.74$–$1.01\,Hz$ with a representative and wave height $H_{wave} = 0.08\,m$ for chamber a chamber spacing range of $a = 0 - 3$ with a wave steepness line representing the breaking threshold 144
6.4 Normalised mean (left) and average peak power (right) for M-OWC and M-OWC BW bidirectional models for a frequency range of $f_{wave} = 0.74$–$1.01\,Hz$ and wave height range of height $H_{wave} = 0.05$–$0.1\,m$ . . 145
6.5 Normalised pressure drop and reverse pressure drop time series example plot for exhale and inhale processes, respectively, for the twin turbine rectifying system for a representative frequency of height $f_{wave} = 0.94\,Hzm$ and wave height $H_{wave} = 0.08\,m$ 147
6.6 Normalised pressure drop and reverse pressure drop time series example plot for exhale and inhale processes, respectively, for the single turbine rectifying system for a representative frequency of height $f_{wave} = 0.94\,Hzm$ and wave height $H_{wave} = 0.08\,m$ 148
6.7 Total pneumatic losses and reverse losses plotted against wave steepness for all BW models for all regular wave frequencies $f_{wave} = 0.74$–$1.01\,Hzm$ and wave heights $H_{wave} = 0.05 - 0.1\,m$ 149
6.8 Wave to hydraulic power η_{WH} (left) and hydraulic to pneumatic η_{HP} (right) power conversion efficiencies plotted against wave steepness for both bidirectional and unidirectional BW models for all regular wave frequencies $f_{wave} = 0.74$–$1.01\,Hzm$ and wave heights $H_{wave} = 0.05 - 0.1\,m$ 151
6.9 Reflection Coefficient at peak spectral frequency due to Breakwater Structure (top) and Unidirectional models (bottom) for wave frequencies $f_{wave} = 0.74$–$1.01\,Hzm$ and wave heights $H_{wave} = 0.05 - 0.1\,m$ . . 152
6.10 Average effective (left) and total (right) CWR for all BW models plotted against wave frequencies $f_{wave} = 0.74$–$1.01\,Hzm$ and for wave heights $H_{wave} = 0.05 - 0.1\,m$ 153
6.11 Energy absorption (top left), reflection (bottom left), transmission (bottom right) and available extraction (top right) coefficients for all BW models plotted against a wave frequency range of $f_{wave} = 0.74$–$1.01\,Hzm$ for a representative wave height of $H_{wave} = 0.07\,m$ 154
6.12 Illustration of energy split for external quantities (reflected, transmitted and absorbed energy) (left), and OWC internal quantities (extracted, stored and lost energy) (right) for an example wave run of frequency $f_{wave} = 0.94\,Hz$ and wave height $H_{wave} = 0.08\,m$ 156
6.13 Box and whisker plots showing energy balance ratios data in the form of the mean, median, 25% deviation range, minimum and maximum values for each irregular wave period $T_z = 0.99$–$1.34\,s$, and for the non-BW M-OWC and all three BW models (bidirectional and unidirectional) 158

7.1 Sliced view through the YZ plane of the domain and geometry of the M-OWC bidirectional (left) and ducted variation (right) pneumatic system models with labelled boundary conditions 166
7.2 Cross section slice (YZ plane) of the numerical mesh of the M-OWC bidirectional model with a focused window of the mesh structure around the orifice and a cross sectional focus of the mesh at the manifold wall 167
7.3 Cross section slice (YZ plane) of the numerical mesh of the M-OWC bidirectional ducted variation model with a focus window of the mesh structure around the orifice and a cross sectional focus of the mesh at the duct wall 168
7.4 Entire domain of NWT model with the geometry of the OWCs, a cross sectional sample of the mesh along the domain length and a focus window on the mesh around the WEC. Cell zones and each boundary condition labelled as surfaces in the 3D image and lines in the 2D cross sections 170
7.5 Comparison of transient free surface displacement caused by wave generation at the position of WG_1 in the NWT domain and experimental tank with theoretical wave profiles over time for 2nd and 3rd order stokes waves 173
7.6 Contours of free surface elevation from birds-eye-view (XZ Plane) in sequence to illustrate transient wave generation process over first 10 periods for a representative frequency of $f_{wave} = 0.94\,Hz$ and wave height of $H_{wave} = 0.08\,m$ 174
7.7 Contours of velocity magnitude from symmetry plane view (XY Plane) in sequence to illustrate transient wave generation process over first 10 periods for a representative frequency of $f_{wave} = 0.94\,Hz$ and wave height of $H_{wave} = 0.08\,m$ 175
7.8 Example of the transient adaptation of the solver time step during test simulation using the adaptive time step method and the iterations per time step to reach residual criteria 176
7.9 Pneumatic bidirectional model average and range of Y+ values across the entire orifice wall (a) and along central line around the circumference of the orifice wall (b) for coarse and fine grids 178
7.10 Mean (left) and average peak (right) pneumatic power plots for the pneumatic bidirectional model validation comparison between experimental and CFD results for both coarse and fine grids for the frequency range $f_{wave} = 0.74$–$1.01\,Hz$ and wave height of $H_{wave} = 0.08\,m$ 179
7.11 Mean (left) and average peak (right) pneumatic power plot comparison between CFD results of the M-OWC bidirectional model and ducted variation for the frequency range $f_{wave} = 0.74$–$1.01\,Hz$ and wave height of $H_{wave} = 0.08\,m$ 180
7.12 Comparison of velocity magnitude contours and vectors in the YZ plane between CFD results of the M-OWC bidirectional model (a) and ducted variation (b) for exhale and inhale processes for a representative frequency of $f_{wave} = 0.94\,Hz$ and wave height of $H_{wave} = 0.08\,m$ 182

7.13 Comparison of turbulent viscosity contours and velocity vectors in the YZ plane between CFD results of the M-OWC bidirectional model (a) and ducted variation (b) for exhale and inhale processes for a representative frequency of $f_{wave} = 0.94\,Hz$ and wave height of $H_{wave} = 0.08\,m$ 183
7.14 Comparison of velocity magnitude profiles at OWC2 outlet for exhale and inhale processes for constant wave height of $H_{wave} = 0.08\,m$ and frequency range $f_{wave} = 0.74$–$1.01\,Hz$ for the M-OWC Bidirectional model and a representative frequency $f_{wave} = 0.88\,Hz$ for the ducted variation model 184
7.15 Comparison of static pressure profiles along a vertical line through the height of OWC2 and into the manifold/duct for exhale (left) and inhale (right) processes for constant wave height of $H_{wave} = 0.08\,m$ and frequency range $f_{wave} = 0.74$–$1.01\,Hz$ for the M-OWC Bidirectional model and a representative frequency $f_{wave} = 0.88\,Hz$ for the ducted variation model 186
7.16 Example plots of final and penultimate periods for normalised orifice flow rate illustrating the best and worst cases of periodicity error . . 188
7.17 Mean power comparison between CFD and experimental results for the OWC array for chamber spacings $a = 0.5,\ 1\ and\ 1.5$, for a representative wave frequency of $f_{wave} = 0.88\,Hz$ and wave height $H_{wave} = 0.08\,m$. 189
7.18 Comparison of CFD and experimental results for Internal and external RAOs for the OWC array for chamber spacings $a = 0.5,\ 1\ and\ 1.5$, for a representative wave frequency of $f_{wave} = 0.88\,Hz$ and wave height $H_{wave} = 0.08\,m$ 190
7.19 Mean and Average Peak Power comparison between CFD and experimental results for the M-OWC bidirectional model and breakwater variation for a representative wave frequency of $f_{wave} = 0.88\,Hz$ and wave height $H_{wave} = 0.08\,m$ 191
7.20 Experimental and CFD computed time lag between external gauge WG_{EX} and IGLs for OWC1 and OWC2 for chamber spacings $a = 0.5,\ 1\ and\ 1.5$ for the array simulations only(left) and for all three simulated models (right) 192
7.21 Example plot of the external and internal level time histories with labels of points that are relevant to the following analysis 193
7.22 Contour plots of velocity magnitude and vectors of velocity in the XZ plane for chamber spacings $a = 0.5,\ 1\ and\ 1.5$ and the four phase points $\phi_{EX} = \pi/2,\ \pi,\ 3\pi/2,\ and\ 2\pi$ 194
7.23 Contour plots of velocity angle in the YZ plane (see Fig. 7.4) for chamber spacings $a = 0.5,\ 1\ and\ 1.5$ and the four phase points $\phi_{EX} = \pi/2,\ \pi,\ 3\pi/2,\ and\ 2\pi$ 195
7.24 Contour plots of velocity magnitude and vectors of velocity in the YZ plane (see Fig. 7.4) for chamber spacings $a = 0.5,\ 1\ and\ 1.5$ and the phase points where the internal level crosses the external: $\phi_{EX} = \pi,\ and\ 2\pi$ 196

7.25 Birds-eye view of contours of surface elevation for OWC array model and for chamber spacings $a = 0.5,\ 1\,and\,1.5$ 197
7.26 Contour plots of velocity magnitude and vectors in the YZ plane for the M-OWC bidirectional model and breakwater variation for chamber spacing $a = 1$ and the four phase points $\phi_{EX} = \pi/2,\ \pi,\ 3\pi/2,\ and\,2\pi$. 198
7.27 Contour plots of velocity angle in the YZ plane for the M-OWC bidirectional model and breakwater variation for chamber spacing $a = 1$ and the four phase points $\phi_{EX} = \pi/2,\ \pi,\ 3\pi/2,\ and\,2\pi$ 199

8.1 The TRL levels for a wave energy converter with the illustration of the development path of the Waves2Watts device 209
8.2 Conceptual model of the W2W floating breakwater M-OWC in a style most similar to that of the original patent 212

A.1 Differential pressure sensor calibration test results 230
A.2 Picture of Phase 1 experimental set-up for hydrodynamic tests 231
A.3 Phase 1 W2W M-OWC skeleton with calibrated copper strip ILGs out of tank close-up 231
A.4 Internal heave amplitude sensor calibration test 232
A.5 Phase 1 W2W M-OWC skeleton with copper strip ILGs installed in the wave tank for calibration tests 232
A.6 Render of Phase 1 pneumatic experimental model intermediate one-way valve with incline for transfer between 1^{st} and 2^{nd} stage 233
A.7 Render of Phase 1 pneumatic experimental model inlet one-way valve with for 1^{st} stage 233
A.8 Phase 1 W2W conept M-OWC model installed in wave tank for pneumatic tests 234
A.9 Phase 1 W2W Conept M-OWC model auxiliary air volume tanks and connecting hoses installed in wave tank for pneumatic tests 235
A.10 Live snapshot of inhale process during pneumatic testing of the Phase 1 W2W conept M-OWC 235
A.11 Live snapshot of Exhale process during pneumatic testing of the Phase 1 W2W conept M-OWC 236
A.12 Phase 2 M-OWC bidirectional manifold model installed in the tank . 236

B.1 Location of EMEC Billia Croo test site and wave data source site . . 237
B.2 Polar histogram plot for the wave direction at the EMEC Billia Croo test site 238

C.1 Reflection coefficient (top) and reflection line distance (bottom) results in empty tank reflection tests 240

D.1 Phase 2 M-OWC Bidirectional Model Full Reflection Results 241
D.2 Phase 2 M-OWC Bidirectional Breakwater Model Full Reflection Results 242
D.3 Phase 2 M-OWC Unidirectional Single Model Full Reflection Results 243
D.4 Phase 2 M-OWC Unidirectional Twin Model Full Reflection Results . 244

D.5 Segments of the irregular time series generated incident wave that frequently yielded bad results across all models and wave runs 244

E.1 Time series of generated compared with recorded incident wave in empty tank 245
E.2 Jonswap spectra generated compared with recorded incident wave in empty tank 246

List of Tables

2.1 Summary table of all M-OWCs reviewed with details of the number of OWCs, turbines, PTO system type, highest stage of development and references 71

3.1 Generic set of regular wave runs for Phase 2 M-OWC experiments . . 76
3.2 Filtered and selected regular waves range runs from EMEC data for use in experiments 80
3.3 Set of irregular waves runs used in the Phase 2 M-OWC experiments 81
3.4 The OWC model dimensions for the Phase 1 hydrodynamic experiments 90
3.5 OWC model (1:50 scale) dimensions 92

4.1 Average peak and mean power values calculated with Equations 3.7 and . 3.6 respectively, for the singular OWC and the W2W M-OWC concept 120

7.1 The breakdown of computing resources utilised and average computing time for both numerical models developed and their respective coarse and fine grids 161
7.2 Metrics and dimensions used for Coarse and Fine meshes of the pneumatic system models: M-OWC Bidirectional and ducted concepts . . 168
7.3 Metrics and dimensions used for Coarse and Fine meshes of the Numerical Wave Tank simulations including the OWC array and M-OWC Bidirectional geometries 171
7.4 Fluid properties for primary and secondary phases in the NWT simulations 171
7.5 All periodicity errors calculated for OWC orifice flow and orifice pressure for NWT simulations 187

8.1 Summary of all experiments carried out in Phase 2 work with details of changing variables and wave runs 206

B.1 Full wave run for use in experiments, filtered and selected regular waves range runs from EMEC data 239

Nomenclature

Acronyms

AEP	Annual Energy Production
BDC	Bottom Dead Centre
BW	Breakwater
CAPEX	Capital Expenditure
CFD	Computational Fluid Dynamics
CFL	Courant-Friedrichs-Lewy
CGE	Centre of Global Eco-innovation
CRL	Commercial Readiness Level
CWR	Capture Width Ratio
DFT	Discrete Fourier Transform
DAQ	Data Acquisition
EMEC	European Marine Energy Centre
FFT	Fast Fourier Transform
FS	Free Surface
HEC	High-End Computing
HPC	High-Performance Computing
ILG	OWC Internal Level Gauge
IP	Intellectual Property
JONSWAP	Joint North Sea Wave Project
LCOE	Levelised Cost of Energy
LUREG	Lancaster University Renewable Energy Group
LU	Lancaster University
MWL	Mean Water Level
M-OWC	Multi-Oscillating Water Column
MR	Multi-Resonant
NPV	Net Present Value
NS	Navier-Stokes
NWT	Numerical Wave Tank
OWC	Oscillating Water Column
PW	Pearson-Moskowitz
PDE	Partial Differential Equation
PISO	Pressure Implicit with Splitting of Operators
PTO	Power Take-Off

OPEX	Operational Expenditure
RANS	Reynolds Averaged Navier-Stokes
RAO	Response Amplitude Operator
REWEC	Resonant Wave Energy Converter
SIMPLE	Semi-Implicit Method for Pressure Linked Equations
SME	Small-Medium Enterprise
SWL	Still Water Level
TDC	Top Dead Centre
TPL	Technology Performance Level
TRL	Technology Readiness Level
UDF	User Defined Function
VOF	Volume of Fluid
WG	Wave Gauge
WEC	Wave Energy Converter

Symbols

Roman Letters

a	chamber spacing	$[-]$
A_o	orifice area	$[m^2]$
B	width	$[m]$
c	individual wave propagation velocity	$[ms^{-1}]$
c_g	wave group velocity	$[ms^{-1}]$
C_d	discharge coefficient	$[-]$
C_t	turbine flow coefficient	$[-]$
CWR_E	effective capture width ratio	$[-]$
CWR_T	total capture width ratio	$[-]$
d	length of the column parameter vector.	$[-]$
D_{owc}	OWC draft	$[m]$
d_w	OWC wall thickness	$[m]$
dY	spacing between inner OWC edges	$[m]$
E_A	absorbed wave energy	$[J]$
E_E	extracted energy	$[J]$
E_I	incident wave energy	$[J]$
E_L	energy loss	$[J]$
E_R	reflected wave energy	$[J]$
E_S	stored energy	$[J]$
E_T	transmitted wave energy	$[J]$
f	frequency	$[Hz]$
f_0	resonant frequency	$[Hz]$
$f_{Nyquist}$	Nyquist frequency	$[Hz]$
f_s	sampling frequency	$[Hz]$
F	OWC freeboard	$[m]$
g	gravitational constant	$[m^2s^{-1}]$
h	water depth	$[m]$
H	wave height	$[m]$
H_S	significant wave height	$[m]$
ILG_i	OWC internal level gauge	[-]
k	turbulent kinetic energy	$[m^2s^{-2}]$
K	wave number	[-]
k_r	reflection coefficient	$[-]$
k_t	turbine flow coefficient	$[kg^{-1}m^{-1}]$
k_{WG}	WG calibration coefficient	$[-]$
L_{owc}	OWC outer length	$[m]$
L_1	upstream pressure tap distance	$[m]$
L_2	downstream pressure tap distance	$[m]$
$L_{pnTotal}$	total pneumatic loss	$[-]$
n	number of half periods	$[-]$
N	number of periods	$[-]$

O	orifice area ratio	$[-]$
P_{hydr}	hydraulic power	$[W]$
P_{mech}	mechanical power	$[W]$
P_L	power loss	$[W]$
P_{owc}	pneumatic power from OWC	$[W]$
P_{pn}	pneumatic power	$[W]$
P_{wave}	power in unit width of wave	$[Wm^{-1}]$
Δp_o	pressure drop across orifice	$[Pa]$
p	internal air pressure	$[Pa]$
PE	periodicity error	$[\%]$
Q_o	orifice flow rate	$[m^3s^{-1}]$
Re	Reynolds number	$[-]$
s	wave steepness	$[-]$
S	OWC water plane area	$[m^2]$
S_m	momentum equation source term	$[Nm^3]$
t	time	$[s]$
t_L	time lag	$[s]$
T	wave period	$[s]$
u	u-axis velocity component	$[ms^{-1}]$
u_τ	friction velocity	$[ms^{-1}]$
u'	instantaneous fluctuating velocity	$[ms^1]$
U_0	free stream velocity	$[ms^1]$
v	y-axis velocity component	$[ms^{-1}]$
$\vec{V}$	velocity vector	$[-]$
V_{air}	volume of air	$[m^3]$
w	z-axis velocity component	$[ms^{-1}]$
WG_{EXi}	OWC External Water Level Gauge	[-]
WG_i	Water Level Gauge	[-]
Y^+	Non-dimensional Wall Distance	[m]
Z_i	OWC internal heave displacement	[m]

Greek Letters

α	volume fraction	$[-]$
β_d	up and downstream diameter ratio	$[-]$
δ	boundary layer thickness	$[m]$
Δp	pressure drop	$[Pascal]$
η_{HP}	hydraulic to pneumatic efficiency	$[-]$
η_{WH}	wave to hydraulic efficiency	$[-]$
η_{WP}	wave to pneumatic efficiency	$[-]$
ε	scale factor	$[-]$
λ	wavelength	$[m]$
μ	dynamic viscosity	$[kg\,m^{-1}s^{-1}]$
μ_t	turbulent viscosity	$[kg\,m^{-1}s^{-1}]$
ω	frequency	$[rads^{-1}]$

ϕ	phase	$[rad]$
ϕ_L	phase lag	$[rad]$
ρ_{air}	density of air	$[kgm^{-3}]$
$\bar{\bar{\tau}}^R$	Reynolds shear stress tensor	$[-]$
ζ	free surface level	$[m]$

Subscripts

air	property of air	$[-]$
$water$	property of water	$[-]$
$Inner$	inner dimension	$[-]$
max	maximum value	$[-]$
m	mean value	$[-]$
min	minimum value	$[-]$
$Outer$	outer dimension	$[-]$
seg	segment property	$[-]$
T	total value	$[-]$
$wave$	property of wave	$[-]$

Superscripts

$*$	normalised value	$[-]$
^{m}	model scale	$[-]$
^{F}	full scale	$[-]$
$\overline{x}$	average value	$[-]$

Mathematical Notation

δ_{ij}	Kronecker Delta Function	$[-]$
$\bigtriangledown$	Del operator	$[-]$
$\frac{\partial x}{\partial y}$	first order partial derivative	$[-]$

Chapter 1

Introduction

Ocean Wave Energy

Brief History

Ocean wave energy research has never been more important than in today's fight against climate change with the political pressure around the globe inevitably pushing for development. Although wave energy is still in its infancy compared to other forms of renewable energy, and even other forms of ocean energy like tidal, there remains a large unexploited resource and potential that continually reinforces the need for wave energy to play a big role in the development of the renewable energy mix. In these current political and socio-economic circumstances, greater attention will inevitably fall upon all forms of renewable energy as the pressure builds to increase overall capacity of renewable electricity generation. Although there are aims to increase this capacity and develop more energy efficient systems in the technologies we use day to day, world energy consumption is expected to rise by 28% before 2040 [1], in conjunction with global electricity demand forecasted to rise by 65%, with 85% of that demand expected to come from developing nations [2]. Here in the UK, the electricity generated by renewable sources only grew by 3.9% between 2018 and 2019, suggesting considerable progress in the development of the renewable energy mix has to be made in order to meet net zero targets of 2050, especially wave energy that can

contribute to 15% of the demand seen in 2019 [3, 4].

Ocean wave energy is under constant and steady development as researchers and entrepreneurs globally work to capture the immense and still untapped resource available in the marine environment. With the oceans covering $\sim 71\%$ of the earth's surface, wave energy is one of the largest sources of renewable energy yet to be harnessed effectively[5]. These waves are formed due to the interaction between strong offshore winds and the ocean surface over large areas and thus, this energy is essentially stored as waves that reach the shoreline having travelled very long distances while suffering minimal energy loss [6, 7]. Other forms of renewable energies are less power dense than both wave and tidal energy, with a typical density of 2–3 kWm^{-2} (with respect to the vertical plane orthogonal to the wave propagation direction) across a wave farm compared to an upper value of $0.6\,kWm^{-2}$ on wind farms. The lack of consistency and predictability with alternative forms such as wind and solar means that production is only possible for $20-30\%$ of the time in the UK, whereas wave energy can harvested from up to 90% of the time, however, the diversity of this resource and its extraction is far more complex. The nature and characteristics of ocean waves create several challenges in wave energy conversion and the variety of wave energy conversion concepts still indicate a distinct lack of convergence of technologies and hence the ongoing need for research and innovation in this field [5, 6, 8].

Current Status

Challenges and Barriers

Issues that affect or impede the progression of wave energy extraction technologies are either technological challenges or economic, social and environmental barriers. Wave energy converter design faces several great technological challenges, the major being the irregular and slow $0.1\,Hz$ wave frequency and behaviour that must ultimately become a smooth $50\,Hz$ required before feeding into the UK national grid. Perhaps the most significant challenge for WECs and offshore industries in general, is the extreme marine environment and hostile operating conditions. These inhospitable

conditions reinforce requirements for quality structural design, wise material choices, and survivability or mitigation methods. Storms result in wave power levels in excess of $2000\,kWm^{-1}$ [6], which not only tests structural integrity but is also worthless for power generation as these are extreme and infrequent occurrences, which devices are not tuned for and is therefore as futile as a flat ocean.

Aside from technological challenges, the external barriers can be categorised as detailed by O'Hagan et al. [9]; complex planning processes, administrative procedures, environmental impact assessment process, and interactions with other marine users and stakeholders. Wave energy devices are said to have a much lower environmental impact than other forms of ocean energy like tidal energy due to creating a form of costal protection in nearshore applications and in most cases there's less chance of animal strike. However, it is not necessarily proven that wave energy is overall less environmentally impactful. For example, it is not certain how, many large structures, underwater noise and electromagnetic fields from underwater cables may affect marine life along with long term affects such as on downstream costal impacts and moorings [10]. More than environmental issues, economic and social impacts need to be the focus of these external factors; these include quantifying positive socio-economic impacts and cost-benefit analyses. Despite the long list of external barriers, it is expected that as technology converges and development progresses, so will solutions to these external barriers.

Costs of Wave Energy

The cost of energy production is quantified with the Levelised Cost of Energy (LCOE) metric. As seen in Figure 1.1, this is dependent on the capital, and operational and maintenance costs, but more importantly with greater significance, the annual energy production [11]. Aside from improving performance and efficiencies to see an increase annual production, both capital and the operational and maintenance costs can be significantly reduced in with innovative designs, large scale deployment and hybrid or synergetic deployments. Hence, a WEC must be scalable to provide opportunities for array deployment or for integration with other applications. Thus, WECs must be at

least in the megawatt capacity realm ($> 1\,MW$) to become economically worthwhile [12]. Exemptions to the necessity of large scale WECs would be for niche off-grid applications such as fisheries, offshore platforms, small isolated communities or islands. Example of this are the deployment of the $200kW$ WEC at King Island, Tasmania and the microgrid plant deployed by Carnegie Clean Energy in Garden Island, Western Australia to serve a naval base [4]. In any case, where WECs can be scaled with respect to multiplying wave interaction systems (e.g. OWCs, point absorbers) in a larger system in order to increase capacity, as opposed to scaling dimensions beyond optimal values, significant reductions to the LCOE can be made so long as extra infrastructure or deployment costs outweigh benefits.

A 2015 case study including an OWC device and several sites on the Portuguese coast found a LCOE in the range of 81–109 EUR/MWh (59–79 $/MWh$) [13]. Another 2017 source gives an estimate of 31–74 EUR/MWh (27–65 $/MWh$)[1] for large and small devices respectively [12]. The LCOE for the average WEC is difficult to quantify with the small amount of data available due to the current development stage and the diversity in WEC types. At these lower development stages an accurate LCOE is difficult to forecast prior to full scale sea demonstrations since there are additional variables to consider at each level of scaling. Even at commercial sea demonstrations the uncertainty can be from -15% to $+20\%$ [12]. It is clear that WEC development is the most costly aspect in the lifetime costs of a project, accounting for 22% of total costs [10]. Installation of a farm therefore, without additional subsidies, makes the comparative capital costs of other energy sources such as fossil, nuclear and majority of renewables more attractive [14]. However, although the initial capital costs are high, without the need for fuel purchase, revenue becomes a function of the energy yield, hence the importance of annual energy production [15].

[1]Exchange rates used are average rates for year of publication from exchangerates.org.uk: EUR/GBP = 0.7263 (2015) and 0.8766 (2017)

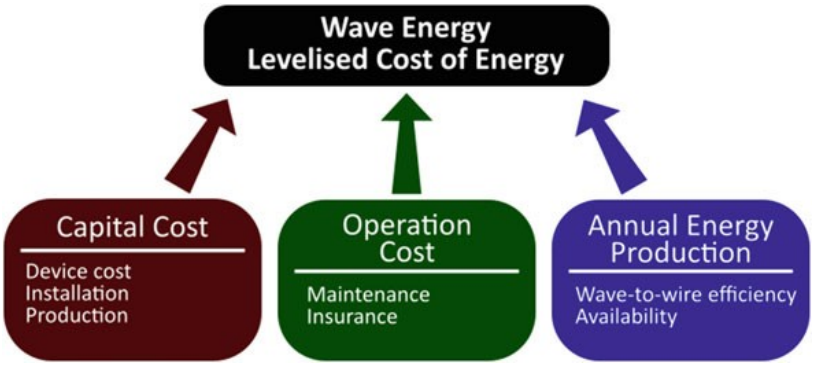


Figure 1.1: *Breakdown and description of the components that make up the Levelised Cost of Energy (LCOE) metric [12]*

Potential, Forecasts and Targets

There are many past and ongoing studies into wave energy resource that reveal the potential for both global [15–20] and local UK waters [21–23]. There are three different categories of ocean energy resource: theoretical, technical and practical. Theoretical is the quantified amount of energy available in a given area that could be captured and technical is the amount of this theoretical energy that can be affectively captured using a given technology. Practical resource then considers all constraints that may prohibit or affect energy harvesting in particular sections of a given area, for example environmental constraints and industrial interactions like fisheries or shipping routes. Total worldwide theoretical ocean energy resource is estimated to be between $45,000$ and $130,000\,TWh/year$, a range that exists due to variations in yearly weather and methods of estimation. Ocean thermal energy makes up the largest proportion of this theoretical potential followed by wave energy accounting for around $29,500\,TWh/year$ [24]. The UK and Western Europe are among the regions with the highest available wave energy resource as seen in Figure 1.2 [25]. The UKs theoretical potential is between 250 and $600\,TWh/year$ [16], which is roughly 35% of Europe's wave energy resource [26] and could 'theoretically' meet the UKs electricity demand of $323\,TWh$ as generated in 2019 [27]. Differences between theoretical and practical resource predictions here are around $70\,TWh/year$. [28, 29].

Since there can be disparities between resource quantification, the variance of estimations across literature that suggests there is a need for an accurate database

[16]. This is particularly important when considering WEC deployment, as devices can be best suited to particular locations and hence, accurate resource characteristics should be considered from the outset to allow for optimal extraction of the available resource [16, 30].

The current installed global capacity of all ocean energy technology types is $0.5\,GW$ ($2.31\,MW$ of wave energy), however it is projected that this could be $10\,GW$ by 2030 – a large increase in capacity that wave energy will play a large role in [24]. A more local and long term target set by the EU being to have an ocean energy capacity of $100\,GW$ by 2050 [31–33]. However, as of the end of 2016, in Europe only $14\,MW$ of ocean energy capacity was installed [34].

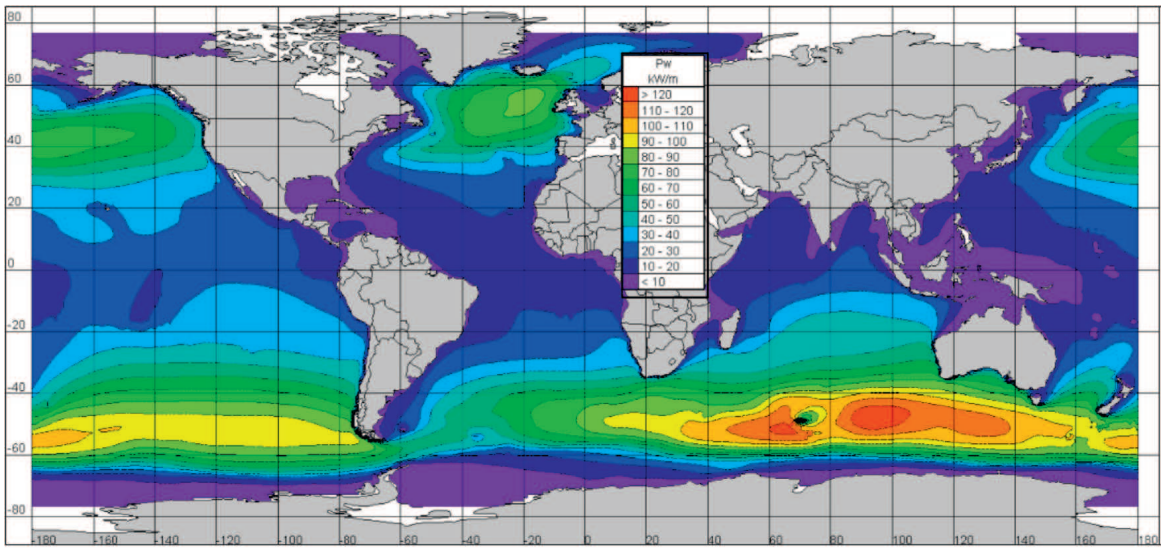


Figure 1.2: *Map illustration of the estimated theoretical global annual mean wave power resource [25]*

Background and Motivation

This project was made possible with partial funding from European Regional Development Fund (ERDF) through the Centre for Global Eco-Innovation (CGE). The CGE manages a large cohort of researchers and their projects across the North-West of England, all in collaboration with Small-Medium Enterprises (SMEs) to provide opportunities in developing a low-carbon future through innovative new technology.

All SMEs provide partial funding as industrial sponsors benefitting from the research as well as acting as industrial supervisors throughout.

The SME partnering in this project is Waves2Watts Ltd. - a company consisting of three directors who possess the Intellectual Property (IP) for a wave energy converter. Prior to this project, Waves2Watts (W2W) had not received any funding to develop this technology, hence the ultimate intention of this project, as per the CGE remit, was to progress the W2W WEC in order to further expand the company's future prospects and contribute towards a low-carbon economy.

The Waves2Watts Wave Energy Converter

History

The Waves2Watts WEC was patented in 2012 by engineering entrepreneur Robin Kyffin and was entitled *'Multistage Air Compressor With Turbine'* [35]. Along with other original design documents, the patent primarily details the operating principles and main structural characteristics of the WEC. The patent was also written in a manner that has kept flexibility in the concept to allow for its evolution during development, meaning it is not overly rigid in its specifications.

Prior to this project the technology of W2W had been the subject of an MSc research project at Bangor University in 2014 [36]. Work mainly entailed numerical simulations of the device chambers in a 2D numerical wave tank and separate air chamber simulations. The conclusions were not taken into consideration at the start of this PhD project since the research was more of an exploratory nature and the technology was only tested in an unvalidated numerical context rather than physically.

Operating Principles

The intended operating principles of the W2W concept incorporates an existing principle known as the Oscillating Water Column (OWC). In this subsection, the background and basic operational principles are briefly discussed.

The OWC concept has been applied worldwide in many different variances, pre-

ferred due to its simple operation with no submerged moving parts, structural robustness, ease of maintenance and versatility to be implemented in a wide range of applications.

As depicted in Figure 1.3 [37], structures are either floating or fixed and consist of a partially submerged open bottom chamber with a large enclosed volume of air above the internal free surface. As a wave approaches, the OWC harnesses the potential and kinetic energy of a wave by using free-surface movement within a column as a piston. Free-surface oscillation occurs as the peak of the wave passes and descends with the trough of the wave causing an exhale and inhale process, respectively, and a bidirectional airflow is generated as a result.

In the wave-to-wire conversion there are substages with two major conversion processes; the first stage being the pneumatic power from hydrodynamic interaction into mechanical power, where the energy of the waves pressurises the working fluid, which is utilised by the air turbine or PTO (Power Take-Off) system. The second stage is then the conversion from mechanical to electrical power using a rotary generator.

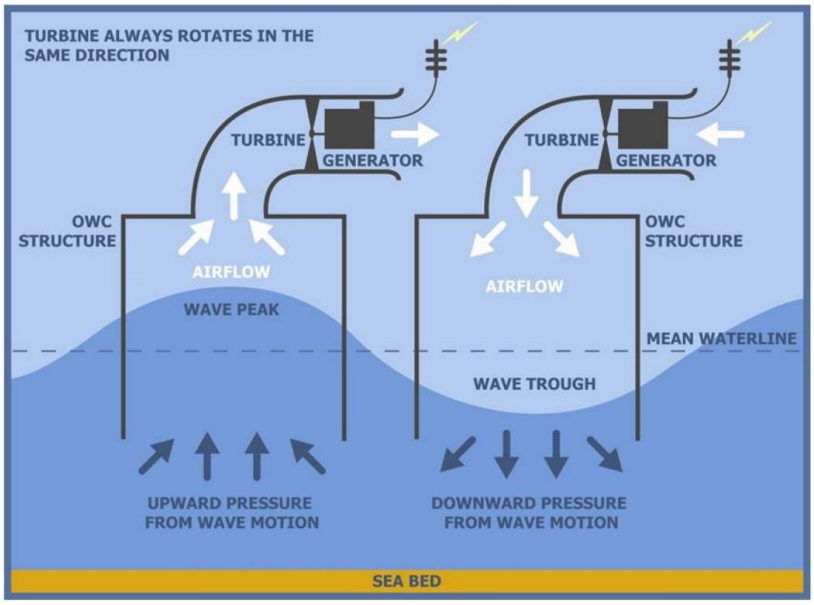


Figure 1.3: *An illustration of the basic Oscillating Water Colum concept and operation in its most general form [37]*

The Concept

The Waves2Watts WEC is described in the patent as a 'multi-stage air compressor', which comprises of several coupled tanks/chambers. As represented in the original design sketch of Figure 1.4 [35], these 'open-bottom' chambers contain a heaving free-surface that subsequently pressurises the air volume, hence why this concept was identified as an Oscillating Water Column based device.

As shown in Figure 1.4, OWC chambers are arranged in series along the length of the device in the direction of wave propagation, in attenuator formation. Each chamber operates as an individual OWC with separated heaving water columns, however, the air is transferred between chambers in an downstream direction following the heaving sequence generated by the wave interaction. This means that chambers are essentially pneumatically coupled with unidirectional valves to encourage airflow in the same direction as the propagating wave response in order to theoretically accumulate higher pressures and a higher unidirectional flow rate.

The overall process (from wave to turbine) begins at the first chamber, as a trough passes causes negative vertical displacement) and air is drawn from the atmosphere, which defines it as an open system. The air is subsequently compressed as the peak of the wave generates a positive vertical displacement in the chamber creating a higher pressure. This temporary pressure drop between the first heaving chamber or fully elevated pressurised column and the subsequent chamber that is experiencing a lower pressure due to a lower or descending water level causes the airflow through the unidirectional valve and into the next (downstream) chamber. This process is repeated to ideally create a multi-stage compression effect across an undefined number of neighbouring chambers until airflow reaches a final stage, the top tank (accumulator), which is then coupled to the PTO system, in this case incorporating a unidirectional air turbine. Overall, the claims of the patent and intention of the W2W is to create an open system capable of generating a high-pressure differential with respect to the atmosphere instead of having additional structures for separate low-pressure ducts – as is done with many other multiple chamber OWCs or Multi-Oscillating Water Column (M-OWC) concepts.

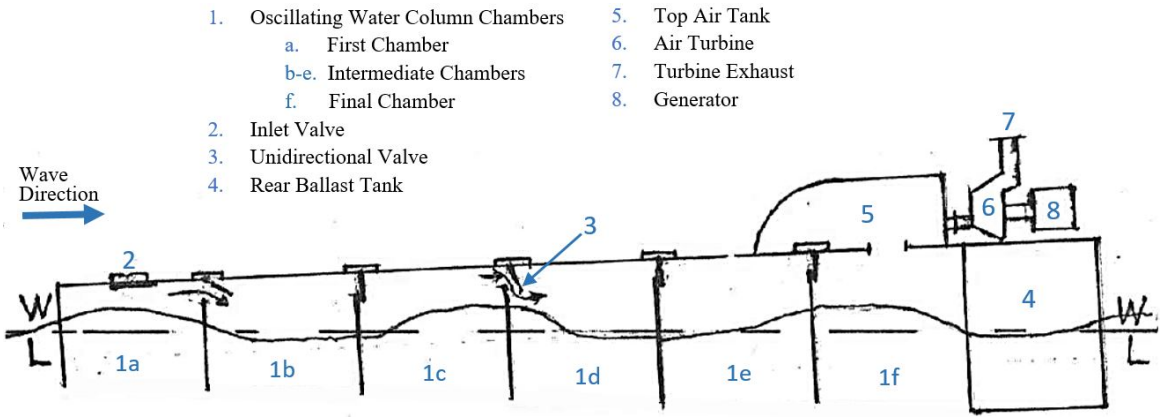


Figure 1.4: *An annotated version of the original design sketch of the W2W concept from the patent forming the starting point of this project [35]*

Besides the energy generation features of the W2W concept, the structure also includes ballast tanks on the sides and rear of the OWC chamber skeleton to provide the appropriate levels of buoyancy.

The patent has been well written to leave certain aspects of the concept wide open to allow room for changes that will inevitably come with development. Some of these aspects are: the device angle or orientation with respect to the wave direction, the number, shape and orientation of the chambers, ballast tank arrangement, and PTO type.

Discussion on the Waves2Watts Concept

Theoretically there are many benefits of the W2W concept, which aim to tackle the disadvantages of the standard OWC concept, while simultaneously superseding or improving on the advantages of the standard OWC. The main advantage of the W2W is the generation of unidirectional airflow, which enables the use of a more efficient unidirectional air turbine as opposed to a bidirectional self-rectifying turbine. While this can significantly improve PTO efficiency, especially with a relatively higher pressure drop, it also adds complexity to the previously simple OWC concept with the inclusion of mechanical valves. Furthermore, with an overly larger structure comes potentially less versatility and higher cost, which must be accounted for with higher efficiencies. Therefore, the Waves2Watts WEC must not only generate a more desir-

able and smoothed output but an increased output by a factor equal to the number of chambers.

Technology Development Assessment for WECs

The W2W has not been the subject of any experimental modelling prior to this project, therefore the operation and performance of the W2W WEC was solely speculative. Hence, this would involve physical modelling of the device or its individual subsystems in a wave tank in order to determine if operation would be viable. Innovation plays a key part in WEC development and the stage at which ideas are initially put to the test is known as the Concept Verification stage. Wave energy technologies, like any other, have a development process outlines, the main of which is known as the Technology Readiness Level (TRL) scale. The TRLs and development protocols, [38–41], outline the necessary steps to be taken during WEC development to finish with a viable and attractive deployment proposal. Although the content in these levels vary slightly, especially between engineering applications, Figure 1.5 summarises the general content for each level of a WEC development application [42]. Each level represents a functional and lifecycle state of readiness. Starting with concept verification, whereby technology must demonstrate intended operational principles and indicate potential for a continuation of development as a technology worthy of investment. The potential competitiveness of the technology cannot and should not be deciphered at this stage since the main focus is proof of operational viability.

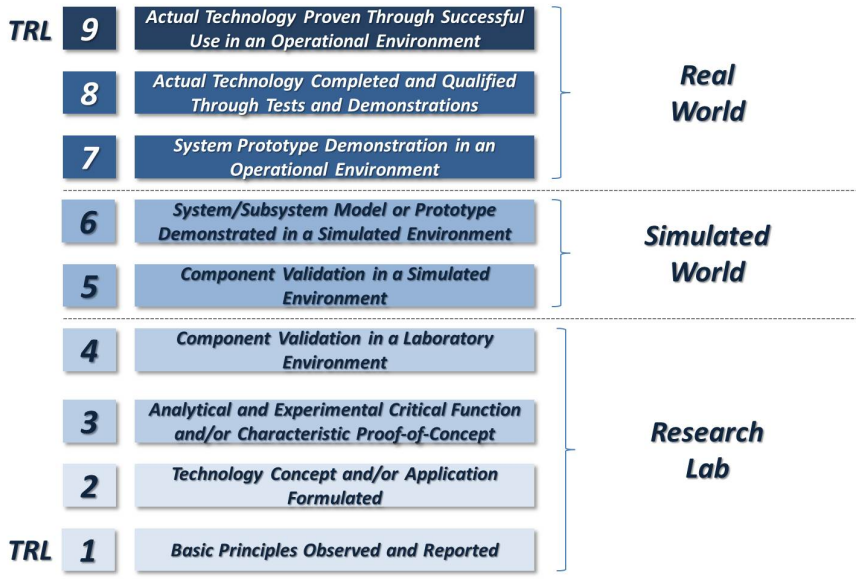


Figure 1.5: *The generalised Technology Readiness Levels scale for the technological development of wave energy converters [42]*

Attaining the criteria of each successive TRL is vital as the cost of financial investment increases significantly but as confidence in the technology grows this investment becomes more and more warranted. The TRL scale, which is used to gauge technical maturity mostly is complemented by the Technical Performance Levels (TPLs), which rate economic potential based on additional points of social, environmental and legal acceptability and are also largely based on the LCOE and its components as discussed above: capital and operation expenditure and overall energy extraction performance [12]. These economic factors are not necessarily solely based on energy production related costs but all relevant cost drivers from manufacturing through to deployment and operational management. At low TPLs (levels 1-3) are technologies that are not yet economically viable, hence performance and cost drivers are large barriers to financial viability. At high TPLs (7-9) the technology must be competitive against other energy sources, ideally without additional financial support structures [12, 43]. Hence, while the TRL is more focused on the readiness of the technology from a commercial stand point, the TPL is concerned with the techno-economic performance of a WEC [44]. Since both are ultimately dependent on the Cost of Energy (COE), they are interlinked with a relationship that can be seen in Figure 1.6.

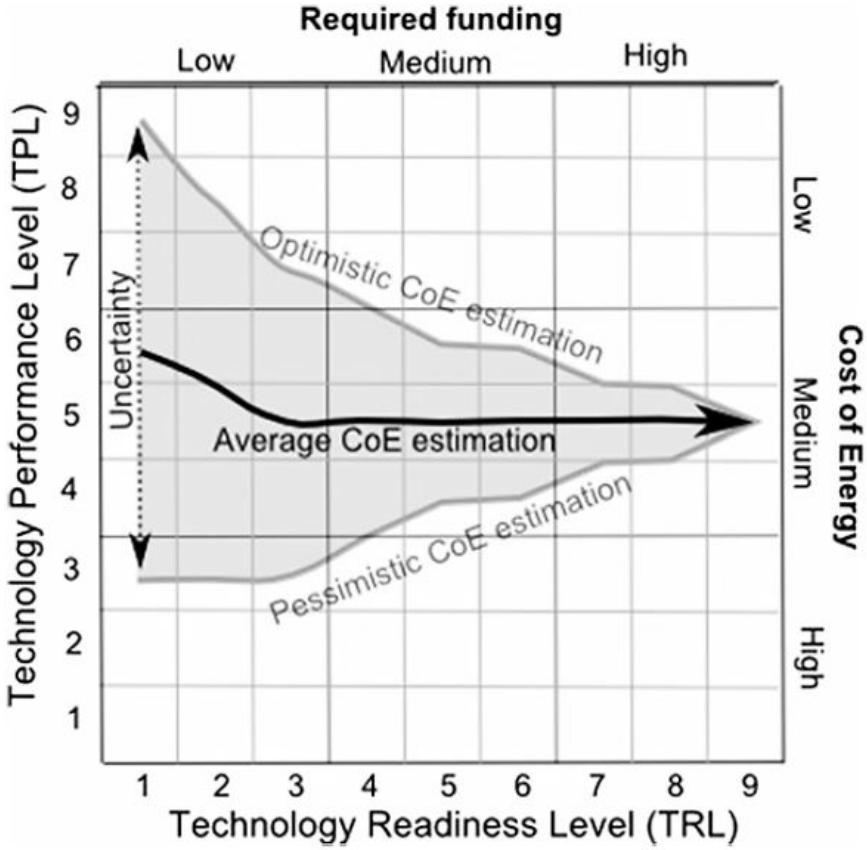


Figure 1.6: *Technology Readiness and Performance Levels plotted against required funding and the cost of energy [12]*

In the latter stages, indexing is complemented by the Commercial Readiness Levels (CRLs) index, a financial based protocol [45]. Due to the large and demanding financial support, WEC technology should present an attractive investment opportunity to provide a competitive alternative to not only non-renewable but other renewable sources and other WECs. Based on a number of factors, currently the highest competition from within the wave energy sector is the multi-point absorber and attenuator WECs, which have the highest deployment attractiveness in the USA and UK, respectively [11].

Aims and Objectives of Research

The primary objective of the PhD research is to verify the W2W concept as described in the patent and proceed with identified areas of development to bring the technology

from TRL 1 to low TRL4. Although this project is centred around the W2W WEC, among the main objective and goals for development of the technology are multiple research questions that need to be answered. These questions form the research aims that make up Phase 1 and Phase 2 of this project.

Phase 1 features the original design of the W2W WEC as per the details of the patent. From the operating descriptions presented in the patent there were two main research questions that formed the aims of Phase 1:

1. Determining the feasibility of achieving efficient hydrodynamic performance while attaining opposite free surface responses in adjacent chambers - ascending internal free surface in the first chamber and descending in the neighbouring chamber and so on.

2. Understanding the effects on performance and behaviour of pneumatically coupling OWC chambers in attenuator formation while restricting airflow to only travel in the direction of the propagating wave through the device. Particular focus is on whether the pressure accumulates with the positive response of each chamber and does the energy extraction process benefit from this.

The research of Phase 2 involves a significant evolution whereby the W2W device concept is improved substantially via a progressive manner of modelling by answering research questions in a pragmatic and sequential order. These research questions are initially aimed to provide insight to performance differences when scaling up the number of OWCs in a system. These investigatory points are framed like so:

1. Determine performance differences between a single chamber OWC, an OWC array as an M-OWC and a modular M-OWC when modelled on a level playing field. The success of combining the extracted power at different stages of the OWC conversion process, namely at the pneumatic stage with the modular M-OWC.

2. Ascertain the effects of change in M-OWC orientation from attenuator and terminator with respect to device operational behaviour, versatility and deployment attractiveness.

3. Quantify the differences caused by spacing between OWCs for M-OWC concepts on hydrodynamic performance and the capture efficiency as a result across the width of the wave.

   Following this study of progression from singular to multi OWC concepts, the modular M-OWC with such versatility and potential also poses additional research questions, which are aimed to be answered in the same manner, by modelling variations in the same setting to determine:

4. The effects of breakwater integration schemes on M-OWC performance as well as overall effectiveness as a breakwater. i.e. can such a device fulfil dual roles in an integration scheme.

5. Determine benefits of unidirectional over bidirectional pneumatic systems and whether it yields more desirable performance with respect to pneumatic power extraction.

6. Can a numerical model reliably predict the performance of a 3D M-OWC model and provide additional insight into device behaviour not observable in the experimental setting.

Thesis Structure and Overview

This section gives a short overview of the contents of the eight chapters that comprise this PhD thesis:

Chapter 1 gives an introduction to the thesis topic outlining the motivation of the project along with the background details into the technology and the objectives that form this research.

Chapter 2 contains an overview of relevant wave theory and in-depth literature review of wave energy technology, more specifically OWCs, M-OWCs, PTOs and synergetic deployments. Applicable theory and the application of CFD in WEC

development is outlined. Finally, a summary and discussion concludes the chapter by highlighting the gaps and unanswered research points in the literature.

Chapter 3 contains the methodology for the experimental modelling covering set-up, design of models, analysis methodology and discussion behind all of these decisions made.

Chapter 4 covers Phase 1 of the research, which contains the project's verification investigations on the original W2W concept and all associated experimental modelling involved in realising the research aims 1 and 2.

Chapter 5 is the beginning of the research carried out in Phase 2 of the project, covering the start of investigations into M-OWC behaviour compared to a single OWC and various changes in operating conditions, covering research aims 3 to 5.

Chapter 6 is a continuation of Phase 2 with the addition of the breakwater modelling, reflection and frequency domain analysis, as well as the testing of three different PTO models (research aims 6 and 7).

Chapter 7 contains all of the numerical modelling carried out for pneumatic system and Numerical Wave Tank models and the analysis supporting the conclusions made on the previous experimental data (research aim 8).

Chapter 8 includes the conclusions of all the research presented, a discussion and recommendations for future work.

Chapter 2

Literature Review

Ocean Wave Theory

Wave Generation and Propagation

There are various types of water waves characterised by their frequency that are generated by one or more of the external forces that interact with the free surface of the oceans (Figure 2.1 [46]). Perhaps the most obvious and observable of these external forces is the wind, which with the help of the surface tension created in the air-water interface, develops capillary waves. Greater interaction from strong offshore winds over large distances called a fetch, creates large waves known as swell or gravity waves, hence, those restored by gravity. These waves are able to travel thousands of miles with very minimal dissipation in energy, in fact often increasing in energy in further local wind conditions. These ocean swells only dissipate their energy at the distant shores they travel to or during impact with any offshore structures. This is the great attractiveness of waves, that although they are essentially an indirect form of solar and wind energy from far offshore, they transfer this energy to our coastlines.

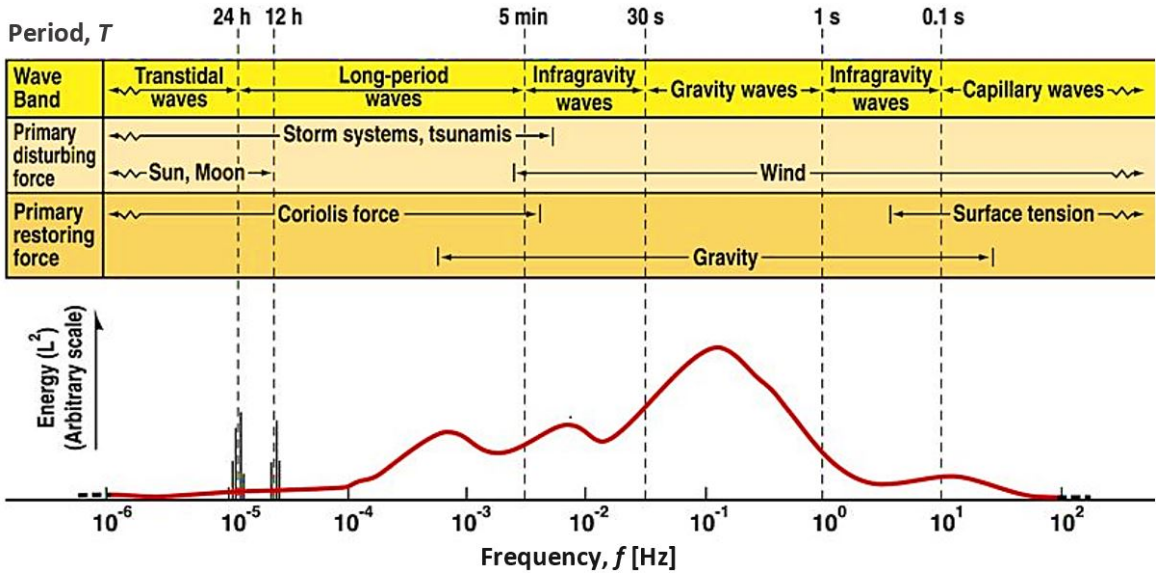


Figure 2.1: *Wave energy spectrum illustrating the range of different wave types across all frequencies with their respective disturbing and restoring forces and relative energy levels [46]*

Beneath the displacing free-surface caused by a propagating wave is what is known as a water column. Although waves cause free surface displacement, they do not transport mass since the path of particles beneath the surface in this column have a closed path due to their orbital motion. These orbital paths reduce in radius as depth increases with the largest forming the crest of the wave at the free-surface; this is illustrated in Figure 2.2 among other key wave characteristics. The interaction between this water column and the seabed increases as relative depth reduces, transitioning between classifications known as deep, intermediate or shallow water waves, causing the wave to shoal, which decreases wavelength and velocity due to an increase in steepness eventually causing the wave to break. Depending on the wave characteristic or motion to be exploited, wave energy harvesting is possible within all of these wave regimes, which are defined within the following limits:

$$Deep\,water\,wave \left\{ d \geq \frac{\lambda}{2} \right. \tag{2.1}$$

$$intermediate\,water\,wave \left\{ d < \frac{\lambda}{2} \right. \tag{2.2}$$

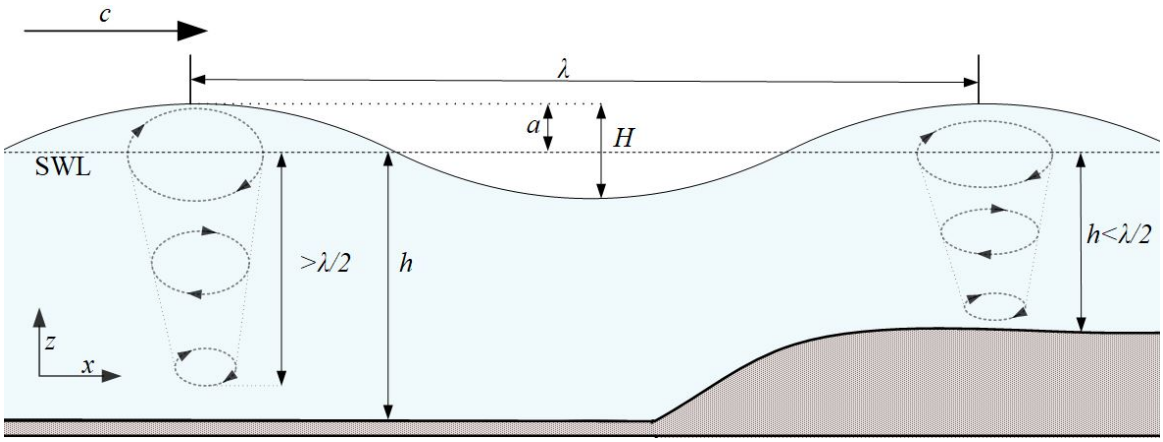


Figure 2.2: *Characteristics and properties of water waves and illustration of deep and intermediate water waves in the XZ plane*

Linear and Non-Linear Wave Theory

Linear Wave Theory

Also know as Airy's Theory, linear wave theory expresses the spatial and time dependent free surface profile $\zeta(x,t)$ as first order linear equation (Eq. 2.3). In order for waves to be considered as a linear wave it must be possible to describe the free surface profile with the linear first order expression:

$$\zeta(x,t) = \frac{H}{2}\cos(\frac{2\pi x}{\lambda} - \frac{2\pi t}{T}) \tag{2.3}$$

Hence, linear wave theory is only a first order expression and therefore has the simplest of wave profile shapes, it therefore simplifies wave mechanics and allows for the straightforward derivation of further wave properties. For deep water waves, linear wave theory only holds accurate for smaller amplitude waves and at lower steepness where non-linear effects are negligible , generally, the ratio of H/λ or steepness must be < 0.02 or $1/50$. For shallow water waves, the limit is more dependent on the relationship between wave amplitude and depth due to the shoaling effect.

Since the restoring forces of a deep water wave is caused by gravity, the speed an individual wave, known as phase velocity c, results in the dispersion relationship, linking the period of a wave and its wavelength [47]:

$$\lambda = \frac{gT^2}{2\pi}\tanh(\frac{2\pi h}{\lambda}) \tag{2.4}$$

The energy in a wave is equal to the sum of the potential energy (E_P) and kinetic energy (E_K). This energy is expressed as the total energy per unit width of the wave crest in Equation 2.5 [48].

$$E_{wave} = E_P + E_K = \frac{1}{8}\rho g H^2 \lambda \tag{2.5}$$

The potential energy of a wave is a result of the vertical displacement z of the free surface. The kinetic energy is due to the orbital motion of water particles beneath the free surface of a propagating wave and within the water column as depicted in Figure 2.2 and is a function of the period and depth only [47]. This aforementioned water column with particles of orbital velocity paths have the horizontal and vertical velocity components u and w, respectively:

$$u = \frac{H}{2}\omega\frac{\cosh\left(K(h+z)\right)}{\sinh\left(Kh\right)}\cos\left(Kx - \omega t\right) \tag{2.6}$$

$$w = -\frac{H}{2}\omega\frac{\sinh\left(K(h+z)\right)}{\sinh\left(Kh\right)}\sin\left(Kx - \omega t\right) \tag{2.7}$$

Where K is the wave number equal to $2\pi/\lambda$.

Non-Linear Wave Theory

As the free-surface shape of a wave changes, not only due to intermediate or shallow depths but perhaps local conditions such as wind, their description requires different orders of non-linear expressions. Figure 2.3 shows these different theories and their ranges of eligibility with respect to terms relative depth (on the $X-axis$) and relative wave height (on the $Y-axis$) [12]. This reiterates that such non-linearities are not solely caused in shallower depths due to shoaling but also due to profile altering interactions or increased steepness caused by local wind conditions. While shallow waves are completely non-linear, the linear theory covers a broad range of intermediate and deep water waves. The more common non-linear theories for these regimes are

the 2^{nd}, 3^{rd} and 4^{th} order Stokes theories in order of increasing steepness up to the point of the critical steepness level of $s \approx 0.142$.

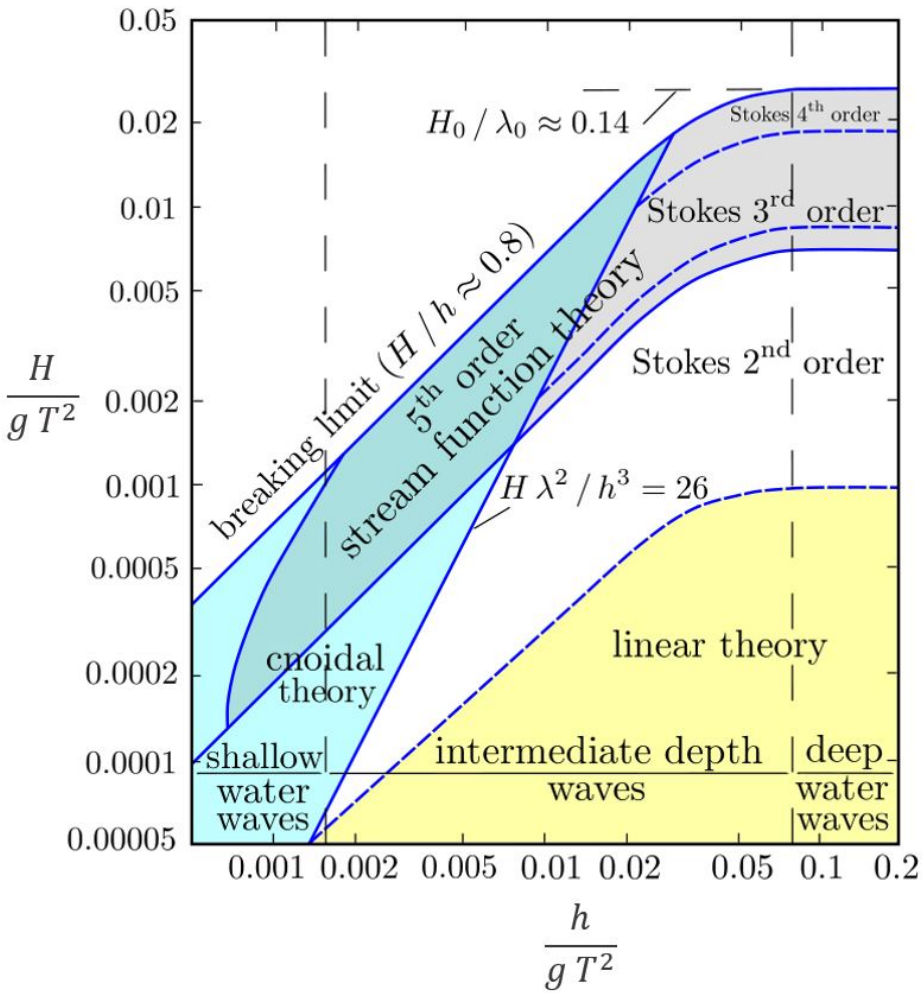


Figure 2.3: *Identification of wave theories for linear and non-linear waves according to terms of relative water depth and relative wave height [12]*

Regular and Irregular Waves

In an ideal world ocean waves would be regular, monochromatic and predictable for much easier energy harvesting. Of course, these waves can be created in an experimental setting but in the real world, waves are irregular and often also random. Figure 2.4 illustrates the added complexity real world waves add to the energy extraction challenge as the shapes of these signals are somewhat mimicked in the output power signal often requiring substantial post-processing and smoothing [49]. Although in ex-

perimental investigations it is beneficial to observe how WECs might react to regular waves, it is important to also understand the effects of irregular incident waves.

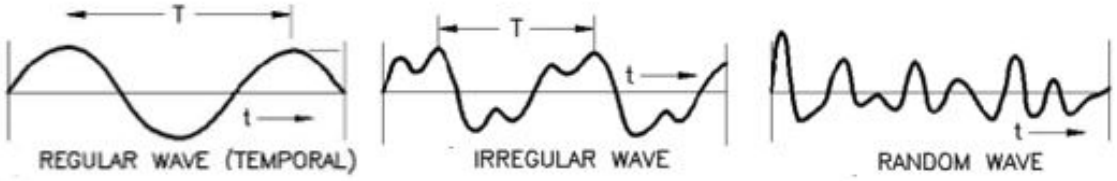


Figure 2.4: *The different wave regime categories illustrated by plots of the free surface in the time domain [49]*

The data from regular waves can be relatively simple to analyse since the identical periodic nature of the wave is reflected in the results but for irregular waves this becomes more complex. However, the Fourier Series theorem states that any wave or oscillatory signal is essentially the sum of many regular monochromatic signals of different amplitudes, frequencies and phases:

$$\zeta(t) = \sum_{i=0}^{\infty} a_{wave} \cos(\omega\, t - \phi) \tag{2.8}$$

Therefore, through carrying out a Discrete Fourier Transform on a wave signal (Eq. 2.9), one can convert a signal into the frequency domain to derive the spectra and determine the energy density, total energy, peak frequencies, harmonics, significant wave heights and much more in the signal segment analysed.

$$X(k) = \sum_{n=0}^{N-1} x(n) e^{\frac{-j2\pi kn}{N}} \tag{2.9}$$

This becomes extremely useful for not only analysing irregular wave data but also for characterising sea states. The time series data for processing must be sampled at a rate greater than twice the peak frequency according to the Nyquist sampling frequency or limit:

$$f_{Nyquist} = \frac{1}{2} f_s \tag{2.10}$$

The Nyquist frequency is also known as the folding frequency, since in the case that

this condition is not met, where there is not at least two sample points per oscillation, the spectrum generated will not be accurately representative and will be distorted [38].

Several characteristic irregular sea states exist as a result of the live monitoring of wave data in the field followed by Fourier analysis to obtain spectral shapes and subsequently models such as the JONSWAP and Pierson-Moskowitz (PM) models [50]. The chosen spectral model used in thesis this is discussed in the following sections.

Wave Energy Converter Technology

Endeavouring to harvest ocean wave energy is not a new concept but interest is very much dependent on our energy demand and therefore urgencies. Of course, the lack of certainty in crude oil reserves and the climate change disaster has stirred significant attention with a joint invested interest to meet our energy demands in a less impactful, secure and sustainable way. Despite sharp fluctuations in interest and urgency, wave energy technologies in particular are yet to converge unlike other types of renewable energies since there are over one thousand WEC patents with very few that have progressed into development, let alone full-scale demonstration or commercialisation [25]. Several extensive reviews of all WEC technologies can be found in literature [31, 34, 51–54], and more specific reviews exist for specific types such as the OWC [55, 56]. Although such reviews list known WEC concepts and devices in development, true numbers in development are uncertain.

Classifications

With a very large number of WEC patents also comes a large variety in operational methods, orientations and deployment applications. Therefore, WECs can be characterised with many sub-categories, the most common classifications being by their operational concepts, their locations with respect to the shoreline, their state of buoyancy or water depth positioning and orientation with respect to the incident wave.

These categories and their respective classifications are:

- Operational concepts; (floating/oscillating body, oscillating water column, overtopping, oscillating surge converter, rotating mass, pressure differential)
- Locations with respect to the shoreline; (onshore, nearshore, offshore)
- Deployment state; (fixed, floating, submerged)
- Orientation with respect to the incident wave; (attenuator, terminator, point absorber) [6, 8].

The orientation of a WEC is not exclusive to particular operational types. For example, OWCs exist as point absorbers, attenuators and terminators, with the latter two more commonly relevant to Multi-OWCs. Figure 2.5 illustrates the differences of these orientations with respect to the incident wave direction. Attenuators should be equal to or longer than the incident wavelength in order to affectively attenuate the wave, meaning they are normally very large structures. Their slenderness relative to terminators means they experience less resource although refraction as wave propagates along the device allows the device to see a larger resource than in just the width of the structure. Terminators should also be as large as possible but depending if they're shoreline or not, don't have to be as wide as a wavelength. While attenuators can experience stability issues due to their length relative to changing incident wavelengths, terminators are 'terminating' the wave and therefore need to be extra structurally resilient to surge pressures and impacts compared to the attenuator.

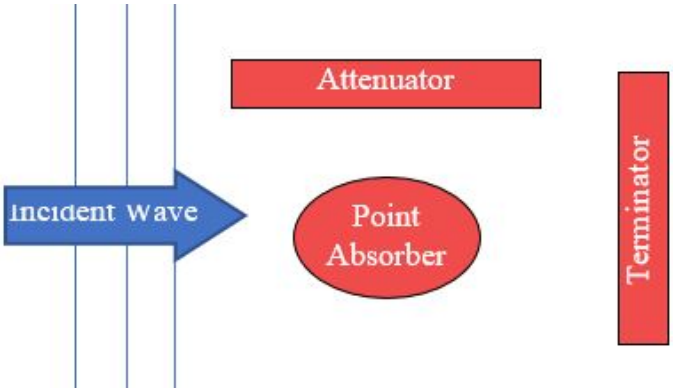


Figure 2.5: *Diagram illustrating the different orientations of wave energy converters with respect to the incident wave direction*

Further sub-categories include those used to characterise alternative WEC operation with respect to different wave-to-wire conversion processes, such as PTO arrangements or unusual characteristics based on biomimetic rules [57]. Some alternative devices somewhat cultivate their own sub-category, such as piezoelectric seaweed [58].

Energy Conversion

Different stages of wave energy conversion for different device types are shown in Figure 2.6 [55], with the path of OWC device highlighted. This is split into the two major conversion stages: wave to mechanical power (1^{st} stage) and subsequently mechanical to electrical power (2^{nd} stage). The key difference between all WEC concepts is their hydrodynamic interaction and thus which characteristic of a wave the WEC aims to exploit and how this interaction translates into the next form of power, be it pneumatic like OWCs, hydraulic or mechanical like point absorbers or surge converters, water flow like overtopping devices, or finally, directly to electricity as with linear generators in heaving point absorbers. These various types exist due to the many characteristics a wave has available for exploitation, for example: heave, surge, pitch, the sub surface pressure field or orbital velocities and more. Despite the quest for technology convergence, it is highly likely that all variations of WEC styles will always exist in their respective niche application, which is an attribute that makes wave energy so unique and diverse.

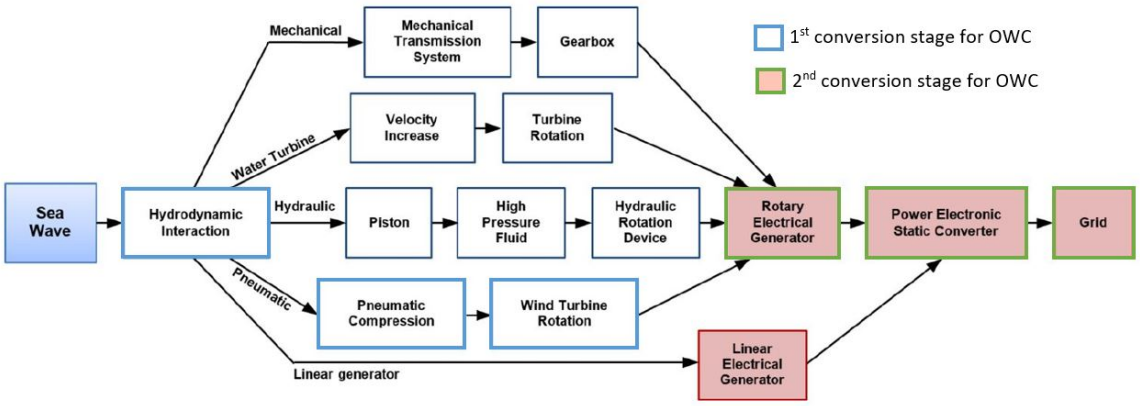


Figure 2.6: *The paths toward wave energy conversion based on the different conversion stages for different WEC types (adapted from [55])*

Oscillating Water Column Development

Origins

Of the main WEC categories listed above, the OWC is one of the most popular, often praised for its robustness, simplicity and versatility. The earliest recorded example of an OWC-like concept is the Bouchaux-Praeique WEC in around 1920 [47]. However, the more official beginnings dates back to 1965 in Japan where engineer Yohsio Masuda implemented the concept into a fairway and weather buoy, which were powered by the waves rated at 70 W and 120 W respectively [59]. Hence, from here on Masuda was considered to be the father of the OWC and later patented the OWC concept and some variations in the 1980's [60] before going on to scale up the concept with a commercial-size device known as Kaimei in Japan (1978), developed by the Japanese Marine Science and Technology Centre (JAMSTEC). The original Kaimei had an impressive 22 OWC chambers but was subsequently reduced to 13 chambers in the second round of sea trials [61]. The JAMSTEC continued development much later (from 1998) with trials of the 'Mighty Whale', a 50m long 3-chamber prototype [62, 63]. Other OWC prototypes were built subsequently, not only in Japan with fixed onshore variations like the shoreline Gully, Sanze, the Offshore Breakwater of Sakata Port, The Kujukuri and Haramachi [64], but also globally, in nations including Norway with the Toftestallen (1985) and India with the Vizhinijam (1990) [65, 66], all of which are notable and influential deployments not only in their respective countries but globally as the OWC concept developed favourable traction.

Devices and Development

A knock-on effect from some of the aforementioned OWC deployments and their variations ultimately led to the decision of the European Commission to include wave energy in the JOULE programme, whereby two onshore pilot OWC plants were constructed. One called the Pico Plant (1999), in the Azores, Portugal, and the other called LIMPET (Land Installed Marine Power Energy Transmitter), on the Isle of Is-

lay, Scotland [56, 67–69]. The LIMPET was the product of a collaboration including the Queen's University of Belfast and Wavegen Ireland Ltd. and was commissioned in 2000 following a smaller capacity prototype constructed in 1991. The LIMPET supplied electricity to the UK National grid (a first in the UK for wave energy) and providing a test and demonstration facility for developing technology such as turbines [70]. Voith bought the power plant in 2005 and it continued to supply electricity despite having faced the largest storms recorded on the Islay until it was decommissioned in 2012. The Pico plant has also since served the wave energy community in facilitating very useful research and development, for example, being involved in six or more European projects. Following a storm on the 17th of April 2017, the Pico Plant suffered significant structural damage, and due to lack of financial support WaveEC made the decision to dismantle the plant in 2018 [67].

Aside from fixed OWCs mentioned, since floating devices such as the Mighty Whale, predominantly just singular column devices have been considered for offshore deployment. For example, as more of a point absorber type OWC like the Spar Buoy, a simple, compact and stable floating axisymmetric device contains the OWC inside the length of the body [56, 65]. A more generic OWC example is Oceanlinx, previously known as Energetech, proposed devices (greenWave, ogWAVE, BlueWAVE) are singular OWCs designed for different water depths and wave conditions. A 1 MW prototype of the greenWave device was launched in Australia in 2013, however due to a transportation incident, the deployment was not completed [71, 72]. Worldwide, OWC deployment has seen the failure of a number of other devices destroyed by the harsh marine environment - devices such as the Toftestallen, Norway; Osprey, Scotland; Pico Plant, Portugal; and the Mutriku in Spain [67, 73, 74].

OWC Arrays

As with other forms of renewable energy, power density is dependent on the capture area or width of the wave and thus this capture area needs to be maximised. Furthermore, the economy of scale is applicable with respect to increasing capture and decreasing capital cost per WEC. However, additional challenges arise with ar-

ray or farm deployment such as mooring, spacing and positioning configurations, due to radiation and transmission effects of many devices in relatively close proximity. Some of these effects have been studied, regarding optimal layout, orientations and configurations mainly through prominently analytical or numerical methods [75–77].

In a study carried out at the Queens University Belfast coastal wave basin, cylindrical shaped OWCs arranged in various configurations of arrays including, terminating, attenuator, diagonal/angled and V-shaped formations were tested. The results of these experiments proved that the terminating array was superior with respect to minimal wave disturbance and highest power capture for configuration with spacing greater than the incident wavelength [78].

Thiruvenkatasamy and Neelamani also conducted spacing experimental tests on 1:50 scale models of free standing caissons for breakwater integration. From this analysis, it is clear that performance is highly dependent on spacing, array configuration and PTO damping. [79]

Evolution of the standard single chamber OWC

Through various concepts, the OWC has evolved beyond the more basic original concept found in the previously mentioned deployments. Naturally these evolutions are steps made to improve on the OWC's disadvantages and/or diversify with integration or synergetic applications.

With respect to the hydrodynamic performance, as conveyed in the investigations by Kurniawan et al. [80] on WECs with compressible volumes, the positive performance characteristics of resonant conditions or frequency matching is found to be very much dependent on the WEC body heave or moving surface. For OWC variations referred to as multi-resonant devices, active WEC body or moving surface must change to become a self-tuning device and to operate efficiently in a wider range of frequencies based on the principle that different lengths of the internal water column effect the resonant period of the OWC [81]. An example of a single OWC multi-resonant device is the Ocean Energy (OE) Buoy, which is based on the Backward Bent Duct Buoy concept [82], having an L-shaped chamber with the inlet facing in the direction of

the propagating wave (away from the approaching crest). The concept was developed by Masuda in 1986 who found that by having an L-shaped duct rather than strictly vertical, the bandwidth of optimal operation increases and therefore improving performance in irregular waves [56, 82].

Multi-resonant capabilities have also been developed for the onshore application where there aren't necessarily the depths to extend chamber lengths. The answer was found with the U-shaped OWC, essentially extending the water column in order to create a tune ability and effectively *'force'* resonance [83]. This concept was subsequently implemented with such devices like the Kvaener [84] and multiple breakwater synergy projects born from the REWEC (Resonant Wave Converter U-OWC), an ongoing retrofit project on the breakwater Italian harbours [85, 86].

As mentioned, the other significant drawback to most singular OWC designs is the bidirectional airflow as a singular OWCs manipulation of the pneumatics in order to achieve unidirectional airflow is difficult. A spar buoy type device called the Tupperwave manages this creating unidirectional airflow by having two air additional chambers above the working OWC, one for the inhalation and one for the exhalation situated downstream and upstream of an air turbine respectively. Therefore, the inhalation that would normally draw the air back through the turbine, acts upstream to maintain the original direction of both airflow and turbine rotation creating a closed system of airflow [87] . Development of this device has been the work of University College Cork, Ireland, where 1:24 scale experiments were carried out. Experiments were ran for both regular and irregular waves with results compared to a conventional spar buoy OWC modelled in the same tests to give fair comparison. Performance results from the Tupperwave device have proven that the concept has potential to rival the original OWC [88].

A concept known as UniWave, being developed by Wave Swell Energy Ltd. from Australia also operates with a unidirectional flow turbine in a singular OWC device. However, airflow is only passing the turbine for half the wave period, which is during the inhalation of the air from the atmosphere. During upward free surface displacement inside the OWC, the pressurised air is exhausted directly to the atmosphere

resulting in atmospheric pressure in the chamber at the maximum OWC displacement amplitude. Small scale (1:30) tests have been carried out from which the peak pneumatic efficiency in irregular waves was recorded at 83% [89]. Deployment of a $200\,kW$ known as the UniWave200 shortly followed at King Island, Tasmania, for validation purposes [90].

Ultimately, additional features could be incorporated into OWC technology to improve further more minor disadvantages of the basic concept. With respect to overall tune-ability, various factors could be made adaptable, such as the turbine damping and air volumes. These characteristics are achievable in the device studied by Kurniawan et al. [91], which uses flexible deformable body, proven to increase bandwidth, to generate airflow between two volumes.

Hydrodynamic Challenges and Survivability

This section reviews research on the survivability aspects of OWCs, aside from regular device demonstrations like the M-OWCs previously mentioned. There remains uncertainty into certain aspects of OWC behaviour such as wave breaking impacts and sloshing both internally and externally, which result in potentially large and structure compromising loads. Hence, one of the challenges facing WEC development and especially OWC development is the structural design and integrity. Wave loads can be external (front wall) or internal of an OWC, which can be the rear wall but also ceiling due to the internal pressures. All of these need to be taken into account during design in order to incorporate sufficient structural strength in the right places to avoid damage. The importance of such considerations are highlighted in the event of damage to a WEC such as the Mutriku plant that suffered damage said to have been caused by cavitation and sloshing during storms in 2009 [74]. Albeit due to use of the incorrect structural materials, the Pico plant had to be dismantled after weathering a fierce storm as previously mentioned [67].

A large measure of the uncertainty in OWC WEC development comes from the lack of understanding and ability to assuredly predict internal and external loads of an OWC in an irregular sea.Forces are highest when the wave is breaking, and therefore

studies generally include shoreline based OWCs such as breakwaters caissons. Various models have been developed in order to predict wave loads but few have proven to provide certainty, especially for irregular sea states conditions.

Using Finite Element computational modelling, Jalon and Brennan [92] investigate the relationship between the operational efficiency of a fixed-bottom OWC and its long-term survivability through fatigue analysis. Several different cases are modelled revealing instances where the improved hydrodynamic efficiency could be a trade-off for accumulated fatigue in one area of the structure. Such work highlights the importance of understanding the effects of particular hydrodynamic phenomena, which are discussed in this section.

One of the earliest examples of experimental modelling of wave load was for the front external walls by Muller and Whittaker [93]. The study investigates the breaking wave loads on the front wall with varying inclination angles: forward incline, vertical and backward incline. The tests included a shoreline OWC model scale 1:36 situated in $17\,m$ long wave tank with a depth of $1\,m$ and instrumented with four pressure transducers in the front wall. It was concluded that the highest impact pressures would be experienced by a wall with a forward incline between 5-10 degrees. Since these experiments there have been a run of small-scale studies into front or rear wall loads from Kuo et al. (1:40) in 2015 [94], Pawitan and Bruce in 2016 (1:81) [95] and Ashlin et al. in 2017 [96].

In 2014, a significant experimental study took place enabling developed models for predictions of wave loads, water column responses, PTO damping, scaling effects and more. This was approximately 1:5 to 1:9 scale testing from the GWK facility in Hannover, Germany, recorded by Allsop et al. [97] and Viviano et al. [98, 99]. Three large caissons were installed across the width of the $307\,m$ long tank, which was $5\,m$ wide and $7\,m$ deep. Front, rear and ceiling walls lined with pressure transducers, with three internal wave gauges and pressure taps around the inhale/exhale orifice to measure flow rate [97–99]. The intention of these experiments was to provide large scale OWC experimental data for the WEC community to aid in the development of a wide range of models, hence the range of instrumentation listed. Pawitan et al.

[100] made use of this experimental data in a comparison with a developed model for predicting pressure profiles resulting in vertical ceiling forces and maximum forces on front and rear walls based on the initial calculation of the referenced Goda pressure estimation model. The intention of such predictions is to provide forces and moment values to consider during structural design and reduce uncertainties. Closed top OWC results showed good correlation with the model predictions for measured pressure and rear wall force. During open top OWC tests, less prediction accuracy of rear wall loads was noted for higher wave steepness, which induced greater amounts of sloshing, hence the model is more reliable for lower steepness waves. However, in terms of prediction of chamber pressure, the model is more reliable at higher wave heights with vertical forces predicted during closed operation were within $\pm 20\%$. Proven to be less predictable were the irregular waves, where pressure measurements and forces were around $60 - 80\%$ over predicted.

Sloshing is the term used to describe the chaotic non-uniform movements of the OWC in the chamber. The occurrence of wave sloshing can happen; as a result of geometrical features that are incorrect for the sea state [101, 102] (as covered in Chapter 4), such as in the external sloshing example from the experiments of Muller and Whittaker [93] with a forward inclined front wall; and as a result of wave conditions such as steepness as mentioned above in the experiments of Pawitan et al. [100]. Sloshing is also said to be excited due to vortex shedding caused by sharp edges of the OWC in the study of Xu and Huang [103].

In earlier experiments of Pawitan et al. [104], scaled version of the Mutriku OWC were modelled to study the occurrence of sloshing during regular and irregular waves. Conclusions state that a large wavelength relative to the OWC width and a higher wave height (especially with a steeper wave), is more likely to induce sloshing and can be encouraged further when damping is reduced. The impact of sloshing on the ceiling of the OWC was significant relative to the pressures under normal operation.

Particle Imaging Velocimetry (PIV) has been used in studies to visualise the flow and vortex generation around the front wall of an OWC and internally by Muller and Whittaker in reference to the LIMPET plant [105] and Lopez et al. [106]. In the

Muller and Whittaker experiments a breaking wave was observed inside the chamber causing impact on the rear wall, which is another form of sloshing that occurs internal to a chamber [105].

Throughout literature, sloshing is regularly observed through different causes but rarely predicted or impact quantified. Considering that sloshing and chaotic OWC behaviour in general is such a regular occurrence and a significant risk to the structural integrity of an OWC, this should be better understood.

An additional phenomenon that can occur during sloshing is venting, the internal water level at the front wall reduces enough to allow air to be drawn into the OWC via the front wall lip [104].

The Multi-Oscillating Water Column Concept

The evolution of the singular OWC over recent years has led to the Multi-Oscillating Water Column (M-OWC), also known as an MOWC [72, 107], which is generally of lesser focus in research but does feature in various reviews [55, 56, 61], although a more specific and focused interest is starting to develop [72, 107, 108].

The versatility of the OWC is still largely untapped with the majority of devices deployed having similar characteristics in terms of operating systems and even applications. Versatility and diversity is achieved in M-OWCs in general, with a wide range of applications and variations in concepts of which there are three main types; OWC array as an M-OWC, segmented M-OWC and the modular M-OWC (illustrated in attenuator formation in Figures 2.7, 2.8 and 2.9). The number of M-OWCs is lower in comparison to singular OWCs, however, recent trends in research are proving that M-OWCs, or multiple OWC deployment at least, is gaining traction. Ultimately the aim of M-OWC concepts is to not only scale up energy production, but to use multiple OWCs to gain either opportunities to increase bandwidth or airflow manipulation to improve performance.

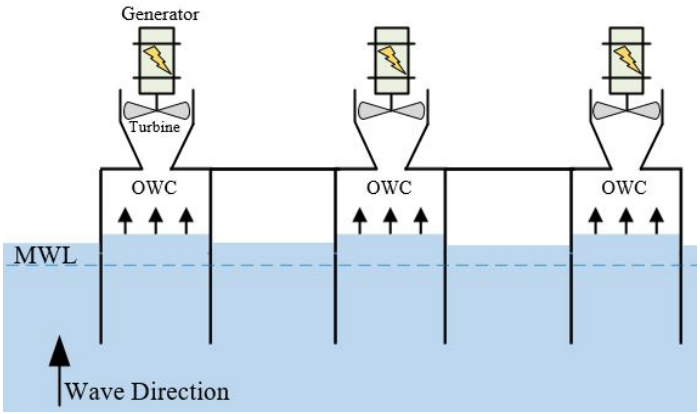


Figure 2.7: *Illustraion of the concept of an OWC array as an M-OWC*

An array of singular OWCs does not qualify as a M-OWC if they are not part of the same structure, which makes them a single device. An OWC array as a M-OWC has multiple singular OWCs operating in isolation of one another with individual PTOs and generators but all being part of a common structure as depicted in Figure. 2.7 [72]. The segmented M-OWC (Figure 2.8) is different from the array with the inclusion of the mechanical coupling of the turbine shafts to allow only a single generator.

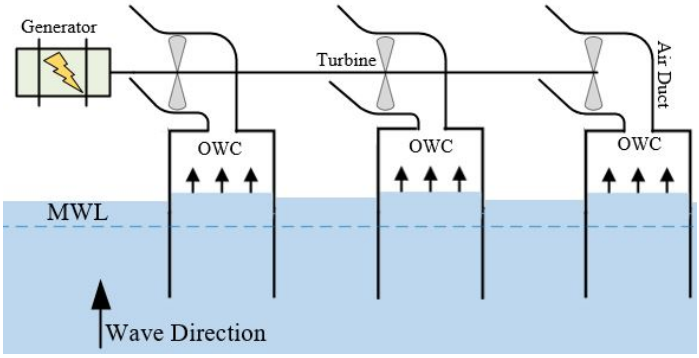


Figure 2.8: *Illustration of the Segmented M-OWC Concept*

A modular M-OWC has multiple chambers contributing airflow that converges prior to the PTO stage. Pneumatic power is combined or accumulated upstream of the single PTO unit, which may contain a single, twin or multiple turbine arrangement. As depicted in Figure 2.9, in its simplest form, the bidirectional airflow from all chambers is fed via a manifold to the PTO. However, this may incorporate further manipulation of the airflow, especially from different orientations of modular M-OWCs

as it will be discussed below.

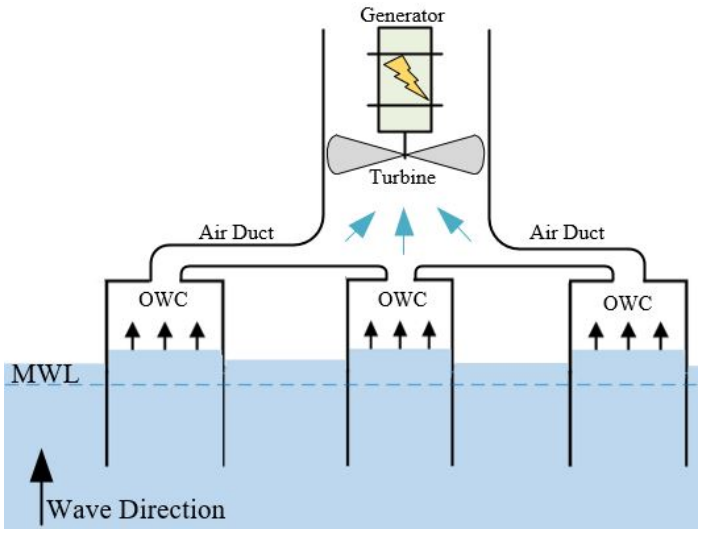


Figure 2.9: *Illustration of the Modular M-OWC Concept*

The modular M-OWC essentially combines and consolidates the power of the individual OWCs at the pneumatic power stage, whereas the segmented M-OWC does so at the mechanical power stage and the OWC array M-OWC at the electrical power stage.

Multi-Oscillating Water Column Devices

A variety of M-OWC concepts exist and development has been steadily emerging with mainly offshore floating devices in attenuator formation. These more modern M-OWC concepts are modular systems, which are arranged with a smaller PTO to OWC ratio in order to obtain higher pressures and steady/unidirectional airflow rates either as an open or closed system. These devices and their features will be briefly reviewed in this section.

A two-chamber device named MORE, based on the M-OWC Seabreath concept was initially investigated in a MARINET project [109] (Fig. 2.10). This floating device consists of several OWC chambers arranged in alignment with the wave propagation (perpendicular to the wave crest). Each OWC creates high and low pressures as the wave peaks and trough pass respectively. Unidirectional valves allow pressurised air during the compression process from each chamber to accumulate in a common

high-pressure duct. Similarly, unidirectional valves allow flow from the low-pressure duct to fill the chamber as the water level recedes creating a negative pressure. The high- and low-pressure ducts create a closed system with potentially more steady high-pressure flow differential across the turbine. An advantage of this closed system is that there will always be a constant supply of air even in less desirable conditions, for example during highly irregular and angled sea states causing more intermittent responses, and also from lower responses due to a larger pressure drop generated between high and low-pressure ducts as opposed to being relative to atmosphere. The early development work of the device has been well documented; initially experimental tests were carried out with a 1:66 scaled device ($1.5\,m$ long, $0.3\,m$ wide) in a wave tank $36\,m$ long, $1\,m$ wide and $1.4\,m$ deep at the University of Padua, Italy [109]. During testing, a very low efficiency was recorded with respect to energy of the incident wave due to the two pressure ducts allegedly being too small. The concept boasts of the ability to harness irregular waves but in fact the pre-turbine performance reduced by 50% [109]. Further work done by Martinelli et al. with the concept includes numerical modelling providing experimentally validated performance predictions [110, 111].

Similar to the Seabreath concept is the Australian invention patented in 2009 [112] developed by iVec named as the Floating Wave Power Plant (FWP) [111] and now known as the Wave Mill under Wave Power Engineering Ltd. [72, 113] (Fig. 2.10). The concept comprises of multiple OWCs creating pressure differential with high- and low-pressure air ducts. The near shore system underwent sea trials in Brisbane, Australia (2009), and believed to have demonstrated very high efficiency ratings. Using a low efficiency turbine, the 30m long prototype generated a maximum efficiency of 81% and minimum of 41%. Including a low efficiency generator, the wave to wire efficiency was calculated to be $16\% - 36\%$ for varying wave conditions, though it is not reported how these efficiencies are calculated and therefore relative to. Costings of production at a commercial scale have been estimated but it appears no further developments were published since 2014 [113].

Another MARINET project involved the M-OWC known as the KNSWING, a ship-like structure with 20 OWCs either side of a central ballast (40 chambers total)

[114–119].This concept is based on the Moody I-Beam Attenuator (1979) [119], with the I-beam cross sectional shape comprising of side entry chambers (Fig. 2.10). The shape of the KNSWING is designed to induce minimal body response in waves, which has been proven in harsh scaled conditions and thus absorbs as much energy as possible through the OWCs [114, 116, 118]. Initial experimental studies were carried out with a 1:50 model at the Hydraulics and Maritime Research Centre (HMRC) facility, University College Cork in 2013 [115–118]. Aside from the various optimisation experimental findings and numerical analysis [119], the performance results were scaled to compare the peak CWR (Capture Width Ratio) with other the Kaimei sea tests (1979 and 1982) and the Moody I-Beam experimental results (1979), all from which it falls short [118].

The LEANCON device, patented in 2007 [120], is a floating V-shaped M-OWC that creates high and low pressures air ducts with an array of many small OWC tubes [56] (Fig. 2.10). The 'boomerang' or 'V' shape, perhaps a terminator/attenuator hybrid (see Fig. 2.5, allows the WEC to capture a larger width of the wave. Theoretically, the large number of tubes create a balancing of forces as localised high and low pressures act within the tubes. The design is compact with air channels built into the structural design and a PTO system that comprises of turbine/s place between high and low pressure channels subject to unidirectional flow, similar to the Seabreath (see Fig. 2.10). The shape of the device and the array of tubes tilted with their openings toward the incident wave crest are intended to minimise wave impact forces and splash. Furthermore, the anchorage position, ideal when on the tip of the bow, helps the WEC to align with wave direction as the two arms cause a balancing effect (Fig. 2.10) [120].

Experimental tests were carried out Kelly et al. at HMRC and numerical modelling with a very similar but smaller model to the LEANCON at 1:50 scale with 32 tubes or OWCs [121]. Reports from a different 1:40 scale experiment conducted at the Aalborg University wave tank contain results for general hydrodynamic performance under various mooring configurations [122, 123]. The bottom standing and floating configurations reached efficiencies of 12.4% (3.56 GW/year) and $7.1 - 12\%$ (2.03-3.43

GW/year) respectively [123]. In December of 2015, a 1:10 scale LEANCON prototype with 104 tubes completed operational and structural tests at sea and was subsequently removed. Deployment is intended for the North Sea, off the Danish coast, after is has been reported that 1:2 scale tests are to be carried out at the DanWEC facility [114].

Most OWCs are either onshore or semi-submerged floating structures unlike the Stellenbosh wave energy converter (SWEC) – a fully submerged shallow water, V-shaped breakwater integrated converter [124] (Fig. 2.10). This M-OWC type, mounted on the sea floor, uses a closed loop unidirectional airflow system created by unidirectional valves and the high and low pressure manifolds [124]. Chances of survivability are greater when submerged but components are exposed to increased corrosion rates. In 1984, Retief et al. carried out experiments on both 2D and 3D models from 1:100 to 1:50 scale [125]. Since then, the SWEC has been the subject of various studies coming out of Stellenbosch University, South Africa [124, 126, 127]. In more recent years, experimental studies with a 1:25 scale submerged single chamber model of the concept had been carried out, reaching a maximum conversion efficiency of 22%. Although the concept is still being considered for specific applications and further development [128], the operational optimisation of the SWEC for these applications is still a working progress [129].

A fixed M-OWC concept and its variations have been the subject of research from Glasgow University initially in 2003 and more recently at University of Technology Sydney. This device is based on a concept with two to four chambers in either a segmented and modular arrangement. Although this concept has been extensively investigated, there are still gaps in the research that are stunting its progression but should be a part of future work [108, 130–132].

Further M-OWC identified devices that have been found in literature but not discussed are the NEL Bottom Standing Terminator, Vickers Terminator and Vickers Attenuator, the NEL Floating Terminator and Attenuator, the OWC Belfast Point Absorber [133].

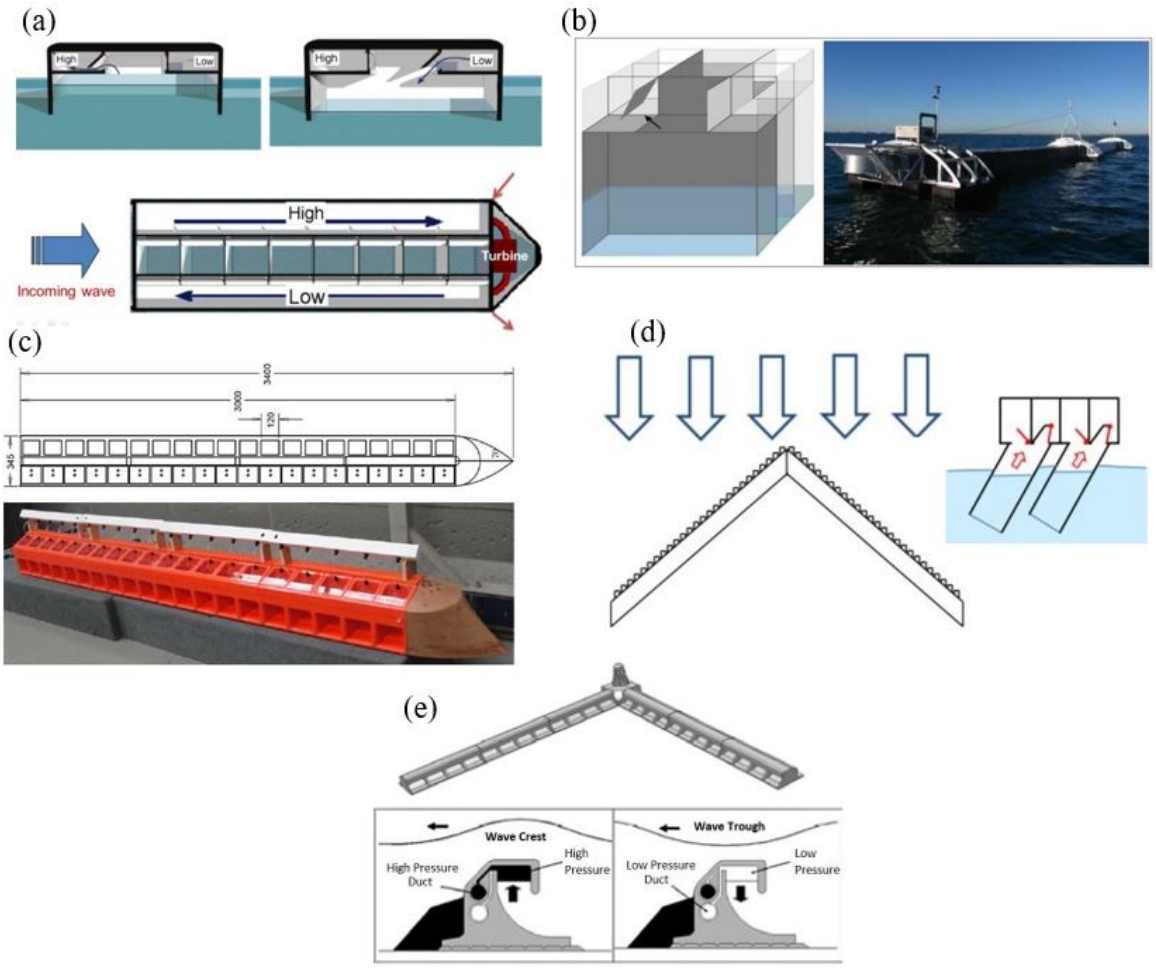


Figure 2.10: *Photographs and Models of Multi-Oscillation Water Column devices and concepts Seabreath (a) [109], Wave Mill (b) [113], KNSWING (c) [119], LEANCON (d) [56] and Stellenbosch (e) [126]*

Multi-Resonant M-OWC Devices

As with singular OWCs, resonance and the ability to tune to resonance is a desired trait. While solving the nature of the airflow with alternative M-OWC designs, if a greater bandwidth or a potential for more resonant peaks could be created, this would certainly set apart the M-OWC concept.

Based on a concept eventually patented in 2007 [134], the Orecon and its variants can be considered as a M-OWC as well as a Multi-Resonant Chamber (MRC). One of these variants, is the MRC1000, which with the Orecon Buoy were the subject of various mooring based experiments at the Oceanide wave tank, France in 2009 [37]

[37, 135]. The design of the Orecon concept, having chambers of varying lengths, offers multiple resonant peaks and hence, great tune ability. In irregular seas, as with the sea state data analysed and plotted in a scatter diagram later in this thesis to reveal variation, can included wavelengths that vary by $> 200\,m$. The concept considers the multi length chambers to suite a wider range of wavelengths to improve hydrodynamic efficiency[134]. The MRC1000 device, reviewed in a 2004 report [135], is a floating offshore, slack-moored, 32m diameter WEC rated at 1 MW (full-scale) with a 3-stage PTO system, which includes an intermediary hydraulic stage. There are reports of wave tank experiments having been carried with five different scaled models ranging from 1:250 and 1:20. Additionally, a 1:10 scale 5 kW prototype was tested at sea with plans for further seat trials in coming years [135]. However, in 2009 Orecon development seemed to have ceased due to financial support issues despite being so close to deployment of the 1 MW WEC [136].

Breakwater Integrations and Synergies

The renewable energy mix is market driven and therefore wave energy needs to become competitive from a costing perspective. With the current cost of wave energy, anticipation of a slow decline due a lag in development and the competitiveness of the energy market continues to increase, the demand for WEC technologies to be innovative also increases. For existing wave energy technologies, this requires the identification of areas to diversify with respect to applications and synergies or integrated systems in efforts to yield a lower cost of energy. The cost of energy production is often quantified with the LCOE. This figure is dependent of three main factors: capital and operational costs, and annual energy production [11, 14, 137]. Hence, if a device had an impressive annual energy production rating but costs a colossal amount to build, deploy and maintain, wave energy would be no closer to large scale commercial deployment than it is today. Such innovation and identification of these alternative applications and synergies are required to make wave energy more competitive option and a viable option for future investment.

As with wind and tidal energy, WECs need to be deployed on a large scale. This

can be done with deployment in multiples as an array of WECs to create wave energy farms, or with coupled M-OWCs – like OWC arrays as a M-OWC, segmented or modular M-OWCs. By capturing a larger area of wave energy resource, the economics benefits also scale up with reduction of the capital costs. Furthermore, from a capital cost perspective, at large scale it allows the opportunity for integration with other applications in synergetic projects, especially for M-OWCs with large platforms.

Combinations of WECs and alternative applications are appealing because the construction costs for both purposes can be shared. For the example of the breakwater integration, there is not only the WEC generating energy but potentially a berth facility, costal protection and marina protection [79].

The potential of these innovative synergies is great and a trend is developing in global research whereby focus is turning to integration of WECs with offshore platforms, structures, energy plants and more.

Furthermore, as will be revealed in the following sections, larger scale M-OWCs often have a decreased number of turbines with respect to the number of chambers, especially with modular M-OWCs. It is apparent that for both an increase in overall efficiency and a reduction in PTO costs for example, the LCOE drops dramatically. The drop is more dependent on the efficiency of a PTO system, however, the combination brings vast reduction. Hence, the focus of these synergy projects should be the opportunity to lower PTO costs and improve their efficiencies at the same time [137]. Although they're not explicitly designed or defined as wave breakers, the majority of deployed OWCs have been fixed and usually onshore like the previously mentioned LIMPET, Pico and the more recent plant on Jeju Island (South Korea), which have been referred to as wave breakers, perhaps in less of a protectional context. [56, 73]. Examples of intentional breakwater synergies such as these are the Vizhinjam in India and in Sakata Port, Japan, and Mutriku in Spain [73, 138, 139], with the latter more famously known as a breakwater integration. The Mutriku plant has accumulated upwards of $2\,GWh$ of contribution to the grid since 2011. As well as a power plant, the breakwater M-OWC also serves as a test facility across two out of the 16 chambers [90]. Multiple singular OWCs in terminating configurations like these, not

necessarily as a M-OWC, but integrated into fixed shoreline defence or breakwater applications are being researched and could be the new direction for these singular OWC deployment especially as a retro fit option [140, 141]. The previously mentioned REWEC3 is also considered as a retro fit option, having been installed in full-scale at a traditional breakwater in Rome, which will eventually be a 2.5MW deployment, with plans for additional multiple locations around Italy such as Genoa and Salerno [85, 90]. Another breakwater retro fit potential is the E-Wave100, which is a two chamber OWC modelled during the MARINET 2 project at a maximum scale of 1:2 [90]. Existing concepts can be considered for potential breakwater integration such as the previously discussed KNSWING that is part of the 'Concrete for Wave Energy Converters' project - a project mainly aimed studying alternative construction methods, lowering costs and increasing survivability and reliability [90].

As well as synergies across other ocean energy fields (in offshore cases), integration of multiple WEC operational concepts exist. There exists multiple examples in literature of hybrid devices that combine an OWC and overtopping device known as an Oscillating and Overtopping Water Column (O-OWC) has been experimentally modelled [142–144].

The number of M-OWCs deployed and undergoing research and development is and always has been comparatively lower than singular OWCs, however, recent trends are showing an increase in research for M-OWCs, or at least multiple OWCs [72].

Through continued research, now there are various different forms of offshore synergies, offshore wind-wave energy for example, which requires large floating or fixed structures to support the tower. Many OWCs and other WEC types have been considered for this application. An example is a turbine structure with 3 OWCs arranged at the base to provide stability and reduce costs for offshore wind turbine platforms [145, 146].

With respect to offshore floating deployments, the OWC array as an M-OWC integrated into large floating platforms and breakwaters is being a common topic in reviews and case studies [19, 147–154]. A great advantage of integration with large-scale synergies is the opportunity of retro fitting, not only with existing ports but also

with breakwater structures around the world.

One example of these concepts that is being implemented is with an array of OWCs used to obtain greater stability of a platform as with the Rho-Cee, a Pneumatically Stabilised Platform (PSP) by Float Inc., which is an Impedance-Matched OWC (IM-OWC). A large array of OWCs located on the underside of the platform improves the stability of the multipurpose platform [155].

The other major but less obvious synergy M-OWC deployment is the Sakata port plant. However, many other examples existing in literature of experimental and numerical modelling of the affects, benefits and performance analyses of the presence of OWCs in breakwater structures large or small, fixed or floating [86, 142, 156, 157]. Such innovative work is the focus of many researchers around the world and forms a large part of work currently being carried out at Lancaster University [72] in the Lancaster University Renewable Energy Group, which is well known for its contributions to the field over the years [158–169].

Examples of more broad and diverse deployment possibilities can be seen in existing concepts with WECs integrated into offshore wind turbine structures [170, 171], breakwaters [152, 172, 173] and general offshore multi-use floating platforms [174]. Similar concepts do not only include OWCs but also point absorbers and overtopping devices integrated with breakwaters [19].

Power Take-Off

As mentioned, the development of PTO technologies has been based on the disadvantage and challenge of OWC technology, namely the bidirectional airflow created by the OWC at a very slow frequency with respect to National Grid frequency. This project is concerned with the generation of this unidirectional airflow and the methods applicable to do so.

Although this project is not concerned with turbine types and performance, the hydrodynamic and pneumatic conversion processes of OWC operation are coupled and therefore inter-dependent. As is such, the overall PTO system types and upstream effects are considered and thus, forms a significant part of this project's literature

review. Hence, this part of the review does not concern the finer details of turbine technology and its optimisation but rather the PTO system as a whole and the development of different variations of systems.

Classification

The PTO system of an OWC WEC is almost always based on single stage pneumatic energy extraction with the exception of two stage hydraulic PTO systems. Extensive reviews exist in literature for mainly single OWC PTO systems [56, 175].

While the structure and operation of the hydrodynamic stage of the OWC is simple, it results in a complex form of power extraction in the subsequent stage of the PTO with bidirectional airflow. Consequently, there have been many approaches to this process mostly stemming from solutions to either implement a self-rectifying turbine to operate despite the bidirectional nature of the airflow, or rectify the air to allow the use of a unidirectional turbine. A map of the categories and their subcategories is shown in Figure 2.11 for a singular OWC but is also applicable for a M-OWC [42].

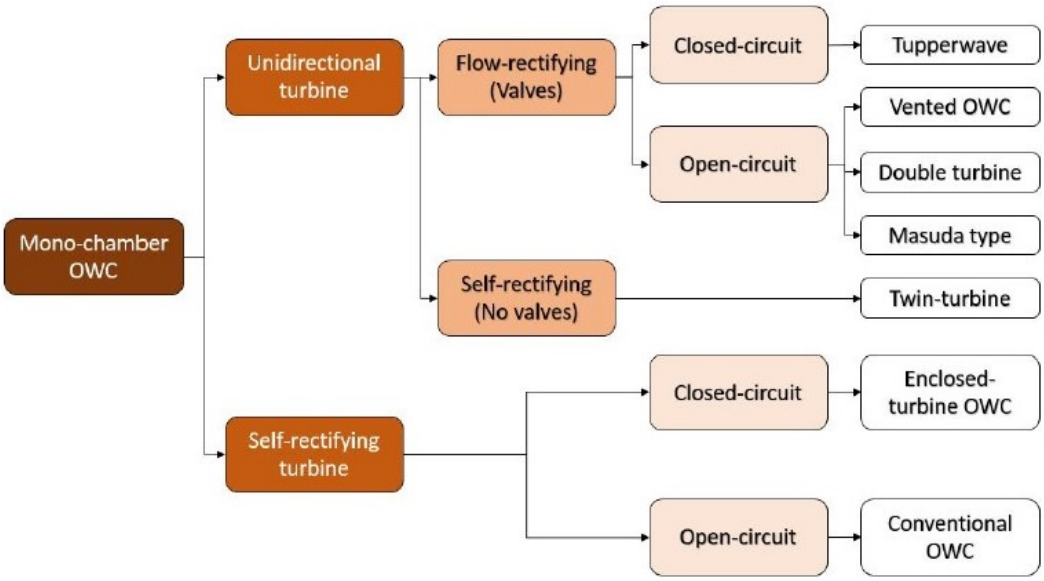


Figure 2.11: *The classifications of PTO systems for OWC concept based WECs [42]*

Bidirectional Self-Rectifying Turbines

Power extraction from bidirectional airflow is achieved with self-rectifying turbines that rotate in the same direction irrespective of the direction of the airflow. Hence, for both inhale and exhale of an OWC the turbine is continuously rotating in the same direction. Self-rectifying turbines, their features, efficiencies and characteristics are well reviewed in literature [176, 177] including the modelling of turbines and their variations for optimization purposes [178–180].

The most common of all self-rectifying turbines is the Wells turbine, patented in 1976 by Dr. Wells of Queens University Belfast (Fig. 2.12) [65, 181, 182]. This turbine is usually considered the 'default' turbine for the OWC. Since the Wells turbine was invented, it has been the subject of a large volume of research and development in relation to its solidity, blade numbers, inclusion of guide vanes and number of guide vanes leading to many variations of the turbine across prototypes around the world: monoplane, biplane, guide vane configurations, radial inlet configurations, counter rotating rotors, variable pitch blades and more [183, 184]. As well as being well researched over the years, the Wells turbine has featured in the deployments of the LIMPET, Pico, Osprey, Mighty Whale [62, 63, 185], Sakata Port [138, 186] and many other concepts under development like the Spar Buoy [56]. The Wells turbine is preferred mainly due to its simplicity and low cost, however its disadvantages are apparent with a loud operating noise, poor starting and stalling characteristics, large axial thrust, small peak operating range and operating range in general, with a peak efficiency range of $\sim$ 60–65% [6, 137]. However, some of the more complex variations like the contra-rotating can achieve up to 75% peak efficiency [].

Second in popularity for OWC self-rectifying turbines is the impulse turbine – a pressure type with connecting arc shaped blades as opposed to the reaction or lift types with aerofoil shaped blades (like the Wells turbine) (Fig. 2.12). Optimization points researched and available in literature include a number of aspects like the inclusion of solidity, blade geometry, guide vanes, additionally counter-rotating rotors and many more [178–180, 187].

It is well known that compared with the Wells turbine, in general, the impulse

turbine is superior in terms of its starting characteristics, no stalling condition, lower rotational speed with a high torque coefficient, lower noise levels and a larger flow coefficient range. However, due to reaching saturation limits earlier than the Wells, it is incapable of handling a larger range of operating conditions. [176, 188]. With these different performance characteristics, the self-rectifying version of the impulse turbine is often well acclaimed, but features in significantly less research. It therefore features in fewer WEC concepts, aside from in various prototypes as a retro fit for research purposes, like the FP7 CORES Project sea trial in Galway Bay, Ireland [189, 190], the Kaimei [183] and the 1991 Indian wave energy plant [191]. Its main disadvantages are its more complex geometrical design and lower peak efficiency. [183].

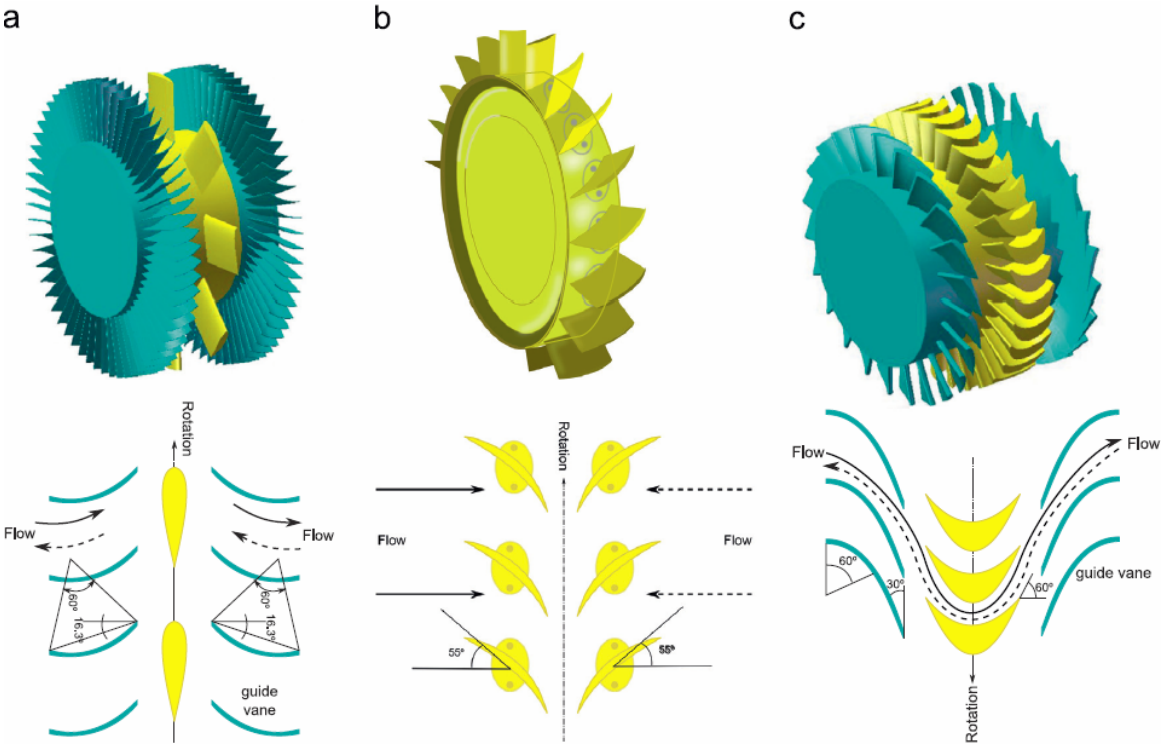


Figure 2.12: *Geometry and illustrations of the main self-rectifying turbines for OWC applications: the Wells (a), Denniss-Auld (b) and impulse turbine (c) [25]*

In more recent developments, an innovative bi-radial self-rectifying turbine has emerged from the H2020 OPERA project, designed by the Instituto Superior Tecnico of Lisbon, Portugal. The turbine has undergone various stages of development, most significantly with a 30 kW prototype manufactured by Kymaner, installed and tested

in sea trials with the spar buoy type OWC MARMOK-A-5 for which impressive average efficiency values were recorded albeit with a simplified control method (56%) [192].

A turbine named the Denniss-Auld turbine is a unique design with a variable pitch control (Fig. 2.12). The turbine was developed by Energetech, which became Oceanlinx (in Australia), to equip the three OWC prototypes of varying characteristics that the company deployed and operated before sinking into liquidation following deployment issues [25, 72, 183, 193]. The turbine has a self-adjusting pitch mechanism, much like the Wells variation but with faster adjustment based on the chamber pressures and a larger angle adjustment range. Hence it has no need for guide vanes, but employs symmetrical aerofoil shaped blades with respect to the chord length as the leading and trailing edges are continuously switching rolls. The turbine achieved a high peak efficiency of 63% without a drop below 35% within the operating range after the peak [194].

One of the less common options of self-rectifying turbines is the Savonius. More commonly known for its use in other applications like wind energy and even as a stand-alone WEC concept [195], the Savonius has a number of long and thin arced blades that are most commonly horizontal axis for OWC applications (Fig. 2.13). Experimental work had been carried out with the Savonius turbine, and in particular in a segmented M-OWC where low efficiencies were recorded [130].

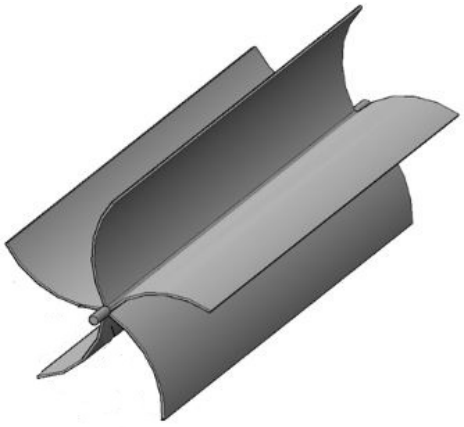


Figure 2.13: *Example of five blade horizontal axis Savonius geometry for PTO in OWC applications [196]*

Unidirectional Self-Rectifying Systems

One of the main attractive points of unidirectional turbines is the lack of need to compromise optimisation in order to facilitate bidirectionality. However, although it has many advantages, the challenge with the unidirectional route altering the upstream airflow conditions.

The concept of unidirectional self-rectifying PTO systems is not to include valves to manipulate the airflow but to be able to extract energy from the inhale and exhale of the OWC/s separately. This can be achieved with a twin turbine setup, where one turbine is dedicated for inhale and the other exhale. While this has not been implemented in a device deployment, variations of the concept have been modelled experimentally and numerically. Frequency domain modelling of a twin unidirectional self-rectifying turbine concept indicated a wave-to-wire efficiency, $\sim 50\%$ [197]. The concept was also experimentally modelled and subsequently validated the wave-to-wire efficiency claims over a wide range of flow coefficients [198] and up to 60% [197] with comparisons of experiments in steady and unsteady flow conditions [199, 200]. Time domain numerical analysis is also carried out, on the concept with varying geometrical features for flow field optimisation purposes and assessment of turbine behaviour in direct and reverse modes. The conclusion of this numerical analysis found that around 1/3 of flow was wasted by the inactive turbine during either an inhale or exhale process. The wasted flow acting on the inactive turbine also produces a negative torque reducing efficiency [201]. In other numerical studies, this original twin turbine system has been modelled and compared against a single impulse turbine case [202].

The waste of flow during turbine reverse mode was then investigated further with numerical analysis and wind tunnel tests on different fluidic diodes proposed for the concept to improve the rectifying effect by reducing flow from the turbine in reverse mode. Although these adaptations are said to potentially improve performance, further work is required to minimise the effects of the diodes presence with respect to the pressure drop induced in direct/forward mode [203, 204].

A further variation exists in literature with numerical analysis of the concept

without fluidic diodes but with two self-rectifying turbines as the twin setup; one Wells turbine as the main turbine and an impulse turbine to act as a booster turbine. The turbines are coupled, with the intention that the Wells turbine would extract with lower flow rates and the impulse turbine with higher flow rates. This research demonstrated an improved starting efficiency of the Wells turbine with the inclusion of the booster turbine [205].

In more recent years the twin turbine concept has had a little more attention with the analyses of two unidirectional radial turbine configurations, an inflow and outflow type. However, these were not only tested as a twin setup but also in a vented OWC case with only one of the above configurations, meaning the counter process is vented to/from the atmosphere [206].

Unidirectional Flow-Rectifying Systems

Closed System Flow rectifying becomes a lot simpler with an M-OWC due to the increased number of OWCs contributing to the airflow, which is a great advantage. In almost all cases, modular M-OWCs are closed systems/circuits. This includes the aforementioned SeaBreath [110, 111], ShoreSwec [125, 126, 128, 129, 207], KNSWING [115–118], and the LANCON [120–123] ((Fig. 2.10). With all these systems, each OWC in the M-OWC device inhales and exhales through one-way valves into the high-pressure and low-pressure ducts respectively. Due to the orientation of these devices with respect to the ideal wave direction, all OWCs are out of phase and therefore inhaling and exhaling at different instances depending on the angle of the sea state, theoretically resulting in smoother and constant airflow caused by the pressure drop between the high and low pressure ducts/manifolds.

Singular OWC closed circuit concepts are rarer due to the losses induced by the valves. However, these concepts do exist [47] and have been the subject of research like the additional chambers mounted above the OWC for high-pressure and low-pressure air from the OWC exhale and inhale process respectively. In between these chambers is the unidirectional turbine [87]. Although the performance results of the Tupperwave were competitive against a comparative Spar Buoy model, the majority

of the losses were due to the one-way valves and their opening time and the excess damping caused as a result [88].

Open System An open circuit/system is the one that inhales and/or exhales from the atmosphere and hence the pressure drop across the turbine is always relative to the atmospheric pressure.

A vented OWC is an open circuit that creates unidirectional airflow by only using half the wave period and vents the atmosphere during the other half of the period. As well as the studies discussed above [206], an example of this is the previously mentioned UniWave concept under development by Wave Swell Energy Ltd. Australia [89]. During inhalation only, when the water column descends, air is drawn from the atmosphere and through a unidirectional turbine. As the OWC is heaving, pressurised air is exhausted to the atmosphere via a valve, which resets the chamber pressure to atmospheric at the maximum internal displacement level [89]. This rationality likely based off such research that proves that the exhalation process is less efficient that the inhalation [208].

An open circuit double or twin turbine concept for an M-OWC is best demonstrated with the WaveMill (Fig. 2.10), an Australian invention patented in 2009 [112]. Originally developed by iVec and named the Floating Wave Power Plant (FWP) [113] it is now under a new name with Wave Power Engineering Ltd. [51, 113]. Essentially cousins of the twin unidirectional self-rectifying concepts discussed above, with the addition of valves and ducts to separate high and low pressures, the turbines are only connected to their respective ducts for the inhale and exhale processes. Hence, similar to the other M-OWCs with closed circuits, each OWC has two one-way valves for inhale and exhale.

For singular OWCs or M-OWCs without valves as part of the OWC chamber there are further rectifying methods, starting with the original Masuda invention of the navigation buoy [56]. The airflow duct from the OWC chamber is connected to a rectifying unit with a unidirectional Francis turbine and four one-way valves [178]. A two-valve dual chamber version of the rectifying system was later tested in the

Kaimei device at sea trials, which reinforced concerns since at this larger scale, the valves proved to over complicate manufacturing, maintenance and operation resulting in poorer performance [56, 178, 209].

These valve systems closer to the turbine rather than at each OWC were rarely considered, due to their impracticality and potential reliability issues at larger scales. The combination of larger flowrates and the required quick response time means that they are unfavourable [56]. Such rectifying valves were first implemented in the PTO system of the original navigation buoys mentioned earlier and the Kaimei, where the unreliability of the valves were confirmed by being found to cause losses by sticking and increased friction.

Numerical Modelling

Numerical methods within fluid mechanics have developed at a staggering pace owing to their value and consequential demand across many applications. Though tools are being developed constantly, they do not necessarily succeed others, rather every tool has its application based on the level of fidelity, phenomena and characteristics desired in the modelling, as illustrated in the Figure 2.14 comparison. Likewise, this research two has featured two models for two entirely different purposes, both of which are presented in this thesis in Chapter 7.

As depicted in Figure 2.14 [210], choice of numerical modelling methods entails a trade-off between accuracy and computational cost. For example, due to the challenge of simulating WECs with a Numerical Wave Tank (NWT) model, often Potential Flow Theory methods are used, the governing equations for which are based on the Laplace equation, hence flow is irrotational. Equations are solved in the frequency domain decreasing the computational cost and making the method well suited to those application in which solutions are frequency dependent, such as wave energy.

Most applicable to full NWT simulations is the method known as CFD, where the governing equations are solved in the time domain and models can be adapted to include for viscous affects, turbulence, heat and more. As such, the accuracy

scale of Figure 2.14 also represents the number of phenomena and physics modelled, which may or may not be necessary or yield higher accuracy, this is dependent on the application. For example, when all fluid/s are or behave as incompressible in the given application, the compressible form of the Navier Stokes equations are not more accurate and add unnecessary additional computational cost.

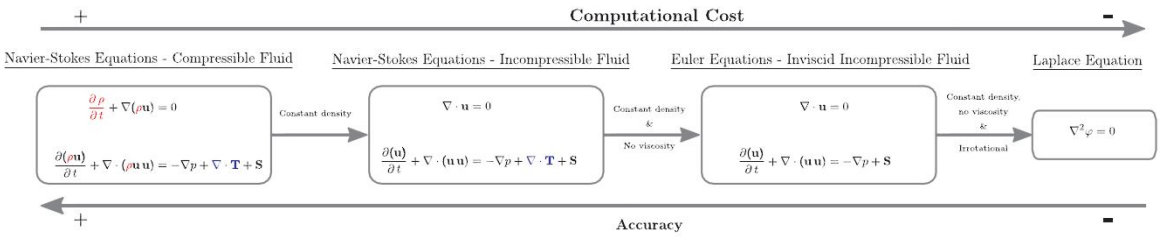


Figure 2.14: *Wave energy numerical modelling methods comparison on a scale of computational costs and fidelity [210]*

Relevant Computational Fluid Dynamics Theory

Governing Equations

The goal of CFD is to obtain a numerical solution of the nonlinear partial differential governing equations that describe Newtonian fluid flow. These are expressed in the Navier-Stokes (NS) equation (Eq. 2.12) and the continuity of mass equation (Eq. 2.11), which for an incompressible fluid solves for three components of velocity $\overrightarrow{v}(u, v, w)$ and pressure, p:

$$\bigtriangledown \cdot \overrightarrow{v} = 0 \tag{2.11}$$

$$\frac{\partial}{\partial t}\overrightarrow{v} + \bigtriangledown \cdot (\overrightarrow{v}\overrightarrow{v}) + \frac{1}{\rho}\bigtriangledown p - \frac{1}{\rho}\bigtriangledown \cdot \bar{\bar{\tau}} = \rho\overrightarrow{g} \tag{2.12}$$

There are several forms of the NS equations depending on the simulation physics, for example the absence of the density term in Equation 2.11 due to incompressibility and a third equation for conservation of energy can be included to model mechanical and thermodynamic energy. The momentum equation (Eq. 2.12) is based on Newton's second law with terms to account for internal and external forces [211].

Modelling Turbulent Flow

Evolution from the Euler equations, which do not consider laminar viscous stresses (external force terms), leads to the simplest form of the incompressible NS equations (Eqs. 2.11 and 2.12), which are suitable for laminar flows where $Re < 2000$. However, once $Re > 2000$, flow begins to become unstable in a transitional state and as Re surpasses the critical level of $Re > 4000$ i.e. inertial forces dominate viscous forces, the flow becomes fully turbulent. The most common approach to capture turbulence is with the use of the Reynolds-Averaged Navier Stokes equations (RANS), which contain two key differences from the NS equations (Eqs. 2.11 and 2.12).

Firstly, the instantaneous flow variables of the NS equations are replaced with time averaged values, for example velocity component $u_i(t)$ becomes the sum of the fluctuating instantaneous velocity $u_i'(t)$ and mean component, $\bar{u}_i$:

$$v_i(t) = \bar{v}_i + u_i'(t) \tag{2.13}$$

This is known as Reynolds Ensembled Averaging. As a result, the conservation of momentum equation includes the Reynolds stress tensor ($\bar{\bar{\tau}}^R$):

$$\frac{\partial}{\partial t}\overrightarrow{v} + \bigtriangledown \cdot (\overrightarrow{v}\,\overrightarrow{v}) + \frac{1}{\rho} \bigtriangledown p - \frac{1}{\rho} \bigtriangledown \cdot (\bar{\bar{\tau}} + \bar{\bar{\tau}}^R) = \rho\,\overrightarrow{g} \tag{2.14}$$

The tensor known as the Reynolds Stress Model has the following formulation:

$$\bar{\bar{\tau}}^R = -\rho \begin{bmatrix} u'^2 & u'v' & u'w' \\ v'u' & v'^2 & v'w' \\ w'u' & w'v' & w'^2 \end{bmatrix} = -\rho\overline{v_i'v_j'} \tag{2.15}$$

Where $\overline{v_i'v_j'}$ are is the Root Mean Square of the fluctuating velocity components:

$$\overline{v_i'v_j'} = \sqrt{\frac{1}{T}\int_T (v_i'v_j')dt} \tag{2.16}$$

Most turbulent modelling approaches are able to adopt the Boussinesq approximation

hypothesis, which instead considers the mean velocity components calculated with Eq. 2.13 and the consideration of turbulent viscosity, μ_t and turbulent kinetic energy, k:

$$\bar{\bar{\tau}}^R = -\rho\,\overline{v_i' v_j'} = \mu_t\left(\frac{\partial v_i}{\partial x_j} + \frac{\partial v_j}{\partial x_i}\right) - \frac{2}{3}\left(\rho k + \mu_t \frac{\partial u_k}{\partial x_k}\right)\delta_{ij} \tag{2.17}$$

Where δ_{ij} is the Kronecker delta function.

There is additional cost with turbulence modelling, but this is a trade-off for a higher quality and reliability in the results to model the flow more accurately. In the application of the RANS equations, the Boussinesq approach requires coupling with additional turbulence models in order to find these turbulence properties μ_t and k. A number of different turbulence models with their variations have been developed for different applications and flow types that provide closure to the RANS equations by relating the mean fluid velocity gradients to the Reynolds stresses through Eddy/Turbulent Viscosity. There are two main methods appropriate for wave energy applications: the $k-\epsilon$ and $k-\omega$ models, the characteristics of which are discussed in the relevant sections of Chapter 6 where these models are implemented [211].

Numerical Grid

The creation of the numerical grid or mesh is arguable the most important process in CFD. As alluded to above, the mesh is the structure of elements or control volumes that make up the fluid flow domain which interface with the geometry of the model in subject and the far field boundaries. Structure and quality of a mesh is vital in order to obtain a stable solution and incur minimal numerical diffusion

The sizing of a mesh in certain regions and local refinement depends on the modelling goals and physics of the flow to be simulated. Turbulence varies significantly in scale and energy levels, which requires careful a selection of the turbulence models used and the mesh refinement in particular regions. But when modelling viscous effects and therefore 'no slip walls' as boundary conditions, turbulence due to boundary layer transition zones and separation or vortex shedding is relevant. The nature of the boundary layer, that is the gradient of the velocity profile in relation to wall prox-

imity changes depending on the fluid properties and wall shear stress. As represented in Figure 2.15 [212], there are several sub layers within the boundary layer. Within the outer layers of a turbulent boundary layer, turbulent stresses are dominant and inner layers are dominated by molecular stresses. Within the overlapping layers, a combination of both are significant. The thinnest layer is the viscous sub-layer, which must be captured in the model in order to fully capture the viscous effects.

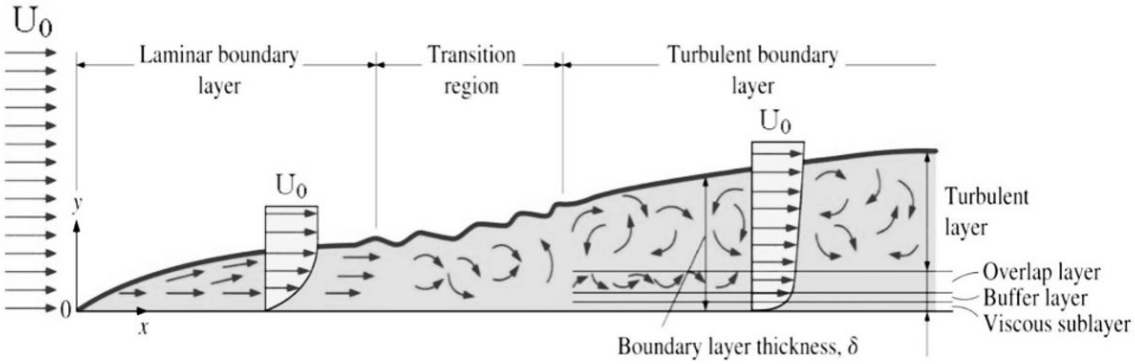


Figure 2.15: *Flow regimes and sub-layers of the boundary layer in the simple case of flow over a flat plate [212]*

The value known as Y^+ is a non-dimensionlised representation of the distance from the wall and the first mesh node, which is non-dimensionlised by the kinematic viscosity, ν, friction velocity (or shear velocity) u_τ, and the physical distance from the wall, Y_{wall}:

$$Y^+ = \frac{Y_{wall} u_\tau}{\nu} \tag{2.18}$$

Ideally, to fully resolve the viscous sublayer of the boundary layer without using any additional models such as wall functions, which approximate the boundary layer with coarse meshes, the mesh should be sufficiently refined such that the first node of the mesh is positioned within the viscous sublayer yielding $Y^+ < 5$ but one should aim for $Y^+ = 1$. Hence, rearranging equation 2.18 for Y_{wall} and setting $Y^+ = 1$ in order to determine the physical distance at which this first node should be from the wall leaves one unknown, u_τ. This can be approximated using the analytical solution for the skin friction coefficient, C_f using the Reynolds number to calculate the anticipated wall

shear stress, τ_w:

$$C_f = \frac{\tau_w}{\frac{1}{2}\rho U_0^2} = \frac{0.664}{\sqrt{Re}} \tag{2.19}$$

Which then allows for the calculation of friction velocity to solve Equation 2.18 to find Y_{wall}:

$$u_\tau = \frac{\tau_w}{\rho} \tag{2.20}$$

Once Y_{wall} has been approximated and implemented in the mesh generation step, once a solution is obtained, as part of the solution verification process, this Y^+ value computed by the solver should be analysed at the regions of interest and the mesh refinement adjusted accordingly. This is due to the variation of the boundary layer thickness that can occur in unsteady cases.

Additional considerations for refinement in the case of wave energy applications are the consideration of the accuracy of the free surface profile and the resolution of the pressure and velocity fields of a wave beneath the free surface based on the specific wave properties. These considerations will be further discussed in the relevant model mesh generation section of Chapter 7.

Numerical Methods and Convergence

The Fluent® solver is finite volume based, meaning the integral form of the governing conservation NS equations are implemented over the control volume or cell volume by first using the divergence theorem to convert the volume integrals into surface integrals that represented the surfaces around a mesh cell. Since Fluent® is a cell centred solver, the discrete scalar values for all variables are referenced the cell centre and cell face values are interpolated using user specified schemes such as first and second order upwind schemes. The choice of these schemes somewhat depends on the pressure-velocity coupling algorithm used and whether they are segregated or coupled types. This thesis contains two different simulation models, therefore the setup changes and reasoning behind various modelling decisions will be detailed in the relevant Chapter subsections.

Since there are no analytical solutions to the governing equations the code solves,

the numerical solution must be both verified and validated. Here solution verification is discussed in more detail since it concerns the concept of solution convergence. The verification of a solution is chiefly determined by the discretisation errors in the solution. The discretisation errors of a solution are made up of two main sub-errors: round-off errors and truncation errors. The round-off errors are due to the limit of precision restricted by the number of decimal places stored by code in the memory. The truncation error is a function of the order of accuracy chosen in the discretisation methods and is essentially the difference between the unknown solution of the governing partial differential equations and the finite volume approximation. The discretisation error over the course of a simulation with a certain number of iterations are expressed as residual errors. Solvers are set to monitor then decrease in these errors through consecutive iterations and determine when the solution is converged based on the user set criteria.

There is no set criteria or rule for determining convergence of a solution but rather the collation of evidence to establish confidence in a solution. As discussed, one piece of evidence comes in the form of the convergence of residual errors but this should not be relied on alone. Additional confidence can be found in through the monitoring of the convergence of particular variables and preferably integrated properties such as force over a surface.

The ability for a solver to reach a converged solution is dependent on the stability of the calculation and the prevention of divergence. A common way of quantifying and ensuring stability with the chosen time stepping method, is with the Courant-Friedrichs-Lewy (CFL) number, which is function of solution variable x, the time step, Δt and the distance between cell centres, Δx:

$$CFL = \frac{x\Delta t}{\Delta x} \tag{2.21}$$

The stability condition of the CFL number varies but for example, an explicit upwind scheme is stable when $CFL < 1$. The CFL number can be monitored throughout a simulation and even controlled with the ability to adapt the time step in order to

maintain solution stability [211, 213].

CFD for Wave Energy Applications

Traditionally, experimental is the main modelling approach taken for WECs but in recent years the use of CFD in wave energy applications has been increasing. Simulations can save significant cost in the development life of a WEC concept by reducing costs of manufacturing multiple models for optimisation, scaling up and investigation the finer details but often more so in the higher TRL. The literature review thus far has indicated a number of instances where numerical modelling has been used in cases most similar to the W2W and this project. There have been significantly fewer NWT simulations for large devices such as M-OWCs due to the added complexity and computational cost whereas single OWCs, especially fixed, have been studied frequently, as can be seen in the compilation in the review of Windt et al. [210]. The fact that $\sim 94\%$ of the 64 CFD study referenced in the review are of fixed OWCs suggests that the computational cost of fully floating WECs is perhaps still not deemed worthwhile.

The main issues with NWT simulations is determining solution convergence and verification, especially when modelling irregular waves and/or WEC motion in multiple degrees of freedom. Furthermore, the amount of different aspects to an NWT simulation requiring validation can be vast, from wave generation, absorption, reflection, hydrodynamic responses, motion responses and any secondary phase responses. It is therefore important to simplify models where possible and select the methods that will give most confidence and limit complications. In ocean wave energy applications the most popular CFD solver is the open source code called OpenFOAM accounting for 39% of the research featured in publications. Commercial codes make up just over half of the research literature with Fluent® being the most popular among them covering 20% overall [210].

Wave Generation

Regardless of wave generation, techniques for modelling a dynamic free surface in a numerical domain require an open channel Volume of Fluid (VOF) model with the

interface between the water and air phase known as the free surface defined at a Still Water Level point (SWL). The VOF model adds an additional transport equation to be solved whereby the Volume Fraction (VF) of the secondary phase (water) is solved in each cell and thereby tracking the interface between the phases. This equation is essentially the continuity of Volume Fraction:

$$\frac{1}{\rho_2}\left[\frac{\partial}{\partial t}(\alpha_2\rho_2) + \bigtriangledown \cdot (\alpha_2\rho_2\vec{V_2}) = \sum_{1}^{2}(\dot{m}_{12}) - (\dot{m}_{21})\right] \tag{2.22}$$

Where subscripts 1 and 2 denote the phase, α_i is the volume fraction and $\dot{m}_{ij}$ is the mass transfer in the direction from the i^{th} to the j^{th} phase [214].

The current techniques found in literature for wave generation can be placed into two categories: dynamic and static mesh methods. The dynamic mesh methods include attempts to model the paddles or pistons that are used to generate waves in physical experimental tanks i.e. moving paddles, pistons, wedges or plungers. In some cases this is possible with a dynamic boundary at the front of the NWT but in most cases require the remeshing of the domain in the local area. This adds significant computational cost for arguably marginal benefits but in some cases can be somewhat reduced with the use of the overset mesh method.

Rather than the movement of a physical object or surface to generate waves, static methods use the manipulation of flow either within a zone or at the boundary. The former refers to the relaxation zone method whereby a target solution with specific free surface elevation and sub surface velocities can be 'relaxed' into the solution and subsequently cause the wave to propagate out of the zone in the desired direction [215]. An alternative manipulation method called the mass source method, and variation known as the impulse source method, create bidirectional waves from the point of generation away from domain boundaries where a source essentially forces a free surface displacement. The evolved method implements this over a small zone with additional manipulation to continuity equation with source terms [210].

The final static method is the wave boundary condition, which can either be implemented using the built in methods that certain solvers such as Fluent®, or using

User Defined Functions to manipulate the velocity inlet boundary condition (also an option with Fluent®). The latter option involves prescribing the time dependent functions for free surface elevation and velocity components. This static method is by far the most popular due to the non-invasive approach and less computationally demanding [214].

Wave Absorption

In an NWT model, wave absorption is just as crucial as in an experimental study in order to minimise reflection from the rear wall. Methods used for wave generation can also be implemented for absorption at the opposite end of the domain, such as the relaxation zone [143], boundary manipulation and dynamic mesh methods [210].

The most simplistic method is the inclusion of a slope, which operates exactly as physical beach allowing the wave to dissipate its energy. The disadvantage of this method is the increased expense of modelling a breaking wave, which can be minimised but is an additional challenge.

The final non-invasive method that could best represent a lot of experimental tank physical beaches with complex geometry is the numerical beach. This is essentially a region defined in the domain, usually covering the same volume as the physical beach it represents, where damping is used to dissipate the energy of the wave before reaching the rear boundary. Within this region a source term S_m is added to the momentum equation, which contains damping terms that increase along the length of the prescribed beach region. The Fluent® code uses the following equation to define the source term:

$$S_m = -[C_1\, w + \frac{1}{2} C_2\, \rho\, |w|\, w]\big(1 - \Big(\frac{z - z_s}{z_b - z_s}\Big)\Big)\Big(\frac{x - x_s}{x_e - x_s}\Big)^2 \tag{2.23}$$

Where z_s is the vertical position still free surface, z_b is the vertical position of the NWT floor, x_s is the horizontal starting point of the numerical beach zone, x_e is the end of the zone and w is the vertical velocity component. Coefficients C_1 and C_2 are linear and quadratic damping coefficients applied in the x (horizontal) and z (vertical)

directions, respectively [213].

An alternative method of implementing a numerical beach is adding a porous zone. All numerical methods can be fine tuned and are most appropriate when physical beaches are not appropriate to be replicated in an NWT e.g. mesh beach [214].

Numerical Modelling of OWCs

This section gives a review of numerical studies in literature relevant to OWC types studied in this thesis: single chamber OWCs in the centre of the domain and M-OWCs.

Although CFD provides the opportunity to scale-up models to full-scale, often the numerical models are based of those experiments carried out in test tanks for validation purposes. This is despite the surprising fact that it is more cost cost-effective for very small scales (1:100) to model experimentally due to computational costs of running simulations [216].

An exception to these small-scale simulations is the full-scale simulations of Scarpetta et al. [217] based on the full-scale deployment of the REWEC. Such a scale requires a large domain length of $1km$ and water depth of $15m$. Despite the lack of validation, visualisation of fluid streamlines and therefore identification of loss generating areas, and quantification of performance values based on this such as absorption and pneumatic power are possible. Scarpetta et al. [218] are among the first to model an integrated breakwater using CFD. The breakwater was a submerged type containing an OWC, compared alongside a regular solid breakwater. Results determined that wave transmission downstream of the breakwater was reduced with the presence of the OWC. The orifice method is normally used to model PTOs, however in CFD porous medium can be used to model the effects of turbine instead [218].

Various numerical studies into the hydrodynamic and pneumatic behaviour of OWCs exist, often with more focus on one over the other. However, it has been proven to be more insightful to consider the energy distribution from the incident wave, that is, how much is absorbed, reflected, transmitted or dissipated through losses. To understand the path of the energy, not only provides a wholistic representation of the system, but also sheds light on the efficiency and performance of various parts and

therefore provides optimisation studies. Determining where losses are occurring by understanding where energy is lost in the system; through hydrodynamic interactions, reflection, pneumatics and so on. This methodology is well laid out and put into practise in work such as from Fleming et al. [219], and Simonetti and Cappietti [143], which will feature later in the thesis.

The Elhanafi et al. research group have carried out a significant number of CFD based studies on OWC operation, mainly using the commercial STAR-CCM+ ® solver and this energy balance methodology introduced. Elhanafi et al. [220] simulated a fixed bottom OWC geometry validated against internal air pressures and water column response from a referenced experimental source. Results highlighted the delicate balance of PTO damping with its negative affects either side of optimum. It was also noted that the increase in PTO damping increased the phase shift between internal and external surface elevations. Using the same validated NWT model in a subsequent studies, Elhanafi et al. [221, 222] studied the hydrodynamic impacts and behaviour for a non-bottom fixed OWC with varying wall depths and thicknesses. Consolidating the evident benefits of asymmetric lip submergence depths (front lip twice the wave height) and lip thickness set to 12% relative to the chamber length, the hydrodynamic efficiency peaked as high as 79%. Such was the impact of lip submergence on OWC performance, Elhanafi et al. [223] simulated a floating OWC to study the 3D affects with varying wave heights. These simulations were based on experimental studies from the $100m$ long Australian Maritime College towing tank with a 1:50 scale floating OWC. In the conclusions of this work, it is highlighted that 2D simulations significantly overpredict hydrodynamic efficiency. From this study and those proceeding, lip submergence is clearly impactful on hydrodynamic efficiency but is also sensitive to wave heights. Unless an OWC has the ability to reactively adjust the submergence according the incident wave height, the lip submergence should be at least equal to the amplitude of the maximum wave to be expected at the deployment site, else venting may occur [223]. The same experimental investigation and therefore NWT model was used an additional studies on wave forces [224] and survivability as a result of damage [225]. The experimental runs for the former study on wave forces

included force transducer instrumentation to measure vertical and horizontal impacts for varying PTO damping levels and incident wave characteristics. In general wave height and wavelength increase yields all around higher forces, as would be expected. Even though the horizontal forces were greater (12 times those vertical) throughout all test runs, changes in magnitude proved to be insignificant across damping values, whereas vertical forces increase with damping, especially at larger wavelengths [224].

Kammath et al. [226] carried out 2D CFD simulations on a fixed bottom OWC to investigate hydrodynamic behaviour. The model was validated against experimental data and used to study the streamlines beneath the free surface for different wavelengths and wave steepness. Ultimately this work was to validate the porous media method used to provide PTO damping and pave the way for subsequent numerical investigations into the effects of PTO damping on hydrodynamics [227]. Observations from this combined work show that, once again, increased wave steepness and wave height has a significant effect on hydrodynamic efficiency and increased PTO damping causes higher internal pressures while supressing the response of the internal free surface. Hence, the hydrodynamic efficiency is sensitive to PTO damping, which improves it to a certain limit then becomes unfavourable. As a result, PTO damping should be tuned to the particular incident wave conditions rather than solely the geometry, if possible [226, 227].

Dai et al. [216] investigate the effects of scaling OWC by modelling OWCs of different scales experimentally and numerically. Since the scale ratio between the OWCs was 3:1, there were two different physical wave tanks were used so as not to compromise the comparison by keeping the blockage constant. The numerical studies allowed for the simulation of another OWC model and NWT three times larger than the largest physical model. The authors note that the disagreements between scales in CFD are mostly due to dissipation in the NWT model, highlighting the fact that is important to keep the mesh strategies identical when regenerating meshes for different wave runs or geometries. Furthermore, regarding the uncertainty of wave generation, it is recommended that instead of relying on the CFD code to generate the wave requested, there is a calibration process whereby the input wave characteristics are

tuned to simulate the wave required i.e. those recorded in the experimental data [216].

Vyzikas et al. [215] contains the development of a numerical model using the open-source CFD solver OpenFOAM. The authors mention that the only disagreements notable between experimental and numerical results data are found in internal OWC air pressures and are said to be due to reflected waves as a result of poor wave absorption downstream of the OWC, the method for which was the inclusion of a relaxation zone. This highlights the importance of an affective a wave absorption method. Additional free decay tests were carried out, providing a positive answer to the question as to whether good performance predictions can be attained with reduced computational cost.

Celik and Altunkaynak [228] combines the use of the porous media PTO method and the free decay tests in 3D numerical simulations to establish hydrodynamic parameters using free decay tests. The numerical model was successfully validated in replicating the free decay tests to determine radiation damping and added mass coefficients.

The referenced CFD research thus far have been all been single fixed OWC simulations situated in the middle, or some distance from the rear wall of their respective NWT – most relevant to the research of this thesis. It has been highlighted that computational cost and accuracy have an inverse relationship. Often 3D affects are argued to be negligible considering the computational cost that would be incurred. As a result, 3D simulations are much less common, especially for M-OWCs. However, one of the two M-OWC CFD studies found which include 3D modelling is from Elhanafi et al. [229] who experimentally validate 2D and 3D models of a single and dual-chamber M-OWC-like attenuating concept. The main purpose of the modelling was to study affects changes to the submerged geometrical characteristics such as draft and lengths of the chambers, including unequal dimensions between the two chambers. The authors agree with the conclusions of earlier work [223] by stating that the front lip should draft should be minimised as much as possible before venting becomes a risk. Chamber length and PTO damping however are parameters that require tuning to the wave conditions although optimal values can be determined for

a range of wave periods. Most novel about these conclusions is the point that a dual-chamber attenuating M-OWC device will extract more energy than a single chamber, for no extra wave width of resource. However, although the first chamber can be optimised as if it were a regular single chamber OWC, the second chamber should be of larger length in order to capture longer wavelengths more effectively, hence the device wave period range is extended. This is similar rational to the multi-resonant devices mentioned previously, only instead of multiple drafts, different chamber lengths are used to achieve a similar outcome. The addition of the second chamber was said to increase the Capture Width Ratio (CWR) to up to $\sim 138\%$ compared to the single chamber model. The reason for such a large CWR is the formation of the OWCs as attenuators – additional chambers exist to extract more energy from the same width of the wave. Exceeding 100% implies the wave has drawn resource from a width wider than the OWCs, especially following the first chamber extraction.

Shalby et al. [230] modelled a four-chamber attenuating OWC array type M-OWC, also experimentally validated. The objectives of the study involved determining the effects of wave height, periods and PTO damping for such a device. The device was noted to be sensitive to wave height, with performance significantly dropping off with increase due to over damping causing a supressing of the internal free surface response and therefore compromising pneumatic power extraction. From the first chamber, performance decreased as the wave interacted with one chamber after the other. Despite this the device was reported to have achieved a 76% CWR for the larger period waves, which is interestingly less than the aforementioned dual-chamber concept.

Summary and Discussion

This chapter has provided an extensive review and discusses the overarching development of the OWC concept as wave energy converters, its evolved variations more specifically the M-OWC and relevant experimental and numerically modelling studies. This thesis is based on M-OWC development with strong interest in their benefits

against its predecessor, different PTO systems and the potential for integration with breakwaters.

The OWC has been the subject of research for many years but a very small number of devices have reached deployment. However, this is the case across all WEC technologies due to a lack of convergence, with perhaps a slight exception to those devices requiring less financial investment and therefore risk, i.e. retrofitted point absorbers/wave activated bodies. Despite these points, the OWC concept and devices are proven competitive from an efficiency performance standpoint compared to other WEC categories. This can be seen from the hydrodynamic efficiency, which is generally characterised by the CWR, a ratio between captured power and the resource of the wave per unit width. Babarit [52] reviews the available CWR data for devices across many WEC categories revealing the competitiveness of the OWC.

Without considering performance values, the benefits of the OWC over other WEC types are obvious and due to several attributes. Firstly, the simplicity of the required structure geometry and device operation. Although OWCs are very large structures, for example the LIMPET covered $169m^2$ [68] of the water's surface and pose significant civil engineering challenges, the geometry is not complex. With just the free surface oscillating inside the chamber, there are no submerged moving parts, which results in easier maintenance and contributes to another crucial attribute; the robustness and longevity of the overall operation and structure. This has been proven with the ~ 20 years operation of the Pico power plant, even though the failure of the structure was attributed to poor construction techniques and hence the lifecycle of an OWC like this could be considered to exceed 20 years [67]. Finally, the OWC has great advantage with its versatility with respect to deployment, geometric characteristics and applications.

The main points that require development, or the negative characteristics, are found within two areas; the first being within the pneumatics with the suboptimal performance of the energy conversion due to the bidirectional nature of the airflow. Through alternative methods as discussed, unidirectional airflow is possible, which is much more desirable for obvious reasons but can add complexity to the upstream

system.

The second key disadvantaged area is within the hydrodynamics; there is lack of bandwidth or tune ability of OWCs to the ever-changing incident wave frequency. Hence, the slow oscillatory fluctuations that are not rectified or smoothed by the PTO system are worsened by the inconsistent fluctuations from an OWC that is sensitive to changes in wave frequency, which has optimal performance at its resonant frequency that is rarely experienced in an irregular sea state. While the bandwidth of the PTO can be adjusted to improve performance across a wider range of frequencies, devices are not adaptable from a hydrodynamic perspective and cannot be tuned to changing wave conditions since their resonant frequency is determined by the geometrical characteristics of the OWC (as will be covered in the next chapter) and thus having a smaller bandwidth of optimal operation than would be possible [81].

Innovations based on the OWC concept and various endeavours in research aim to resolve these key disadvantages, although most are concentrated on the former point (pneumatics and PTO systems), since significant improvement is predicted to have a greater overall effect on power smoothing and performance. Although still under development, the M-OWCs have the potential to provide promising results, through the various innovative concepts under consideration, and support the progression and further development of wave energy as another serious contender in the renewables energy mix. The premise of M-OWCs is clear since it is widely known that ultimately, as with wind and tidal energy, WECs must be deployed on a large scale or in multiples as either arrays of individual devices or coupled, like segmented or modular M-OWCs for example, in order to benefit from the high density of the energy resource and the greater economic benefits of large scale. Yet it is not necessarily proven that WEC arrays in the case of the OWC is more beneficial overall than an M-OWC, which allows for greater manipulation of the unsteady oscillatory hydrodynamic wave power available. Furthermore, the interaction of OWCs in close proximity has been studied in some ways in literature for an OWC array but not an M-OWC. Hence, further research within this area to fairly assess these benefits is required, more from a wave energy conversion performance standpoint than overall cost of deployment analysis at

this stage.

More pertinently, this review has covered the two main aspects of overall OWC development that is considered the most crucial in research today in order to improve wave energy competitiveness by ultimately lowering the LCOE through upscaling deployment, diversification through innovative synergies, and performance enhancement through PTO system improvements. The two areas refer to the lowering of capital costs, and potentially improvement of annual production through greater efficiency of large-scale deployments and M-OWCs.

The true performance of modular M-OWCs vs its predecessors is ambiguous in literature. This is due to the large range variation of devices in different conditions and scales. Furthermore, the measure of efficiency cannot necessarily be trusted since especially with attenuator devices, the wave resource the device sees along the length of the structure is greater than quantified in the width of the wave due to refraction/diffraction. Hence, fair comparative analysis needs to be carried out in order to understand the key differences and benefits of the Modular M-OWC. The research of this thesis ever endeavours to measure performance parameters with a comparative predecessor baseline such as an isolated single OWC and array.

Not only in providing opportunity in scaling but the M-OWC, in general, generates opportunity for a wide range of different applications and variations in synergy projects. Identification of these innovative and cross sector beneficial technologies alternative applications and synergies are required in order to transform wave energy prospects as a competitor and a feasible option for commercial deployment. Offshore synergies could play a large part in wave energy development with potential offshore platforms, large structures like breakwaters, energy plants or wind turbine platform integration. This review has highlighted the case of the breakwater more, since these carry the benefits of already existing as an established technology and form of costal defence, which can also provide retro fitting options.

As seen among some of the existing M-OWC concepts, the M-OWC provides opportunity for the manipulation of airflow prior to the PTO system to generate unidirectional airflow, and in the case of the Modular M-OWC often for a single

unidirectional air turbine. Not only is unidirectional airflow more desirable for greater annual energy production and noise reduction, but in Modular M-OWCs often comes with a reduction in the number of turbines per OWC. The summary of all the M-OWCs reviewed is presented in Table 2.1 to highlight not only the pattern development but also the gap. The pattern being the movement toward either M-OWCs with fewer unidirectional turbines than the number of OWCs in closed systems or OWC arrays as M-OWCs with individual bidirectional PTO units. The gap exists with a lack of integration schemes with M-OWC open systems. The Waves2Watts WEC can offer a consolidation of all the benefits that come with emerging patterns and fill the gap.

It is believed that the Waves2Watts WEC can fit the concept of an open system Modular M-OWC with a unidirectional PTO system integrated in a breakwater. This fills many gaps in the current technology and ticks many boxes in lowering the ultimate success metric for wave energy converters, the LCOE. Aside from annual energy production, which is commonly given the most attention, the capital costs and operational costs are hugely influential components that are often after thoughts. The benefits of the proposed concept within these components is firstly in the integration scheme with the shared construction and maintenance costs, simplified construction with existing techniques, easy access and simplified grid connection. This can also yield the additional benefits of having a large multifunctional structure capturing the energy that would otherwise be dissipated but instead could potentially supply the local community or isolated island with electricity.

A final point to reinforce from a capital cost perspective is the reduction in capital cost due to the reduction in the number of turbines per OWC with this concept. It is well known that PTO efficiency needs to improve and if achieved will make a considerable dent in the LCOE, which is what an optimised unidirectional aims to do [11]. It can also be seen from this review that the reduction of the number of turbines per OWC stands to make a significant difference in the LCOE, since the PTO system is currently said to account for $20 - 30\%$ of total capital costs [12]. Hence, the PTO system not only strongly affects all LCOE components, which is why it is such a focal point in OWC technology development. For many years, the risk or trade off of a

unidirectional PTO system and/or a rectifying system has not been deemed worth it but the evidence in literature reveals a slow but necessary change in thinking on this matter.

The pitfalls of OWC development and the key areas to investigate are clear. Furthermore, the proposed M-OWC breakwater integration concept offers a potential solution to all of these points with the nature of its operational characteristics and can fill a gap in the current development path with the intended deployment as a breakwater integrated M-OWC.

Finally, the use of CFD within wave energy applications is still relatively new with only simple models being subjected to research while the relevant tools and methods continue to be developed and standardised practise. Minimal modelling has been carried out for M-OWC models and none on modular M-OWCs, highlighting the infancy of CFD in WEC development, especially at lower TRLs. Hence, without standardised methodology and with the significant variation between simulation cases, all NWT modelling should be carried out to a high standard. However, numerical simulations have shown promise in recent studies as reviewed in this Chapter, with successful validation across a wide range of studies and providing numerous methodology learnings which are applied in this thesis. To the best of the author's knowledge, there have been no full 3D modular M-OWC CFD simulations published in literature.

WEC Name	Company/Institution	Sub-categories	OWCs	Turbines	PTO System	Max. Scale	Latest Pub.	Refs.
Mutriku	-	Fixed Nearshore M-OWC Arrray Breakwater	16	16	Bidirectional Wells Biplane	Full Scale	2020	[74, 139, 231–233]
Sakata	-	Fixed Nearshore Segmented	~ 5	2	Bidirectional Wells Monoplane	Full Scale	2004	[138, 186]
MORE/ Seabreath	MARINET	Floating Modular	≥ 2	1	Unidirectional Closed System	36 m Length	2014	[109–111]
KNSWING	MARINET	Modular M-OWC Attenuator	40	≥ 1	Unidirectional Closed System	1:50	2015	[114–118]
Wave Mill/ iVec	Floating Wave Power Plant/ Wave Power Engineering Ltd.	Modular M-OWC Attenuator	> 4	2	Unidirectional	30 m Length	-	[112, 113, 234]
LEANCON	Aalborg University and HMRC	Modular M-OWC Attenuator V-Shape	104	≥ 1	Unidirectional Closed System	1:10	2013	[114, 120–123]
Stellenbosch	Stellenbosch University	Modular M-OWC Attenuator V-Shape	-	-	Unidirectional Closed System	1:25	2017	[124–129]
Waves2Watts	Lancaster University and Waves2Watts Ltd.	Modular M-OWC Terminator	≥ 2	≤ 2	Unidirectional Open System	1:50	2020	[72, 107, 235, 236]
MRC1000	Orecon	MRC Modular M-OWC	> 2	-	2 Stage Hydraulic	32 m Diameter	2009	[37, 134–136]
REWEC3	-	Fixed Nearshore M-OWC Array Breakwater	3	3	Bidirectional Wells Monoplane	Full Scale	2019	[85, 86]
-	University of Glasgow/ Taiwan National Science Council/ University of Technology Sydney	Segmented/ Modular M-OWC	≥ 4	≥ 4	Savonius	Lab Scale	2019	[108, 130–132, 230, 237]

Table 2.1: *Summary table of all M-OWCs reviewed with details of the number of OWCs, turbines, PTO system type, highest stage of development and references*

Chapter 3

Design of Experiments and Methodology

The ultimate goal within WEC technology development is to demonstrate operation with physical models. In the early stages, this is generally achieved at 1:50 – 1:100 scale in wave tank test facilities. This thesis includes a study carried out across a number of different physical models in iterative steps to answer the research questions posed in Chapter 1. This chapter provides the details of the experimental and numerical modelling methodology adopted for the research of this thesis, covering how the physics of the OWCs is captured through instrumentation and analysed during experimental modelling, details on the wave tank test facility, generation of sea states and the design of physical models. The model design process and methodology presented in this chapter follows the order of the overview of the research chapters and their contexts as listed in the Thesis Structure and Overview of Chapter 1.

Experimental Wave Tank Facility and Setup

Wave Tank and Equipment

Physical modelling was made possible with use of the Lancaster University Renewable Energy Group (LUREG) wave tank facility, which has the dimensions $11 \times 2.5\,m$

with an adjustable depth of $0 - 0.9\,m$. Figure 3.1 shows the details of the tank, the capabilities and setup of which will be covered throughout this chapter.

Kept consistent throughout all experimental modelling was the method for data. A National Instruments cDAQ-9172® chassis was used with a NI9205® module for reading analogue voltage signals and an NI9237® module with Wheatstone bridge wiring configuration for the pressure sensors. Data channels were sampled at $250\,Hz$ (maximum capacity for the number of channels) and conditioned within the LabVIEW® software with a custom-built Virtual Instrument (VI) and interface (Figure 3.1).

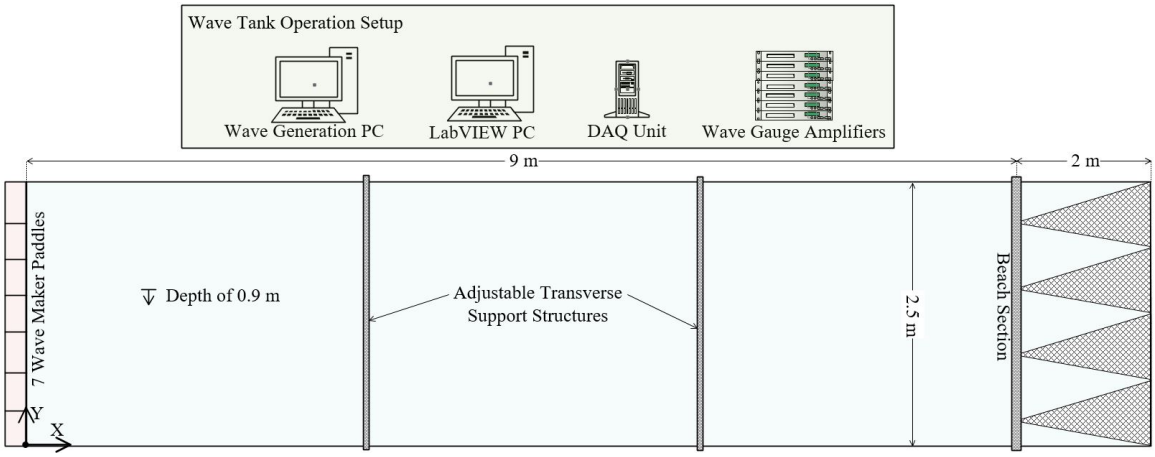


Figure 3.1: *Detailed schematic of dimensioned LUREG wave tank with wave generation and absorption features, and operation equipment setup*

Sensors

Since the operation of an OWC involves the dynamics of two fluids, water and air, variables associated to movements of these are the most crucial to capture, i.e. external and internal free surface displacement, air flow rate and pressure drop. Each experimental setup features a number of External Wave Gauges (WGs) and Internal Level Gauges (ILGs), used to capture this displacement of the free surface either as a wave propagates through a fixed point in the tank or causes the surface internal to the OWC to respond, respectively. Both WGs and ILGs are resistance water level gauges with individually amplified outputs. Prior to each experimental session gauges were calibrated by recording the change in voltage induced (ΔV) due to 0.06

m displacement (Δz) to give a calibration coefficient, K_{WG}:

$$\kappa = \frac{\Delta V}{\Delta z} \tag{3.1}$$

The air pressure sensors used were differential gauge type with a range of $\pm 1743\,Pa$, which were pre-calibrated. To establish further confidence in the calibration of these sensors, a calibration check was carried out with a digital manometer (Kane 3200 differential pressure meter, which has a range of $\pm 9999\,Pa$ and a resolution of $1\,Pa$). Both instruments were tested simultaneously with both being tapped into a partially submerged container lowered and raised at various intervals. Values were compared and plotted (See Appendix A Figure A.1), which proved that there is minimal error in the linear relationship provided by the manufacturer for calibration.

These differential air pressure sensors were always mounted with the primary inlet tapped into the position of interest and the counterpart port exposed to atmospheric pressure and clear of any areas with fluctuating air velocities. In earlier experiments an additional temperature and humidity sensor was incorporated into the models out of curiosity. This was created from two board mounted chips: a temperature and humidity transducer, which were contained inside a bolt shaped sensor casing manufacture inhouse to allow the sensor to tap into the OWC chambers. Fluctuations in temperature and humidity were insignificant and therefore the acquisition of this data was stopped and sensors omitted from the subsequent tests.

Wave Generation

As conveyed in Figure 3.1, waves are generated in the LUREG wave tank with seven paddles driven by motors and belts and controlled by the Edinburgh Wave Design® software. The range of waves that can be generated are restricted by mechanical limitations and the wave steepness. The critical steepness which marks this limit is the theoretical threshold at which waves begin to break, which is at $s \approx 0.142$, where steepness is defined as:

$$s = \frac{H}{\lambda} \tag{3.2}$$

Figure 3.2 [238] reveals these limits as a function of wave frequency, since this determines whether the amplitude is the limiting factor or the paddles mechanics. The paddles pivot through a maximum angle of $\approx$ 20 degrees in either direction with a displacement that is dependent on the hinge position and paddle size. This range of displacement limits lowest frequency waves achievable to be $\approx 0.65\,Hz$. Some extra motion is also included as an additional margin to take into account the active force absorption by the paddles. As shown in Figure 3.2,when increasing in wave frequency, the limiting factor is no longer paddle angular displacement but the steepness of the wave and therefore the amplitude is limited for a chosen frequency. These steepness limits are software set to avoid breaking waves but can be overridden with the additional wave synthesis software. Although the paddles provide reactive absorption of any reflected waves along with a $2\,m$ long mesh-type beach at the opposite end of the tank, which absorbs the transmitted wave to minimise reflection, if there is excessive reflection (normally at longer wavelengths) this also affects the paddles ability to generate a given wave amplitude accurately.

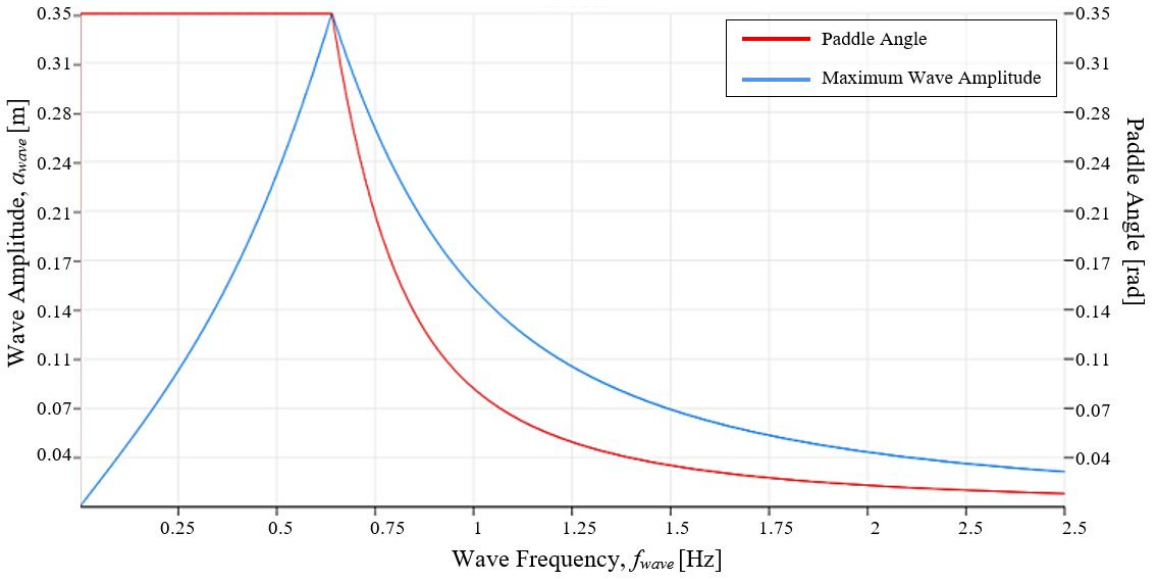


Figure 3.2: *Wave tank maximum wave amplitude achievable and paddle angle required are plotted against wave frequency conveying the limitations in wave generation using paddles [238]*

The width of the paddle is also a limiting factor but for wave angle range instead,

Wave Height, H_{wave}	Wave Frequency, f_{wave}	s_{max}
0.06 m	0.8 - 1.4 Hz	0.086
0.08 m	0.8 - 1.4 Hz	0.115
0.1 m	0.8 - 1.4 Hz	0.1

Table 3.1: *Generic set of regular wave runs for Phase 2 M-OWC experiments*

although angled waves are not generated for the experimental studies of this thesis. The capability of the wave paddles for generation did not create any limitations for experimental testing since the achievable range of wave amplitudes and frequencies mentioned were sufficient. With a maximum water depth of $h = 0.9\,m$, most wave generated were of the deep-water regime with some intermediate waves according to the following condition [47]:

$$\frac{\lambda_{wave}}{h} \leq 0.5 \tag{3.3}$$

Despite some waves at the lower end of the frequency range breaching this condition, no intermediate wave affects were observed.

Regular Waves

The Phase 1 experiments (Chapter 4), for both hydrodynamic and pneumatic tests, only entailed regular wave runs to further simplify the experiments ensuring good observability and attaining periodic behaviour. These regular wave runs therefore included wave heights (H_{wave}) in the range of 0.06–0.14 m and a frequency range (f_{wave}) of 0.8–1.4 Hz, which was the maximum range of waves suitable for the physical geometry. Increments between wave heights and wavelengths was generally kept to 0.02 m and 0.2 Hz, respectively. For the earlier Phase 2 experiments (Chapter 5), the regular wave run range was slightly more refined with a further lowering of the maximum a wave height to $H = 0.1\ m$ at higher wave frequencies, and an increased maximum frequency at lower wave heights in order to omit those that would be too steep, hence keeping the maximum steepness $s_{max} < 0.142$. The range of regular waves generated for the experiments within these limitations are summarised in Table 3.1.

Sea State Scaling

As the research of this thesis developed, the experiments needed to more accurately represent real world sea states through testing with regular and irregular wave runs. Real wave data time series histories were supplied by EMEC from their Billia Croo site to represent a Northwest Atlantic climate (see location details in Appendix B Figure B.1 and are used with more focus in this Chapter. This specific sea state is not of particular interest, it was chosen due to its availability to be representative of generic or expected field conditions for testing (as this is a test site location) and wave energy harvesting. Hence, this data was used to improve credibility of the experimental modelling, rather than quantify site specific energy capture.

The wave history between the two years was very similar when comparing the corelating months, therefore only one year time history of was used, since this was deemed representative of the wave climate based on the limited data available. The history analysed was to obtain most frequent occurrences of Significant Wave Height, H_S and Zero-Crossing Periods, T_Z. Figure 3.3 shows these time series over one year with a sample frequency of 30 minutes. The wave resource is presented in Figure 3.4, where H_S and T_Z values have been discretised in bins of $0.5\,m$ and $0.5\,s$ respectively. Wave direction was also discretised and plotted in a polar chart in Appendix B Figure B.2, although multi-directional waves were not considered or generated throughout the research of this thesis.

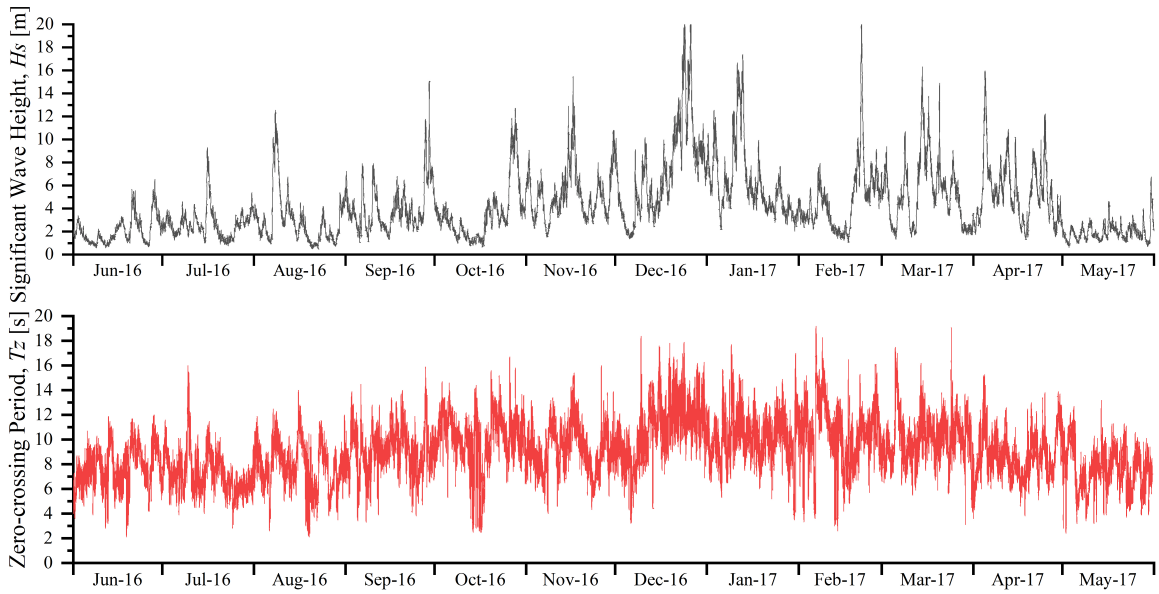


Figure 3.3: *Time series of significant wave height and Zero-crossing period from Billia Croo over one year sampled every 30 minutes provided by EMEC*

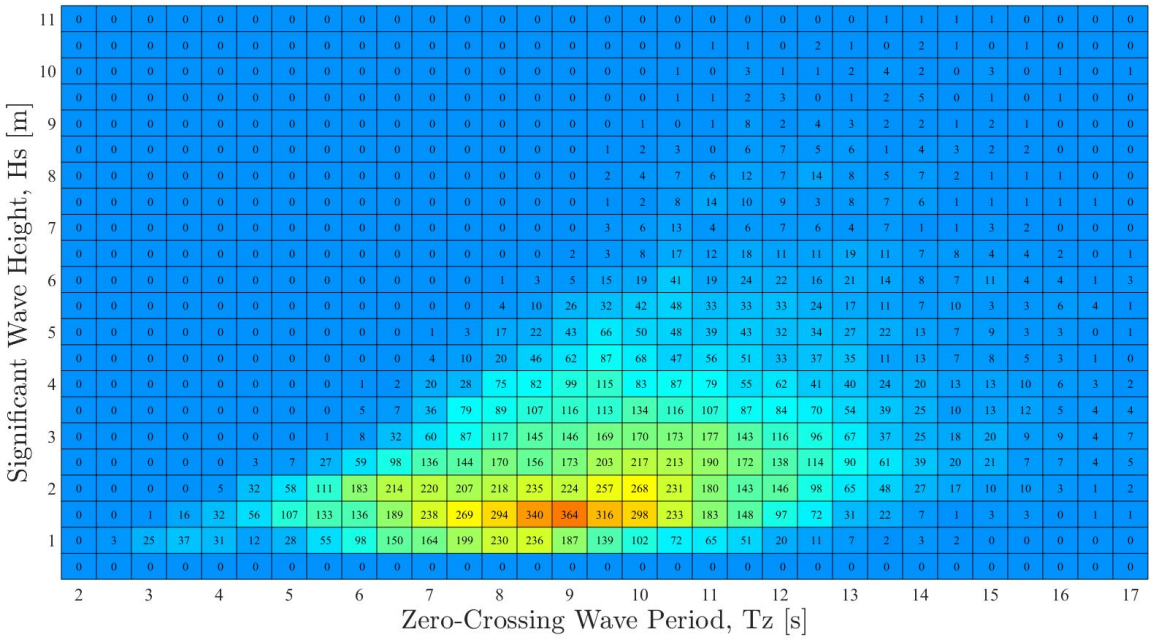


Figure 3.4: *Full scale wave matrix showing number of occurrences for values of zero-crossing wave period and significant wave heights over the one year of history data*

Selection of the waves based on the most frequent occurrences and tank limitations then followed with further filtering as illustrated in Figure 3.5. With the most frequent top 80 waves identified, the limitations of the experimental facility were taken into

account with respect to the wave periods and the saturation line, which also indicates the maximum steepness of the wave before crashing. A total of six wave periods at $Tz^F = 0.5\,s$ were chosen based on these factors and the range of wave heights for each period consisted of a minimum $H = 0.05\,m$ to the maximum possible due to the steepness constraint. These limitations can be seen in the selection of the waves as indicated in the plot of Figure 3.5.

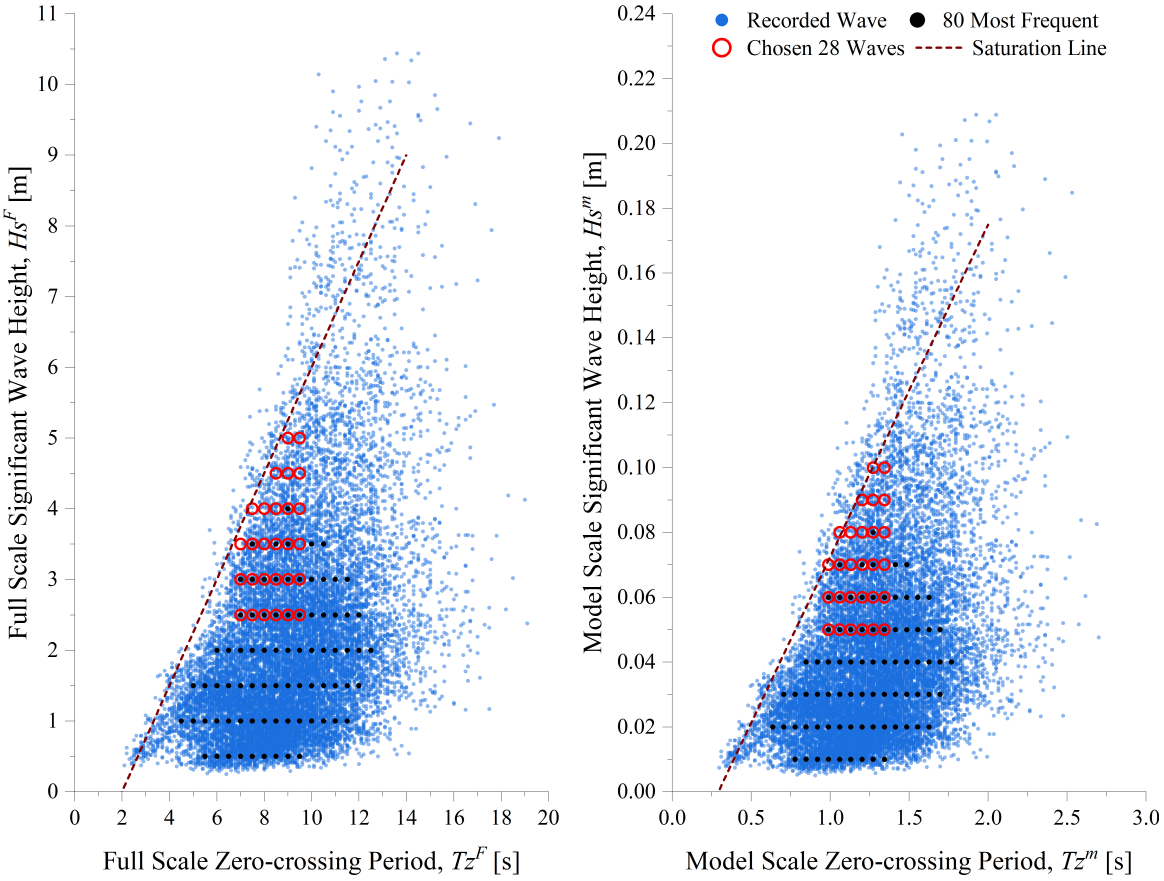


Figure 3.5: *Wave occurrence distribution and illustration refinement method by highlighting the top 80 most frequent waves and the chosen 28 waves on full scale (left) and model scale (right) plots*

Scaled Sea State Runs

A range of waves were chosen and reduced to 1:50 scale for the test regime based on the most frequent periods and a number of wave heights in increments of $0.01\,m$ at each period within the limits i.e. below a critical steepness but great enough to observe operation at this small scale (Figure 3.5). This yielded a total of 28 regular

Full Scale	1:50 Scale	
Tz^F	T^m	H^m
7	0.99	0.05 – 0.07
7.5	1.06	0.05 – 0.08
8	1.13	0.05 – 0.08
8.5	1.2	0.05 – 0.09
9	1.27	0.05-0.1
9.5	1.34	0.05 - 0.1

Table 3.2: *Filtered and selected regular waves range runs from EMEC data for use in experiments*

waves as listed in Table 3.2 (an expanded list can be found in Appendix B Table B.1).

Irregular Wave Runs

In order to test with irregular waves, energy spectra was created for each wave period chosen for the regular run as shown in Table 3.3. An in-house Matlab® code was used to generate the spectra according to the Joint North Sea Wave Project (JONSWAP) model. Although the JONSWAP model was used by default due to it's use in the in-house code, it is still suitable for these experimental tests. Firstly, as mentioned above, the intention is to generate field representative conditions in these irregular wave runs rather than site specific. Alternative spectra models are the Pearson-Moskowitz (PM) and Bretschneider, both of which can be represented by the JONSWAP model which has more variables, including an enhancement function that facilitates a smaller fetch such as in the North Sea. Hence, although this spectra was developed for North Sea climate specifically, it is certainly not limited to this and it has the ability to facilitate the spectral shapes of the alternative models [239]. Finally, due to the limitations of the wave tank, such spectra cannot be perfectly recreated, as can be seen from the plots of the simulated JONSWAP spectra vs the wave tank generated spectra can be found in Appendix E Figure E.2.

The process of generating the spectra involved first generating a white noise signal the length of the desired time series in order to create random distribution of amplitudes. This was then transformed into the frequency domain with the Discrete Fourier Transform function, and subsequently multiplied with the JONSWAP spec-

tra, which was created using model Equation 3.4 for the frequency range $f(i)$. The results were then subjected to an Inverse Discrete Fourier Transform to create the time series. The JONSWAP model was run for each period Tz, at significant wave height of $Hs = 0.05\,m$. Value γ was kept constant at $\gamma = 3.3$. Plots of this simulated time series vs the wave tank generated time series can be found in Appendix E Figure E.1.

$$S_J(f) = T^{-4} f^{-4}(i)\, e\left[(-1.25\, T f(i))^{-4}\right] \gamma^{e\beta} \tag{3.4}$$

Zero-crossing Period, Tz	Significant Wave Height, Hs	Run Time t_{max}
0. 99 s	0.05 m	300 s
1.06 s	0.05 m	300 s
1.13 s	0.05 m	300 s
1.2 s	0.05 m	300 s
1.27 s	0.05 m	300 s
1.34 s	0.05 m	300 s

Table 3.3: *Set of irregular waves runs used in the Phase 2 M-OWC experiments*

Analysis Methodology

An incident wave with a potential energy component due to vertical free surface displacement and kinetic component due to the orbital motion of water particles beneath the surface (Equations 2.6 - 2.7), causes the oscillation of the water column inside an OWC chamber. This then causes air to be pumped in and out of the OWC with the rising and falling of the internal free surface. Hence, the operation of the OWC is a multi-phase system and this section covers the methodology into how each element of OWC performance is measured and analysed in the research of this thesis.

Post-Processing and Data Analysis

Consistent quality control measures of data is important to ensure inaccuracies or error does not propagate through the analysis process. Therefore, quality assurance

measures were implemented throughout the experimental modelling process starting with sensor calibration. The in-house wave gauges and amplifiers were re-calibrated before every experimental session and purchased sensors calibrations checked through tests before installation. Sampling rates were set to a maximum to ensure possibility of capturing any unexpected behaviour, which meant filtering took place to reduce the data points giving an opportunity to remove anomalies. In most cases anomalies were identified during testing and the tests were re-run. Test cases were ran multiple times in order to attain reliable averages and ensure that multiple data sets existed and correlated well. From a data security perspective, all data was plotted live on the PC screen during test runs, while being processed, exported and backed-up in the background.

Throughout all experimental data analysis, Matlab® has been used to condition and post-process results, along with Origin Pro® for visualisation and figure generation. Since this research concerns the operation of a WEC within the first stage of energy conversion, the wave, hydraulic and pneumatic forms of power are measured and are of most interest at this experimental modelling stage. While wave power will be covered in Chapter 2, where wave theory is discussed, the methods used to derive hydraulic power and pneumatic power throughout the research will be described here.

All plots in Chapters 5, 6 and 7 contain commercially sensitive data and are therefore normalised using the following method:

$$x^* = \frac{x}{x_{max} - x_{min}} \tag{3.5}$$

where x^* is the normalised variable and x is the original variable. Time series analysis is kept constant throughout experiments and the eventuating terms thereof. Time series are generated for all variables measured, namely from the WGs, ILGs and pressure transducers. Aside from further frequency domain analysis, these time series are used to find Average Peak Values and Mean Values, primarily for the analysis of regular wave runs due to the periodic nature of the responses. Mean values of variable x are found by integrating the time series of the variable over N periods as shown in

Equation 3.6 with the example of x_m. Although the longest integrating time period was used in analysis to determine these values, smaller periods yield reliable estimates due to the periodicity of the responses.

$$x_m = \frac{1}{NT} \int_t^{t+NT} x \, dt \tag{3.6}$$

Average peak values for variable x, are found by taking the average of the maximum values from n half periods in order to account for the two power peaks or absolute flow and pressure peaks in a single period from exhale and inhale processes:

$$\bar{x}_{Peak} = \frac{1}{n} \sum_{i=0}^{n} x_{max} \tag{3.7}$$

Hydraulic Power

As the wave causes the internal water surface of the OWC to displace in both directions – ascending and descending, the positive and negative pressures generated enable this power to be quantified as a hydraulic power since the free-surface is acting as a piston and essentially doing work on the 'working fluid', the air. Hence, this can be found with the velocity of the free surface, $\dot{z}$ and the OWC air pressure, p_{owc} :

$$P_{hydr} = \dot{z} \, p_{owc} \tag{3.8}$$

where,

$$\dot{z} = \frac{dz}{dt} = \frac{z_t - z_{t-1}}{t_t - t_{t-1}} \tag{3.9}$$

Empirical Flow Rate and Pneumatic Power

In the chamber, the velocity of the air inside the chamber is very small and it is therefore safe to assume that pressure is uniform but not near the orifice. Throughout literature, orifice plates have been used in OWC experiments to model the PTO since the quadratic pressure drop best replicates the effects of damping of a non-linear turbine such as the impulse turbine. The damping of the turbine is coupled

and therefore very similar to the damping of the OWC, hence optimal pneumatic OWC damping should be determined [240]. Damping created by the orifice plates can therefore be varied to find the optimal by interchanging plates with different diameters. Where diameters are changed during experiments, the desire is to achieve maximum performance for WEC model comparison purposes. Damping is required for energy extraction but overdamping causes a suppression of the internal free surface response [227]. In 'real life' optimal damping varies during operation. Orifice plates are expressed as a percentage defined by their area, A_o, with respect to the water plane area of the OWC, S:

$$O = \frac{A_o}{S} \times 100\% \tag{3.10}$$

Additionally, orifice plates are commonly used as a method in creating pressure drop to determine fluid flow rates in various configurations and is an industry standardised method as per ISO 5167-1 [241]. With the positioning of a pressure tap either side of an orifice plate measuring differential gauge pressure, with the external tap in atmospheric conditions, this pressure drop (Δp_o) can then used to find the flow rate through the orifice with the following empirical equation:

$$Q_o = A_o V_o = A_o C_d \sqrt{\frac{2\Delta p_o}{\rho_{air}(1-\beta_d)}} \tag{3.11}$$

The discharge coefficient, C_d is found with a standard equation based on the $\frac{1}{2}D$ model and is a function of the Reynolds number, Re, and the geometrical ratio between the upstream diameter and the orifice diameter, β_d [241]:

$$C_d = (0.5959 + 0.0312\beta_d^{2.1} - 0.184\beta_d^8) + 91.71\beta_d^{2.5}Re^{-0.75} + \frac{0.09\beta_d^4}{1-\beta_d^4}F_1 - 0.0337\beta_d^3 F_2 \tag{3.12}$$

where coefficients for the $\frac{1}{2}D$ model are $F_1 = 0.4333$ $F_2 = 0.47$ [212]. This discharge coefficient can ultimately be used to express the turbine flow coefficient, k_t [242]:

$$k_t = (2\rho A_o^2 C_d^2)^{-1} \tag{3.13}$$

Although there are slightly different forms of the C_d equation for differing geometries and set-ups, all were tested throughout the experiments during model changes and yielded identical values in most cases. Pneumatic power extracted from an OWC at the respective orifice plate is then found using the absolute value of the empirically derived orifice flow rate and its associated pressure drop:

$$P_{pn} = \Delta p_o \cdot |Q_o| \tag{3.14}$$

Measured pressure drop and subsequently flowrate is very sensitive to the precision of the orifice diameter [216]. For this reason, the orifice plates first involved cutting the external diameter and mounting holes out with the laser cutter, followed by a very careful process on the lathe to get the internal diameter to a tenth of a micrometre precision consistently across duplicated orifices.

Power Comparisons

The Capture Width Ratio (CWR) is often used to express the effectiveness of power conversion by a WEC by considering only the capture width as a leading characteristic. It should therefore be used with caution but despite this has become a means of comparing WEC conversion efficiency in a rudimentary way and is often used across the field for WEC comparison. However, it isn't believed to be an accurate representation of a WECs efficiency for comparison with other WECs, rather a useful tool when cross comparing models within the same experimental project.

The CWR is essentially ratio of the power extracted by the WEC and the power of the wave across the WEC width. For the purpose of comparing the performance of the models tested, in this research the CWR is calculated in two forms; one with respect to the power in the wave across the effective width, B_E and the second across the total width, B_T:

$$CWR_E = \frac{P_m}{P_{wave} B_E} \tag{3.15}$$

$$CWR_T = \frac{P_m}{P_{wave} B_T} \tag{3.16}$$

The effective, or 'working' width, B_E is essentially the product of number OWCs and the internal water plane width B_{inner}, hence B_E remains constant at $3B_{inner}$. The total width, B_T is the total width of the structure – the distance between opposite outer walls:

$$B_T = 3B_{owc} + 2dY \tag{3.17}$$

Reflection and Energy Balance Analysis

Wave Reflection

As covered in the literature review with various references [143, 219, 220], measuring wave reflection becomes a crucial part of determining device absorption efficiency. The calculation of wave reflection was achieved with the implementation of the Gaillard et al., three probe method appropriate for non-angled waves such as these [243]. This method was incorporated in a Matlab® model used in the analysis of some models and requires three probes specifically spaced according to the method and the wavelength of each wave run:

$$\left.\begin{aligned} dx_{01} &= 0.1\,m\ (const.) \\ dx_{12} &= 0.3\lambda \\ dx_{23} &= 0.6\lambda \end{aligned}\right\} \tag{3.18}$$

In this case, with regular waves runs, this method yields both an energy spectra of the incident and the reflected wave, which are used to determine the respective mean wave heights, H_m:

$$H_m = \sqrt{8m_0} \tag{3.19}$$

where m_0 is the zero moment and is found by integrating the spectra. The energy spectra at WG locations were all generated per the spectral analysis methodology stated in Chapter 1 and used to determine mean wave heights in the same manner. This is then used to determine the energy in the incident and reflected wave with the general expression for the energy in a wave:

$$E_{wave} = \frac{1}{8}\rho g H^2 \lambda \tag{3.20}$$

The reflection coefficient is then found with the following ratio:

$$K_r = \frac{H_R}{H_I} \tag{3.21}$$

Irregular waves do not result in a periodic behaviour and therefore require a different approach. Firstly, an approach was used to split the time series into segments of $NN = 2048$ samples ($t_{seg} = 8.192\ s$), a value chosen in order to obtain sufficient frequency resolution without making sections too small. Then instead of finding the significant wave height from all spectra, the following equation was used to determine the total energy in the segment:

$$E_{Segi} = \frac{m_0}{\rho\, g} \tag{3.22}$$

Energy values across all segments can then be considered for their individual segment or summed over the number of segments (N_{segs}) to find the total energy of the time series.

Energy Balance Analysis

Prior to the pneumatic energy extraction, efficiencies can be determined through an energy balance study, based and developed from the work of Simonetti et al. [143] and other variations as discussed in the literature review [220]. Figure 3.6 details the energy components and the path of conversion for the OWC up to mechanical power, P_{mech}. Since this is a fixed device, the rules of conservation of energy require that the energy in the width of the incident wave (E_I), has to be accounted for the energy of the reflected wave (E_R), transmitted wave (E_T) and absorbed energy (E_A):

$$E_I = E_R + E_T + E_A \tag{3.23}$$

The absorbed energy can then be split into energy that is extracted as measured at the orifice (E_E), stored energy due to the oscillating water surface inside the OWC

(E_S):

$$E_A = E_E + E_S + E_L \tag{3.24}$$

where the general losses (E_L) term is the only unknown. The stored energy is the potential energy as a result of the heaving internal water column [143]:

$$E_S = \frac{\rho g Z_i^2 B_{inner}}{16} \tag{3.25}$$

This balance method is used to determine and accurately represent the path of the incident wave energy for the different models and for both regular and irregular wave runs.

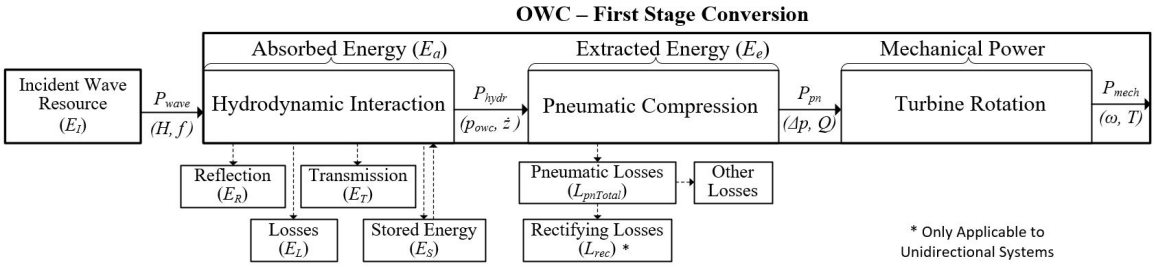


Figure 3.6: *Overview of OWC first stage energy conversion detailing sub-stages and associated quantities*

Physical Model Design

This thesis includes an evolution of the physical models that become progressively more complex in terms of phenomena to capture and understand. Therefore, each model was conscientiously designed to serve the purpose of experiment and facilitate the answering of the relevant research questions. This section walks through the design of said physical models and the reasoning behind the design decisions made.

A building block for all models are the OWC structures themselves, which only vary in size between earlier experiments and are otherwise kept constant with respect to material, fixings and construction. The OWC walls and lid were constructed with clear Perspex® of $0.01\,m$ thickness assembled with screws to secure the sides and lid for easy adjustment and sealed airtight. The models remained fixed throughout

all modelling and were secured to the support beams that stretch across the tank width(see Fig. 3.1) with four long metal brackets per OWC. The brackets hung the OWC from the support structures and had slots in order to facilitate any adjustment in draft required (see Fig. A.2 of Appendix A). Note that throughout all changes in geometry, chamber drafts were kept sufficient to avoid venting [104].

Models remained fixed in order to simplify experiments, model characteristics, and to ensure the points of interest were observable. Furthermore, the characteristics and processes of interest are not substantially affected with a fixed model – if anything, performance is improved due to the absence of relative movement.

General Model Setup

For both the hydrodynamic and pneumatic experiments of Phase 1, the tank setup remained simple as shown in Figure 3.7. Each OWC chamber has a its own Internal Level Gauge (ILG) and external Wave Gauge (WG_{EXi}), both positioned on the centreline with respect to their chamber lengths, hence in phase. Further wave gauges WG_1–WG_3 are positioned upstream of the OWCs across the width of the tank to capture the incident wave in real time.

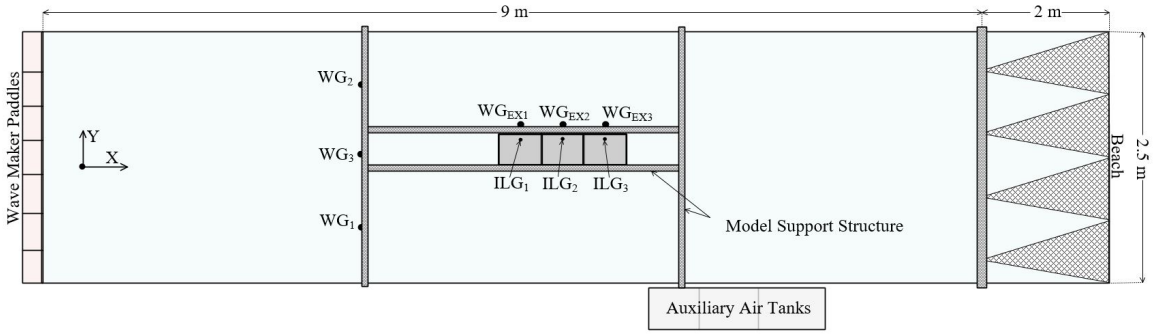


Figure 3.7: *The LUREG wave tank facility dimensions and setup of the experimental model, support structures and water level gauges for the Phase 1 experiments*

Phase 1 Hydrodynamic Modelling

Initially, just three of the five OWCs that were manufactured for these experiments were assembled and installed in the tank. Referring to Figure 3.8, the dimensions of

these three chambers assembled and mounted in attenuator configuration are found in Table 3.4. Photographs of the model in situ can be found in Appendix A Figure A.2. Since the interaction with the air volume in the water column was not of interest in this particular experiment, the lids of the chambers and PTO modelling was omitted.

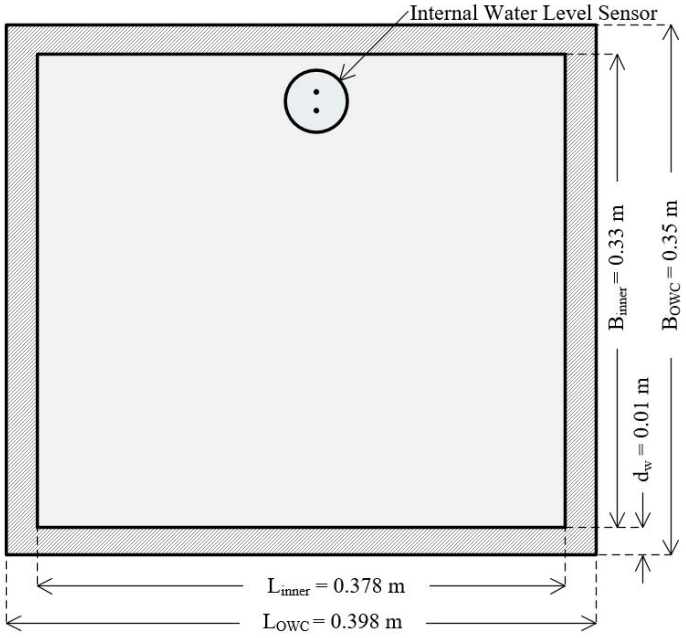


Figure 3.8: *OWC model geometry for the Phase 1 hydrodynamics experiments*

Characteristic	Dimension
L_{owc}	0.398 m
B_{owc}	0.35 m
D_{owc}	0.36 m
L_{inner}	0.378 m
B_{inner}	0.33 m
D_{inner}	0.35 m
D_{sub}	0.2 m
dw	0.01 m

Table 3.4: *The OWC model dimensions for the Phase 1 hydrodynamic experiments*

Phase 1 Pneumatic Model and OWC Scaling

Since these pneumatic experiments took place following the hydrodynamic tests, the geometry was adjusted to achieve more optimal operation according to both relative wavelength and the wave data gained from the European Marine Energy Centre (EMEC). In these early experiments, this data was used to determine a rough scale of the experimental model based on the mean wavelength at a the Billia Croo site. The mean wavelength at the site was taken to determine the resonant frequency (f_0) required. All other dimensions were kept proportional making the OWC length (L_{owc}) the characteristic dimension. Scaling was then achieved mainly through Froude scaling law which requires keeping the ratio between inertial and mass properties constant as

seen in Equation 3.26. These ratios result in different Froude scale factors depending on the variables required to scale, which are then used in Equation 3.27 for conversion.

$$Fr = \frac{F_{inertia}}{F_{mass}} = \frac{\nu^2}{gL} \tag{3.26}$$

$$\varepsilon = \frac{X^F}{X^m} \tag{3.27}$$

Where superscripts ^{F} and ^{m} denote full and model scale, respectively. Moreover, further consideration into the device scale must be taken due to the added consideration of the air and thermodynamics. Although the geometry of the OWCs could be scaled using standard Froude scaling laws, the scaling down of the systems air volume had to take into account the changes in compressibility between a large and small-scale volume. During an OWC there is a slight lag between the airflow through the orifice and the internal water level displacement due to the compressibility of the air which acts as a temporary energy store. A reduction in air volume and therefore compressibility compromises this spring like effect and in turn the hydrodynamic behaviour of the OWC. As found in literature, the compressibility-scaling factor ε^2 should be used instead of the Froude equivalent for volumetric scaling, ε^3 so as to scale down compressibility or springing effect of the air volume correctly [244]. This meant an additional $0.216\,m^3$ of air volume per OWC had to be provided without compromising the scaled OWC geometry or hydrodynamic behaviour. This was done so with the use of auxiliary tanks for each OWC partially filled with water and connected with flexible hoses directly from the lid of the OWC (see Appendix A Figures A.8 and A.9). These updated dimensions are listed in Table 3.5 and refer to the geometric layout of Figure 3.9. Overall, the scale of the individual OWCs was reduced 1:50 scale with the aim achieving a piston operation across a larger frequency range with a higher λ_{rel}.

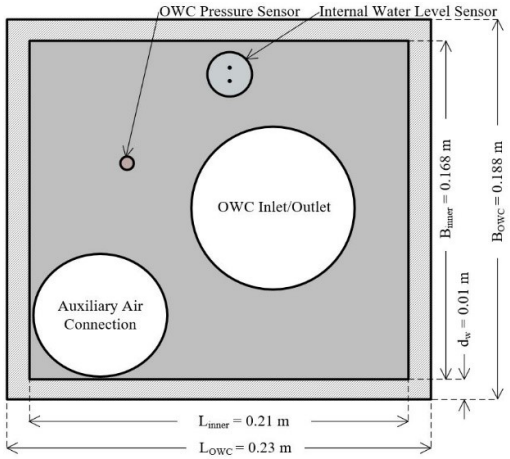


Figure 3.9: *Plan view of the Phase 2 OWC Geometry (1:50) with relevant dimensions, and positioning of orifices and transducers*

Dimension	Scale Factor	Full Scale	1:50 Scale
L_{inner}	ϵ	10.5 m	0.21 m
B_{inner}	ϵ	8.4 m	0.168 m
D_{owc}	ϵ	8.4 m	0.168 m
F_{inner}	ϵ	6.3 m	0.18 m
λ_{wave}	ϵ	-	-
D_{ai}	ϵ	8.4 m	0.168 m
D_{owc}	ϵ	8.4 m	0.168 m

Table 3.5: *OWC model (1:50 scale) dimensions*

With the addition of OWC lids and the requirement to seal them airtight, new ILGs were created. Replacing the standard two-pronged resistance water level gauges were two copper tracks mounted on the inside of the OWC side wall. Prior to testing these new gauges were validated against the original level gauges, Appendix A Figure A.4 contains a validation plot and pictures in of the strips in the model are Figures A.3 and A.5.

As previously mentioned, the intention of these experiments is to determine how the first chamber (1^{st} stage) contributes to the subsequent chamber (2^{nd} stage) and whether pressure is accumulated and performance is enhanced compared to a singular OWC.

Valve Design

As detailed in the W2W patent (Fig. 1.4), unidirectional valves are required at the inlet of the first OWC and in between all intermediate OWC chambers, in this case in between the 1^{st} and 2^{nd} stage. For the purpose of these experiments the outlet of the second chamber will feature an orifice in order to model PTO damping. As detailed, the reason for using orifice plates in OWC experiments to mimic PTO damping effects by generating a quadratic pressure drop that subsequently yields a flow rate, which

can be calculated using the appropriate empirical equations. An outlet valve was initially tested with intentions of including an accumulator tank with an orifice plate outlet to partially isolate the 2^{nd} stage from PTO effects, however, the outlet valve proved difficult to model reliably and would compromise the aims and objectives of the experiments.

No suitable unidirectional valves could be outsourced meeting the criteria for reliable modelling of the intended processes i.e. low opening and sealing pressures. Therefore, various valves were made at LU and tested for suitability. There were two main types that where manufactured and tested: those that were designed using CAD and created through additive manufacturing, and those made from varying thickness of rubber with shallow scores to create a hinge effect. The flap design was considered superior to other types such as butterfly due to having to be actuated by the airflow only – opening and closing in response to pressure gradients. The valves were tested in the inlet position of the 1^{st} stage by carrying out single chamber compression tests, which tested the pressure at which the valves would close, how well they sealed shut (resultant leakage), at what pressure they reopened and how far they opened in order to allow maximum airflow on inhale. The valves to connect the OWCs were then tested with the same scrutiny although with additional experimentation by adding weights to improve closing and sealing. The additive manufactured valves were mounted at 45 degrees to allow for gravity to assist in closing and sealing while the rubbers where mounted vertically with the hinge at the top of the orifice.

Overall, the additive manufactured valves were outperformed the rubber variety due to their rigidity. The thinner rubber valves were better than the thicker, but deformed easily and failed to close effectively in the intermediate case. The additive manufactured valves were selected and further optimised due their quick response and ability to seal, especially with the addition of an O-ring. The hinges were lubricated to ensure minimal friction and consistent action. The passage through the valve was sanded to ensure smooth surface for airflow through the valve, albeit the effects would be negligible. Additive manufacturing as a process to manufacture the valves proved to be valuable by having the ability to rapidly make and test valves and iteratively

design. The performance of these valves once the design was decided upon did not warrant an alternative material or method of manufacturing the parts. Figure 3.10 contains the Solidworks® assembly of the two chamber experimental model and a closer look at the valves can be found in Appendix A Figures A.6 and A.7.

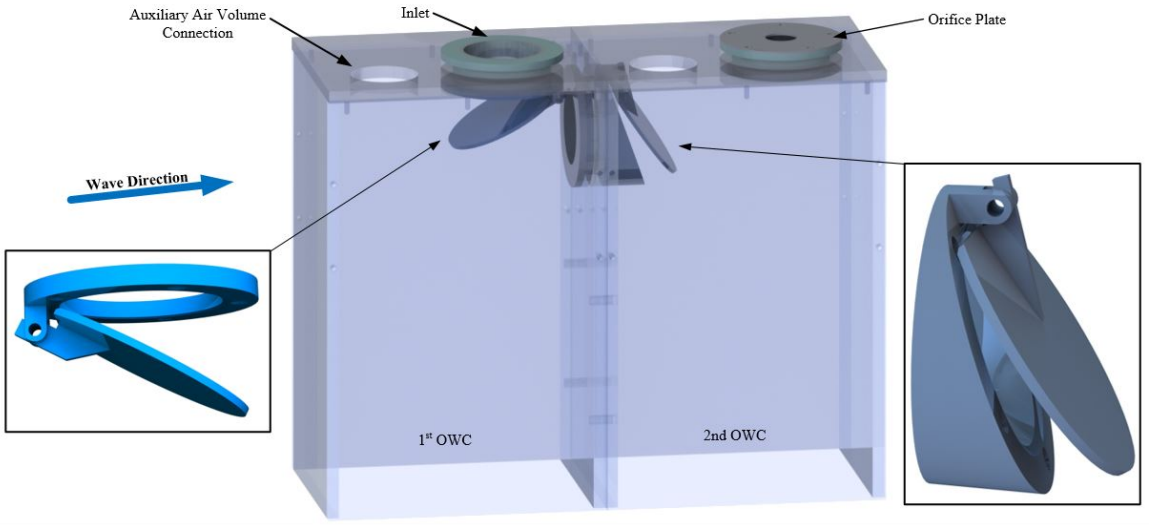


Figure 3.10: *Physical 1:50 scale two chamber W2W model for Phase 1 pneumatic experiments with inlet and intermediate flap valves, and outlet orifice plate*

Phase 2 Tank Setup and Geometry

The experiments of Phase 2 are split into two studies comprising of a total of five different models: an OWC array and M-OWC bidirectional M-OWC, which form Chapter 5; a bidirectional M-OWC, and the bidirectional M-OWC, unidirectional single and twin turbine M-OWC breakwater models, which form Chapter 6. The tank setup varies between these two studies – the first of these setups is detailed in Figure 3.11 details and includes adjustable beam structures that span across the width of the tank to support the fixed models that are now transverse (terminating formations), a different configuration of WGs, and an additional air tank is added for the third OWC.

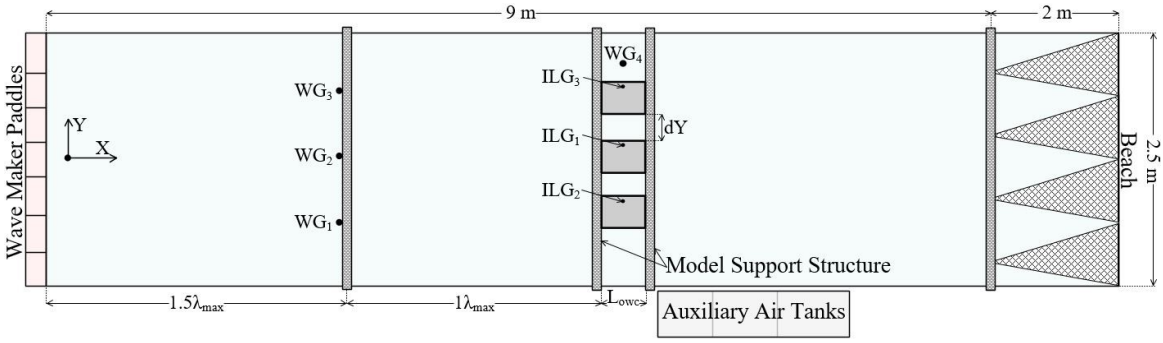


Figure 3.11: *Setup of the LUREG wave tank for the first block of Phase 2 M-OWC experiments for modelling M-OWCs in terminator configuration with adjustable OWC spacing*

The subsequent studies include a final setup that mainly include the alteration in positions of probes (or WGs) to allow additional analysis of the incident, reflected and transmitted wave. Figure 3.12 details these alterations showing the new total five WGs for measuring external amplitudes forward of the model (WG_{1-3}), to the side aligned with the centre of the OWCs (WG_4 or WG_{EX}) and behind the structure (WG_5). Each chamber contains an Internal Level Gauge (ILG_{1-3}), positioned on the centreline of the OWC/s with respect to the chamber length and therefore aligned with the external WG_4.

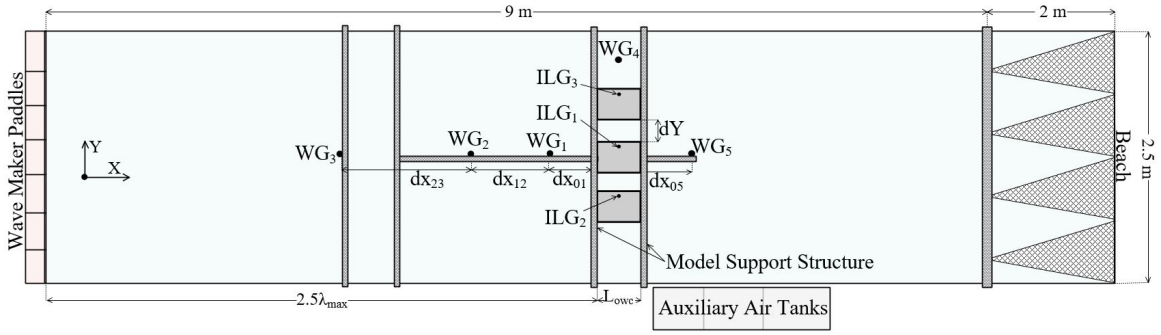


Figure 3.12: *Setup of the LUREG wave tank with the details and dimensions of the wave probe layout, model positioning and support structures.*

OWC Array Model

An OWC Array is classed as an M-OWC device if the multiple individual OWCs are part of or mounted within the same structure. Hence, the OWCs operate in isolation

with individual PTOs and generators but are combined in a common structure. The array here essentially a row of OWCs in terminating configuration, where their front walls are aligned parallel to the incident wave crest as seen in Figure 3.13. Spacing in between chambers, a, is expressed as a function of the inner OWC water plane width B_{inner}:

$$a = \frac{dY}{B_{inner}} \tag{3.28}$$

where dY is the distance between the edges of the water plane area of neighbouring OWCs (Figure 3.11). Spacing is increased at intervals of $0.5a$ for the range of $a = 0$ to $a = 3$. The mounting structure across the width of the tank supports the OWCs and provides easy adjustment of the spacing. Pressure sensors are tapped into the lids of each OWC as with the previous models.

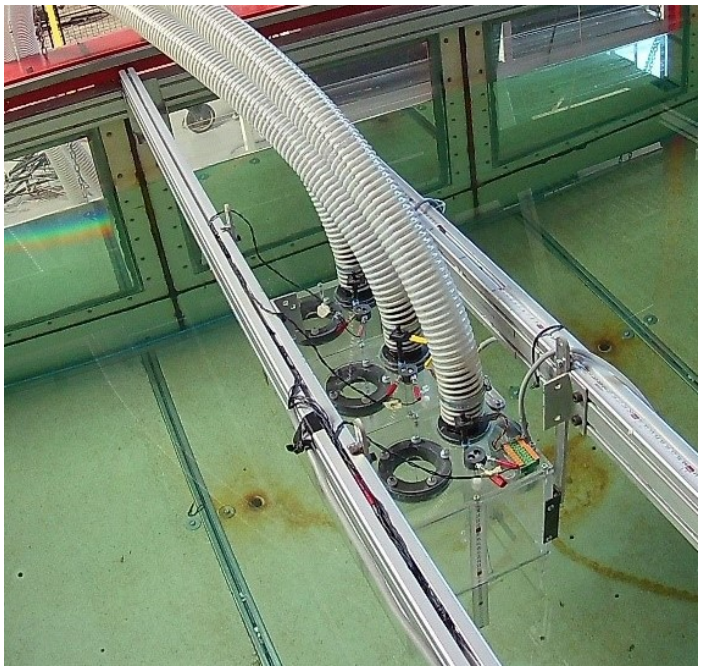


Figure 3.13: *Example picture of the OWC array M-OWC model in situ at the LUREG wave tank with zero spacing*

M-OWC Bidirectional Model

As defined, a Modular M-OWC has multiple OWCs providing airflow that converges prior to the PTO system. This could include a final air chamber like an accumulator,

high/low pressure ducting, or additional manipulation of the airflow e.g. a rectifying system. Most commonly, the Modular M-OWC concept is used in closed systems with unidirectional airflow and PTO systems [72]. In this case, bidirectional airflow is captured at the inlet/outlet of the ducting or manifold. Again, this sustains this pragmatic approach and makes the model comparative with the previous models with bidirectional airflow.

To achieve the coupling of OWCs, a manifold is added to take the flow from each chamber to a single pipe where an orifice plate is situated as shown in Figure 3.14. As with the OWC array, spacing could be easily adjusted, however, with the M-OWC there was the added complexity of the replacing the ducting lengths at each interval and ensuring airtight joints. Pressure transducers were mounted in the OWCs and on the non-atmospheric side of the orifice plates at appropriate distances according to the correct standards as discussed earlier in this chapter. The changes to the OWC lid for this model including an adapted two wire ILG, are shown in Figure 3.9.

These are by no means an optimal layout or design but is a result of the experimental model progression and keeping as many aspects as possible constant, for example, OWC lid geometry.

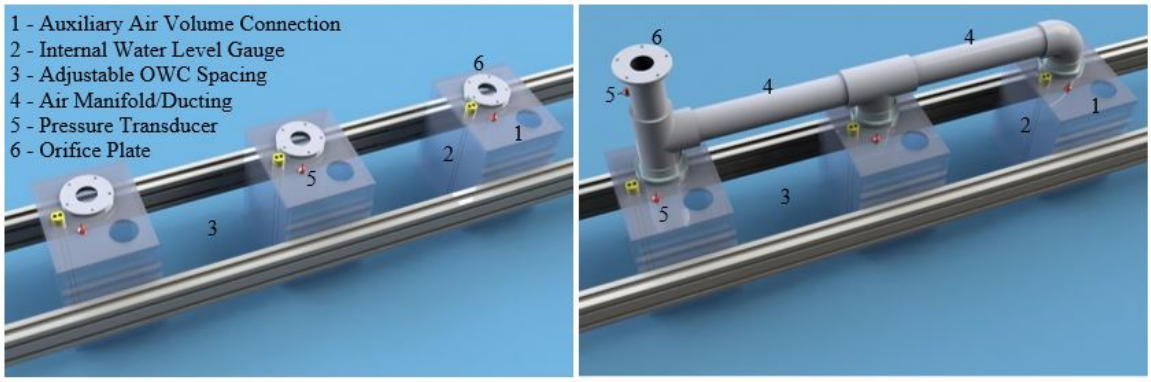


Figure 3.14: *Annotated renders of the 1:50 design and layout of the OWC array (left) and M-OWC (right) models*

Breakwater Modelling

The M-OWC bidirectional model remains a three-chamber fixed model with a manifold combining airflow from all OWCs prior to the PTO. One slight alteration was

made by moving the outlet above the centre OWC rather than the end in expectation of better performance. A picture of the model installed in the tank can be found in Appendix A Figure A.12.

As depicted in Figure 3.15, the model has the ability to be installed with and without blocking structures in between the chambers to represent the function of a breakwater (BW), rather than a passive device. The removable structures were folded into shape from 1.5 mm thick steel sheet and fastened to the OWC walls. These were only manufactured for a set spacing of the OWCs where $a = 1$, the reason for which will become clearer in the following chapters.

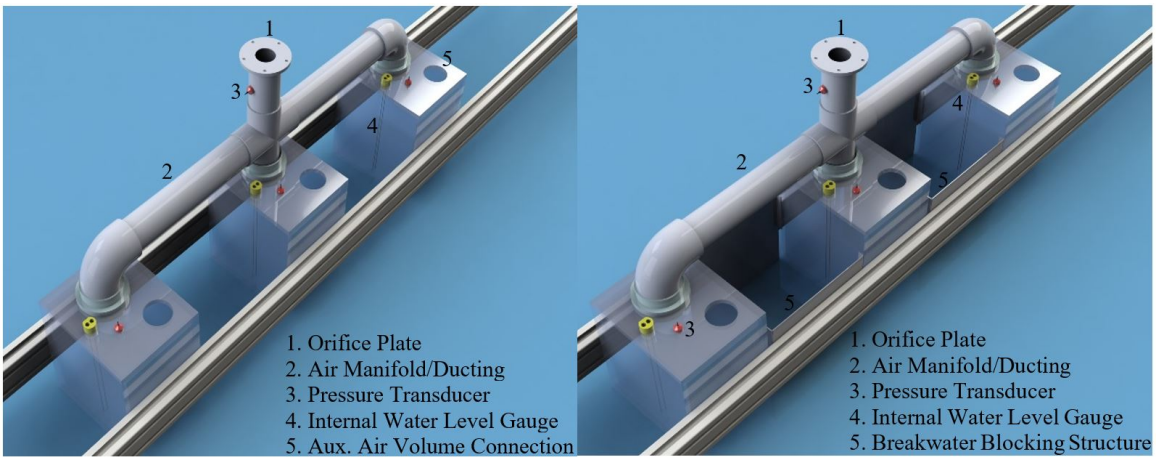


Figure 3.15: *In situ M-OWC bidirectional model with centred outlet (left) and M-OWC bidirectional breakwater model with blocking structure between OWC chambers (right)*

Unidirectional PTO Models

The M-OWC models with unidirectional PTO systems consist of the same OWC setup as the bidirectional model with the BW blocking structure included but with a single or twin unidirectional airflow orifice system. The single and twin unidirectional models are illustrated and labelled in Figure 3.16.

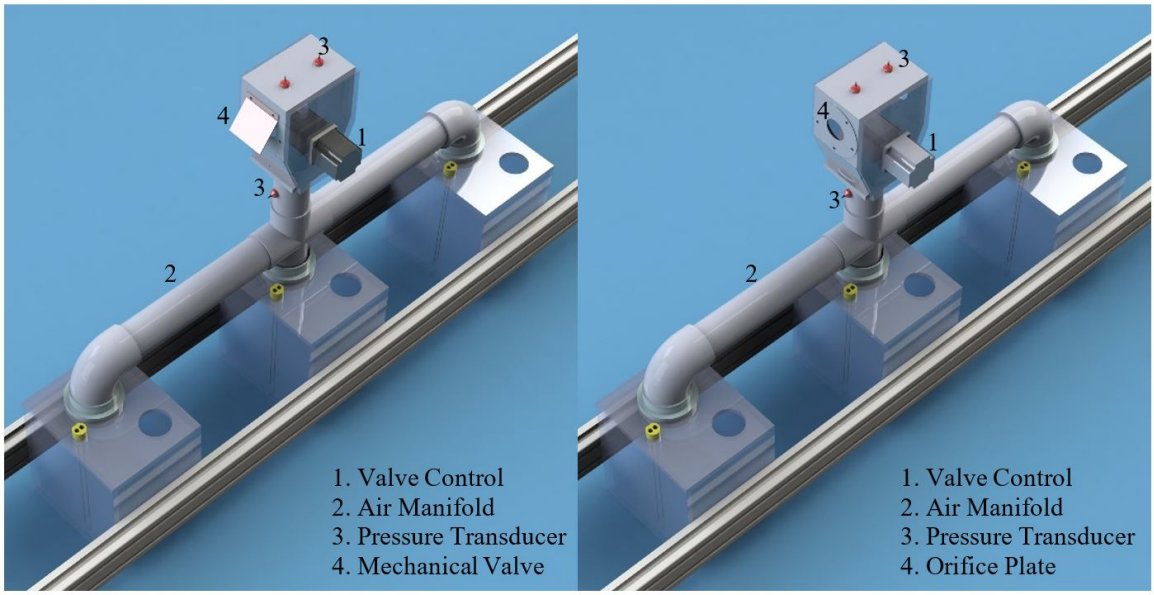


Figure 3.16: *In situ airflow rectifying unidirectional M-OWC breakwater models with single PTO system (left) and unidirectional M-OWC breakwater models with Twin PTO system (right)*

Unidirectional Rectifying PTO System Design

A stepper motor is used to control the position of a flap valve to divert the pressure gradient depending on the process. For the single turbine PTO, in efforts to keep the complexity of this small model minimal and keep the number of 'controlled' valves to a minimum, the interaction of the rectifying unit with the atmosphere is managed with two mechanical thin rubber valves as no alternative suitable valves could be sourced. These valves have a hinge, which allows the valves to operate at minimal flow rates to open and seal effectively. Since they are vertically mounted and they are purely reactive rather than proactive valves, the controlled rectifying flap valve invokes the direction of the exhale or inhale pressure (see Figure 3.17).

The twin turbine PTO setup is modelled with only the controlled diverging valve required to either divert airflow toward the atmosphere through the exhale turbine or from the atmosphere through the inhale turbine during negative displacement (see Figure 3.18).

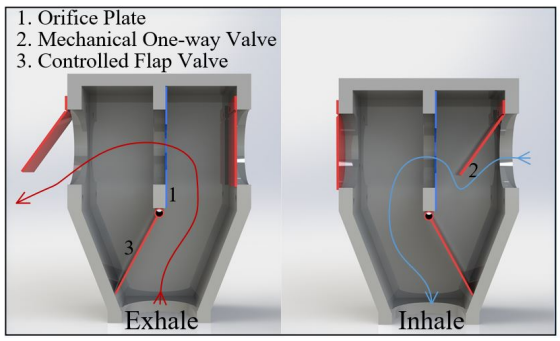


Figure 3.17: *Illustration of exhale and inhale processes for single turbine PTO systems*

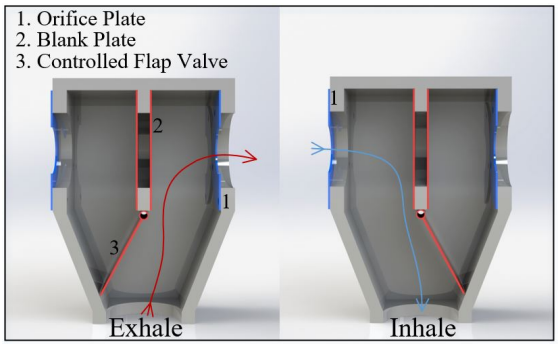


Figure 3.18: *Illustration of exhale and inhale processes for twin turbine PTO systems*

For these experiments, the control of the rectifying valve was chosen to be dependent on the free surface level of the chamber rather than the pressure sign since this had some lag with respect to the internal response. The microcontroller used to interpret the ILG data and make a decision as to the position of the flap was governed by following expression. To control the position of the valve based on identifying the live process from the sign of the free surface level gradient determine with the ILGs data over a suitable time period determined by a given number of samples, σ:

$$(Z_t - Z_{t-(\sigma\Delta t)}) \begin{cases} > 0 \text{ (exhale)} \\ < 0 \text{ (inhale)} \end{cases} \tag{3.29}$$

The valve has been estimated to change position in $0.2\,s$ through microcontroller, which is sampling the ILG of the central OWC at an average rate of $30\,Hz$.

Unidirectional PTO Model Methodology

For the unidirectional models there is a slight change to the calculations for pneumatic power. At the respective orifice plate P_{pn} is calculated using the absolute value of the orifice flow rate for the bidirectional PTO as in chapter 3 but positive only for unidirectional PTOs:

$$P_{pn} = \Delta p_o \, Q_o(>0) \;\; \text{(undirectional)} \tag{3.30}$$

For unidirectional models, during any reverse flow, hence a negative pressure drop, power is similarly calculated for when flow rate is negative:

$$P_{Loss} = \Delta p_o \, Q_o (< 0) \;\; \text{(undirectional)} \tag{3.31}$$

Mean values of these variables (P_{pnm} and Q_{om}) are found by integrating the time series over N periods:

$$P_{pnm} = \frac{1}{NT} \int_t^{t+NT} P_{pn} dt \tag{3.32}$$

Average peak pneumatic power values $\overline{P_{pnPeak}}$, for the bidirectional PTO, are found by taking the average of the maximum values from n half periods in order to account for the two power peaks in a single period from exhale and inhale processes:

$$\overline{P_{pnPeak}} = \frac{1}{n} \sum_{i=0}^{n} P_{pnPeak} \;\; (single) \tag{3.33}$$

The same method is used to find the average maximum pressure, $\overline{p_{max}}$, and average peak flow values, $\overline{Q_{Peak}}$ from peak values of $|Q_{Peak}|$.

For the twin unidirectional PTO, since there is two only one peak per period due to isolated turbines for exhale and inhale processes, these peaks are averaged of N full periods:

$$\overline{P_{pnPeak}} = \frac{1}{N} \sum_{i=0}^{N} P_{pnPeak} \;\; (twin) \tag{3.34}$$

where N is determined by the sample length, Δt:

$$N = \frac{\Delta t}{T} = 2n \tag{3.35}$$

Power is also calculated in between the wave power stage and the extracted pneumatic power stage by considering the hydraulic power:

$$P_{hydr} = \dot{Z} P_{owc} \tag{3.36}$$

Where $\dot{Z}$ is the internal free-surface velocity and p_{owc} is the OWC internal air pressure.

Mean values calculated as above are used to determine conversion efficiency between stages since the total efficiency from wave to extracted pneumatic power η_{WP}, is the product of the both the wave to hydraulic, η_{WH}, and hydraulic to pneumatic efficiencies, η_{HP}:

$$\eta_{WP} = \eta_{WH} \times \eta_{HP} \tag{3.37}$$

This enables total pneumatic losses, $L_{pnTotal}$ in the PTO and/or rectifying system to be calculated in isolation of the hydraulic losses incurred in the OWCs:

$$L_{pnTotal} = 1 - \eta_{HP} \tag{3.38}$$

Chapter 4

Phase 1: Waves2Watts Concept Verification

Introduction and Research Approach

The patent that initiated this research project [35] details the design of the WEC as a concept and is therefore only theoretical until verified. Hence, concept verification forms the initial objectives of the project as earlier defined in Chapter 1 as Phase 1 aims 1 and 2.

Starting with full experimental modelling of the entire W2W model, as described in the patent, was considered to be unwise from the outset. Instead, it was decided that crucial operating principles should be modelled individually at an observable scale. The two areas deemed crucial for operation and therefore chosen to model in isolation were the hydrodynamics and pneumatics of the device. The wave tank setup for these tests can be seen in Figure 3.7.

Hydrodynamics

The design of the layout of the OWC for these hydrodynamic tests can be seen in Figure 3.8 and dimensions in Table 3.4.

A key claim in the patent is the matching of peaks and troughs in the chambers

along the device length. Theoretically, while wave peaks cause the highest internal displacement amplitude or Top Dead Centre (TDC) internally to a given chamber, the subsequent chamber should be in the opposite state – at minimum displacement amplitude or Bottom Dead Centre (BDC). The terms TDC and BDC here not only signify the maximum and minimum internal displacements but the points at which the free surface velocity momentarily tends to zero. In order to meet this condition, chamber lengths should be near equal to half a wavelength as illustrated in Figure 4.1. Therefore, the condition that is required in order to meet this 'ideal' wavelength, λ_{ideal}, can be expressed as in Equation 4.1. This essentially means that the device experiences a response at double the wave frequency, which approaches the Nyquist frequency, equal to twice the maximum response frequency (Eq. 2.10).

$$\left.\begin{matrix}\lambda_{wave} \\ \lambda_{ideal}\end{matrix}\right\} \simeq 0.5L_{owc} \tag{4.1}$$

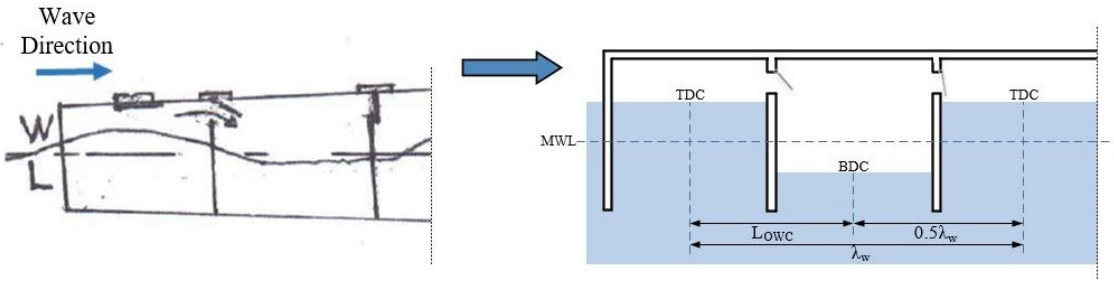


Figure 4.1: *Illustration of intended hydrodynamic interaction sequence of the Waves2Watts concept as described in patent*

The more ideal OWC geometry and suitable model scale for the test tank facility had to be ignored due to this λ_{ideal} condition resulting in a larger structure. Hence, for these initial experiments, geometry was not dimensioned for resonance frequency (f_n) (or wavelength λ_n). However, the resonant frequency was within the test range as predicted by the relationship between resonance and the dimensions of an OWC

of this style Sheng et al. [245] expressed with:

$$f_n = \left(2\pi\left(\sqrt{\frac{D_{owc} + 0.14S^{0.5}}{g}}\right)\right)^{-1} \tag{4.2}$$

Where f_0, the resonant frequency, is related to the wavelength through the dispersion theory for deep water waves:

$$\lambda_n = \frac{gT_n^2}{2\pi} \tag{4.3}$$

Where T_n is the resonant period. The aim of the research of this chapter is to test feasibility of meeting this condition (Equation 4.1), the behaviour and associated hydrodynamic characteristics.

$$\lambda_{ideal} = \lambda_{wave} = \lambda_0 \leftrightarrow f_{ideal} = f_{wave} = f_0 \tag{4.4}$$

Essentially, these tests are to investigate the effect of the relative wavelength, λ_{rel} (Eq. 4.5) in order to determine the feasibility of operation within the λ_{ideal} regime.

$$\lambda_{rel} = \frac{\lambda_{wave}}{L_{owc}} \tag{4.5}$$

With the wave frequency range for testing ($f_{wave} = 0.8 - 1.4\ Hz$), the relative wavelength range is $\lambda_{rel} = 6.454 - 2.108\ m$.

Theoretical Limits

Prior to experimental modelling, it was important to first understand any theoretical predictions based on what observations were to be expected, which will now be outlined in order to aid in discussion and drawing conclusions. The desired 'piston mode' and undesired 'sloshing mode' are primarily dependent on the relative wavelength λ_{rel}. Although sloshing is not solely based on relative wavelength, there is noticeable a threshold at which sloshing begins as it decreases. Two limits exist in literature

from Ning et al. [101], and Evans and Porter [102], respectively:

$$\lambda_{rel} \leq 2 \quad and \quad KL_{owc} \geq \pi \tag{4.6}$$

The second major theoretical limit applicable to this concept is the dependency of pitching stability on the total device length. Generally, if the device length is greater than 70% of the wavelength, then the device will be stable with respect to pitching as defined in the following expression:

$$\frac{\lambda_{wave}}{L_{Total}} \leq 0.7 \tag{4.7}$$

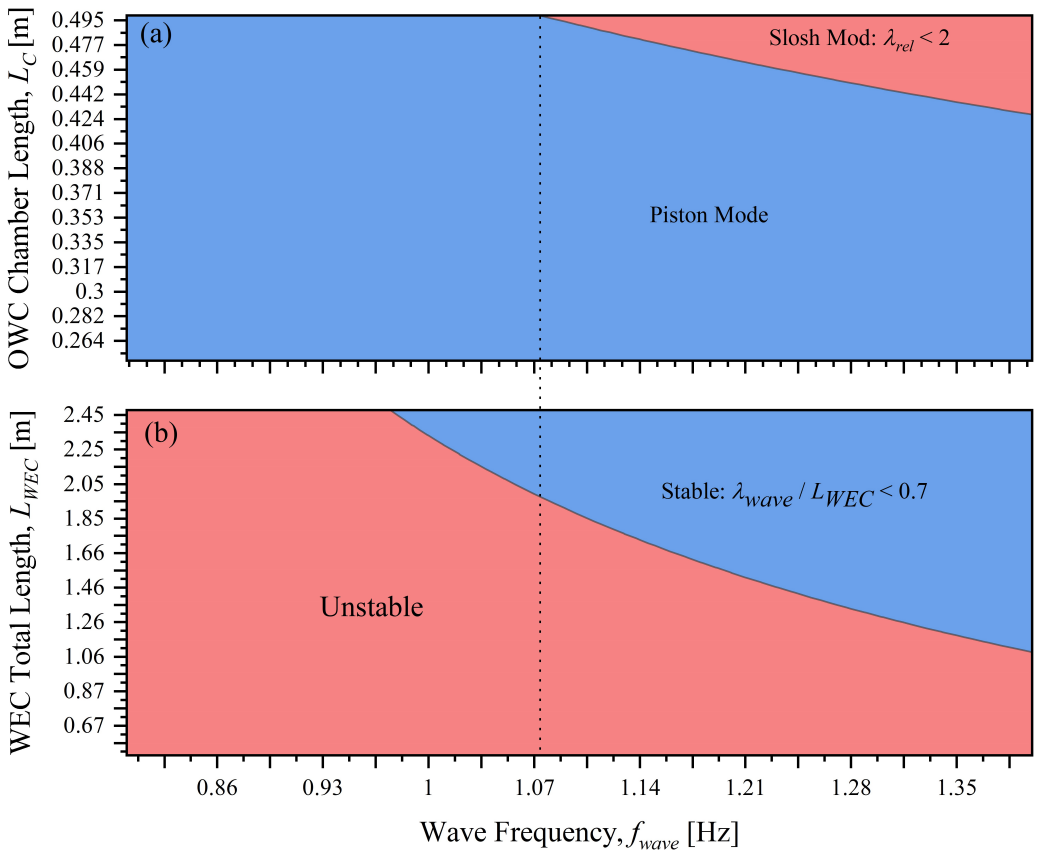


Figure 4.2: *Conditions and thresholds for slosh mode (a) and pitch stability (b) against the testing wave frequency range and relevant WEC dimensions*

Since the W2W concept requires a small relative wavelength, the number of chambers required to achieve a device length that will be stable enough results in a very

long device. Figure 4.2 illustrates the thresholds of these limits based on the expressions of Equations 4.6 and 4.7 with the relevant WEC dimensions and wave frequency range at this experimental scale.

Pneumatics

Perhaps more crucial to the W2W WECs operation as described exactly in the patent is the multi-stage compression process. This is somewhat dependent on the condition of equation 4.1, but can also theoretically facilitate larger wavelengths. Essentially, the positive displacement in one chamber creates high air pressure which opens and flows through a unidirectional valve into the neighbouring downstream chamber, which if the ideal wavelength condition is met, should be in a low-pressure state since the internal free-surface level should be near BDC. This low pressure assists in the flow between chambers by increasing the pressure gradient. As this receiving chamber's level begins to rise and therefore pressurising this volume, the inlet unidirectional valve should close and seal before the outlet unidirectional valve begins to open leading to the subsequent chamber. This process is repeated throughout the given number of chambers in the device, theoretically building pressure as the air flows between chambers in the direction of the propagating wave.

To answer the research question posed by the operational claim of the patent regarding the pneumatic system requires determining how pneumatically coupled OWC chambers in attenuator formation affects performance and whether pressure accumulation to benefit energy extraction is possible. This can be modelled with a simplified version of the W2W mode - two chambers with an intake on the first chamber and outlet on the downstream second chamber, with an intermediate unidirectional valve to allow airflow to travel from the first chamber (1^{st} Stage) into the second (2^{nd} Stage). According to the patent, pressure should build through the stages in the direction of the propagating wave, hence, the 2^{nd} stage should benefit from the 1^{st} stage and yield a performance greater than a singular OWC equivalent. Hence, the reasoning behind the design of the physical model described in Chapter 3 and shown in Figure 3.10.

Results and Discussion

Hydrodynamics

The two variables of most interest in from the hydrodynamic experiments are the ILGs and their associated external $WG_{EX1} - WG_{EX3}$. Example time series for these gauges are plotted in Figure 4.3 for each OWC at wave frequencies $f_{wave} = 0.8,\ 0.92\ and\ 1.2\ Hz$.

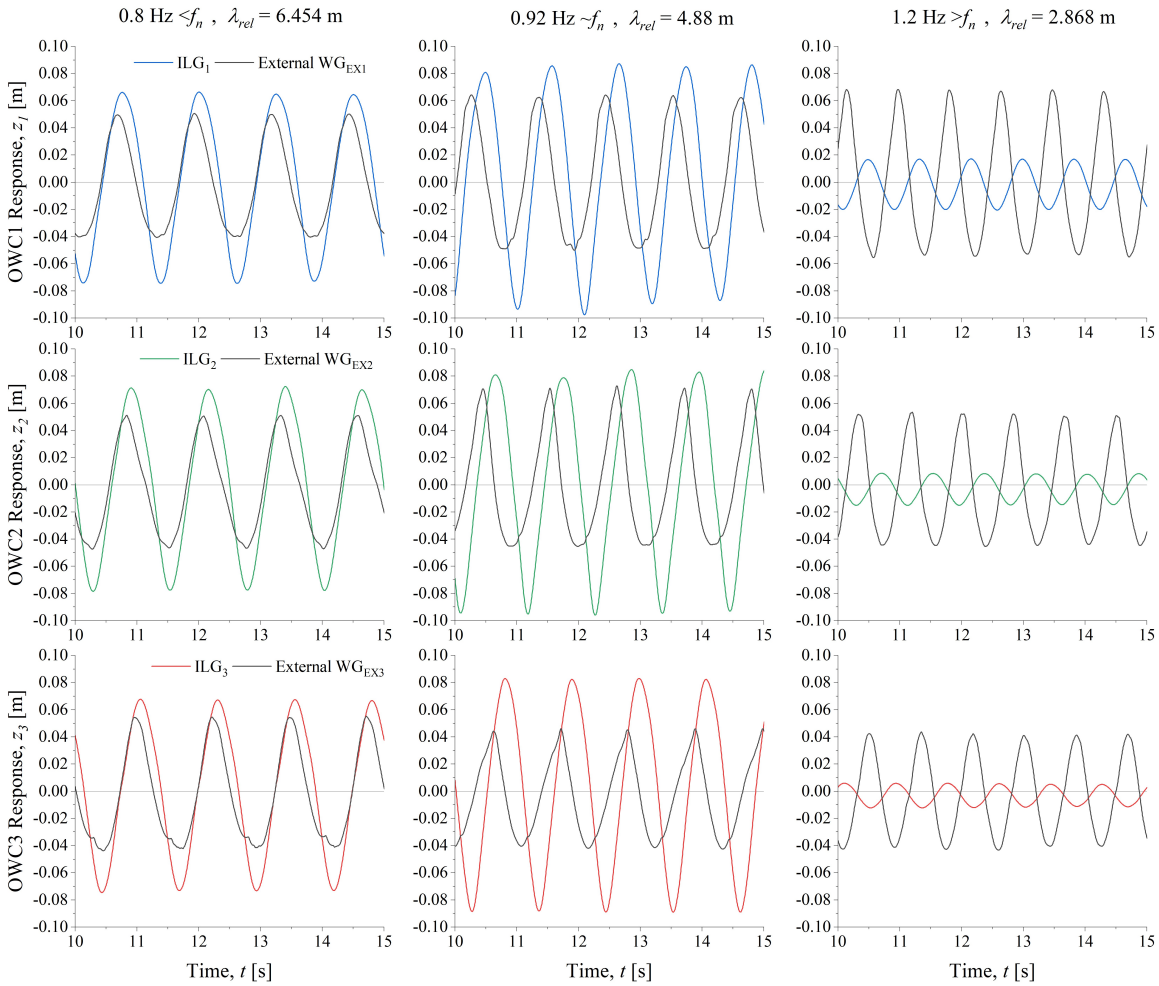


Figure 4.3: *Hydrodynamic response time series for three different example relative wavelengths from all internal level gauges (ILG_{1-3}) and external gauge counterparts (WG_{1-3}) for wave frequencies f_{wave}=0.8, 0.92 and 1.2 Hz at a wave height of H=0.1 m*

Between the OWCs, performance doesn't differ greatly, although a slight shift in the phase of the response can be seen, especially at $f_{wave} = 0.92\ Hz$, where the

response delays slightly as the wave propagates through OWCs. The amplitudes of the responses also vary slightly between OWCs with the middle chamber (OWC2) yielding the highest responses due to structure interaction affecting OWC1 and depleted resource, accumulated viscous and turbulence effects by the time the wave reaches OWC3. Greater phase shifts are noticeable with the change of wave frequency. The lowest frequencies ($f_{wave} = 0.8\ Hz$) and therefore largest relative wavelengths ($\lambda_{rel} = 6.454m$) produces a stable performance with a limited shift in phase response compared to a greater shift at resonant frequency ($f_{wave} = 0.92\ Hz$). At lower relative wavelengths like at $f_{wave} \simeq 1.2\ Hz$ ($\lambda_{rel} \simeq 2.868\ m$), the free surface internal displacement transitions from the desired 'piston' mode into 'sloshing' mode. Both the amplitude and phase of the response reflects the deterioration in performance once entering this mode.

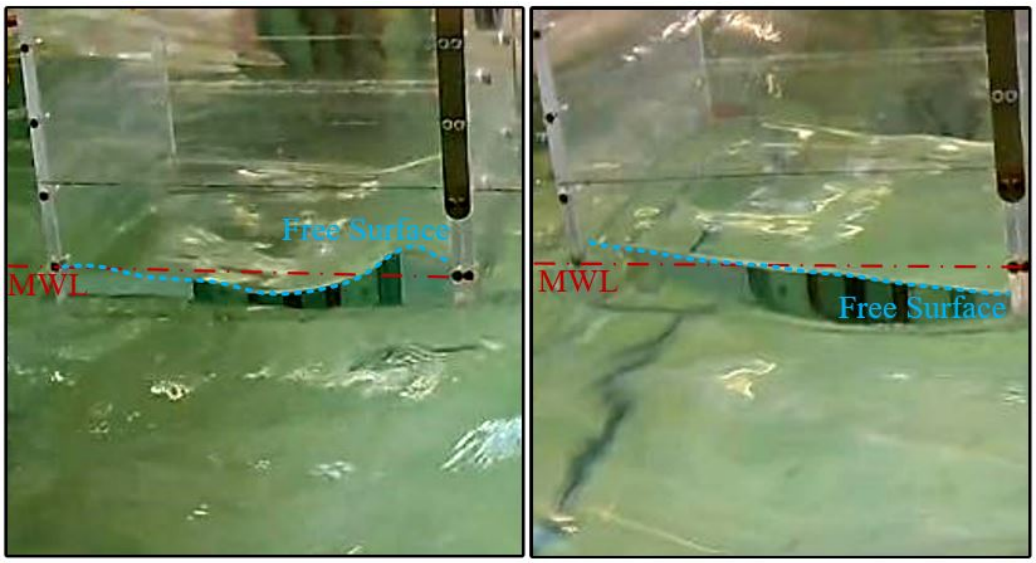


Figure 4.4: *An example and illustration of an OWC operating in piston and sloshing modes with large $\lambda_{rel} = 6.454\,m$ and small relative wavelengths $\lambda_{rel} = 2.868\,m$, respectively*

The transition into sloshing mode is easily observed during experimental testing as the λ_{rel} decreases. Figure 4.4 shows an example of two cases of sloshing occurring with Mean Water Level (MWL) lines plotted for reference. As demonstrate, sloshing is undesirable due to the mean amplitude or displacement of the free surface response inside the chamber. The free surface is far from piston-likeness but is partially below

and above the MWL, thus cancelling out to result in limited displacement amplitude.

Data from the ILGs are acquired and processed as described, but are often expressed herein, in the form of the Response Amplitude Operator (RAO), which is essentially the ratio between the wave amplitude and average peak response amplitude of the free surface recorded by the ILG:

$$RAO = \frac{\overline{ILG}_{Peak\ i}}{a_{wave}} \tag{4.8}$$

Below, Figure 4.5 shows the RAOs for a range of wave amplitudes (a_{wave}) across the frequency range tested. The curves show an obvious peak response at $f_{wave} \approx 0.92\ Hz$, greater amplified due to the absence of the lid and damping, hence why RAOs are greater than one for a large part of the range. However, for higher wave amplitudes ($a_{wave} = 0.06$ and $0.07\ m$) this peak response at the resonant frequency is less than or almost equal to an additional peak at $f_{wave} \approx 0.84\ Hz$, which occurs due to absence of damping but is clearly not the resonant response. The poorer performance of these lower amplitudes is evident based on these trends and therefore the resonant response is expected to be relatively weak. The lack of damping is also responsible for the zig-zag nature of these curves since. Even if there were smaller wave frequency test intervals, the zig zags would still exist in the absence of damping. At wave frequencies of $f_{wave} > 1\ Hz$, the response rapidly worsens namely due to an increase in steepness, hence the smallest wave amplitude has the highest RAO response. As the different RAO lines converge, the poor performance is a result of the decreasing relative wavelength and therefore severe sloshing.

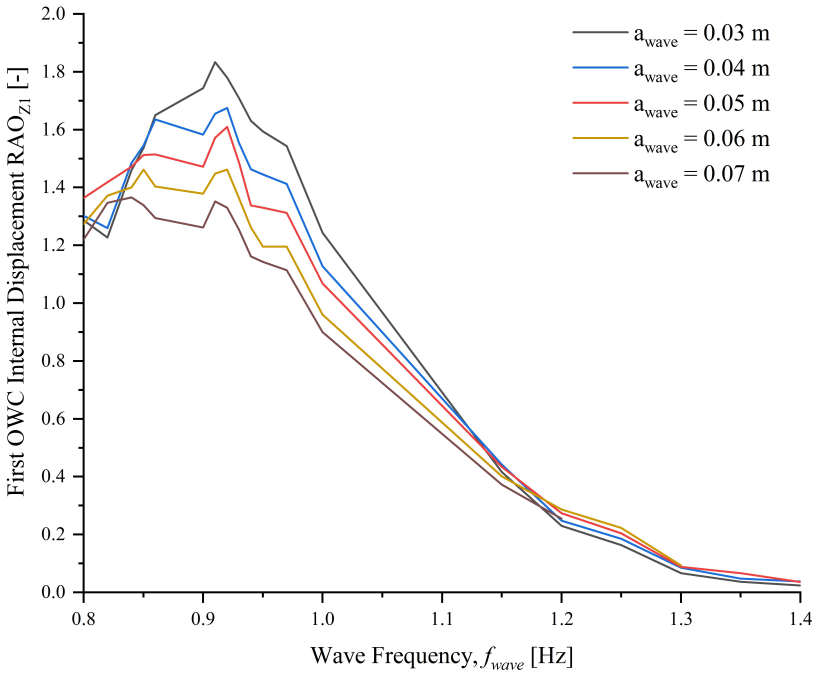


Figure 4.5: *First chamber internal RAOs plotted against wave frequency range* $f_{wave} = 0.8$–$1.4\,Hz$ *for a constant wave height of* $H_{wave} = 0.06$–$0.1\,m$

In Figure 4.6, RAOs are plotted against wave steepness (s) for three wave frequencies, including resonant value of $f_{wave} = 0.92\ Hz$, which yields a significantly greater response, even at high steepness. For $f_{wave} = 0.8\ Hz$ it appears that there is unusual behaviour at lower steepness, however it is suspected that the peak in the curve causing this appearance is an anomaly. During experiments it could be observed that one of the main reasons steepness has an adverse effect on performance is its interaction with the WEC structure. Greater impact between the wave crest and the forward facing WEC wall dissipates the kinetic energy component of the wave, as noted in the literature review [93].

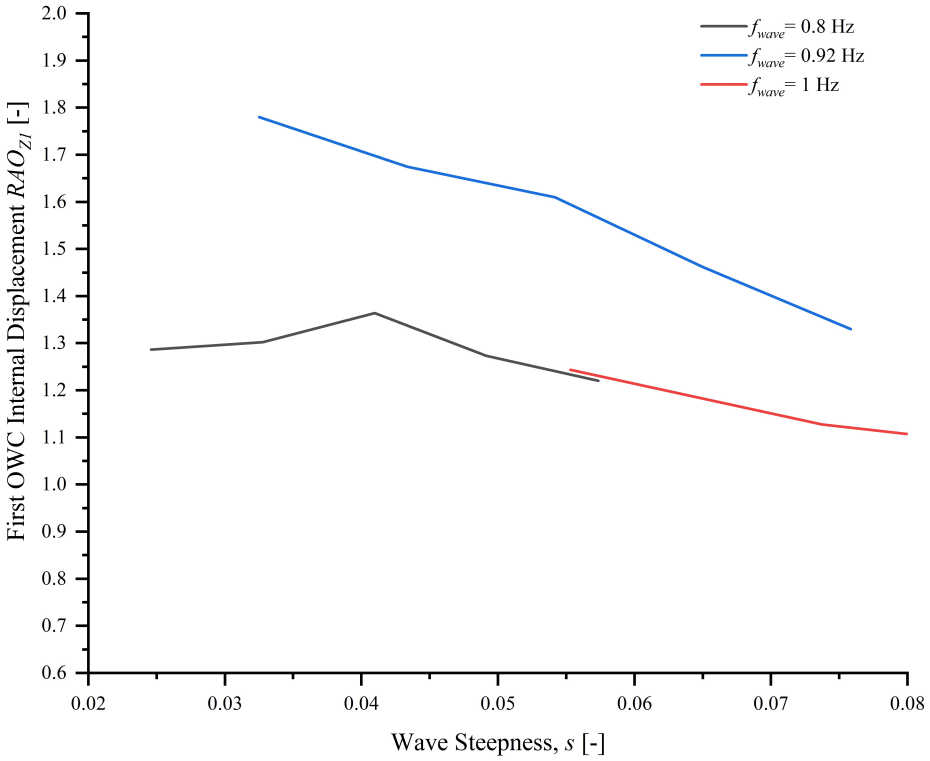


Figure 4.6: *First chamber internal RAO plotted against wave steepness for representative frequencies* $f_{wave} = 0.8, 0.92$ *and* $1\,Hz$ *with a wave height range of* $H_{wave} =$

Pneumatics

Following changes to the geometry from the hydrodynamic tests, further hydrodynamic analysis was carried out with the pneumatic 1:50 scale model in order to determine the resonant frequency of the OWC. Furthermore, the effect of pneumatic or PTO damping must be understood by testing a range of orifice plates to adjust damping and determine the effect on the internal free surface displacement response. Since literature recommends to start damping optimisation at around $O = 1\%$,[229], these experiments feature a range of four orifice plates where $O = 1\%\,, 1.5\%\,, 2\%$ *and* 2.5%. Figure 4.7 shows the response to all orifice plates tested across the frequency range with a constant wave amplitude of $a_{wave} = 0.04\,m$ in this case as an example. The open lid case is plotted alongside, where $O = 100\%$, since without a lid the open area is equal to the surface area of the OWC (Eq. 3.10). The effect of damping is prominent with RAOs of ~ 1.6 at resonance $f_{wave} \approx 0.94\,Hz$ reducing to ≤ 1. The

geometry for this model differs and it is therefore not surprising to see a different curve shape compared to Figure 4.5, especially with a wider frequency range tested with respect to the test points either side of resonant frequency. The difference in behaviour is primarily due to the additional upstream chamber and its impact on the hydrodynamic performance of the OWC2 (2^{nd} stage). It is clear based on the dampened cases that the resonant peak exists, however, the sudden dip makes the subsequent increase appear to be a second peak. Hence, attention is drawn more to the sudden dip rather than there being two peaks, which is a shape that repeats itself throughout experiments but the reason for this phenomena was not further investigated.

No optimal damping was determined for this set of experiments and therefore, orifice plates were constantly interchanged to gain as many results as possible since the behaviour of this device was unknown.

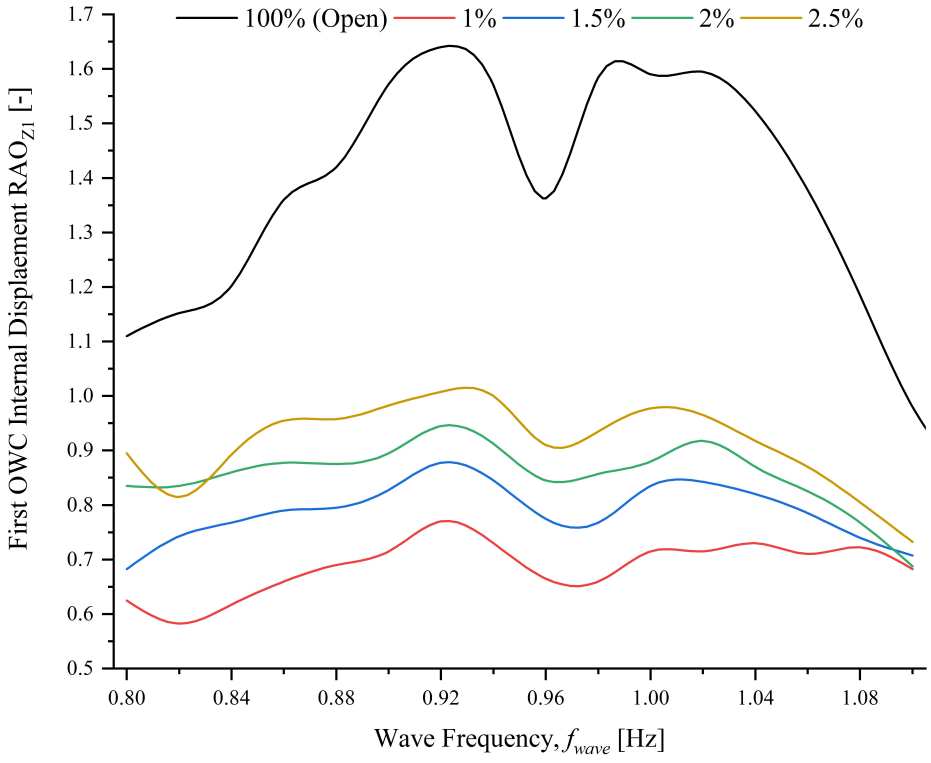


Figure 4.7: *Orifice damping plot showing internal free surface displacement RAOs from the ILG_1 of the new single OWC geometry to be used from this point on for Phase 2 modelling, plotted against a frequency range of $f_{wave} = 0.8$–$1.1\,Hz$, at a constant representative wave height of $H_{wave} = 0.08\,m$ and a range of orifice plates $O = 1, \,, 1.5\,, 2\,and\,2.5\%$*

Time series plots in Figure 4.8 show the pressure generated in both OWC1 (1^{st} stage) and OWC2 (2^{nd} stage) in response to the internal displacement levels for a wave of amplitude of $a_{wave} = 0.04\,m$ and frequency of $f_{wave} = 1\,Hz$ with orifice plate of $O = 1\%$. The 1^{st} stage generates a good negative pressure for inhale, which is followed by a fast and sharp accumulation of pressure as the internal level rises. The pressure consistently shows a short peak above $p_{owc1} \geq 400Pa$ closing the inlet valve followed by a drop to $< 200\,Pa$ where the intermediate valve opens into OWC2.

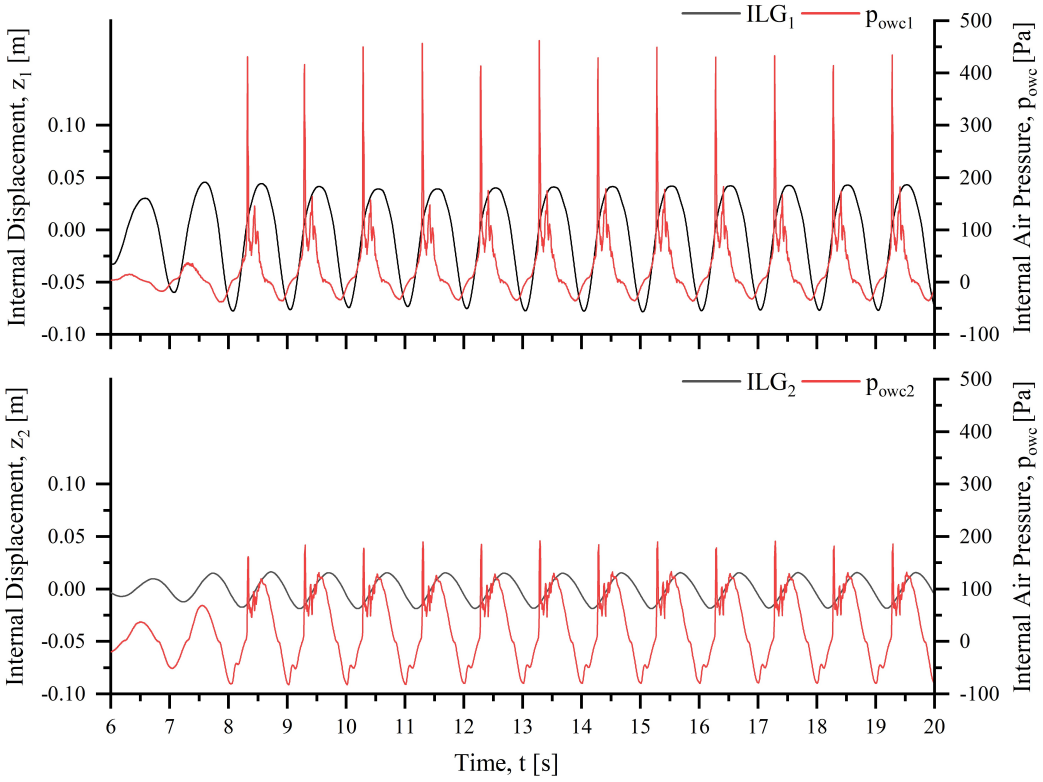


Figure 4.8: *Internal free surface levels (ILG_{1and2}) and internal chamber air pressure (p_{OWC1-2}) time series data plotted for OWC1 (1^{st} stage) (top) and OWC2 (2nd stage) (bottom), for the two chamber W2W attenuator model. Plotted for a representative frequency of $f_{wave} = 1\,Hz$ and wave height $H_{wave} = 0.08\,m$*

The 2^{nd} stage firstly reveals a significant drop in displacement response amplitude with the ILG_2 plot. Clearly, the 2^{nd} stage receives the pressure surge from the 1^{st} stage, as can be seen by a similar but smaller sharp spike ($p_{owc2} < 200\,Pa$). Since this peak occurs during the 1^{st} stage surface response, the 2^{nd} stage surface then responds with perhaps a slightly higher starting pressure than a single stage or singular OWC

would. This 2^{nd} stage fails to exceed or accumulate upon the pressure levels transferred from the 1^{st} stage.

Figure 4.9 shows the pressures of both stages together. Here it is clear that the 1^{st} stage pressure peak directly transfers to the 2^{nd} stage while incurring a drop $> 200\,Pa$. The fluctuating pressure that follows this is the continuation of air flow transferring through the intermediate unidirectional valves. More noticeable in this plot (Figure 4.9), is the inhale pressure amplitudes of the 2^{nd} stage, which are greater than the 1^{st} stage. Although this could mainly be due to the dimensions of 1^{st} stage inlet valve, ideally, unidirectional airflow needs to develop, which with such a strong inhale, is not occurring. Perhaps this is an argument for modelling with even more chambers to determine whether this diminishes completely, leaving a pure unidirectional airflow. Additionally, without inclined and weighted unidirectional valves, perhaps this pressure drop could create a flow.

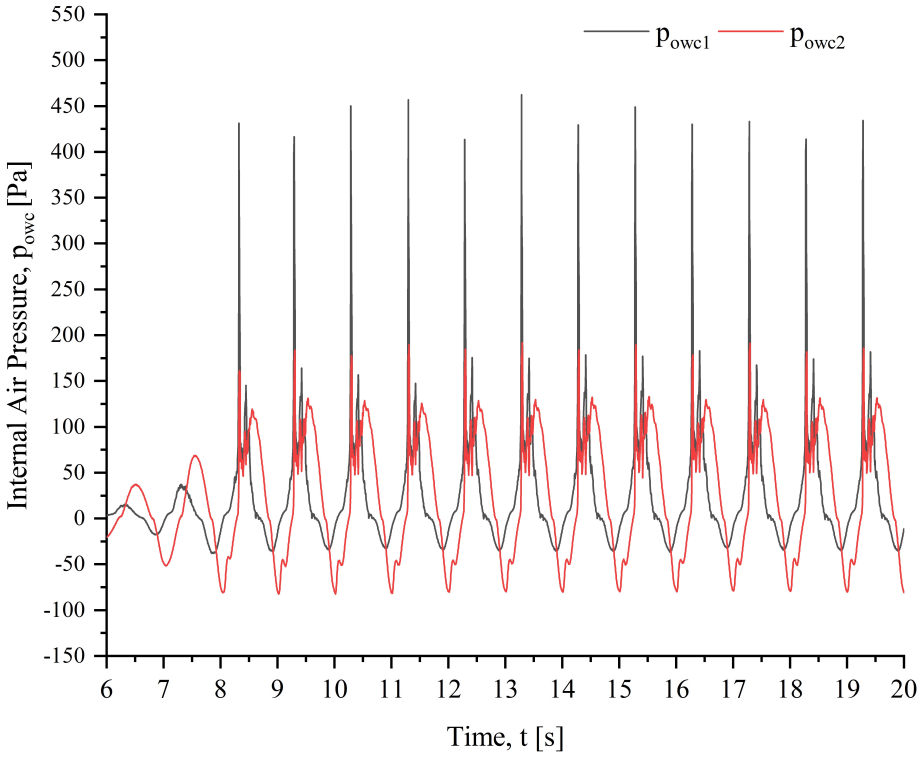


Figure 4.9: *Internal OWC air pressure (p_{OWC1-2}) time series for OWC1 (1^{st} stage) and OWC2 (2^{nd} stage) for the two chamber W2W attenuator model for a representative frequency of $f_{wave} = 1\,Hz$ and wave height $H_{wave} = 0.08\,m$*

The reduced response from the 2^{nd} stage can also be noticed in the results of Figure

4.10, where the RAO_Z and net pressures, p_{Net} are plotted for the same wave amplitude and damping conditions as the time series of Figure 4.9. The net pressure values are useful for comparing performance of exhale and inhale processes, and are calculated from the average peak positive and negative pressures, $\overline{p_{max}}$ and $\overline{p_{min}}$ respectively:

$$p_{Net} = \overline{p_{max}} + \overline{p_{min}} \tag{4.9}$$

Snapshots of the exhale and inhale processes can be found in Appendix A Figures A.10 and A.11. For a singular OWC, the net pressure should be close to zero in order to prove that equal power is being extracted from both inhale and exhale processes; and for the W2W device, which ideally has a higher net pressure since positive pressure should be accumulating, especially beyond the 1^{st} stage. The difference in RAO_Z (Figure 4.10) between $1^{st}$and 2^{nd} stages reflects the observation of the drop in the time series of Figure 4.8. The displacement of OWC1 is almost three times greater than that of OWC2. Similarly, the net pressures are significantly different with a reduction of over half. These net pressures are heavily influenced by the sharp peaks seen in Figure 4.9, however, this accurately reflects the difference in response between the chambers. Net pressures are far from zero due to limited negative inhale pressures.

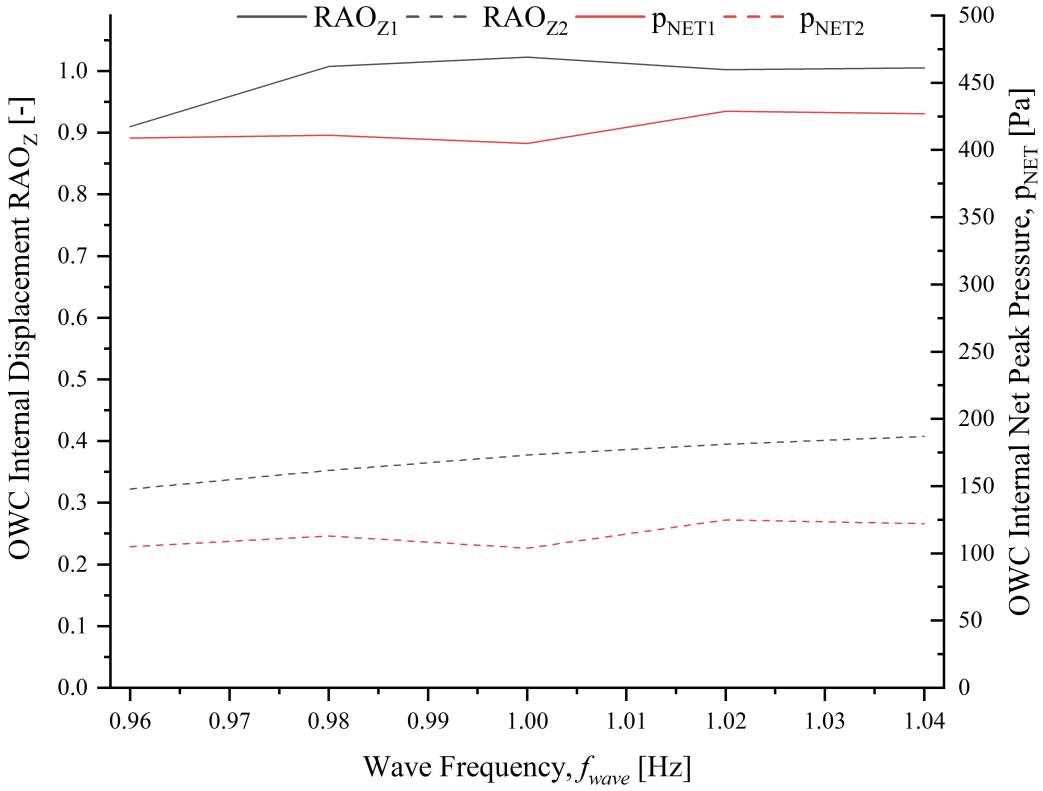


Figure 4.10: *Internal OWC net air pressure (p_{NET1-2}) and internal free surface RAOs (ILG_{1-2}) for OWC1 (1^{st} stage) and OWC2 (2^{nd} stage) the two chamber W2W attenuator model for a frequency range of $f_{wave} = 0.96$–$1.04\,Hz$ and a representative wave height $H_{wave} = 0.08\,m$*

The performance comparison is possible with an equivalent singular OWC, which is equivalent due to being geometrically identical to the chambers of the two-chamber model, the dimensions for which are defined in Table 3.5 in Chapter 3. The singular OWC was mounted in the same position as the 1^{st} OWC and was tested for the same wave amplitude $a_{wave} = 0.04\ m$ and orifice plate $O = 1\%$ across five different frequencies ($f_{wave} = 0.96,\ 0.98,\ 1,\ 1.02\ and\ 1.04\ Hz$) is plotted in Figure 4.11 with an evaluation of pressure ranges. Exhale and inhale pressures are plotted for both 1^{st} and 2^{nd} stages of the W2W concept modelled and for the equivalent singular OWC.

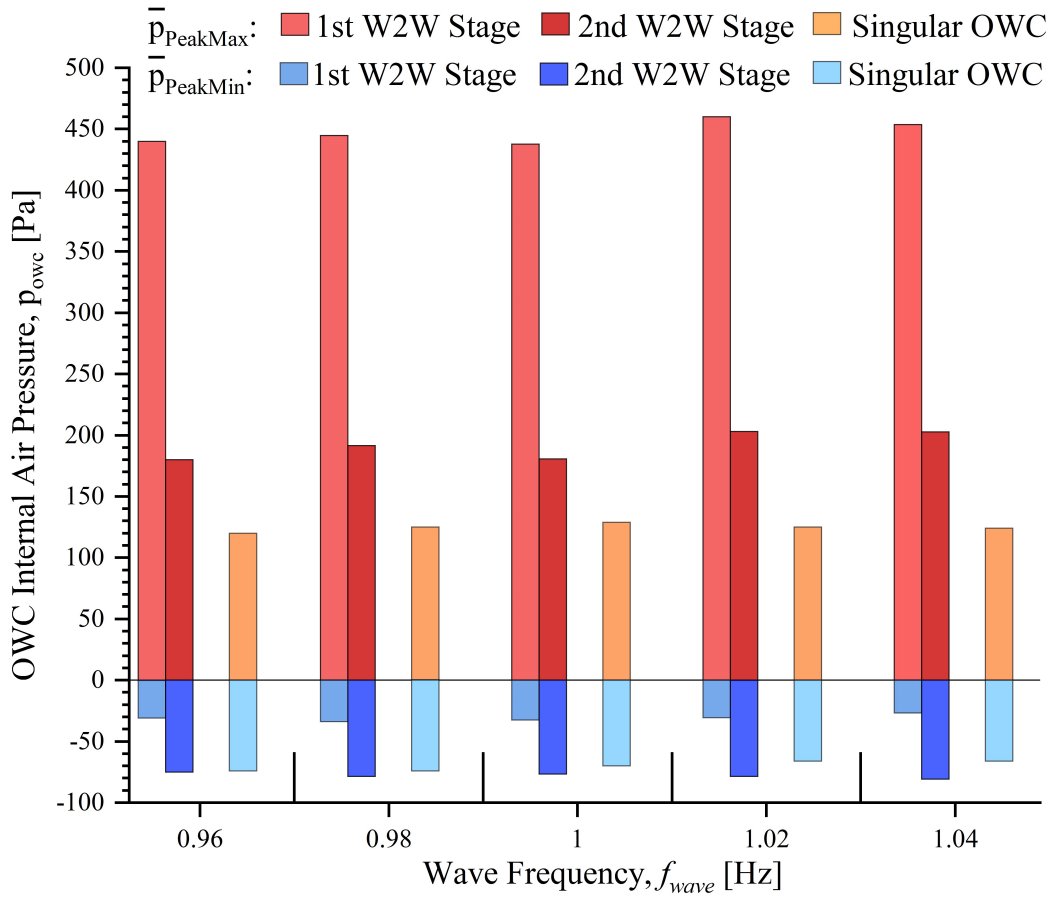


Figure 4.11: *Internal OWC air pressure bar plot illustrating the drop between* 1^{st} *and* 2^{nd} *stages of the two chamber W2W attenuator model compared against the singular OWC for a frequency range of* $f_{wave} = 0.96$–$1.04\,Hz$ *and a representative wave height* $H_{wave} = 0.08\,m$

The 1^{st} stage clearly has a more dominant exhale, generating a more prominent unidirectional flow. This performance cannot effectively be transferred to the 2^{nd} stage, which is reflected in the maximum pressure drop discussed above, and the increased negative inhale pressures reverting the flow back to being bidirectional. The 2^{nd} stage seems to outperform the singular OWC marginally but this is due to the closing of the inlet valve and therefore a much higher peak pressure – a trait not desirable for a singular OWC with bidirectional flow since this would create a very high net pressure and undesirable power curve.

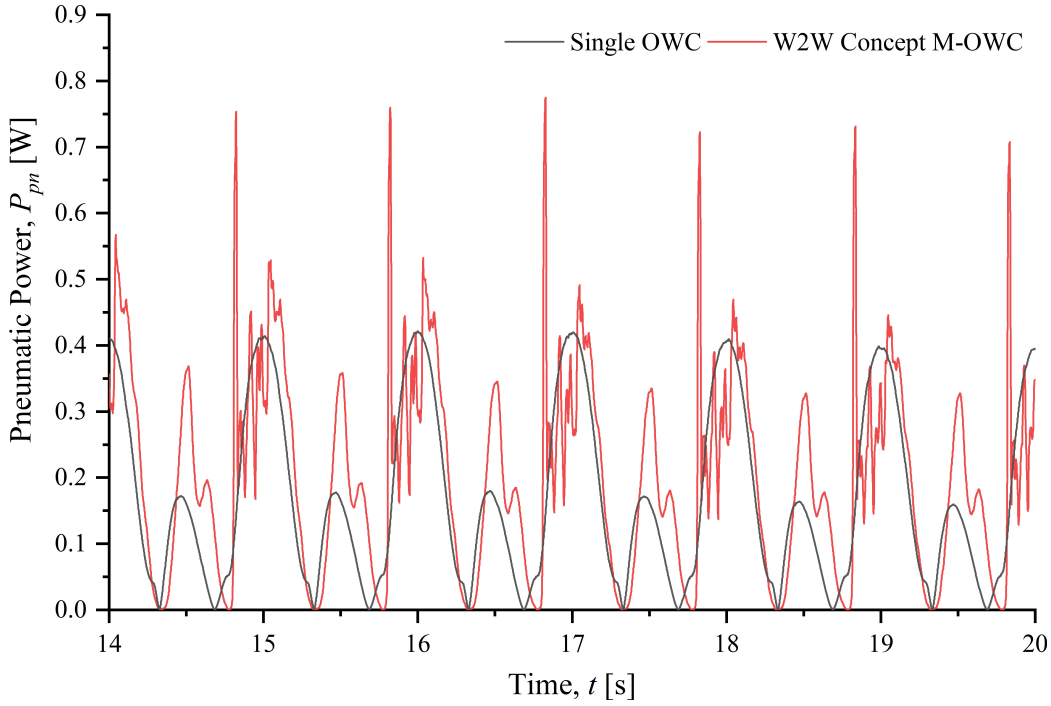


Figure 4.12: *Representative calculated pneumatic power time series comparison between the singular OWC and the W2W M-OWC attenuator concept a representative frequency of* $f_{wave} = 1\,Hz$ *and wave height* $H_{wave} = 0.08\,m$

As confirmed by the power results (calculated using Equation 3.14) in Figure 4.12 and Table 4.1, although the W2W M-OWC reaches high peak powers, the resulting mean power is lower than that of the equivalent singular OWC. This is due to the rapid fluctuation of pressures experienced during valves opening and closed, and the transfer of air between chambers, which is ultimately a result of poor pressure management. The power spike and shape are representative of the pressure plots, as one would expect since the power is derived from pressure drop, however this reinforces that these sudden peaks and oscillations of the W2W M-OWC are undesirable and would take substantial intervention to smoothen and achieve a higher mean power at the generator. Although high pressures are desirable, the use of these high values, especially spikes need to be used else they are futile and potentially damaging. Furthermore, this power output is the response of the 2^{nd} stage, hence with an additional chamber the W2W concept generates a lower mean power with many unsteady fluctuations.

	Singular OWC		W2W M-OWC	
Orifice	Average Peak Power	Mean Power	Average Peak Power	Mean Power
O	$\overline{P_{pnPeak}}$	P_{pnm}	$\overline{P_{pnPeak}}$	P_{pnm}
1%	0.4	0.17	0.68	0.15
1.5%	0.54	0.2	0.73	0.2
2%	0.68	0.24	0.61	0.22
2.5%	0.8	0.28	0.61	0.24

Table 4.1: *Average peak and mean power values calculated with Equations 3.7 and . 3.6 respectively, for the singular OWC and the W2W M-OWC concept*

Discussion and Conclusions

Summary

The Phase1 experiments were mandatory in order to prove or disprove the feasibility of concept verification despite various theoretical indications that this would not be entirely possible. All results discussed are complemented with visual observation of all processes including changes in internal displacement responses, opening and closing of air valves, damping effects, fluid structure interaction and more, some of which were recorded on video and used for additional analysis or illustrations, and photographs (Appendix A).

The approach of these experiments aimed to model two crucial operational processes claimed in the patent, which covered hydrodynamic and pneumatic processes. As observed in the hydrodynamic experiments, the relative wavelength has a profound influence on the effective performance of the heaving free surface internal to the OWC. The condition of λ_{ideal} to match the resonant wave frequency (λ_n) and incident wave frequency (λ_{wave}) (Eq. 4.4) is impossible to meet. This is due to the slosh mode and subsequently poor performance that occurs when the relative wavelength is decreased to approach this condition.

From pneumatic modelling, what is clear is that the high pressures generated by the 1^{st} stage once the inlet valve closes certainly contributes to an initial pressure of

the 2^{nd} stage. However, this transfer of pressure is to the detriment of the 2^{nd} stage since this causes excessive damping resulting in significantly reduced displacement amplitudes and minimal contribution to a further accumulation of pressure.

What is not clear, is whether there is a further factor affecting the sub-par performance of the 2^{nd} stage with respect to the wave resource. With chambers in close proximity and the level of energy exerted on the 1^{st} stage during compression, it isn't clear whether the wave recovers and therefore has sufficient resource for the 2^{nd} stage, especially a more highly damped 2^{nd} stage.

Hence, the research in this chapter has essentially shown the claims made in the patent to not be viable for further development. Furthermore, comparing the W2W concept results with the singular OWC shows that performance, despite the failure to meet the patent claims, does not exceed that of an equivalent scaled singular OWC, which was tested in the same conditions. This further proves that the additional chamber or chambers of the W2W concept do not benefit the overall WEC performance and are therefore not worth the extra structural complications and costs, including added complexity of additional moving parts like valves. This chapter therefore recommends a deviation from the original W2W concept as described in the patent, and that further work on the W2W WEC should feature changes to the operational process while keeping the fundamental descriptions of the patent wherever possible.

Additional Modelling Behind the Scenes

Given that W2W Ltd. directors were acting industrial supervisors in this research project and the initial aims of the project was to achieve concept verification, a number of ideas for reconfiguration were suggested, discussed and subsequently tested in hope of improvements. Suggestions included an alternative configuration with respect to the angle of the device to the incident wave (i.e. as a terminator), staggered chambers with respect to the wave crest width and a reversed stages concept.

The reversed stages concept was the only alteration that was thoroughly tested. It essentially involved turning the device 180 degrees in order to have OWC1 acting as the 2^{nd} stage and OWC2 acting as the 1^{st}. The idea being to have the greater

resource available at the 2^{nd} stage and prevent an overdamped OWC2. However, the results shed light on the discussions above regarding wave resource for OWC2. The 1^{st} stage (OWC2) proved to contribute minimally to the 2^{nd} stage but this time not due to incoming high pressures from a previous stage but rather a depleted wave resource.

Chapter 5

Phase 2: Array and Modular M-OWC Modelling

Introduction to Waves2Watts Phase 2

Following the conclusions of the W2W Phase 1 research presented in Chapter 5, the project had to undergo a slight change in direction, moving from the concept verification of the W2W original concept, into alterations in order to give it the best opportunity to succeed. This required a further literature search into M-OWCs in alternative applications and identifying the gap, in which one could make the W2W fit, which was discussed in Chapter 2.

As defined by Doyle and Aggidis [72], aside from the OWC as a single standalone unit, Multi-Oscillating Water Columns (M-OWCs) are essentially multiple OWCs that are coupled together either at structural level and also a power level, which forms the basis of their variants categorisation. These main categories are: the OWC array (as an M-OWC), segmented M-OWC and modular M-OWC. It is widely known that ultimately, as with wind and tidal energy, WECs must be deployed on a large scale, either as arrays of individual or coupled devices (like M-OWCs) in order to benefit from the high density of the energy resource and the greater economic benefits at larger scales.

The cost of energy production is quantified by the previously discussed expres-

sion called the Levelised Cost of Energy (LCOE), which is dependent on the Capital Expenditure (CAPEX), Operational and maintenance Expenditure (OPEX) and Net Present Value (NPV), but more importantly with greater significance, the Annual Energy Production (AEP) of a WEC deployment [11, 12]. At larger scales the opportunity for integration with other applications increases, which also lowers the capital cost component and sometimes the operational costs of the LCOE, which is expressed:

$$LCOE = \frac{NPV(CAPEX + OPEX)}{AEP} \tag{5.1}$$

The versatility of the OWC is still largely untapped with the majority of devices deployed having similar characteristics in terms of operating systems and even applications. Versatility and diversity is achieved in most existing M-OWCs concepts in general, with a wide range of applications and variations. The number of M-OWCs both conceptually and in research is lower in comparison to single OWCs, however, recent trends in research are proving that M-OWCs, or multiple OWC deployment at least, is gaining traction [72].

Most M-OWC concepts and devices are very large structures, which yields great opportunities for deployment diversification. Examples of these can be seen in existing concepts with WECs integrated into offshore wind turbine structures [170], breakwaters [172] and general offshore multi-use floating platforms [174]. Additional concepts do not only include OWCs but also point absorbers and overtopping devices integrated with breakwaters [19]. Such innovation and identification of these alternative applications and synergies are necessary to make wave energy more competitive and viable option for future investment.

The W2W device should therefore target breakwater integration as a modular open system M-OWC . Of course, this required some changes to the design, most crucially:

- Since it is has the function of a breakwater, the orientation of the device should be as a terminator. While the original patent does not explicitly say that it should be in attenuator configuration, the nature of the process somewhat re-

quires it to be within an attenuating range (±45°), hence this is a significant adaptation but within the claims of the patent.

- The second crucial change is more of an addition, which regards the requirement of an air rectification system prior to a unidirectional turbine. The flow must be unidirectional and the system must be left as an open system, hence flow must be rectified since the original method of unidirectional flow generation was not feasible. Publication output from Doyle and Aggidis [235] is an in-depth review on PTO systems with a focus on M-OWCs and integration applications.

Phase 2 M-OWC Research Approach

This significant change in WEC development poses several research questions, which this chapter aims to answer; those questions are framed in Chapter 1 as Phase 2 aims 1,2 and 3. Ultimately, this chapter focuses on the study of the device as a terminating M-OWC with interest in chamber spacings and model performance compared to similar or predecessor concepts. Hence, this investigation utilises a progressive and pragmatic experimental modelling approach by cross comparing the models of a single standalone OWC, an OWC array and finally, a modular M-OWC under the same environmental and test conditions. It is important for the array to be included understand the effect of spacing between the OWCs and the response both in terms of individual performance and also as a M-OWC total unit. These experiments are in the interest of building context for a breakwater; hence, spacing is only in direction of the wave crest – terminating configuration. Performance and characteristic responses are analysed while varying the values of OWC spacing, damping and wave conditions.

Out of all experimental data obtained for all devices tested across literature, the method of comparison between these can be ambiguous. An extensive review by Babarit [52], compares CWR values across a large number of devices for which such data has been published. While for some cases this could offer a fair comparison and be acceptable, cross-comparing models with respect to this value can add great uncertainty especially considering the variations in methodology throughout literature and the previously discussed low confidence levels in such data across various stages

of development. Ultimately, a reliable method of cross model comparison would involve keeping as many aspects of the experimental modelling constant i.e. wave tank, environment, data acquisition and processing , scale of geometry and compressibility scaling etc. Here lays the premise of this research and its approach, to build fair comparative models starting from a single OWC, progressing onto an OWC array, then an M-OWC and beyond in order to investigate their operational characteristics at their optimal performance with the given conditions and geometries. Fair comparisons between models can be drawn from both the data and observation on aspects of response and performance, which all adds confidence in the conclusions of this pragmatic approach and the final model. The regular wave runs used in these experiments can be found in Chapter 3 in Table 3.1 and the setup of the tank in Figure 3.11. The geometry of the physical models referred to can be seen in Figure 3.14, all of which are built from the individual OWC geometries detailed in Table 3.5 and Figure 3.9.

Results

Power Take-Off Damping

Throughout all experiments, it was found that the pneumatic power response was closer to the phase of the external wave than the response of the water level internal to the OWC chamber. An example of the time series of these values are plotted in Figure 5.1.

Experiments were also ran with zero damping to determine the resonant frequency experimentally and observe the response of the geometry. This was achieved by removing the lids as if the OWC were an open moon pool. With the lid fitted and the inclusion of damping, the resonant point was found to be less prominent in certain conditions with respect to the internal response. The internal water level displacement response is characterised by the Response Amplitude Operator (RAO), which is the ratio of the amplitude of the response and the amplitude of the incident wave. The RAOs can be seen for zero damping (100%) in Figure 5.2.

The estimate of the resonant frequency ($\approx 1Hz$) using Equation 4.2 matches a

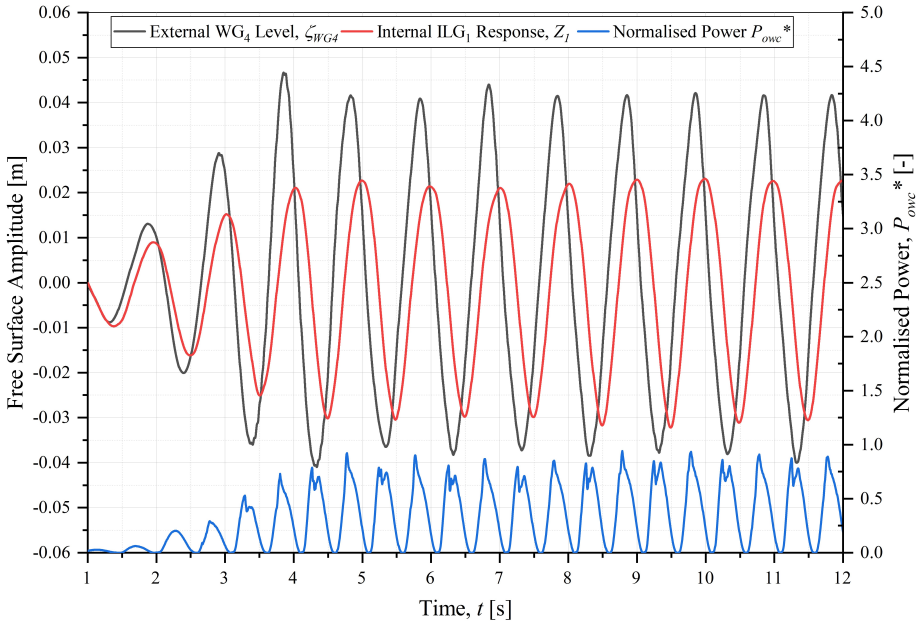


Figure 5.1: *Example of a time series plot (at $f_{wave} = 1\,Hz$) of internal water level, external wave height and power history obtained from the single OWC experiments*

peak found in most of the data presented, however, a more prominent peak is more often found in the range of $0.92 - 0.94Hz$, which is perhaps the true resonant response since it is more consistently the peak response, even when damping is included (Fig. 5.3) The testing in this frequency range allows a comparison between models at their optimal operating range and a higher resolution performance curve. The curves often contain a trough in-between the aforementioned two peaks. At this point during the experiments, some internal sloshing was observed, which can occur at certain frequencies – usually higher frequencies and particular intermediate frequencies. Since the ILG is mounted in the centre of the chamber, the sloshing results in a lower mean water level as the front and rear inner walls experience the higher amplitudes.

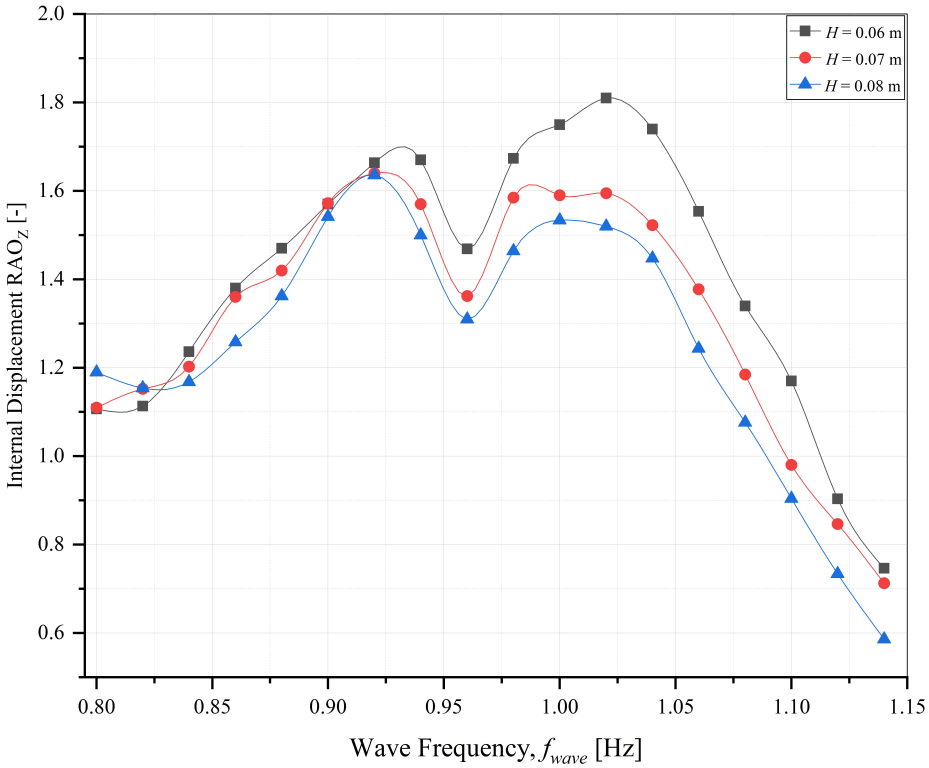


Figure 5.2: *Internal displacement RAOs for the open lid single OWC over a frequency range of* $f_{wave} = 0.8$–$1.14\,Hz$ *for heights* $H_{wave} = 0.06,\ 0.07,\ 0.08\,m$

Damping is applied to the same geometry with the inclusion of orifice plates. The response to the orifice range $1 - 3\%$ is plotted with the 100%, which represents zero damping in Figure 5.3. While more suppressed, the shape of the dampened RAOs follows the case of zero damping. As frequency increases, the responses converge as the relative wavelength shortens to induce severe sloshing. In general, as expected, results show the damping has an inverse effect on the RAO magnitude.

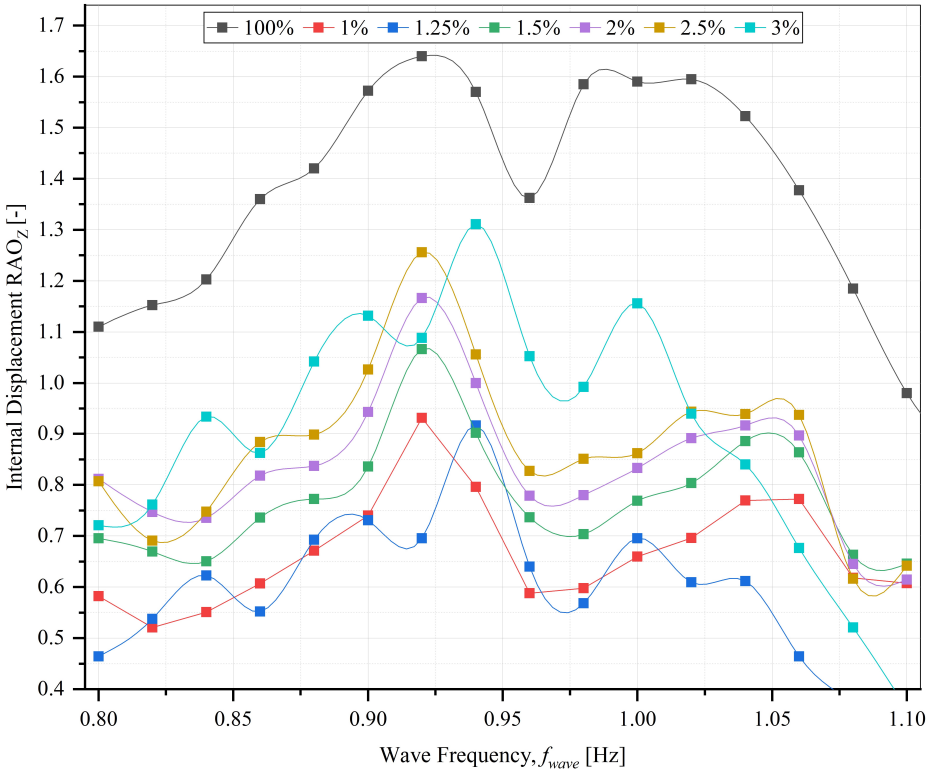


Figure 5.3: *Internal displacement RAO results from the single OWC orifice tests through a frequency range of* $f_{wave} = 0.8$–$1.1\,Hz$ *and a wave height of* $H_{wave} = 0.08\,m$*, with an orifice range* $O = 1 - 3\%$ *with for* 100% *plotted to represent zero damping*

It is more desirable to have an OWC over dampened as opposed to under dampened. However, a high RAO response is positive but not at the expense of power extraction, which ultimately is a function of the pressure drop created. Figure 5.4 shows the effects of damping on the maximum pressure during exhale and the average net pressure, p_{Net}, which is the sum of the average maximum and minimum pressures, expressed as:

$$p_{Net} = \bar{p_{max}} + \bar{p_{min}} \tag{5.2}$$

With lower damping, peak pressures reduce and net pressures indicate that the inhale process in dominant. With orifice 1.25%, peak pressures follow the trend with high values in between 1% and 1.5%; however, the net pressures are closer to zero meaning a balance between inhale and exhale processes, which is more desirable as it yield a smoother power and a higher mean power. Hence, similar magnitudes of power are generated in both processes per wave period – every half period – resulting in a

higher mean power. While constant damping is not suitable for 'real life' operation, without modelling a full PTO system and in the absence of a control system, the perceived optimal damping orifice plate of 1.25% was chosen for all subsequent single OWC experiments.

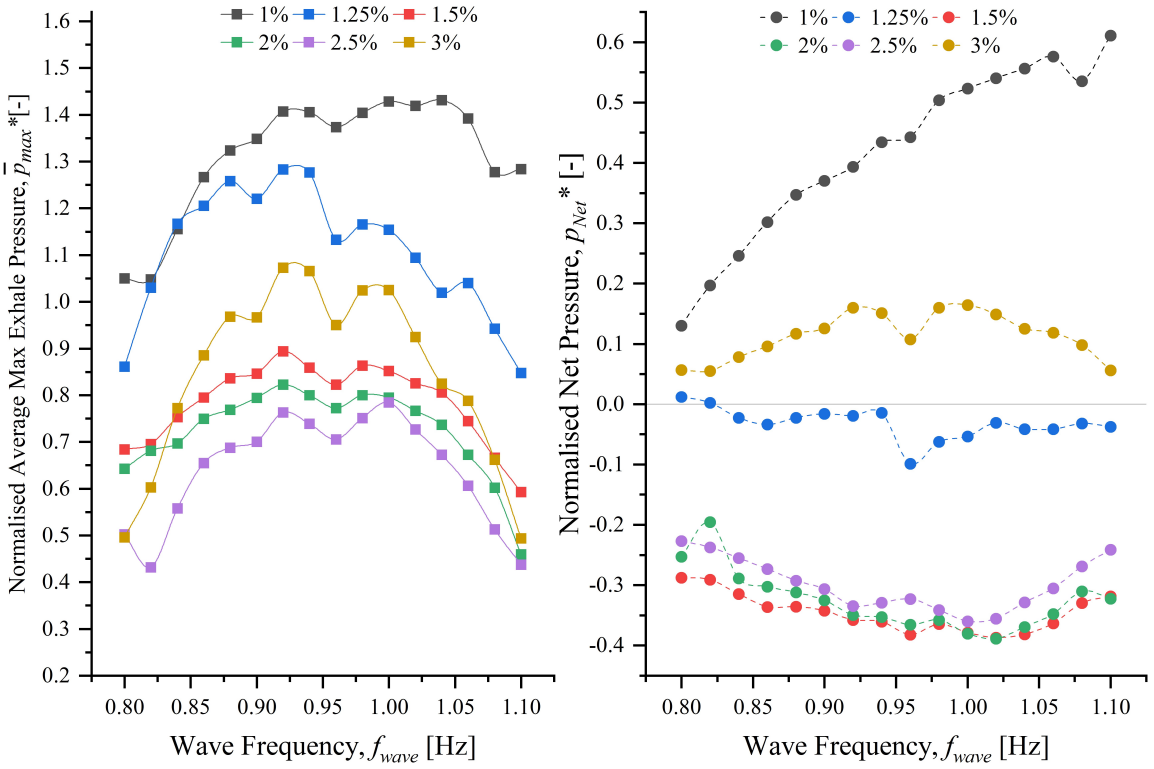


Figure 5.4: *Normalised values of average maximum exhale pressures (left) and net pressures (right) from the single OWC for the orifice plate range $O = 1 - 3\%$ over the frequency range of $f_{wave} = 0.8$–$1.1\,Hz$ and wave height $H_{wave} = 0.08\,m$*

In the case of the modular M-OWC, since there is effectively one orifice plate for three chambers larger orifice plates are required. Where S is still the internal water plane area of a single OWC, it was estimated that 3.75% would be appropriate. A range of $3.5 - 6\%$ were tested to confirm these estimates (Figure 5.5). Again, there is effectively a trade-off between the maximum pressure achievable and the RAO for optimal power, a behaviour also observed in the experiments. The estimated 3.75% was moving forward since it yielded high maximum pressures with a comparatively low cost to the RAOs.

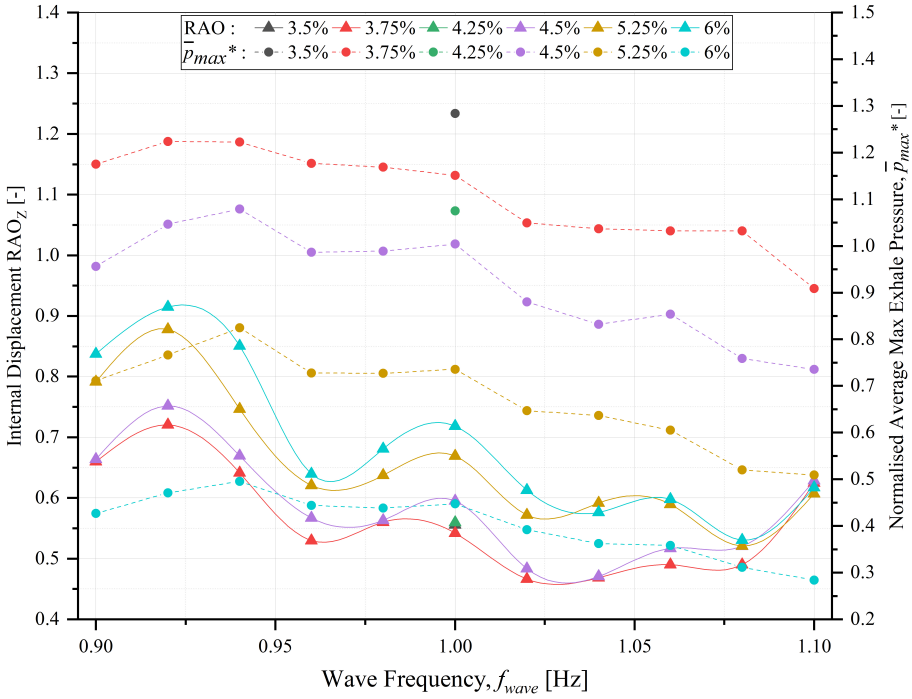


Figure 5.5: *Internal displacement RAOs and normalised values of average maximum exhale pressures from the M-OWC model for an orifice plate range $O = 3.5 - 6\%$, over a frequency range of $f_{wave} = 0.8$–$1.1\,Hz$ and wave height $H_{wave} = 0.08\,m$*

OWC Chamber Spacing

With both the OWC Array and modular M-OWC models and their chosen damping values, OWC spacings were adjusted from $a = 0$ to $a = 3$ in increments of $0.5a$. Since is λ_{max} approaches the tank width $2.5m$, effects were anticipated and closely monitored. No observations were made and it can confidently be suggested that the relatively small width of the tank did not affect these results. The wave angle was not adjusted and the responses of all OWCs were in phase suggesting there were minimal transverse effects. Greater uncertainties became apparent when spacing was increased to $a = 3.5$, resulting in the absence of this spacing in all subsequent tests hence, $a_{max} = 3$. Despite the uncertainties of the effects of the tank width, the overall cross-model comparison conclusions of this work would not change.

Across all results and as is evident in Figure 5.6 where results are plotted for the $1\,Hz$ run, at $a < 1$, performance is affected significantly. Improved performance from $a > 1$ is negligible in most cases but can result in decreased performance as in the

case of the M-OWC. Ultimately, it is ideal to have as many chambers as possible and therefore the least spacing as possible. With a significant increase to $a = 1$, and no certain improvement trends in performance from $a > 1$, this is considered the ideal.

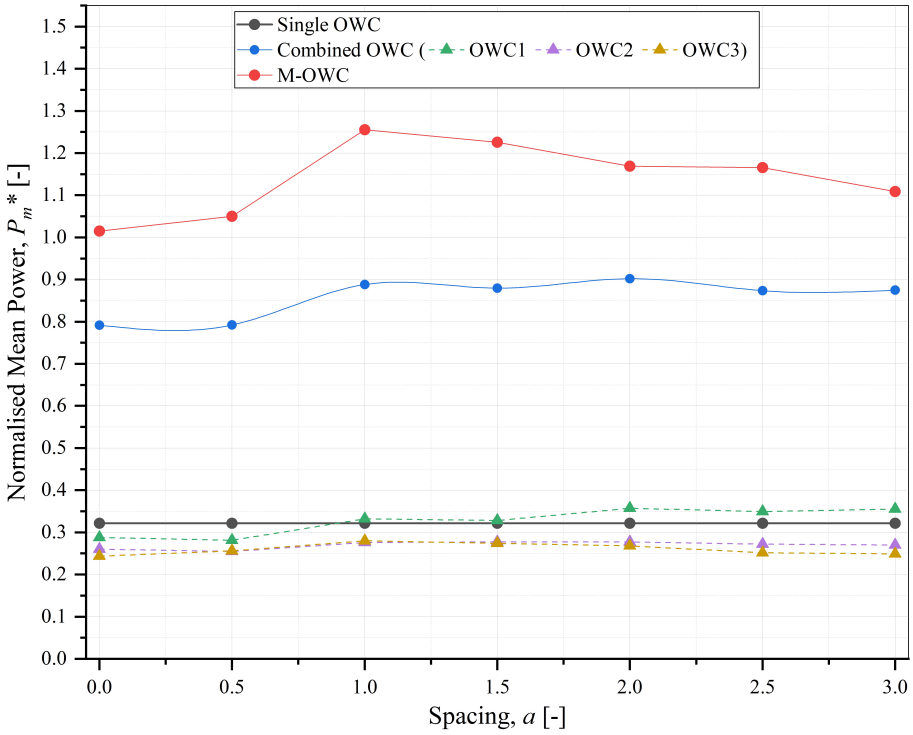


Figure 5.6: *Normalised values of mean power generated by the single OWC, the OWC array and M-OWC model with over a chamber spacing range of $a = 0 - 3$, for a frequency of $f_{wave} = 1\,Hz$ and wave height $H_{wave} = 0.08\,m$*

Against the single OWC, the individual OWCs of the OWC array perform differently. The centre OWC performs best at $a = 1$ where the performance is almost equal to that of the single OWC. The outer OWCs, 2 and 3, do not improve with further spacing, only their impact on the centre OWC is evident. Hence, when $a < 1$ these outer chambers are affecting the resource available for the centre chamber. Despite the distance between the OWCs increasing and therefore the greater the capture width, the outer chambers do not approach the performance of the single OWC.

Figure 5.6 also includes the combined power of the OWC array, which is simply the sum of the power generated by the individual OWCs. Since both outer OWCs under perform, the combined power is less or at very best the equivalent to three single OWCs in isolation. This behaviour is the same across other frequency points,

which suggests that the effect of the resource absorbed by the centre chamber, could be to the detriment to the wave energy outside of this centre channel thus affecting the outer chambers. Once again, the uncertainties of the effects of the tank width do not change this conclusion. Regardless of effects, the spacing improves at $a \geq 1$.

Cross Model Performance Comparison

Capture Width Performance

The CWR is considered in two forms as detailed in Equations 3.15 and 3.16 and is plotted in Figure 5.7 in terms of average and average peak values against wave frequency for all models. For the OWC array, the power absorbed is the combined power of all three OWCs. Note that these models are not optimised and therefore these values are not to be compared with other devices but are only useful for the comparison between these models.

The OWC array does not exceed those values of the single OWC across the frequency range. The modular M-OWC is superior mainly with respect to average peak values. The effective capture width (CWR_E) values are favourable toward both the OWC array and modular M-OWC simply because the overall size of the structure is not considered, only the combined widths of the OWCs. For the single OWC the difference between effective and total width is minimal since the difference in the width component of the CWR_E and CWR_T respectively, is only 0.02 m (twice the wall thickness). In the case of the M-OWC this proves that the device is more efficient with respect to the power in the width of the OWC. In truth, the resource absorbed by the OWCs is greater than the resource in the width of the OWC according to the observations made in the spacing analysis discussed above.

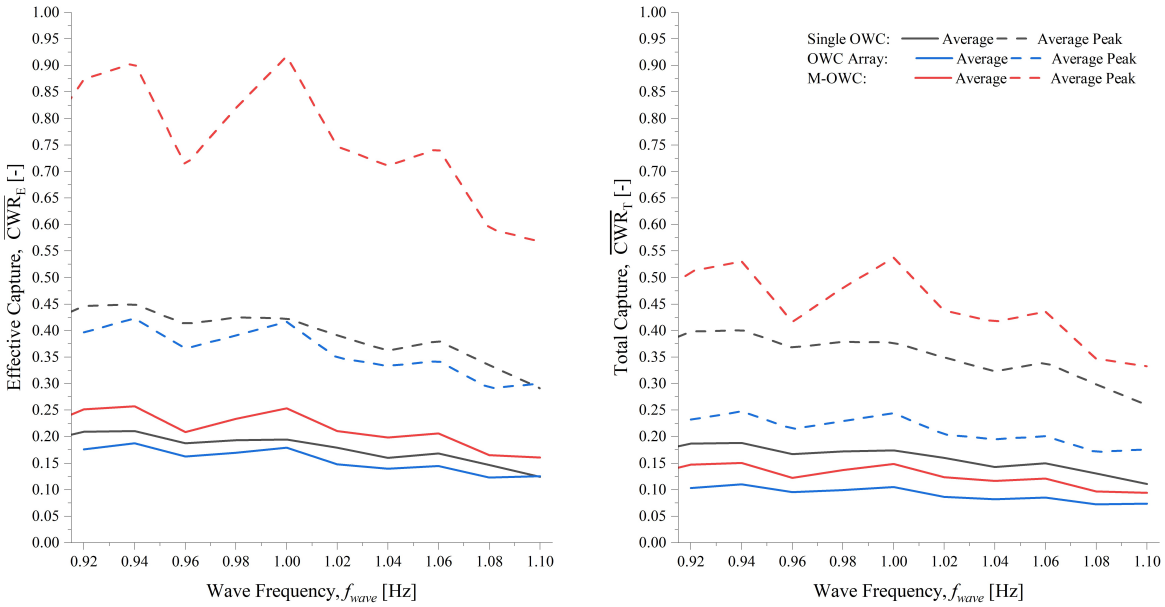


Figure 5.7: *Average (left) and average peak values (right) for the effective and total capture width values plotted as a function of wave frequency for the single OWC, the OWC array and M-OWC models over a frequency range of* $f_{wave} = 0.92$–$1.1\,Hz$ *and wave height* $H_{wave} = 0.08\,m$

In Figure 5.8, CWR values are plotted against OWC spacing for average and average peak values. Here the single OWC serves as a good baseline against the other models. Again, the effective CWR is favourable toward both the OWC array and M-OWC by considering that the wave resource is only three chambers wide despite the spacing. Although the OWC array remains inferior to the single OWC, whereas the average peak effective CWR peaks at the optimal spacing of $a = 1$ for the M-OWC. The M-OWC average peak values for the total CWR are far greater than the single OWC for when $a < 1.5$. With respect to average total CWR, the single OWC is superior over the M-OWC, but only when $a > 0.5$. Hence, at the sub-optimal spacing, because of the decreased width of the structure, the M-OWC is more efficient that the single OWC. Furthermore, despite spacing, the OWC array is always the least efficient especially with respect to the total CWR as spacing increases. As one would expect, with respect to the effective CWR, the OWC array follows the trend of the single OWC when $a > 1$.

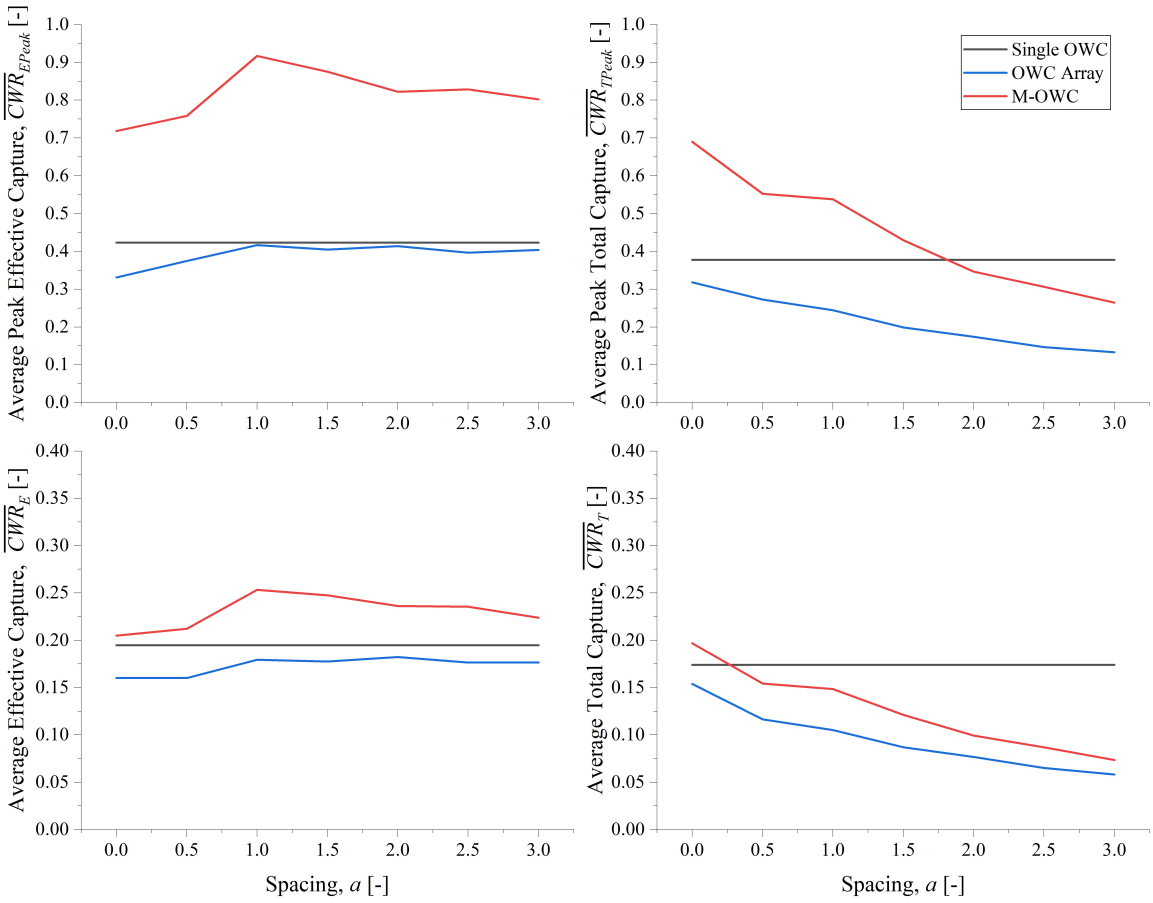


Figure 5.8: *Average (bottom) and average peak (top) values for the effective (left) and total (right) capture width values for the single OWC, the OWC array and M-OWC models plotted against a chamber spacing range of* $a = 0 - 3$*, for a frequency of* $f_{wave} = 1\,Hz$ *and wave height* $H_{wave} = 0.08\,m$

Flow Performance

The purpose of M-OWC WECs, in general, is to multiply the energy production of the device by a factor equal to the number of OWCs or greater if efficiency can be improved in the process. Moreover, with the airflow from all OWCs converging upstream of the PTO system, this should also mean that the flow rates should also multiply by a factor equal to the number of chambers – in this case three.

In Figure 5.9, for the same input wave, the flow and power values are compared for the M-OWC, OWC array and the single OWC. The values of the single OWC are multiplied by three to serve as a useful benchmark. It can be seen that the M-OWC exceeds in generating three times more flow and power than the equivalent three single

OWCs with respect to both mean and average peak values.

The OWC array combined values manage to exceed the single OWC, but is inferior to the three single OWC equivalent across all variables. With respect to mean power, the array model generates at best 2.6 (not 3) times the single OWC. This suggests that poor performances are encountered with individual PTOs in the case of OWCs arrays.

Although these results do not consider the width of the resource (where $a = 1$), the purposes and expectations of the M-OWC are delivered in the multiplication of the flow rates and power production by a factor equal to the number of OWCs and greater. This is something the OWC array fails to achieve, with the crucial difference being the PTO arrangement. These results therefore prove the concept of the M-OWC as being more efficient without considering the capture width in this case.

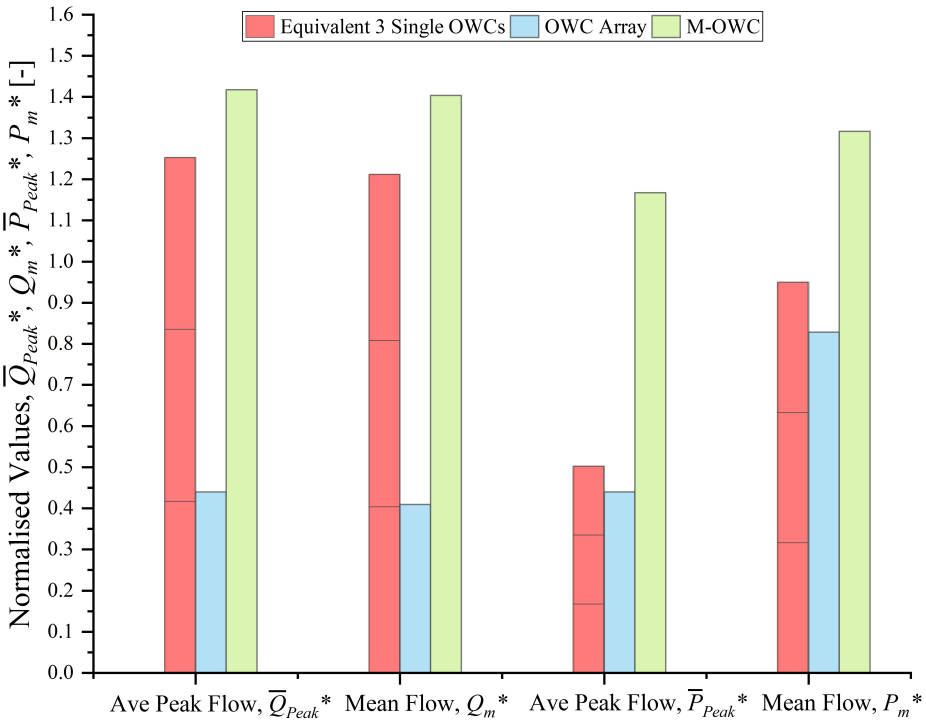


Figure 5.9: *Normalised values for average peak and average airflow, and average peak and mean power for the equivalent of three single OWCs, the OWC array and M-OWC models for the representative wave frequency of* $f_{wave} = 1\,Hz$ *and wave height* $H_{wave} = 0.08\,m$

Conclusions

Three physical models have been investigated in experiments in which hydrodynamic and pneumatic performances have been analysed. Cross model performance comparisons have been carried out with respect to changing variables such as damping and chamber spacing.

The ultimate aim of this research was to investigate the potential benefits of a Modular M-OWC above an OWC Array, which is often considered in M-OWC concepts. This study was conducted with a pragmatic approach in order to provide a fair comparison between models as opposed to comparing the CWRs with abstract devices in different conditions, which can add great uncertainty.

The research questions posed in Chapter 1 (Phase 2 aims 1 and 2) regarding the performance differences and change in characteristics between a single OWC, OWC Array and M-OWC, have been answered through the following conclusions which can be drawn from this chapter's research:

- For the single OWC with the detailed geometry, the orifice plate which creates the optimal damping for the best performance is the 1.25%. This provides high RAOs with minimal cost to maximum pressures. The effects of the air manifold on damping, if they exist, were very difficult to quantify in the results or determine qualitatively. Therefore, using three times the damping condition used for the single OWC was considered to be the best approach to keep these experiments as comparative as possible. Furthermore, the orifice of 3.75% was indeed found to be optimal, therefore optimal conditions were true for all models.

- Spacing of chambers for the OWC array and M-OWC has great effect on the power produced. Optimal is found to be when $a = 1$. When $a < 1$ performance is reduced and when $a > 1$, performance doesn't necessarily increase and can reduce but is ultimately less efficient.

- The individual OWCs in the OWC array at the very best match the performance of the single OWC despite changes in spacing. The OWCs improve after spacing

of $a = 1$, however, only the centre chamber approaches the performance level of a the single OWC. Taking into account the capture width, this means that the OWC array will always be less efficient, even at larger spacings that could not be catered for in these experiments, as the capture width is greater.

- As the intentions of a modular M-OWC is to combine airflow from multiple chambers prior to the PTO to multiply flow rate and consequently power by a factor equal to the number of OWCs, the performance values should reflect this and have proven to do so. In fact, flow and power values are greater than three times the value recorded in the single OWC for a modular M-OWC with three chambers. This proves the concept viable and more so than an OWC array concept as an M-OWC, since the multiplication of OWCs has no benefit on performance due to the individual isolated PTO arrangement.

- For the same wave, the M-OWC produces higher flow rates and power than the OWC array and the equivalent of 3 individual single OWCs. However, with respect to effective and total capture width values, the greater the spacing the less efficient the WEC with respect to the total capture width. Despite this, due to the higher efficiency with respect to the effective width, at lower spacings, even though when $a < 1$ the performance is suboptimal, the total capture width ratio exceeds the single OWC.

The aims and the objectives of this study were fulfilled with the results found. Note that by no means are the models and their geometries currently optimised. The current geometry is a product of the progressive nature of the project and effort to keep as many aspects constant for fair comparative data. Further work includes additional steps in the investigation of the superior performance of the M-OWC, further improvements and its potential in alternative or integrated applications.

Chapter 6

Phase 2: M-OWC Breakwater and PTO Modelling

Introduction

The great potential of M-OWCs lays in their scalability, which is important for all renewable energies, and versatility. This provides opportunity for diverse integration projects and cross-industry synergies resulting in a reduction of capital costs and operational costs as these expenditures are shared. Such synergies only become possible if the research undertaken proves that any integration of a WEC is not to the detriment of the performance of the hosting application, for example, a breakwater, wind turbine structures, fish farm platform or other multi-use large platforms. Hence, for a breakwater integration concept, the WEC must operate efficiently but also act as an affective breakwater, potentially provide a berthing facility, costal protection and marina protection i.e. the benefits should be mutual.

These innovative integration concepts are becoming more of a trend in global research among point absorber, overtopping and OWC WECs, but less so for M-OWCs, which are also a suitable candidate and an untapped potential for large scale integration deployments. As discussed in Chapter 2, many breakwater integration deployments are retrofit options, which also stand to lower costs significantly.

The research of this chapter is concerned with two aspects of Phase 2 M-OWC

breakwater development; the effect of breakwater integration with the M-OWC on performance of both energy extraction and breakwater effectiveness, and the PTO system design options to achieve unidirectional airflow, which are Phase 2 research aims 4 and 5, respectively, as detailed in Chapter 1.

Research Approach

This research is interested in an output of unidirectional air from a PTO system, hence the system is considered as a whole as opposed to investigating turbine types. The approach or PTO system types can be placed into three main categories; the first of which is the self-rectifying category, which includes no manipulation of airflow but the extraction of energy from the bidirectional airflow via the use of a self-rectifying turbine, a turbine that accepts flow from either direction but rotates in the same direction despite its flow direction. These turbines are featured in literature reviews such as from Falcao and Gato [183] and are still undergoing optimisation today. The main types include the most popular Wells, impulse, Dennis-Auld and savonius turbine.

The other two categories for PTO systems involve the utilisation of the more efficient and desirable unidirectional air turbine by creating unidirectional airflow with or without the use of rectifying valves upstream of the turbine making them flow rectifying and self-rectifying systems respectively. For the latter, in the absence of valves substantial losses occur but can be reduced with the use of fluidic diodes as investigated by Okuhara et al. [203].

Flow rectifying systems require valves either controlled or operating mechanically in response to the flow. This was seen first in the Masuda navigational buoy single OWC, followed by the testing with the Kaimei 2 chamber prototype. While showing great potential, the valves were said to have over complicated the OWC concept and were unreliable [56, 209]. Since then, valves are rarely considered in OWC PTO systems but feature commonly in modular M-OWCs concepts to create high and low-pressure ducts prior to the turbine. With the potential gain in overall efficiency with unidirectional airflow, it is fair to say that both airflow rectifying systems and self-rectifying unidirectional systems remain to have potential despite its downfalls.

Especially at larger scales with modular M-OWCs, the trade off to have a single or twin unidirectional turbine system, with or without rectifying valves could be beneficial to overall costs and performance.

The aims of this research can be fulfilled with the following experimental studies; modelling of breakwater integration with respect to sea defence through reflection and absorption, and to determine the viability of a single and twin unidirectional turbine system vs a bidirectional system by considering the manipulation of airflow closer to the turbine with a single and twin rectifying system to compare practical and conversion performance. The wave tank set up for these experiments where reflection is measured is described in Chapter 3, where a sketch including the placement of wave probes can be seen in Figure 3.12. The OWC dimensions are retained from the previous chapter but an assembly of the M-OWC bidirectional and unidirectional models can be found in Figure 3.15 and 3.16, respectively. Design of the PTOs is detailed in Chapter 3 and close up illustration of their operation can be found in Figure 3.17 and 3.18 for the single and twin PTOs, respectively.

These experiments contain wave runs derived from the Billia Croo site detailed in Chapter 3. The regular and irregular wave runs are listed in Table 3.2 and 3.3, respectively.

Results and Discussion

The M-OWC Bidirectional

Orifice tests repeated for the M-OWC Bidirectional model (Fig. 3.15) with the altered outlet and extended wave run with plates either side of the previous optimal (O = 3.5%, 3.75%, 4.25%). Results plotted for the O = 3.75% are show in Figure 6.1, where the effect of wave steepness is visible in the reduction of p_{Net} to yield more even exhale and inhale process, and the increase in RAOs.

Again, with a slightly altered model and setup from the previous experiments, OWC chamber spacing tests were repeated for the modular M-OWC without a breakwater-like-blocking-structure. With a terminating WEC type, as with a breakwater, without

considering varying wave angles, the wave propagates in the direction orthogonal to the M-OWC's front wall, and thus interacts with each OWC in phase. It is therefore possible to visually observe through experiments and prove through the resulting data prove that the distance between these chambers has an impact.

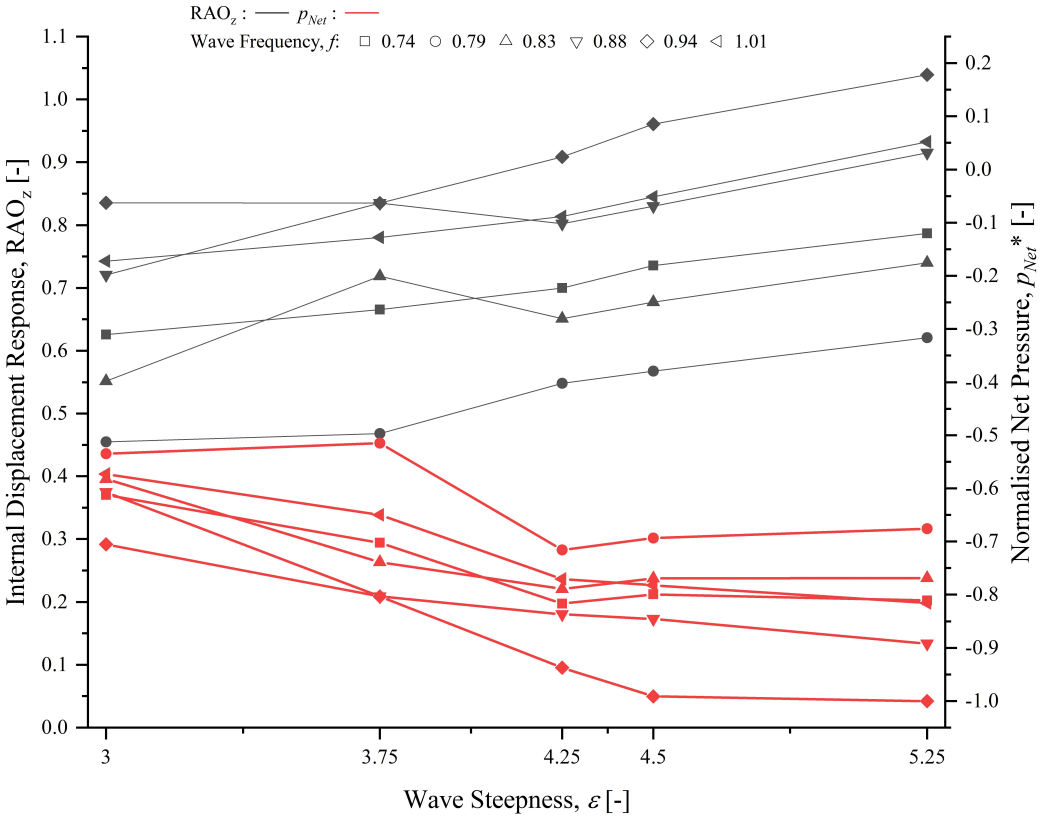


Figure 6.1: *Internal displacement RAOs and normalised net pressure plot for orifice plate damping test with the altered Outlet of the M-OWC Bidirectional for all regular wave run frequencies and a wave heights plotted as a function of wave steepness*

At smaller spacing values, $a < 1$ for example, there is less resource available as chambers share a section of the wave crest width. This is seen in Figure 6.2, where performance is clearly stunted with the close proximity of chambers sharing resource ($a < 1$). This clearly significantly changes at $a \geq 1$ as it appears that chambers have increased individual resource. Ideally, WEC width should be kept as minimal as possible but not to the detriment of performance with respect to wave capture. In early experiments, these suboptimal spacings were compared to that of a singular OWC with the equivalent geometry. Despite the large widths, at these suboptimal

spacings the M-OWC proved to be more efficient with respect to both forms of the CWR (Eqs. 3.15 and 3.16).

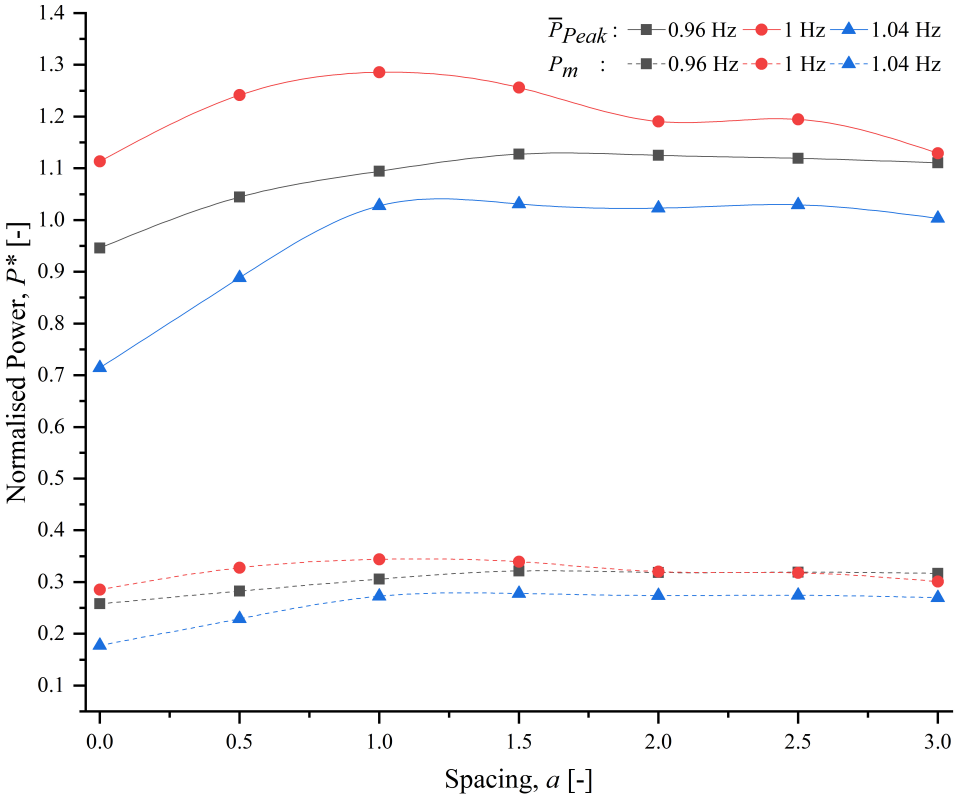


Figure 6.2: *Normalised power plot against an OWC spacing range of* $a = 0 - 3$ *for the altered outlet M-OWC bidirectional configuration for representative frequencies of* $f_{wave} = 0.96, 1 and 1.04\,Hz$ *and height* $H_{wave} = 0.08\,m$

The second effect of spacing, especially for this model with no structure between OWC chambers, is reflection. As would be expected, with greater gaps between chambers, a greater level of transmission reduces reflection. For a larger number of frequency points at a fixed wave height, Figure 6.3 shows this relationship between K_r and the wave frequency, f_{wave}. With the estimated resonant frequency of $1Hz$ for this geometry, the reflection shows a peak response, with a noticeable reduction at $0.98Hz$, where sloshing was observed both visually and in the internal amplitude results data. A clear trend also proves the effect of wave steepness on reflection and subsequently performance mainly due to increased interaction with the front wall of the structure.

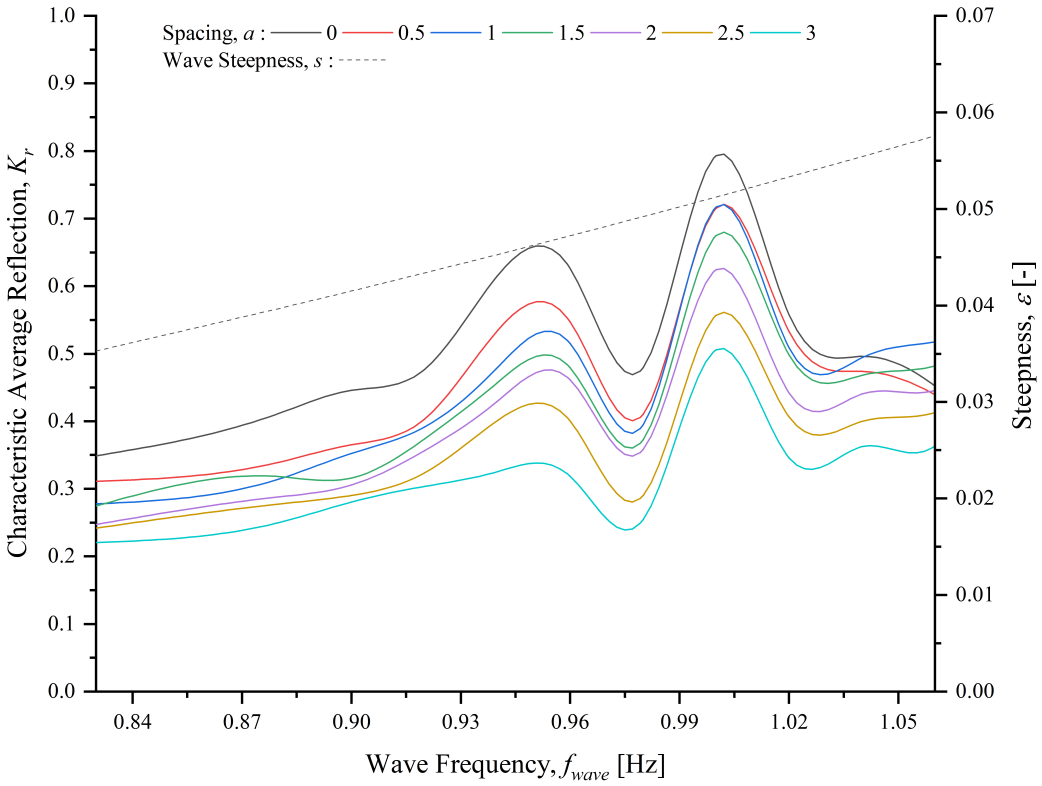


Figure 6.3: *Characteristic average reflection for the M-OWC Bidirectional model plotted against a frequency range of $f_{wave} = 0.74$–$1.01\,Hz$ with a representative and wave height $H_{wave} = 0.08\,m$ for chamber a chamber spacing range of $a = 0 - 3$ with a wave steepness line representing the breaking threshold*

A closer fits exist between the plots for $a = 0.5$ and $a = 1$ at the resonant frequency but less so elsewhere on the frequency range suggesting that this increased reflection at $a = 1$ is not to the determent of performance. Despite having no blocking structure between chambers, this means both higher reflection and performance with less wave transmission is meeting the essential criteria of an M-OWC breakwater namely reduced transmission through either absorption of reflection.

The spacing value of $a = 1$ is considered ideal and is in agreement with previous experiments carried out on the equivalent OWC array and M-OWC. With the added complications of the subsequent models' geometries in this investigation, the spacing is kept constant at $a = 1$ from herein.

The M-OWC Breakwater Effect

Breakwater Performance

Experiments with the M-OWC bidirectional model carried out with and without a blocking structure between OWC chambers allows for direct and fair comparisons between models, of which this section presents.

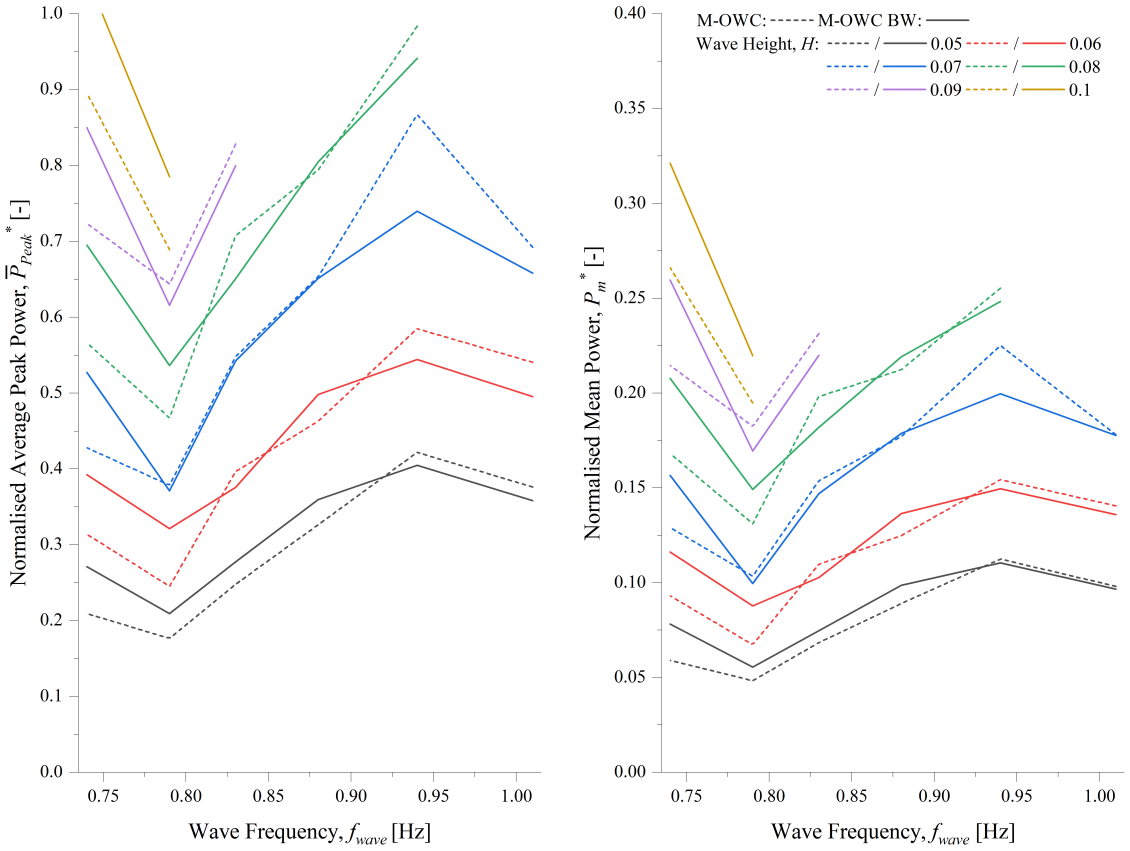


Figure 6.4: *Normalised mean (left) and average peak power (right) for M-OWC and M-OWC BW bidirectional models for a frequency range of* $f_{wave} = 0.74$–$1.01\,Hz$ *and wave height range of height* $H_{wave} = 0.05$–$0.1\,m$

Performance of the models plotted in Figure 6.4 with and without the blocking structure is shown in terms of average peak power and mean power (normalised with respect to the range of the data) for varying wave heights revealing the effect of wave steepness. The negative effects of the blocking structure can be seen for the resonant frequency and cases with steeper waves, hence, at the highest frequencies and wave

heights. At lower frequencies, differences are generally positive for the breakwater-type model, even at higher wave heights.

Despite these mixed effects, it is evident that the effect of the BW structure has greater effect on reflection than the pneumatic power extracted. This is an overall positive outcome, since it proves that the addition of the structure is not to the detriment of the WEC performance.

Unidirectional Models

Both single and twin unidirectional M-OWC PTO models (Figs. 3.17 and 3.18) were tested in equal conditions and wave runs. Blocking structures were installed throughout following the results of the PTO experiments.

Single Unidirectional PTO

As described, the single PTO model contains one controlled valve and two mechanical airflow controlled one-way valves. These valves or processes are by no means optimised and therefore incur losses. Figure 6.5 shows an example of a time series plot of the pressure drop across the single orifice plate.

Since this system is an air rectifying system for a single unidirectional PTO, the direction of the pressure gradient shouldn't change to ensure 'forward' operation. Instead, the working fluid pressure sign acting from the OWCs changes with respect to atmospheric pressure. During negative displacement, the inhale process is caused with a reduction of pressure with respect to atmospheric pressure, which is diverted to the downstream side of the orifice plate in order to draw airflow from the atmosphere, through the orifice plate and into the OWC chambers. During positive displacement, the OWCs exhale causing a positive pressure drop with respect to the atmosphere, which is directed upstream of the turbine and out to the atmosphere.

Due to the imperfections of this system, the pressure drop direction across the orifice plate does change during rectifying process as indicated by the negative back pressure line of Figure 6.5. Back pressure such as this is undesirable for unidirectional

turbine operation and is considered as 'reverse' operation. In this analysis, the back pressure is considered purely as loss rather than negative power. At this model scale, this is due to rectifying flap valve leakage and lag. Relative to the wave period at this scale, the reaction and execution time has a greater effect on performance than at larger scales.

Additional losses come from the work required to open and close the mechanical one-way valves and any leakages also found here, all of which is very difficult to quantify experimentally.

Despite these imperfections, the single PTO unidirectional rectifying system yielded respectable results by successfully rectifying airflow using just three valves and sufficiently achieving dominant flow in the principle or forward pressure drop direction.

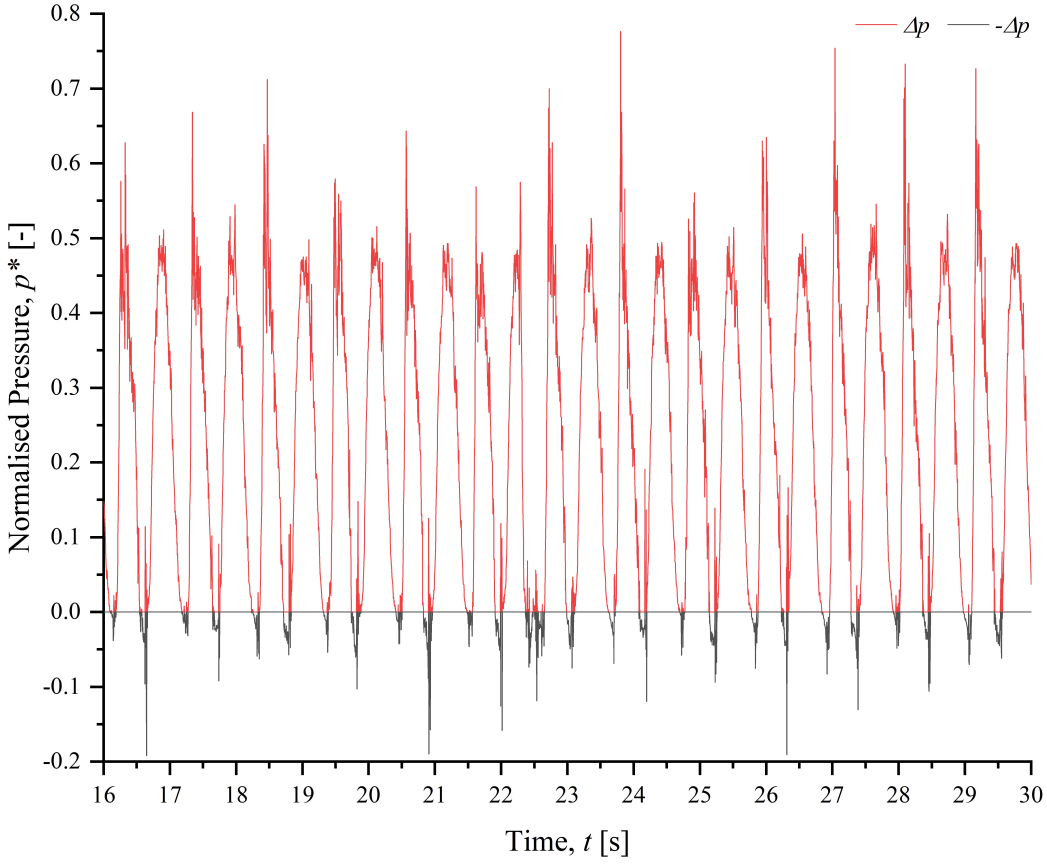


Figure 6.5: *Normalised pressure drop and reverse pressure drop time series example plot for exhale and inhale processes, respectively, for the twin turbine rectifying system for a representative frequency of height* $f_{wave} = 0.94\,Hzm$ *and wave height* $H_{wave} = 0.08\,m$

Twin Unidirectional PTO

The twin model is absent of any mechanical one-way valves, since it only requires the flap valve. The exhale process generates a positive pressure drop inside the manifold with respect to atmospheric pressure creating airflow, which is diverted by the flap valve toward the exhale orifice plate. The inhale process creates a negative drop with respect to the atmosphere and the airflow is diverted through the inhale orifice plate. Losses in this system are all due to flap valve leakage and lag, which cause adverse pressure gradients as represented in Figure 6.6 for both exhale and inhale processes.

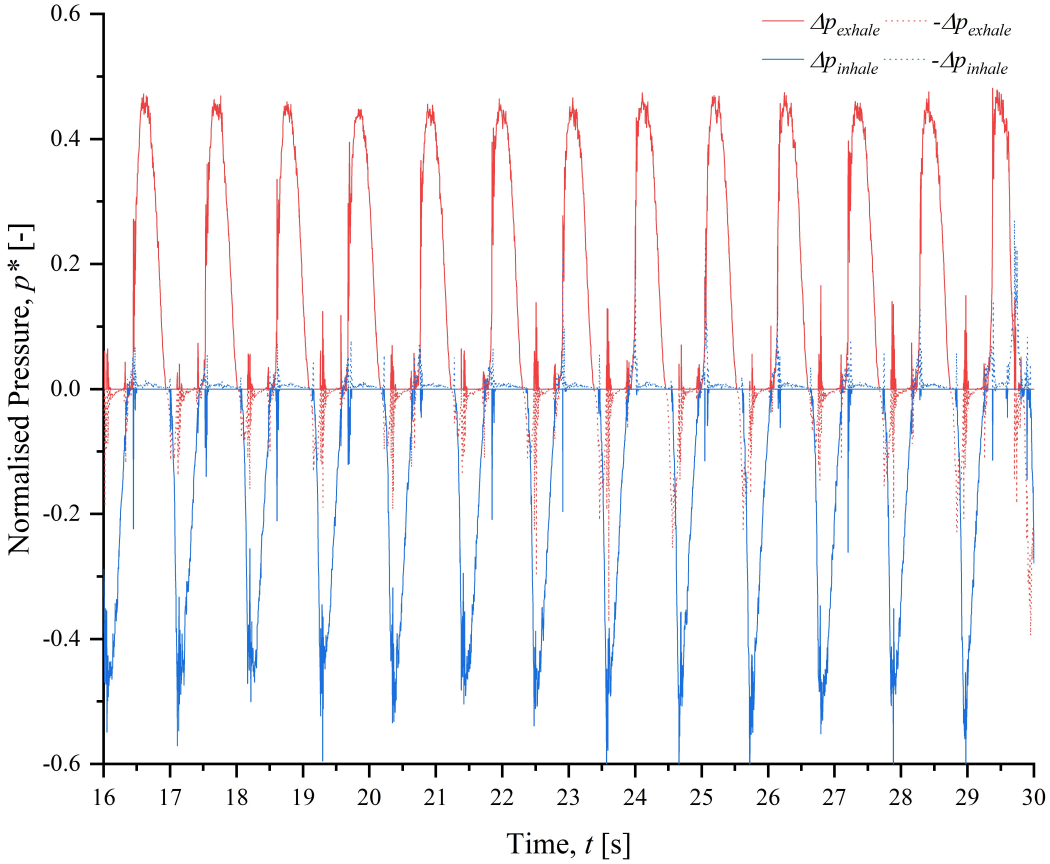


Figure 6.6: *Normalised pressure drop and reverse pressure drop time series example plot for exhale and inhale processes, respectively, for the single turbine rectifying system for a representative frequency of height* $f_{wave} = 0.94\,Hzm$ *and wave height* $H_{wave} = 0.08\,m$

As is the case with the bidirectional M-OWC model, the inhale process is dominant as seen in Figure 6.6 with higher peaks of negative are pressure compared to the rounded peaks of positive pressure during exhale. Plot lines of the reverse pressure

drop show the effect of leakage as the pressure sign of the counter process affects the pressure drop across the should be inactive orifice plate.

Operational Losses

Since specific losses in the PTO system cannot be deciphered and therefore quantified from this experimental data, the overall pneumatic losses are calculated and plotted in Figure 6.7 vs wave steepness for all 28 waves. Total pneumatic losses of the system are calculated with respect to the quantified absorbed power in the OWC – the hydraulic power.

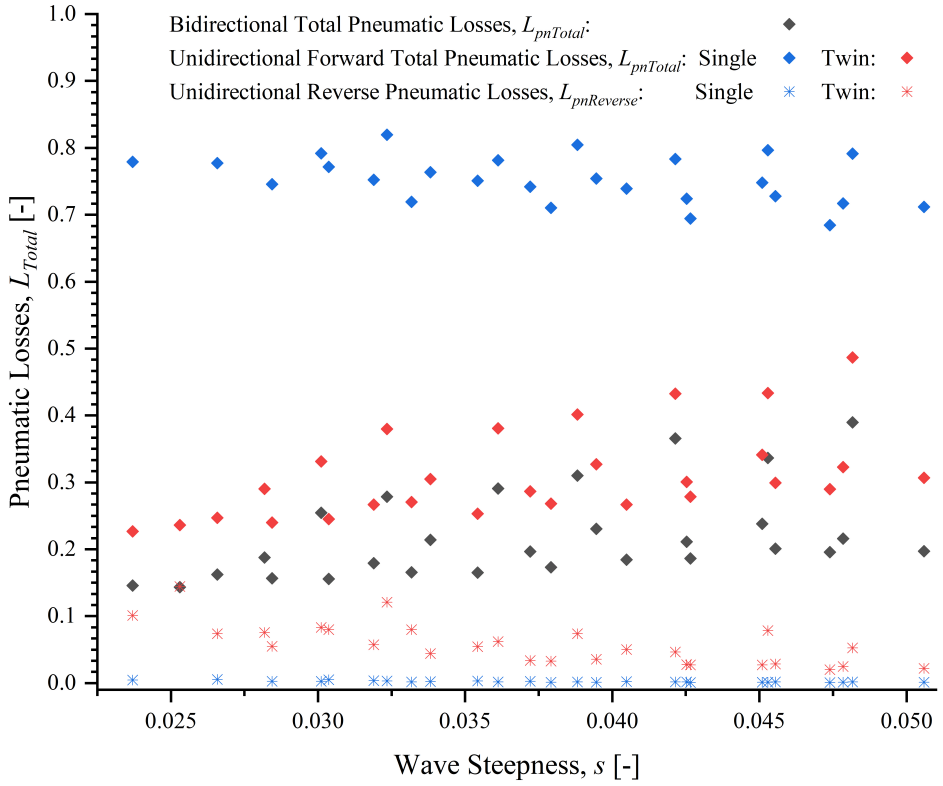


Figure 6.7: *Total pneumatic losses and reverse losses plotted against wave steepness for all BW models for all regular wave frequencies* $f_{wave} = 0.74$–$1.01\,Hzm$ *and wave heights* $H_{wave} = 0.05 - 0.1\,m$

The loss due to the reverse operation of the model PTO created during the air rectification process is part of this total loss but can be calculated separately with the

recorded back pressure:

$$P_{pnReverse} = \frac{P_{pnmReverse}(-\Delta p)}{P_{hydrm}} \tag{6.1}$$

With no rectification system for the M-OWC bidirectional model, there are just total loss figures plotted.

The loss due to back pressure is relatively small compared to the total pneumatic loss (< 0.13), especially for the single system. Interestingly, the greatest back pressure loss is found with the twin system due to leakage of the flap valve and a lack of the one-way mechanical valves preventing a pressure drop between the atmosphere. This is perhaps why the single system has less reverse losses because the atmosphere is sealed off by the adverse pressure gradient. However, this is difficult to verify since additional leakage loss could be affecting the pressure drop of the forward operation of the single system but with the twin this is more apparent due to there being no change in sign of the pressure drop.

Despite higher back pressure losses for the twin system, its losses approach that of the bidirectional system. Hence, further improvement of the system and its modelling could increase its competitiveness. This is also reflected in the hydraulic to pneumatic power conversion efficiency (η_{HP}) plot of Figure 6.8.

The efficiency of wave to hydraulic power conversion (η_{WH}) process is difficult to fully isolate from the hydraulic to pneumatic conversion process since the rectification system and damping affects clearly affect this efficiency. This can be seen in Figure 6.8 where for η_{WH}, the bidirectional model differs somewhat from the unidirectional rectifying models, which shadow one another, but in no particular pattern.

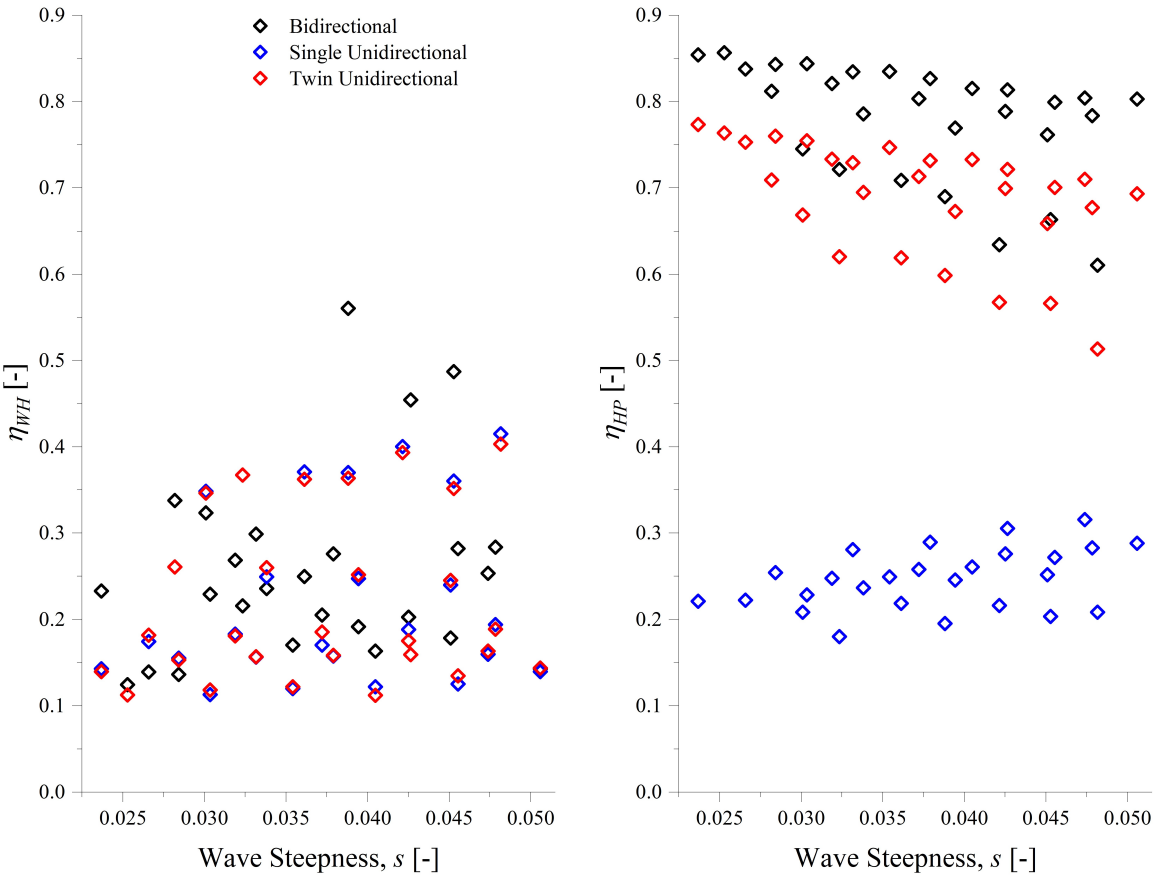


Figure 6.8: *Wave to hydraulic power η_{WH} (left) and hydraulic to pneumatic η_{HP} (right) power conversion efficiencies plotted against wave steepness for both bidirectional and unidirectional BW models for all regular wave frequencies $f_{wave} = 0.74$–$1.01\,Hzm$ and wave heights $H_{wave} = 0.05 - 0.1\,m$*

Four Model Cross Comparison

Induced Reflection

Reflection coefficients at the peak frequency Kr_{Peak}, are plotted for all four models in Figure 6.9. Understandably, the greatest difference and increase is evident with the addition of the breakwater blocking structure and higher wave frequencies. The original M-OWC shows the least reflection without the breakwater structure, although both models are similar in the lower frequency range. The unidirectional models have the same shape across the spectra as the M-OWC bidirectional. The shape of the M-OWC BW and the common low frequency shape of the models matches the reflection

shape of the empty tank experiments carried out. These experiments were carried out in order to assess the effectiveness of the beach and the reflection expected in the absence of the tank (see the results in Appendix C Figure C.1).

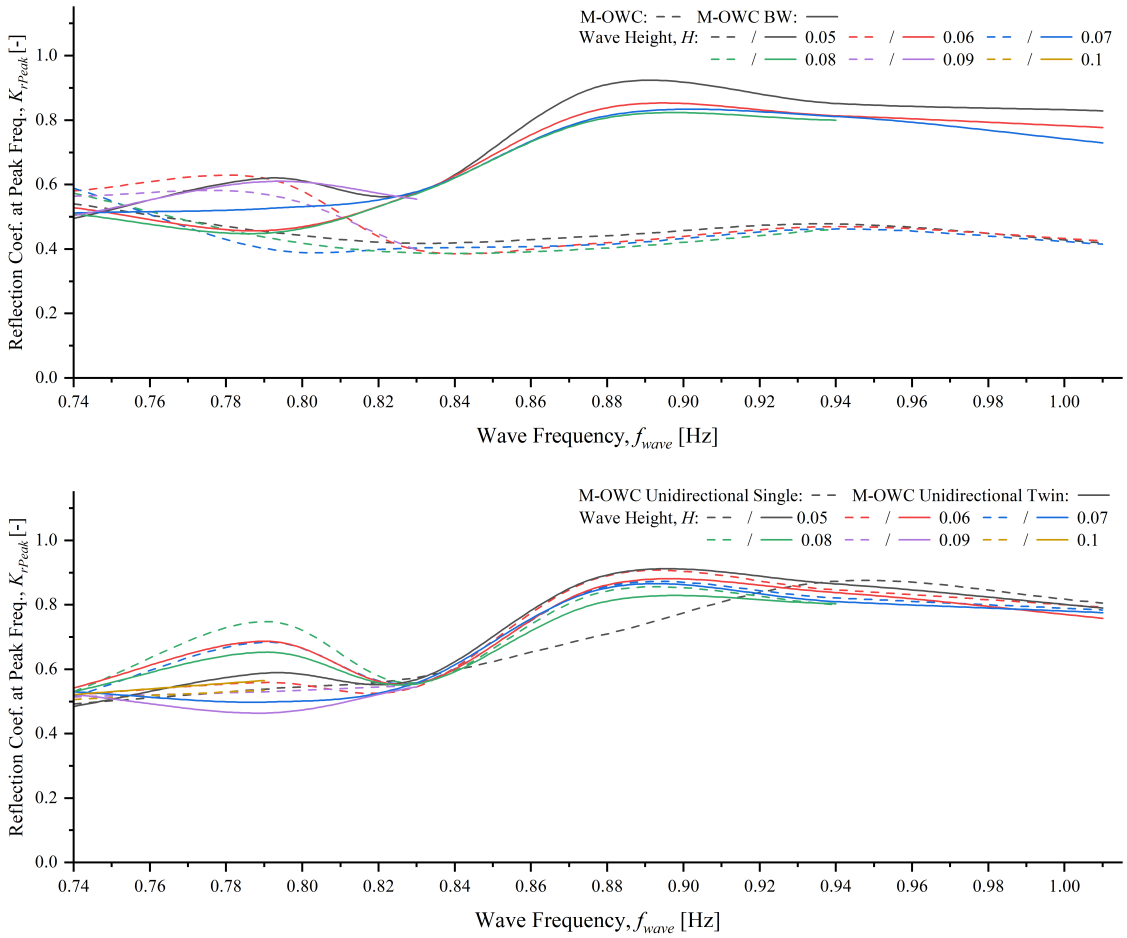


Figure 6.9: *Reflection Coefficient at peak spectral frequency due to Breakwater Structure (top) and Unidirectional models (bottom) for wave frequencies* $f_{wave} = 0.74$–$1.01\,Hzm$ *and wave heights* $H_{wave} = 0.05 - 0.1\,m$

Capture Width Performance

The CWR expressed in both forms (CWR_E and CWR_T) are plotted against wave frequency for all models for different wave heights in Figure 6.10.

With the fixed spacing of $a = 1$, all models in this comparison have the same effective and total capture widths. The capture of the bidirectional M-OWC is far more varied than the unidirectional models for changing wave heights. Efficiencies

converge closer to the lower end of the frequency range, but due to the pneumatic losses of the rectifying systems rather than hydrodynamic losses as discussed, the unidirectional airflow models are inferior across the steeper waves. While the twin model surpasses the bidirectional model at low frequencies and approaches it at less efficient wave heights at higher frequencies the single model is not competitive.

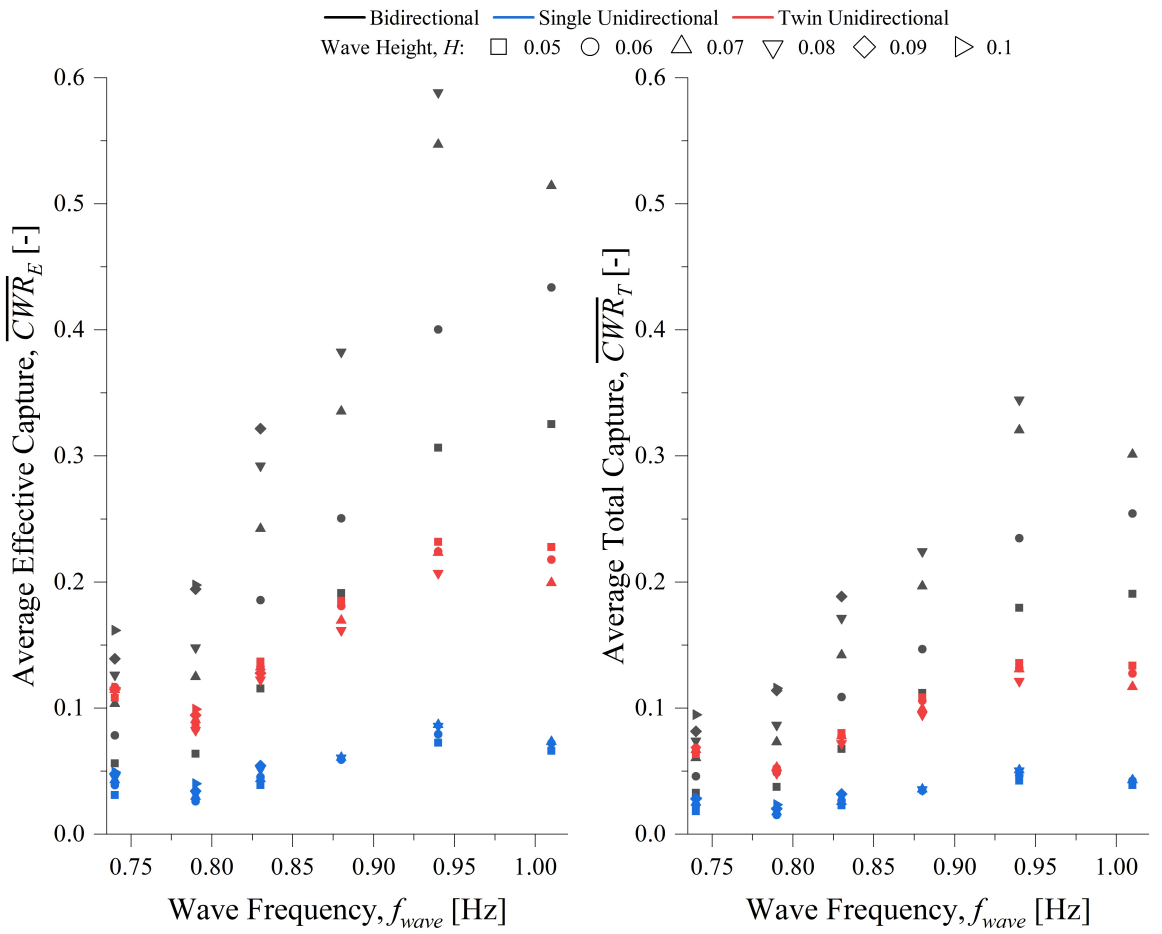


Figure 6.10: *Average effective (left) and total (right) CWR for all BW models plotted against wave frequencies* $f_{wave} = 0.74$–$1.01\,Hzm$ *and for wave heights* $H_{wave} = 0.05 - 0.1\,m$

Energy Balance Analysis

Knowing the distribution of the incident wave energy is useful in understanding how the device is performing as a WEC and as a breakwater. Furthermore, since there must be a conservation of energy, this allows one to determine additional areas in which this energy has been dissipated or lost. The incident wave energy (E_I) should

be accounted for in the external distributions, that is the reflected (E_R), transmitted (E_T)and absorbed energy (E_A). Within the absorbed 'internal' energy by the OWC, there should be a combination of the extracted energy from the PTO (E_E), the energy loss (E_L), and stored energy (E_S). These losses are unaccounted for due to the limitations of experimental modelling but will include turbulent and viscous losses.

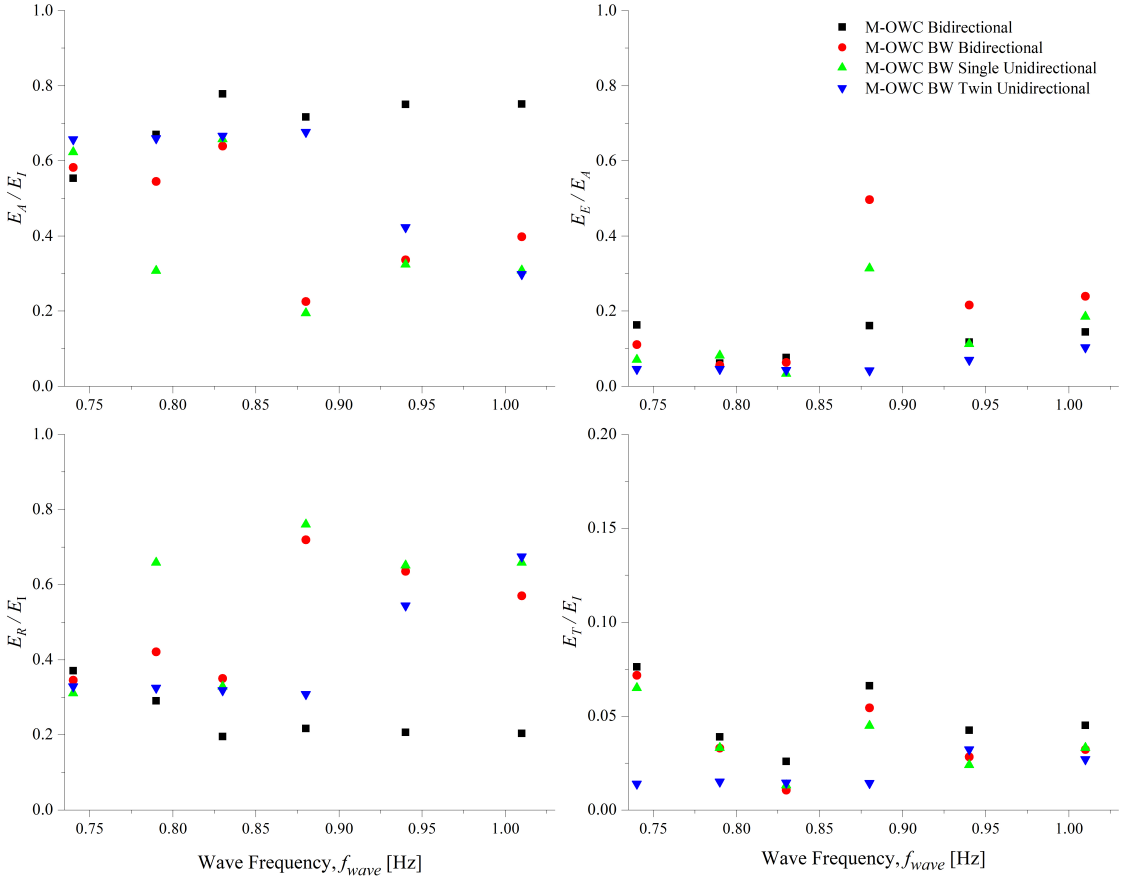


Figure 6.11: *Energy absorption (top left), reflection (bottom left), transmission (bottom right) and available extraction (top right) coefficients for all BW models plotted against a wave frequency range of* $f_{wave} = 0.74$–$1.01\,Hzm$ *for a representative wave height of* $H_{wave} = 0.07\,m$

Figure 6.11 represents these energy values as ratios with respect to the incident wave for the external distributions (E_R, E_T, E_A) and the overall absorbed energy for the internal distributions (E_E). As would be expected and made clear with the data, the breakwater models containing the blocking structure absorb less energy especially at higher frequencies when waves are steeper. Hence, the energy reflected mirrors this with converse high reflection for these breakwater models. Between the three

breakwater models, the bidirectional exhibits marginally higher absorption for equally marginally lower reflection. In light of the very low transmission, particularly for the breakwater models, it seems that the majority of the energy that doesn't get absorbed in the breakwater model, reflects rather than transmits. This would vary for different size drafts and terminating width percentages but for a nearshore fixed breakwater is expected. The level of reflection vs transmission means the wave maker paddles were required to absorb and adapt as opposed to relying on the beach absorption.

The internal energy plot of Figure 6.11 (E_E/E_A) reiterates the inefficiency of conversion between hydraulic and pneumatic power. The extracted energy (E_E) with respect to the absorbed energy (E_A) reveals the inefficiency of the air system since the absorbed energy term also includes the stored energy of the OWCs, (E_S). Despite Figure 6.11 indicating that the wave to hydraulic power conversion efficiency (η_{WH}) is greater than hydraulic to pneumatic (η_{HP}), it is evident that the airflow system, rectifying or not, has great effect on the hydrodynamic performance. Since a breakwater is designed to eliminate transmission, all breakwater models have successfully displayed this trait.

Figure 6.12 further illustrates the energy split for an example wave run where transmission is 3.8%. In this case abortion is 22% greater reflected energy but the energy loss takes account for 86% of this absorbed energy with only 13% extracted. It is evident that the WEC performance and therefore the effectiveness of the breakwater is strongly linked and dependent on the performance of the PTO system and its ability to extract the energy available at absorption in these models.

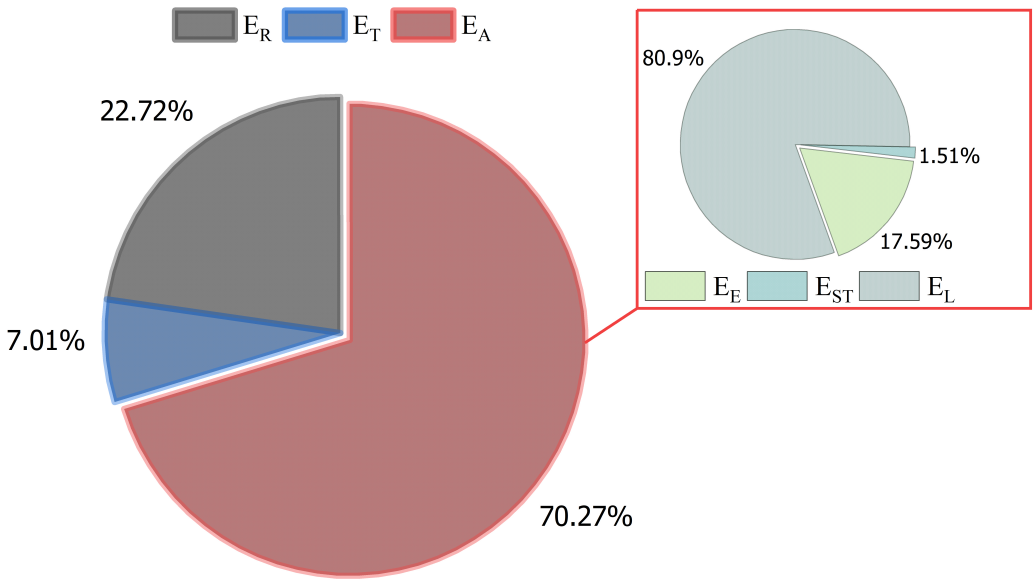


Figure 6.12: *Illustration of energy split for external quantities (reflected, transmitted and absorbed energy) (left), and OWC internal quantities (extracted, stored and lost energy) (right) for an example wave run of frequency* $f_{wave} = 0.94\,Hz$ *and wave height* $H_{wave} = 0.08\,m$

Irregular Energy Balance Analysis

The irregular wave runs were ran for 300 seconds, which yielded a lot of samples. Time series were split into segments of 2048 samples so as to reduce the fluctuations as much as possible in the segment windows and obtain satisfactory frequency resolution. Throughout the analysis, energy balance was mainly achieve, however, across all waves and all models, there were common segments that yielded results that were clearly incorrect. This is due to the over prediction of reflection in segments containing significant change in free surface amplitude i.e. between low and high energy levels. These segments are marked in an example time series plot in Appendix D Figure D.5. This effect can also be the case when waves are still forming at the start of an experiment for example. In the regular wave study, the analysis of data was always started at 8 seconds so as to skip this section of wave generation, therefore although the wave generation in the irregular times series is less obvious, the same start time

was used.

Due to the range of amplitudes and the irregularities of the wave runs, values from all segments are displayed in the form of range plots for each wave period and each model in Figure 6.13. Patterns from the regular results above are reflected in these irregular results. Transmission remains very low for all waves and gradually increases with the increase of wave period. Reflected energy is similar to regular wave results although the difference between the breakwater models and the original M-OWC bidirectional model without the blocking structure is reduced. This is irregularity of the incident wave and the lag of the reflected wave and their interaction.

In most cases the absorption energy ratio is lower than the reflected, especially at higher periods. Bidirectional models remain very similar with respect to all ratios. Unidirectional models are not comparable across most ratios, as the single exhibits greater reflection, higher transmission, lower or more erratic absorption and significantly lower extraction. The M-OWC BW Unidirectional twin is superior across all waves compared to the other models with respect to lower reflection with lower transmission combatted with the higher absorption and extraction. It is evident that the unidirectional single has a highly inefficient PTO system due to the difference between absorption and extraction, especially at $T_Z \leq 1.2\,s$. Overall, it seems that the irregular wave runs benefit the unidirectional twin model. Although the magnitudes of reflection recorded are similar to those in the regular wave runs, it is not yet full understood how an irregular incident wave run interacts with a reflected wave and whether this interaction can be beneficial or detrimental to WEC performance.

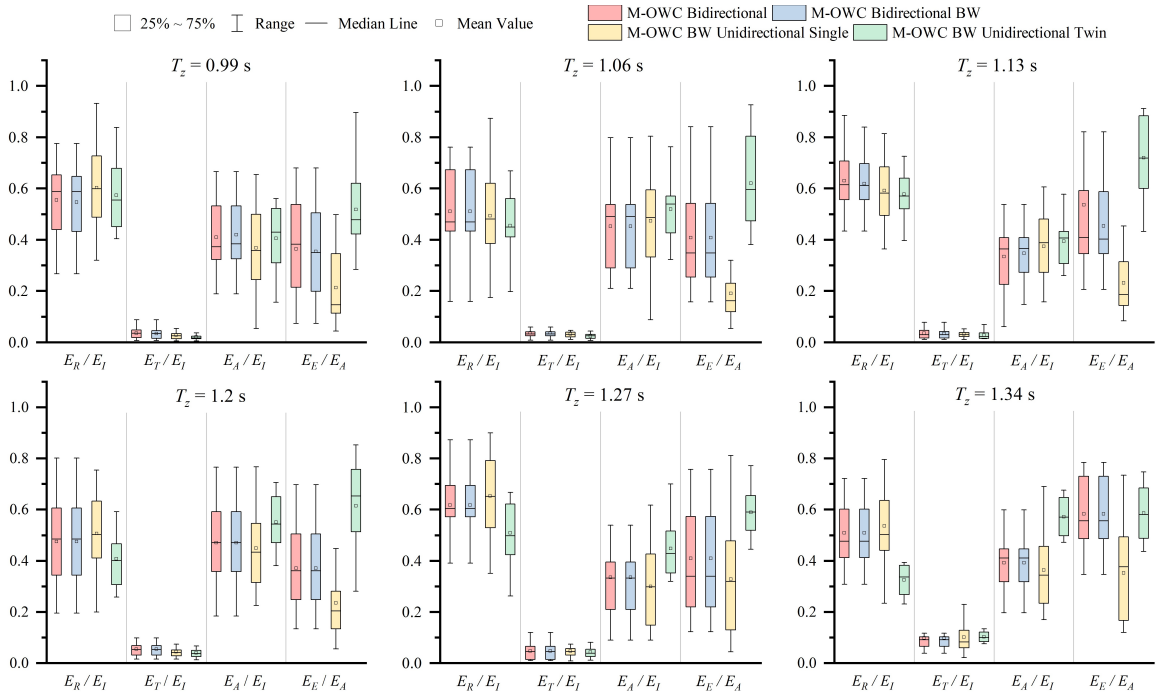


Figure 6.13: *Box and whisker plots showing energy balance ratios data in the form of the mean, median, 25% deviation range, minimum and maximum values for each irregular wave period $T_z = 0.99$–$1.34\,s$, and for the non-BW M-OWC and all three BW models (bidirectional and unidirectional)*

Conclusions

This chapter presents the findings of an investigation into different M-OWC models and their potential in breakwater applications. This work is part of a larger project that aims to determine this potential in recognising that large-scale integration projects such as M-OWC breakwater synergies are required in order to reduce the cost of wave energy and increase attractiveness with multi functionality. Therefore, this work is interested in the benefits of scaling up the OWC concept into an M-OWC that is not only integrated into a breakwater structure but aims to improve conversion efficiency by rectifying airflow for unidirectional turbine application.

The single unidirectional model is far from ideal due to the complexity of modelling such a system at the scale while attempting to maintain a level of simplicity with reactive mechanical horizontal one-way valves. Performance of the twin unidirectional model suffered fewer losses but both incurred pneumatic loss due to leakage of the

flap control valve and therefore adverse pressure drops across orifice plates. Lag of the flap valve also greatly affected performance since the wave period at small-scale results in a computation and reaction time that is relatively very small respect to larger scales and therefore affecting a greater proportion of the wave period.

Inclusion of a breakwater-like-blocking structure between OWCs proved to have little effect on the power extracted but caused a reduction in absorption with respect to the incident wave at steeper wave runs as reflection increased. Overall, the inclusion of the structure proved that the WEC is affective at absorbing and reflecting wave energy and minimising transmission – ticking the dual functionality aspect of the integration concept.

The conversion process between hydraulic and pneumatic power stages incurred significantly more loss than the wave to hydraulic process for the M-OWC bidirectional and twin unidirectional models. The twin model exhibits pneumatic conversion efficiency close to that of the bidirectional model. Proving the potential of a more optimised system of this style.

Valves in OWC WEC systems are often frowned upon due to their potential to add to unreliability, complexity and maintenance factors. However, due to the nature of airflow in M-OWCs, often mechanical valves are required to add some control, and as in the case of the twin setup, one is minimum.

With a unidirectional turbine of higher efficiencies, and potential to mechanically couple twin turbines, this could be a strong alternative, especially for M-OWCs. For an M-OWC, a twin turbine system still results in a lower number of turbines per OWC compared with OWC arrays as M-OWC like Mutriku. Hence, with a reduction of losses in a twin rectifying concept such as that tested in this paper, the consideration of a more efficient turbine could be used to gain and possible surpass the overall wave-to-wire efficiency of the WEC.

Chapter 7

Numerical Modelling of M-OWC Concepts

Introduction

Premise

Following the conclusions of the experimental work, there was an opportunity to focus on CFD modelling to support existing conclusions and expand on certain hypotheses. In the original proposal of this project, CFD was intended to be used, albeit for purposes of a higher TRL level i.e. for optimisation purposes of a well-established W2W WEC design with a validated model from the experimental data. Instead, the CFD research of this chapter is more investigatory with the intention to take a closer look at WEC operation and gain further understanding into the hydrodynamic phenomena observed in the experimental testing, answering the final question posed in the research aims of Chapter 1 (Phase 2 aim 6). Secondly, the W2W concept developed in this project has changed significantly from the original patent sketches and the experimental geometry was designed for modelling simplicity, hence the final concept will look different again following the next iteration of development, especially once optimised. These reasons led to the two different CFD models developed and presented in this chapter: the pneumatic system of the M-OWC bidirectional model

and the full Numerical Wave Tank (NWT) model, which include geometry of both the OWC array and the M-OWC models. The remainder of this chapter will detail the specific methodology of these two studies, design on models and their analyses and conclusions.

Numerical Code and Computing Resources

As covered in the literature review of Chapter 2, ANSYS Fluent® is a well-established commercial CFD solver for which LU has both research and HPC licenses. These licenses could therefore be used in conjunction with the High-End Computing server (HEC) at LU, which has more than 10,000 cores for parallel computing. These reasons shaped the decision to model using the modules of the ANSYS® package and Fluent® as a solver. The specific resources HEC used in this research are detailed in Table 7.1 with the average computational time recorded for each of the models and meshes, which is expressed as hours of computational 'clock' time per second of run/flow time.

	Pneumatic System Model		Numerical Wave Tank Model	
	Coarse	Fine	Coarse	Fine
Average Computation Time $[hr\ s^1]$	2.404	3.12	12.39	17.51
CPU	40-core Dell C6420: dual Intel(R) Xeon(R) Gold @ 2.40 GHz			
Memory	192G of 2666 MT/s DDR4			

Table 7.1: *The breakdown of computing resources utilised and average computing time for both numerical models developed and their respective coarse and fine grids*

Parallel computing was not used for any post-processing; a combination of ANSYS CFD-Post®, Paraview®, Matlab® and Origin Pro® were used throughout for analysis, visualisation and local data capture.

Design of CFD Models and Methodology

One particular numerical method known as Computation Fluid Dynamics (CFD) has over time become a very powerful tool owing to its high and ever-increasing fidelity and

decreasing computational cost due to the increasing of computing power with a lower price tag. Its use within engineering is rapidly growing and as the relevant models and methodologies improve through continual development, applications for the use of CFD grow, which includes wave energy converter modelling. The application of CFD methods in the wave energy field and the applicable theory is discussed in the literature review of Chapter 2. The overview of the methodology, i.e. how the tool was used, the resources used and the individual processes, is discussed here and in more detail in the relevant sections of Chapter 3 since the methodology varies between the simulations.

It is important to note that this research uses a commercial CFD code as a tool as opposed to developing specific CFD methods for this project and therefore only considers the relevant theory and methods applicable to the chosen software and solver.

Model Geometry and Numerical Grid

In wave energy applications, the model geometry includes two structures: the WEC and the bounds of the fluid domain, both which may include subdivisions of volume or surfaces. The domain is then divided into a mesh or grid of control volumes, which the solver will individually compute the fluid variables chosen to model. Hence, the generation of the grid can have significant effect on the solution causing errors, instability and inaccurate results. It is therefore crucial to first understand the nature of the flow to be captured and the modelling goals from the outset, that is, which phenomena is most crucial to capture for reliable results and ultimately model validation.

While mesh generation is largely automated with most tools, there still contains a considerable amount of work in controlling the tool to create a high quality mesh through use of different methods and settings for global and local mesh control. Not only should a mesh be refined in the correct areas but good quality must be obtained before pre-processing begins. The quality of a mesh can be determined through metrics such as cell skewness and orthogonal quality. As with most tools, the options for 3D elements that can be specified in different zones include: tetrahedral, hexahedral,

polyhedral, and pyramid [213].

Solver, Computational Resources and Post-processing

The resources of LU meant that the ANSYS® software package was available with research licenses and additional High-Performance Computing (HPC) licenses for parallel computing. The ANSYS® package includes all necessary setup modules for geometry modelling and mesh/numerical grid generation as well as post-processing modules. Two CFD solvers applicable to wave energy applications are integrated into the package and Fluent® was deemed most appropriate and therefore used throughout. The solver is given the model geometry and mesh information in order to begin the pre-processing, which is the setup of the solver to prescribe the physics of the model, boundary conditions, numerical schemes and solution monitoring. Once the solver has been run for the specified number of iterations and timesteps, the solution data is written to a data file (or multiple files for transient simulations), which essentially stores each variable for each cell or vertex of the mesh. Additional data files can also be set up for either solution monitoring or specific data extraction e.g. at certain time intervals, locations or user defined variables.

In order to read the formatted output data files, post-processing software is required. This software usually imports the case (domain and mesh information) and offers a wide range of data visualisation options for rendering as well as extracting data from specific points, lines and zones in the domain. This project used a combination of ANSYS CFD-Post® and Paraview® for data visualisation and local data capture, Matlab® for additional data processing and Origin Pro® for further data visualisation and graph plotting.

Verification and Validation

The results of CFD simulations should be heavily scrutinised or else are deemed completely worthless. This is because a CFD simulation, especially if not setup correctly with extreme care can yield arbitrary results and give hopeful users the results they

are looking for.

Before one can take confidence in results the solution must be first verified and validated. Verification is answering the question: have the partial differential equations been solved correctly. This requires determining whether the solver has reached an acceptable level of solution accuracy. The convergence of particular variables over iterations in conjunction with sufficient reduction in discretisation errors is a common measure of this. The definition of these errors from a numerical perspective are discussed in Section 2 of Chapter 2 [246].

Validation of the results is ultimately answering the question: have the correct modelling choices been made i.e. the correct equations, time step, discretisation schemes, boundary conditions. Validation, unlike verification is nothing to do with the CFD code and it's ability to yield results that can be validated, but the user inputs. Ultimately, confidence in validation can be achieved with empirical modelling but is often too complex and therefore most appropriately achieved by matching with experimental results. Most CFD simulations in research applications should have an experimental counterpart on which the model is based and therefore the results should reflect [246].

In accordance with the good practise laid out in this methodology for the use of CFD, this research has always endeavoured to verify and validate numerical models developed as revealed in the relevant sections.

Pneumatic System Model

The modelling the pneumatic system in isolation was carried out following the initial difficulties in validating the entire NWT model. The full NWT model poses challenges with respect to verification and validation with the number of effects and phenomena required to model in order to match all results for wave generation, absorption, reflection, and OWC hydrodynamic response and the output pneumatic power of the modelled PTO. In some cases, one could neglect the need to match some of these results and therefore focus on a particular area e.g. OWC hydrodynamic response. As opposed to disregarding the pneumatic system entirely given the validation chal-

lenges, the system was modelled in isolation in order to individually validate and analyse its behaviour.

Additionally, a second pneumatic geometry was simulated to study the changes in performance between the manifold system that was created during experimental testing with pipes, and a common duct system, which is a minor and inquisitive step toward optimisation and preferred structural design. Hence, the ducted variation is a step closer toward the original W2W WEC concept shape and is ultimately where the W2W directors prefer to end up. As previously mentioned, the manifold system was a by-product of the progression of the project and served its purpose. However, it is important to understand the performance induced by any changes to the geometry in the intermediate section of the pneumatic system will have, which is the section most subject to change given the rudimentary manifold piping adopted in the experiments. Furthermore, as the number of OWCs increases once the concept is scaled further, it is important to understand what direction the change should take to converge the flow from all OWCs.

Model Setup

Aside from the method used and detailed in the following subsections, two other modelling approaches were trialled for this analysis, which included dynamic meshing. The dynamic mesh approach was used to model the movement of the free-surface as recorded in the experiments with a moving wall acting as a piston. This was achieved using two different types of dynamic meshing methods: a standard re-meshing method and an overset mesh method. The former re-meshes the entire region that the wall/piston is oscillating within each timestep, while the overset mesh method does not require remeshing but instead alters the intersecting interface between a background mesh and the dynamic overset mesh each time step. Both of these approaches to representing the free-surface as a moving piston resulted in significantly more computational cost, although less so with the overset method.

The chosen approach was to prescribe dynamic time dependent pressure inlet boundaries on the underside of the OWCs. Thus, rather than using the time history

of the ILGs from the experiments to represent the moving free-surface, the internal OWC air pressure was used, which further simplified to the simulation.

Geometry, Mesh and Boundary Conditions

The geometry of the M-OWC bidirectional model is identical to the physical WEC model of the experiments (Figure 3.15)with a slightly shorter internal depth of the OWCs, disregarding the draft of the OWC (Figure 7.1). Crucially, all dimensions of the physical model were included in the CFD geometry in order to ensure all flow characteristics are captured.

The ducted geometry replaces the piped manifold with an enclosure placed on top of the OWCs with the orifice situated at the end of the structure (Figure 7.1). The lids of the individual OWCs retain the large inlet/outlet hole for this iteration. Without modelling the hydrodynamics of the OWC, any changes to damping will not be captured in the performance of the pneumatic system. Therefore, in order to have reliable results the crucial dimensions are kept constant: the OWC dimensions and the orifice diameter.

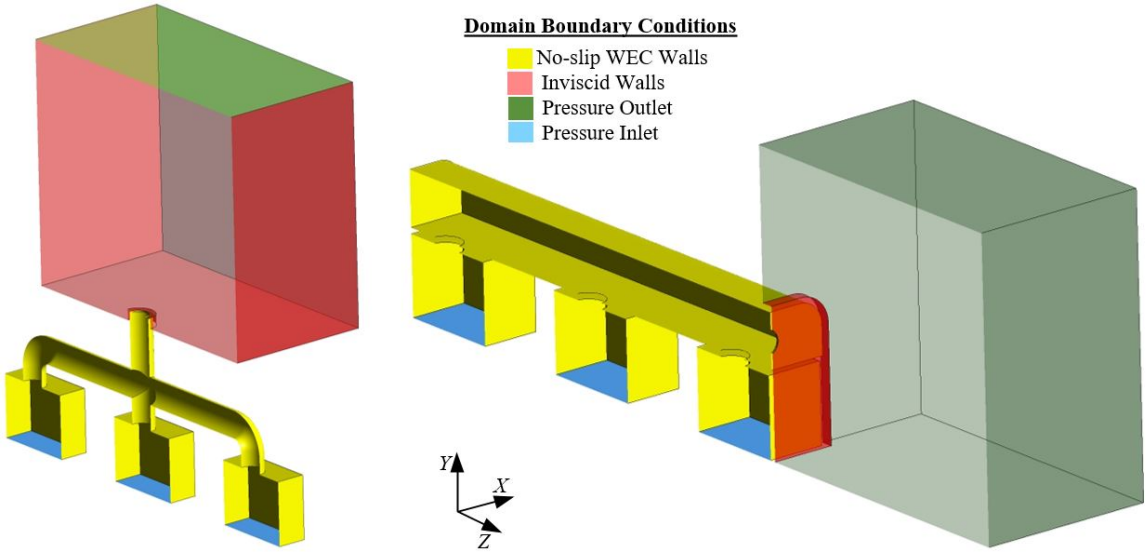


Figure 7.1: *Sliced view through the YZ plane of the domain and geometry of the M-OWC bidirectional (left) and ducted variation (right) pneumatic system models with labelled boundary conditions*

Figures 7.2 and 7.3 show the cross section of the mesh in the YZ plane to illustrate

the structure of the mesh for the experimental bidirectional and ducted variation models, respectively.

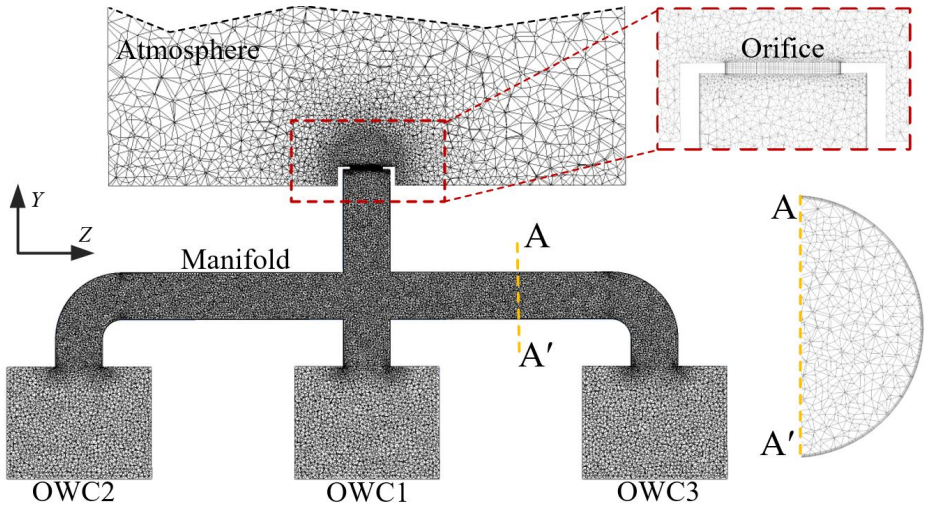


Figure 7.2: *Cross section slice (YZ plane) of the numerical mesh of the M-OWC bidirectional model with a focused window of the mesh structure around the orifice and a cross sectional focus of the mesh at the manifold wall*

The mesh was generated with unstructured tetrahedral elements in the majority of the volume, which grow from regions of increased refinement. These regions are the no-slip walls of the manifold/duct and the orifice plate region, which is the only region meshed with structured hexahedral. The no-slip walls of the manifold and the orifice region, as highlighted in Figure 7.1, are lined with compressed structured triangular prisms known as inflation layers, which grow at a rate by 20% at each of the 10 layers. The first layer height from the no-slip wall is known as the Y_{wall} value. These Y_{wall} settings were estimated based on the nature of the flow using Equations 2.18 - 2.20, and later reduced in the generation of the fine mesh to confirm a mesh independent solution. The Y_{wall} values and total element counts are listed in Table 7.2 for the coarse and fine meshes for both the standard bidirectional and ducted variation models. The fine mesh contains $\sim 75\%$ more elements due to this increase refinement in the inflation layer and the other regions of the mesh which are refined to the same level proportionally. The coarse mesh grows in element count between the experimentally based M-OWC bidirectional and duct model namely due to the additional volume of the duct.

	Experimental M-OWC Bidirectional Model		Duct Model
	Coarse	Fine	Coarse
Y_{wall}	5×10^{-5}	2.5×10^{-5}	5×10^{-5}
Total Elements	2,504,580	4,384,197	3,207,462

Table 7.2: *Metrics and dimensions used for Coarse and Fine meshes of the pneumatic system models: M-OWC Bidirectional and ducted concepts*

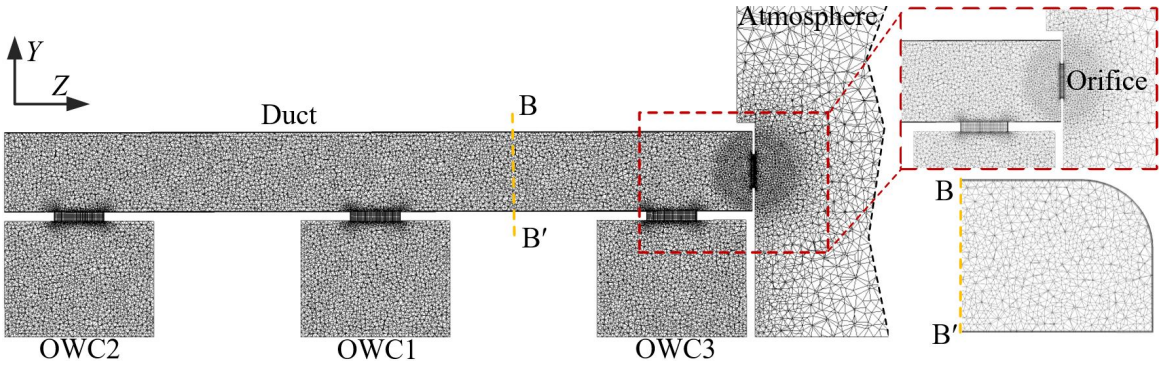


Figure 7.3: *Cross section slice (YZ plane) of the numerical mesh of the M-OWC bidirectional ducted variation model with a focus window of the mesh structure around the orifice and a cross sectional focus of the mesh at the duct wall*

Numerical Models and Schemes

The viscous turbulence RANS model selected for this case was the $k-\omega\,SST$ for its strength in modelling near wall turbulent flow for full boundary layer resolution and also detached turbulent flow, more specifically applicable in the larger duct model and the atmospheric region. The solution scheme used was the SIMPLEC algorithm with second order upwind accuracy for pressure, momentum and turbulence variables. The solution time step was kept constant at $\Delta t = 0.004\,s$ due to matching the pressure sample rate of the OWCs in the experiments. Although this was not necessary from a computational perspective (solver stability or expense wise), this meant that that raw data from the experiments could be used with no filtering or smoothing. No temporal independence test was carried out with this model since the selected time step was sufficiently small and increasing it wasn't deemed necessary based on computation time. Further general operating conditions included in the model setup are atmospheric pressure $(101,325\,Pa)$ and gravity in the negative Y direction.

Full Numerical Wave Tank Model

Geometry, Mesh and Boundary Conditions

The domain of the 3D NWT model was dimensioned to match the LUREG wave tank internal dimensions exactly (Figures 3.12), excluding gaps in the floor at either end of the tank that exist for tidal flume operation. Likewise, the relevant WEC models used in the NWT simulations match their counterparts detailed in the experimental chapters (Figures 3.13 and 3.15, Table 3.5). Simulations are run for the OWC array, the M-OWC bidirectional model and its breakwater variation.

Since all WEC types tested from the experimental modelling to be included in the NWT simulations are symmetrical, this meant that the domain size could actually be halved. This is made possible by using a symmetry plane which assumes all flow is symmetrical and therefore allows the solution to be reflected about the declared plane. This plane and the other boundary conditions can be found in the domain illustration of Figure 7.4. A velocity inlet, which will be discussed in the following subsection is found at the front of the domain ($X = 0$) in place of the wave paddles. All walls of the tank, including the floor, one side wall and the back wall are all considered as inviscid walls. This decision was made based on the level of refinement required to model no-slip boundaries and the mesh quality and computational cost this would compromise. Furthermore, although the walls of the WEC are modelled as no-slip walls, the mesh in contact with them externally is not refined because changes in performance is suspected to be dependent on the general hydrodynamics of the wave and internal hydrodynamics rather than viscous effects of no-slip walls, which cover a relatively small area. Finally, the upper boundary was prescribed as a pressure outlet set to $0\,Pa$ gauge pressure with a domain operating pressure of $101,325\,Pa$.

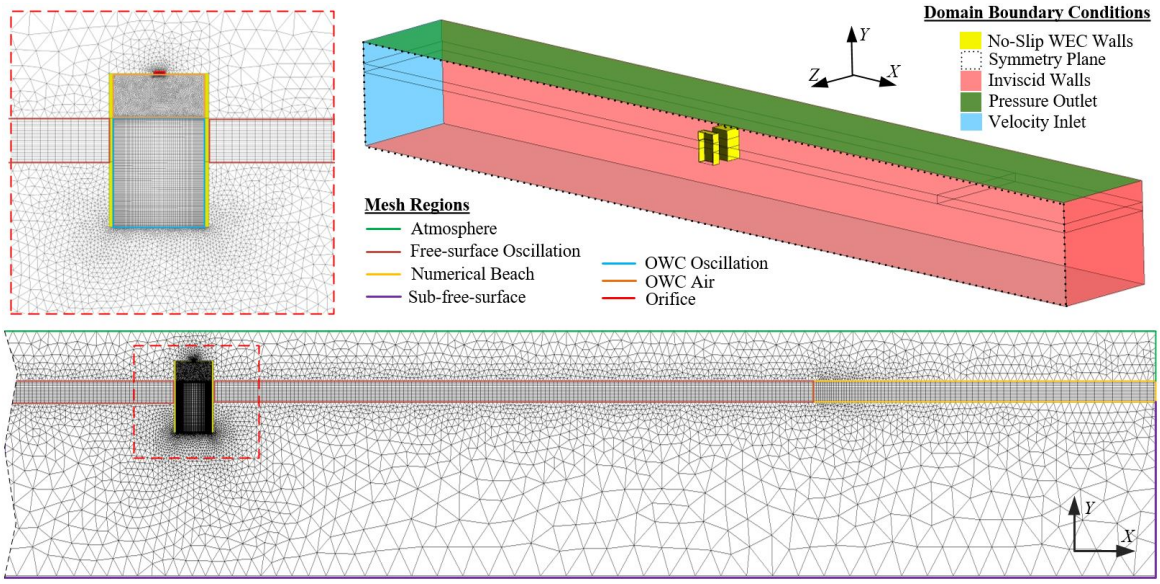


Figure 7.4: *Entire domain of NWT model with the geometry of the OWCs, a cross sectional sample of the mesh along the domain length and a focus window on the mesh around the WEC. Cell zones and each boundary condition labelled as surfaces in the 3D image and lines in the 2D cross sections*

The domain was split into seven mesh regions or cell zones, primarily in order to better control mesh sizing and refinement (see highlighted in Figure 7.4). To most precisely and accurately model the position of the free-surface, cell zones within the region of possible free surface movement are meshed with structured hexahedral elements, which includes the free-surface oscillation strip, the internal OWC water region and the numerical beach zone. The region of possible free surface movement is defined as any region within $Y = \pm 0.75H$ where the Mean Water Level is set to $Y = 0$. It is these structured elements, namely the free-surface strip that were used to characterise the level of refine used for the fine and coarse meshes. Refinement levels between meshes was not only changed between coarse and fine meshes but also between waves since each mesh was created with a Cells Per Wavelength (CPW) and Cells Per Height (CPH) value, which defines the node spacing or element size in the X and Y direction respectively. The ratio between CPW and CPH is defined by the wave steepness. These values for fine and coarse meshes can be seen in Table 7.3 with the example of the wave run of $f_{wave} = 0.88\,Hz$ and $H = 0.08\,m$ used to calculate the relevant element sizing and total element count. This method also allows a consistent

	Coarse	Fine
CPW	75	100
CPH	11	20
$\Delta x_{Element}$	0.0236	0.0177
$\Delta y_{Element}$	0.0073	0.004
$\Delta z_{Element}$	0.0354	0.0266
$\Delta y_{InternalElement}$	0.0075	0.005
Total Elements	3,777,156	4,983,166

Table 7.3: *Metrics and dimensions used for Coarse and Fine meshes of the Numerical Wave Tank simulations including the OWC array and M-OWC Bidirectional geometries*

Property	Phase 1	Phase 2
Fluid	Air	Water
Density, ρ (const.)	1.225	998.2
Dynamic Viscosity μ	1.789×10^{-5}	1×10^{-3}

Table 7.4: *Fluid properties for primary and secondary phases in the NWT simulations*

level of refinement to be create across meshes for different wave runs.

The sub-free-surface cell zone and atmosphere zone contain unstructured tetrahedral mesh elements with nodes conformal to those at the intersecting cell zone interfaces. The automatic mesh algorithm is set to be sensitive to areas of increase refinement and restricts the rate of element growth from those areas to 20%. Refinement levels in the air only cell zones of the WECs in the NWT model, the orifice and OWC air zones, exactly match those detailed in the pneumatic modelling section of this chapter and contain structured and unstructured elements, respectively.

For an open channel simulation, the model requires the setting of the floor (at $Y = -0.9\,m$) and the Still Water Level (SWL) or MWL (at $Y = 0\,m$) to patch the regions of the two phases. The primary and secondary phases with the properties listed in Table 7.4 are air and water, respectively.

Wave Generation and Absorption

As mentioned in the literature review of Chapter 2, there are a few different methods of wave generation and absorption in NWT models, the plausibility of which may

vary depending on the solver used. In the early part of this research project, two additional methods of wave generation were trialled with a 2D NWT, which were the implementation of a User Defined Function to prescribe orbital velocities at the velocity inlet and a dynamic paddle. The former was deemed no more beneficial over the eventually adopted method, and the paddle approach proved to be too computationally expensive and problematic for little to know benefit aside from modelling the experimental wave tank more accurately in a physical sense.

In recent years, ANSYS Fluent® has increased become increasingly more capable at modelling surface gravity waves with the open channel flow. These waves are generated with the specified wave theory model at the velocity inlet boundary by prescribing the transient free surface profile and orbital velocities beneath the free surface (Eqs. 2.6 and 2.7). With the additional consideration of restoring forces by allowing phase interaction with surface tension coefficient constant at 0.0731 and gravity in the negative Y direction, the wave should then propagate through the domain from the inlet boundary.

Following various wave generation tests and the comparison of the wave profile generated in the tank for the same wave run, the non-linear 3^{rd} order Stokes Wave model was used. An example comparison of the theoretical, experimental and CFD generated wave profiles are compared in Figure 7.5 for an example wave of height $H = 0.08\,m$. It was determined that the 3^{rd} Order Stokes wave, although not perfectly matching the experimental wave, generated the nearest wave profile in the NWT with respect to face steepness and matched peak amplitudes. Trough amplitudes proved difficult to match across all the test waves generated. The wave generation process could have been tuned better using the various constants available in Fluent® or even altering the input heights or get better agreement. As discussed in the literature review, sometimes this is necessary to match the experimentally recorded profiles better [216].

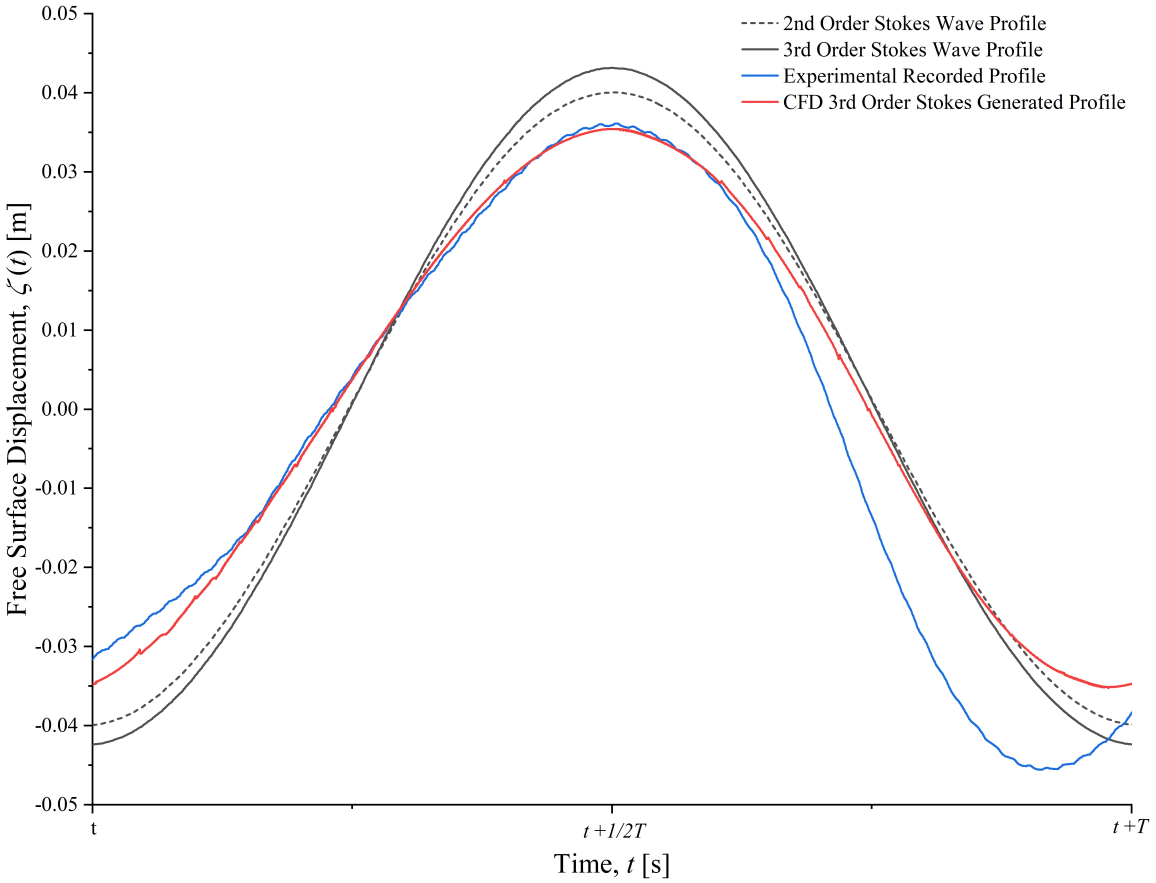


Figure 7.5: *Comparison of transient free surface displacement caused by wave generation at the position of WG_1 in the NWT domain and experimental tank with theoretical wave profiles over time for 2nd and 3rd order stokes waves*

Wave generation is by far the costliest aspect to NWT simulations. To illustrate the simulation time required to successfully generate a wave, the transient generation and propagation has been captured at intervals of one wave period with the contours of Figure 7.6 and 7.7, which show free surface elevation from above in the ZX plane and velocity magnitude on the symmetry plane (YX plane), respectively. As can be expected based on these plots, significant hydrodynamic interaction with the OWC is only noticeable at $t \approx 10T$. Cautiously, to save computational cost, the domain of a new simulation starting at $t = 0$ could be initialised with the data of a suitable run of $t = 3T$. Of course, this is only possible for the same wave and model setup and ensuring the wave inlet is at the correct phase.

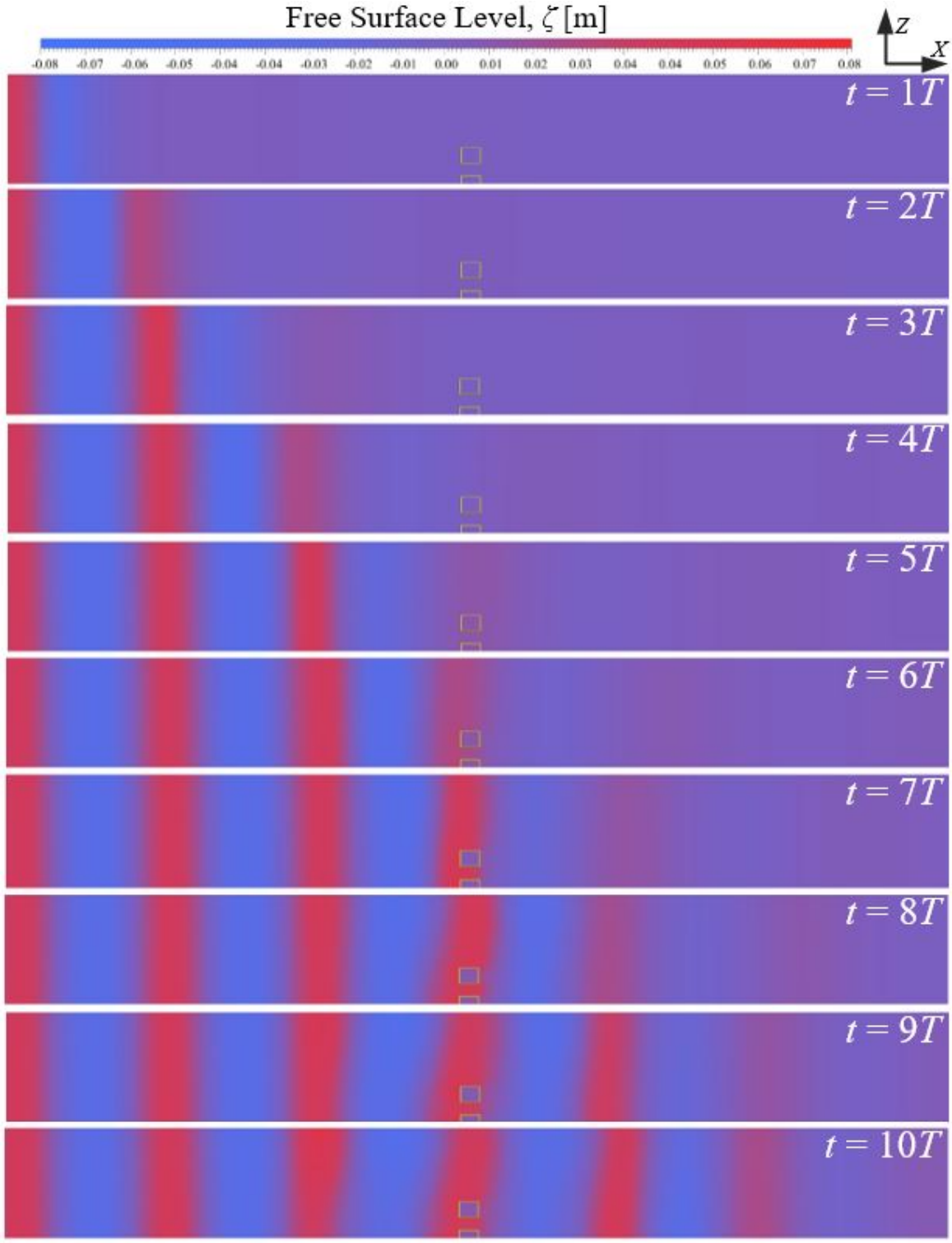


Figure 7.6: *Contours of free surface elevation from birds-eye-view (XZ Plane) in sequence to illustrate transient wave generation process over first 10 periods for a representative frequency of* $f_{wave} = 0.94\,Hz$ *and wave height of* $H_{wave} = 0.08\,m$

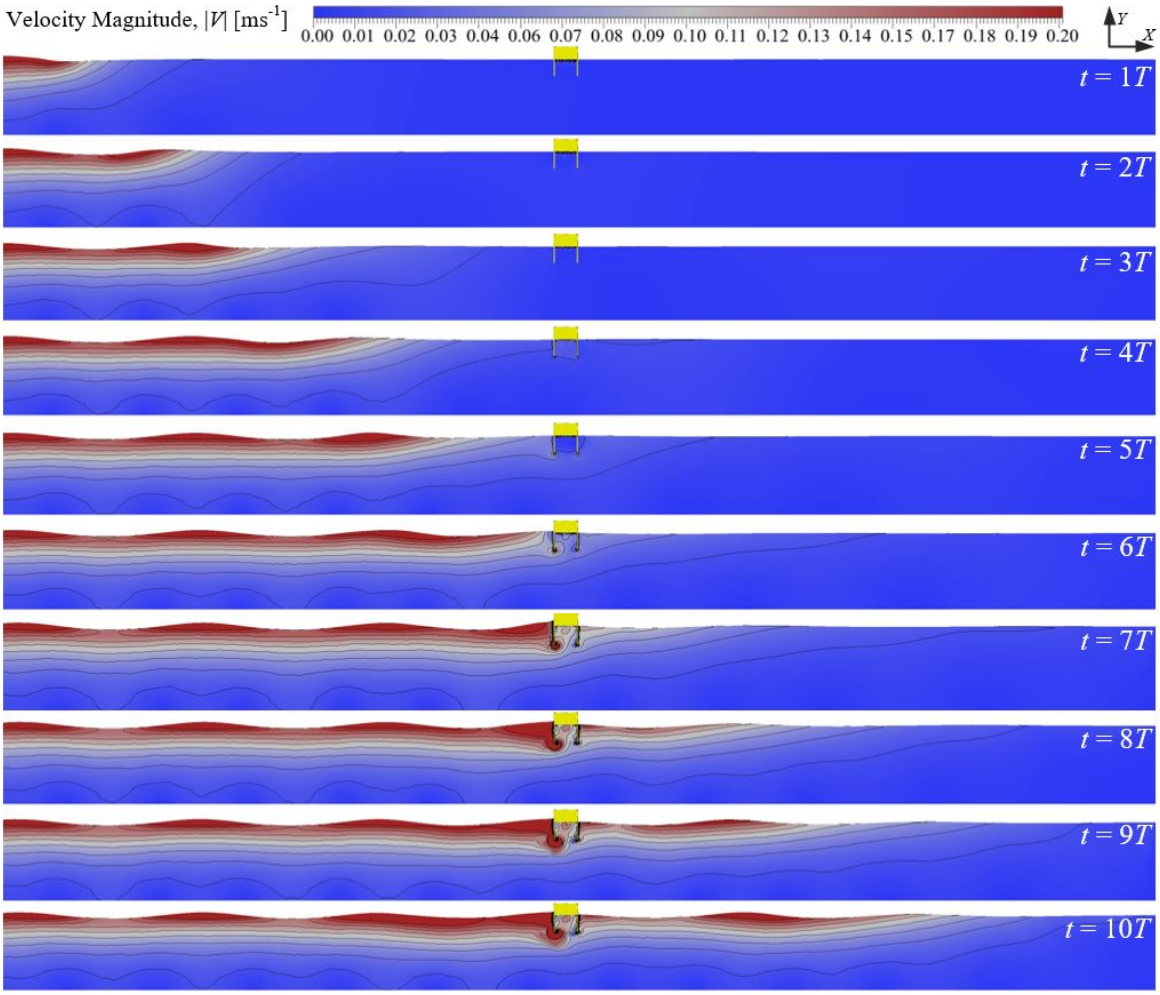


Figure 7.7: *Contours of velocity magnitude from symmetry plane view (XY Plane) in sequence to illustrate transient wave generation process over first 10 periods for a representative frequency of* $f_{wave} = 0.94\,Hz$ *and wave height of* $H_{wave} = 0.08\,m$

As with the mesh beach in the experimental wave tank, the numerical beach is prescribed within the counterpart numerical beach zone highlighted in Figure 7.4 and the region of the sub-free-surface directly below this zone where $9 < X < 11$. This is where the source term of Equation 2.23 is added to dissipate the energy of the wave. The mesh in numerical beach cell zone is permitted to grow with respect to $\Delta x_{Element}$ as X increases toward the back wall to aid in dissipating the wave.

Numerical Methods and Discretisation Schemes

Turbulence model $K-\omega\,SST$, a 2 equation model was selected for the same reasons of those mentioned in the pneumatic system model. The open channel explicit VOF

model coupled with the level-set function enabled due to its increased ability to track a complex interface in cases of 2 phase flow with higher accuracy. This comes with an added computational cost due to an additional transport equation but improves the overall solver stability and the benefits of a higher resolution free-surface, especially inside the OWC, outweighs the cost [213].

The Pressure Implicit with Splitting of Operators (PISO) algorithm was used with second order accuracy for momentum and turbulence variables, Geo-Reconstruct method for Volume Fraction and PRESTO! for pressure.

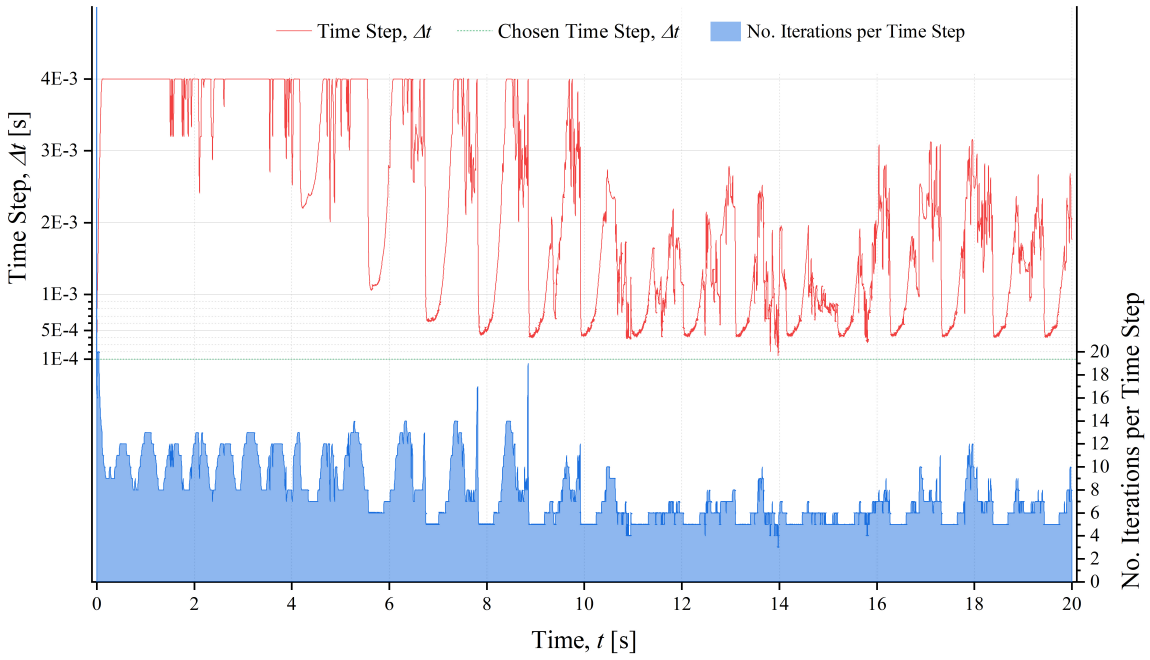


Figure 7.8: *Example of the transient adaptation of the solver time step during test simulation using the adaptive time step method and the iterations per time step to reach residual criteria*

As opposed to carrying out a time independence study, the variable time step method was used to determine a suitable timestep. This method uses the CFL condition (Eq. 2.21) in order to adjust the time step size after each step has converged to the residual criteria of $\leq 10^{-4}$. The variable method is run for a full test simulation with the limit of $CFL \leq 1$, allowing the solver to vary the time step size from a minimum of $\Delta t = 10^{-6}\,s$ to a maximum timestep of $\Delta t = 0.004\,s$. Figure 7.8 shows how the time step was adapted throughout the course of the 20 second test simulation

and the iterations taken to reach the residual criteria. Throughout all tests, the time step varies significantly, hence the difficulty in determining a suitable timestep using conventional methods. In this case, the minimum time step reached was $\Delta t = 10^{-4}\,s$. Following further tests, this time step was determined most suitable to sustain a stable calculation throughout all wave runs and WEC geometries.

Pneumatic Model Simulations Results and Analysis

Mesh Independence and Validation

Due to the oscillatory nature, and not necessarily periodic nature of the transient pressure prescribed at the inlet boundaries, one of the few methods for determining a solution was the sufficient reduction in residual errors. The reports the residuals each iteration and the criteria for the solver to advance a time step is the reduction of the residuals to $\leq 10^{-4}$.

Another major key step in the solution verification process is the mesh independence test. This requires the generation of sequentially finer meshes to justify that a chosen level of refinement, (usually referred to as 'coarse') is sufficiently refined to capture the flow. Hence, the solution should not drastically change with additional refinement. Very applicable to this case in guaranteeing there is sufficient refinement is ensuring that a $Y^+ = 1$ (Eq. 2.18) is achieved on the no-slip walls of the model in order to accurately capture the effects of the boundary layer as discussed in Chapter 2. Although the fast oscillatory nature of the airflow may not allow for the attachment of the boundary layer in such a small time period, this would be most important at the orifice where the flow velocity is accelerating and reaches its highest velocity, which means the boundary layer is at its thinnest. Hence, the mesh refinement should be sufficient enough to ensure the viscous sublayer of the boundary layer is fully resolved and therefore the solution is nearest to the physical experiments. In Figure 7.9, for both the coarse and fine grids for wave $f_{wave} = 0.88\,Hz$ and $H = 0.08\,m$, the Y^+ data is plotted, which has been extracted from the entire orifice inner wall and circumferential line sliced halfway along the orifice wall. An average and the full range of Y^+

values are plotted over time to illustrate the variation in the boundary layer thickness throughout the wave period as the flow rate changes.

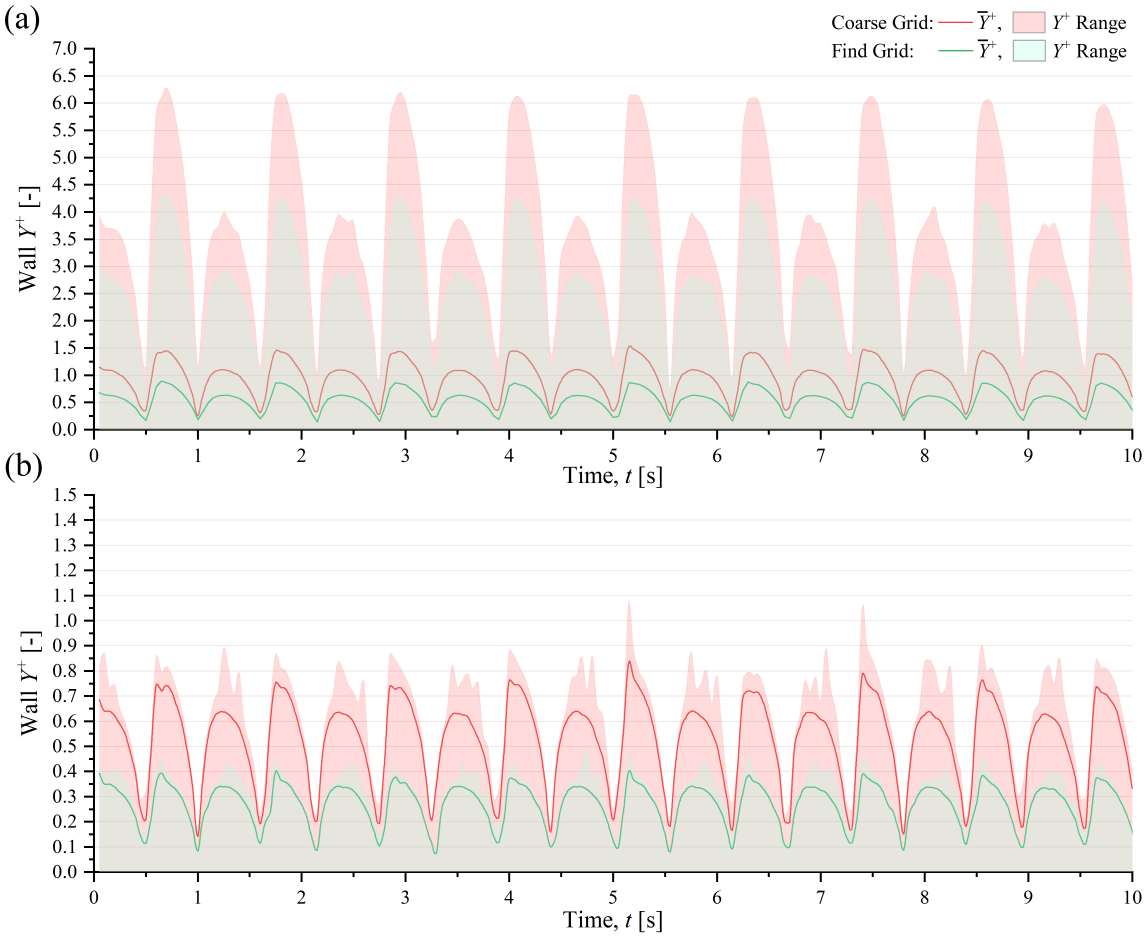


Figure 7.9: *Pneumatic bidirectional model average and range of Y+ values across the entire orifice wall (a) and along central line around the circumference of the orifice wall (b) for coarse and fine grids*

The surface plot of Figure 7.9 shows a larger range than the line plot, namely due to the leading (upstream) edges of the orifice plate and the unsteadiness created. Despite this, the average is still < 1.5. It is recommended that a maximum of $Y^+ < 5$ is sufficient. The line plot shows a Y^+ well below 1 for both the range and the average. Despite the additional refinement of the Y_{wall} in the fine mesh, (Table 7.2), the range and average does not significantly reduce for the surface plot to justify the level of additional refinement. The level of refinement is deemed sufficient for boundary layer resolution, especially given the low range and average of the line plot ($Y^+ < 1$).

Furthermore, this provides evidence of sufficient solution accuracy in the region most important with respect to the pneumatic power measurements by which the model is validated.

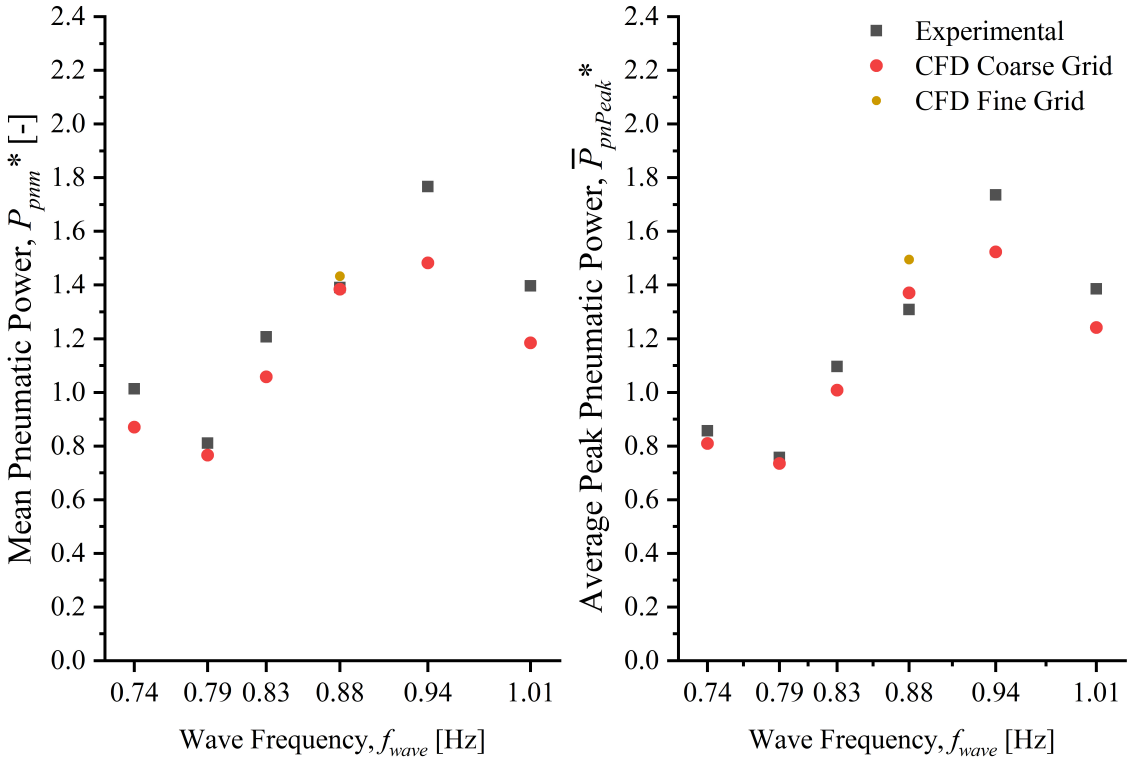


Figure 7.10: *Mean (left) and average peak (right) pneumatic power plots for the pneumatic bidirectional model validation comparison between experimental and CFD results for both coarse and fine grids for the frequency range* $f_{wave} = 0.74$–$1.01\,Hz$ *and wave height of* $H_{wave} = 0.08\,m$

The assessment of the Y^+ data above is reflected in grid comparison plot of Figure 7.10, where there is no closer agreement to the experimental results from the fine grid. The coarse grid in some cases agrees very closely with the experimental results for values of mean and average peak power but does not match the entire set of results exactly. Where results do not match, which is at the higher frequencies, the model provides a good approximation and matches the shape of the response through the frequency range. Once more, with the current numerical method, the fine grid does not provide a closer solution, hence, to increase agreement with experimental results, potentially more computationally expensive turbulence modelling would be required.

It is also important to note that the grid refinement process was done considering only one wave, where $f_{wave} = 0.88\,Hz$, which shows the closest agreement.

Pneumatic CFD Model Comparison

The ducted model simulations were run for the same waves and values of mean power and average peak power are compared with the original manifold geometry M-OWC in Figure 7.11. The ducted model is clearly less efficient but displays a similar trend throughout the frequency range.

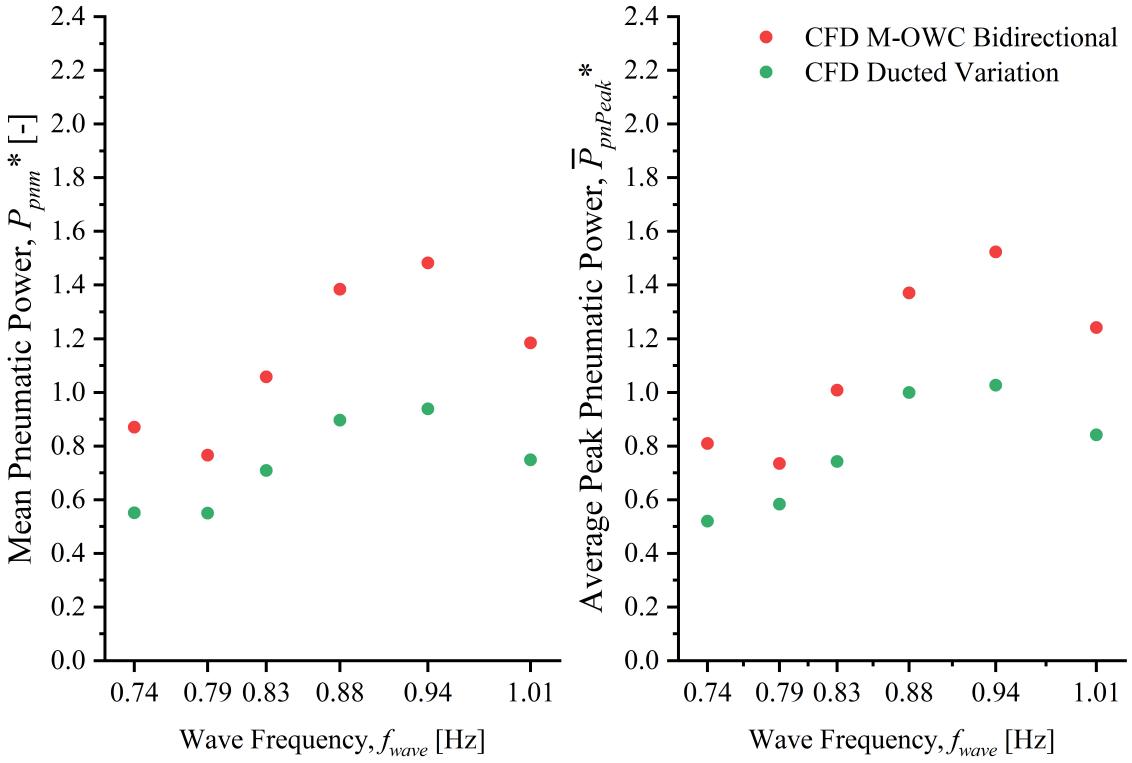


Figure 7.11: *Mean (left) and average peak (right) pneumatic power plot comparison between CFD results of the M-OWC bidirectional model and ducted variation for the frequency range* $f_{wave} = 0.74$–$1.01\,Hz$ *and wave height of* $H_{wave} = 0.08\,m$

One of the greatest benefits of CFD solutions is the ability to read many different variables at every cell face or point in the domain. For wave run $f_{wave} = 0.88\,Hz$ and $H = 0.08\,m$, Figure 7.12 shows contours of the normalised velocity magnitude, $|\vec{V}^*|$ and arrows of velocity vectors for the exhale and inhale processes for both simulated models. Exhalation and inhalation processes can be clearly identified here by the

acceleration of air downstream of the orifice and the contour colouring shows the path of the air along with the vectors. For the manifold model, during exhale, it can be seen that each OWC chamber exhausts and contributes toward the airflow at the converging joint upstream of the orifice. This is not the case with the ducted model as the pressure increase in OWC nearest the orifice causes an exhale that works against the exhale of the outer two OWCs. While a strong exhale at the orifice is still produced with the resource of this closest OWC, the outer OWCs are left to equalise as flow circulates within the duct.

During the inhale process, the manifold model shows a big flaw that was unobservable during experiments. With a clear, unhindered path from the orifice to the centre OWC it is not clear that the outer OWCs inhale much at all. The high velocity toward the centre OWC and therefore reduction in pressure causes a suction at the manifold junction resulting in a very small exhale from the outer OWCs. The ducted model does not suffer from this as the pressure gradient into a larger volume causes the duct to fill with each OWC inhaling to varying degrees. The furthest OWC benefits the most with a more direct path for the flow from the duct and the main inhale stream. Whereas the nearest OWC to the orifice almost begins to suffer the same fate as the outer OWCs of the manifold model due to the high velocities of the inhale through the orifice being situated nearer to the OWCs inlet/outlet.

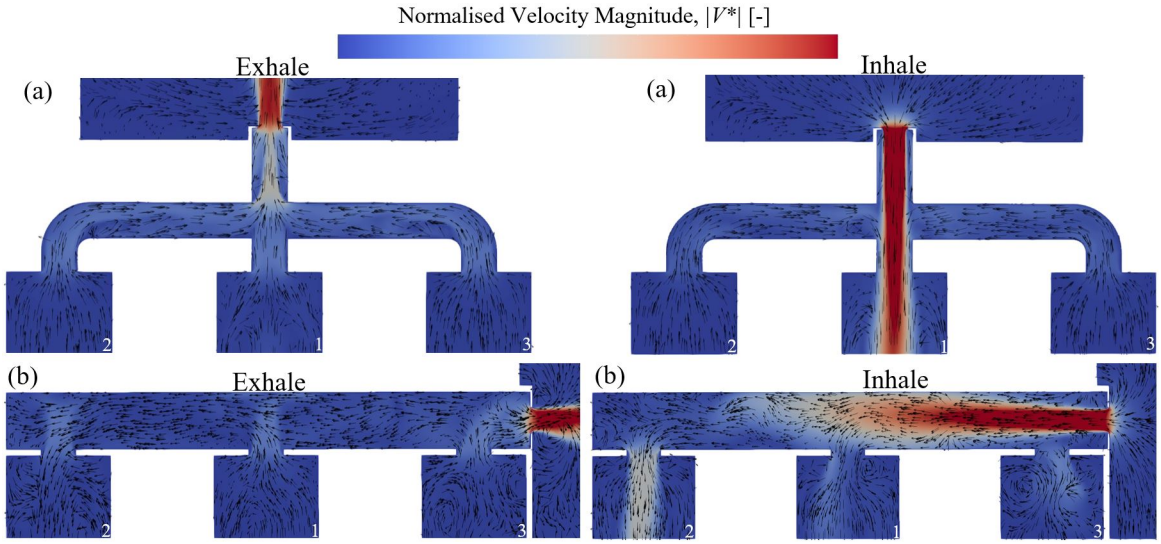


Figure 7.12: *Comparison of velocity magnitude contours and vectors in the YZ plane between CFD results of the M-OWC bidirectional model (a) and ducted variation (b) for exhale and inhale processes for a representative frequency of* $f_{wave} = 0.94\,Hz$ *and wave height of* $H_{wave} = 0.08\,m$

Contours of turbulent viscosity in Figure 7.13 for the same simulation, models and time steps help to reinforce the points made thus far. Arguably the most ideal process is the exhale of the manifold model where flow remains fairly steady. The inhale process sees a lot more unsteadiness due to the flow rate entering into the centre OWC from the atmosphere through the orifice and the entrained flow from the outer OWCs causing circulation and turbulent flow inside the chamber.

The ducted model shows a little unsteadiness in the exhalation process as the duct volume fills with exhausting flow from the first OWC (closest to the orifice), partially from the centre OWC, which creates circulation due to poor exhaustion out through the orifice. Inhalation sees a great level of unsteadiness as the duct fills from the atmosphere and each OWC inhales. The acceleration of the air from the restriction of the orifice into the middle of the duct then results in circulation and unsteadiness as the air is drawn into the individual OWCs.

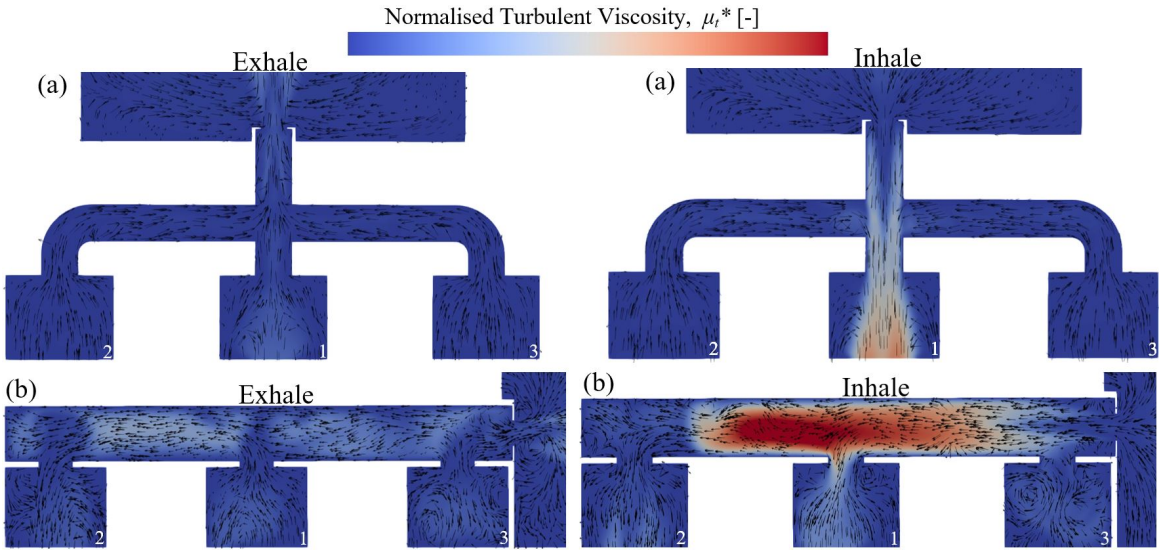


Figure 7.13: *Comparison of turbulent viscosity contours and velocity vectors in the YZ plane between CFD results of the M-OWC bidirectional model (a) and ducted variation (b) for exhale and inhale processes for a representative frequency of* $f_{wave} = 0.94\,Hz$ *and wave height of* $H_{wave} = 0.08\,m$

From these contour plots it is easy to see that flow of the air entering and leaving each OWC through the inlet/outlet restriction is key to the performance of the whole system. This can be looked at in more detail with the plot of Figure 7.14, where the Y velocity component (V_Y) profile is plotted from a line in the YZ plane positioned horizontally through the centre of the inlet/outlet hole of both OWC3s. The $X-axis$ of the graph of Figure 7.14 represents the is the position along the $Z-axis$, where the value is normalised by the length of the line, and therefore the diameter of the hole. Note that values of normalised velocity have been normalised with respect to their own individual ranges, hence the individual profiles and change magnitude relative to their maximums are of interest as opposed to cross comparing absolute magnitudes. These OWCs are considered of most interest in this analysis due to their more unexpected behaviour noted in the contour plots above.

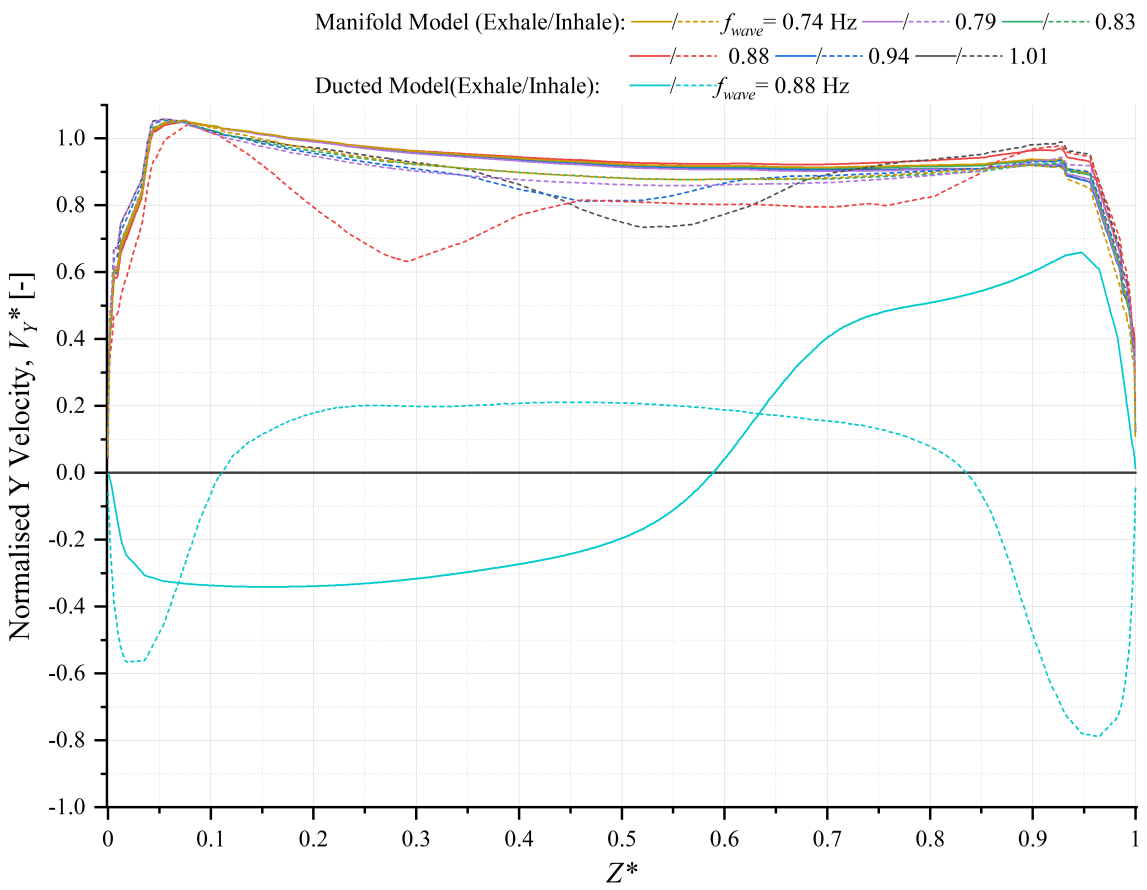


Figure 7.14: *Comparison of velocity magnitude profiles at OWC2 outlet for exhale and inhale processes for constant wave height of $H_{wave} = 0.08\,m$ and frequency range $f_{wave} = 0.74$–$1.01\,Hz$ for the M-OWC Bidirectional model and a representative frequency $f_{wave} = 0.88\,Hz$ for the ducted variation model*

The edges of all profiles start from $V_Y \simeq 0$ due to the no-slip boundary condition that requires air velocity at the wall to equal zero. The manifold model displays a consistent exhale profiles, as was expected from the contour plots, and what is expected with from a pressure drop profile induced by air passing through a circular restriction. The exhale process of the ducted model however appears to be a mix between an exhale and inhale. The inhale of OWC3 in the ducted model appeared to be stronger but experiences an adverse pressure drop in the centre of the, which causes the flow to reverse leaving the majority of the inhale volume flowing on the outer section of the hole. The inhale process of the outer OWCs in the symmetrical manifold model display a more pitiful inhale as discussed, which is further highlighted with a positive velocity profile suggesting an exhale with the slightest more unsteadiness and

deformity.

As flow is induced by a pressure gradient, it is helpful to look at the pressure profile along the path of the air. Figure 7.15 displays the pressure profile along a straight vertical line in the YZ plane positioned in the centre of OWC3, starting at the lower most point of the OWC and ending at the upper most point in the domain along that line (dissecting the WEC wall). Since the starting point begins what is essentially the pressure inlet of OWC3, the static pressure values are normalised with respect to the value at this point. Hence, the profiles are again individually normalised and are comparable only with respect to shape and relative change. The coordinates are plotted on the $Y - axis$ and are normalised with respect to the length of the line.

Using the exhale process of the manifold model as a good example, the pressure drops with the increase of Y as the path is headed into the manifold and the pressure builds from the bottom of the OWC at the pressure inlet boundary. This profile is a desirable as a large pressure drop is created in the exhale direction through the OWC outlet but is then compromised by the bend in the manifold piping inducing losses as would be expected. The exhale profile of the ducted model shows a similar shape but sees a much larger increase in pressure as the line approached the top of the ducting. The inhale process for the ducting model displays a large range in pressure compared to the manifold model. This pressure drop is created in the correct direction but the line dissects the high velocity region found in the duct volume, which affects its ability to inhale. As seen above, the manifold model is actually exhaling from these outer OWCs, which can be seen in the pressure profile where there the pressure drop is minimal and reversed in the inlet hole region during inhale.

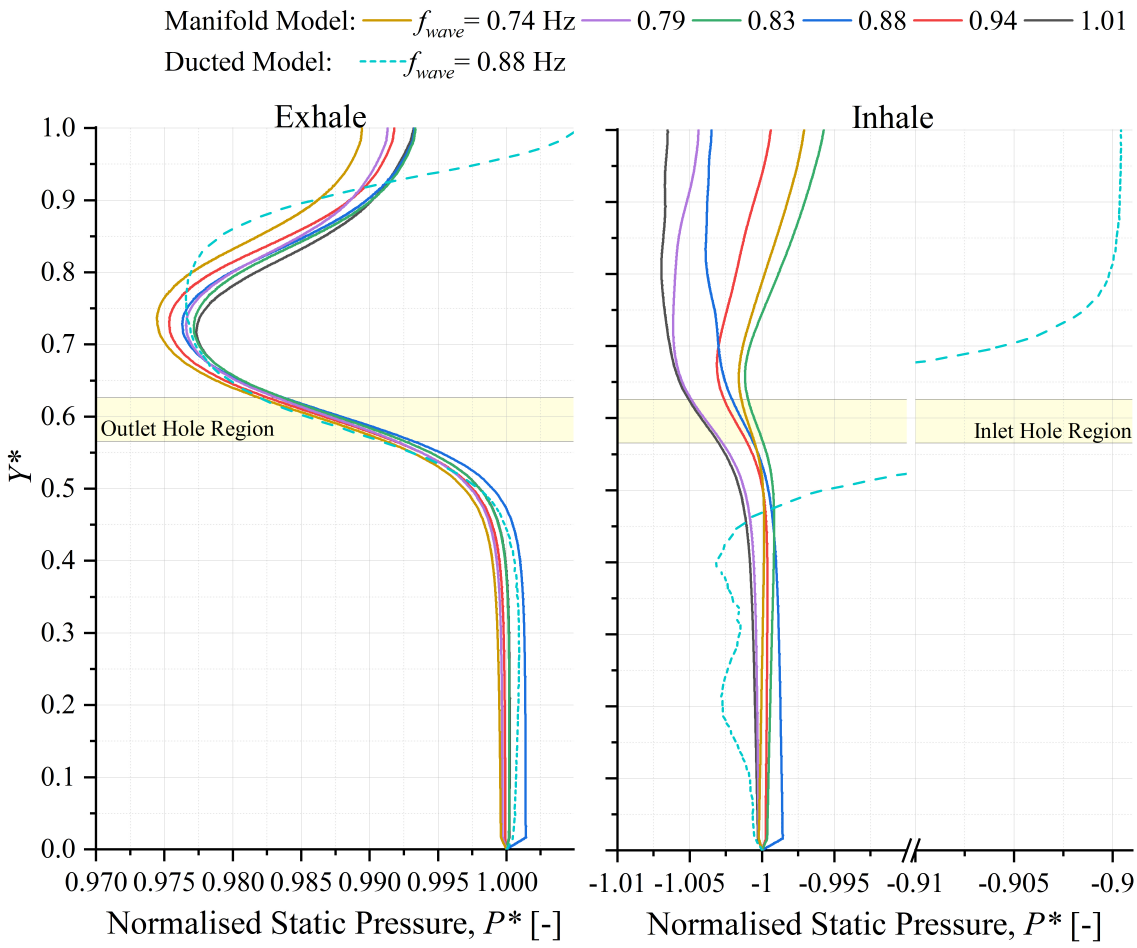


Figure 7.15: *Comparison of static pressure profiles along a vertical line through the height of OWC2 and into the manifold/duct for exhale (left) and inhale (right) processes for constant wave height of $H_{wave} = 0.08\,m$ and frequency range $f_{wave} = 0.74$–$1.01\,Hz$ for the M-OWC Bidirectional model and a representative frequency $f_{wave} = 0.88\,Hz$ for the ducted variation model*

Numerical Wave Tank Results and Analysis

Verification and Validation

Solution verification in the case of the NWT is determined with the sufficient reduction of the residual errors as mentioned above, and also applicable for this case is reaching sufficiently small periodicity error. Since the wave regimes used in these NWT simulations are regular, a periodic solution should develop as seen in the experimental results. Using Equation 7.1, the Periodicity Error of variable x, $(PE_x\%)$

	OWC Array Coarse Grid			OWC Array Fine Grid	M-OWC Coarse Grid	M-OWC BW Coarse Grid
Spacing, a	0.5	1	1.5	1	1	1
Flow PE, $PE_Q\%$	0.04	2.78	0.05	0.35	0.13	1.17
Pressure PE, $PE_p\%$	0.06	0.05	0.08	0.89	0.22	0.27

Table 7.5: *All periodicity errors calculated for OWC orifice flow and orifice pressure for NWT simulations*

is calculated between the full final and penultimate wave periods.

$$PE_x\% = \frac{\sqrt{\frac{\sum_i^N (x_i^{Final} - x_i^{Final-1})^2}{N}}}{|\overline{x^{Final}}|} \times 100\% \tag{7.1}$$

For instances such as the array models where pressure and flow are not combined at a single orifice section, the variables are combined for this calculation:

$$x_{iCombined} = x_{iOWC1} + x_{iOWC2} \tag{7.2}$$

These errors are collated in Table 7.5 for all models ran in the NWT simulations and their coarse and fine grids.

Best case and worst case examples of the final and penultimate periods are plotted in Figure 7.16, for the normalised variable of orifice flow rate, Q_i^*. Also plotted is the difference between the final period value and its penultimate period counterpart to more easily visualise the difference. The best and worst cases have errors of 0.04% and 2.78%, respectively. The plot illustrates that the worst case of periodicity error is visually an acceptable fit and can be considered a periodic solution. Generally, a periodicity error of $PE_x\% \leq 5\%$ is acceptable in verifying a periodic solution.

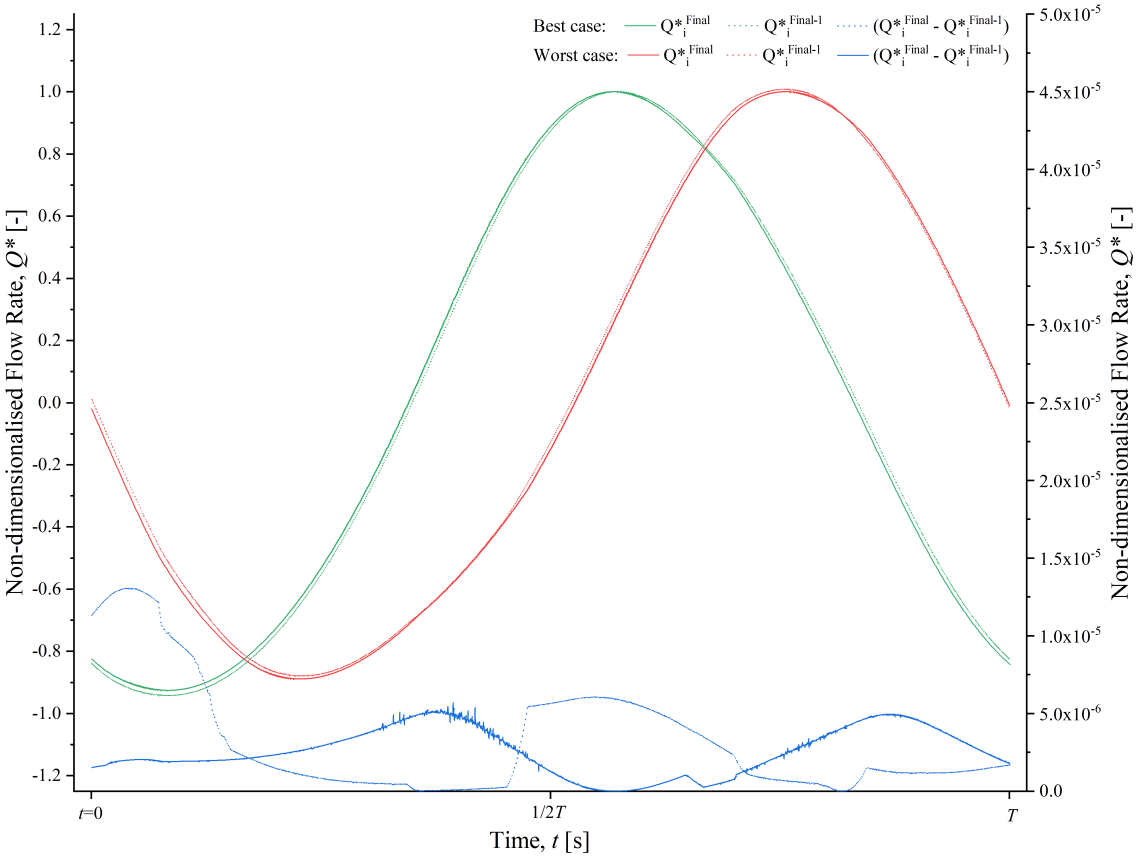


Figure 7.16: *Example plots of final and penultimate periods for normalised orifice flow rate illustrating the best and worst cases of periodicity error*

With respect to solution validation, results of the CFD simulations and the experimental tests for the OWC array with three different chamber spacings are compared in Figure 7.17 with variables of mean power and average peak pneumatic power. Additionally, comparison of internal and external free surface RAOs are plotted in Figure 7.18. These are for one wave run where $f_{wave} = 0.88\,Hz$ and $H = 0.08\,m$. Only certain values show agreement with the majority of values showing a fair difference. However, in most cases the trends across the three different chamber spacings is agreeable, especially between $a = 0.5$ and $a = 1$, which is the difference that was most important to capture in order to study the increase in power resource that comes with the increase in spacing.

For the peak power values of Figure 7.17 the fine mesh results are included, which show good agreement with the coarse mesh results. This gives confidence that solution

can be considered as being independent of additional refinement at this chamber spacing, which is of greatest interest, and the coarse mesh was therefore used for the remainder of the cases.

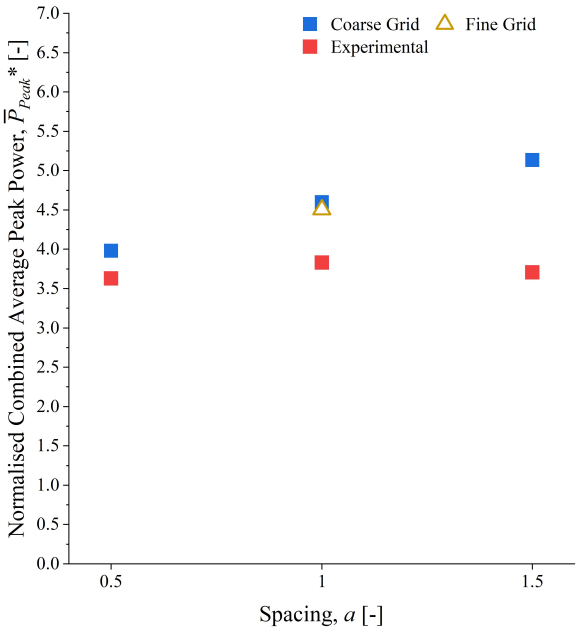


Figure 7.17: *Mean power comparison between CFD and experimental results for the OWC array for chamber spacings* $a = 0.5$, 1 *and* 1.5, *for a representative wave frequency of* $f_{wave} = 0.88\,Hz$ *and wave height* $H_{wave} = 0.08\,m$

The plotted RAOs in Figure 7.18 show much less agreement in terms of magnitude, however again the trends match between $a = 0.5$ and $a = 1$ for the ILGs. In general it appears that CFD over predicts incident wave height at WG_3 and under predicts at all gauges at the WEC both internal and external. This difficulty in matching the hydrodynamics of the NWT with the experimental tank is what led to the decision to model the pneumatic systems of the M-OWC bidirectional model in isolation.

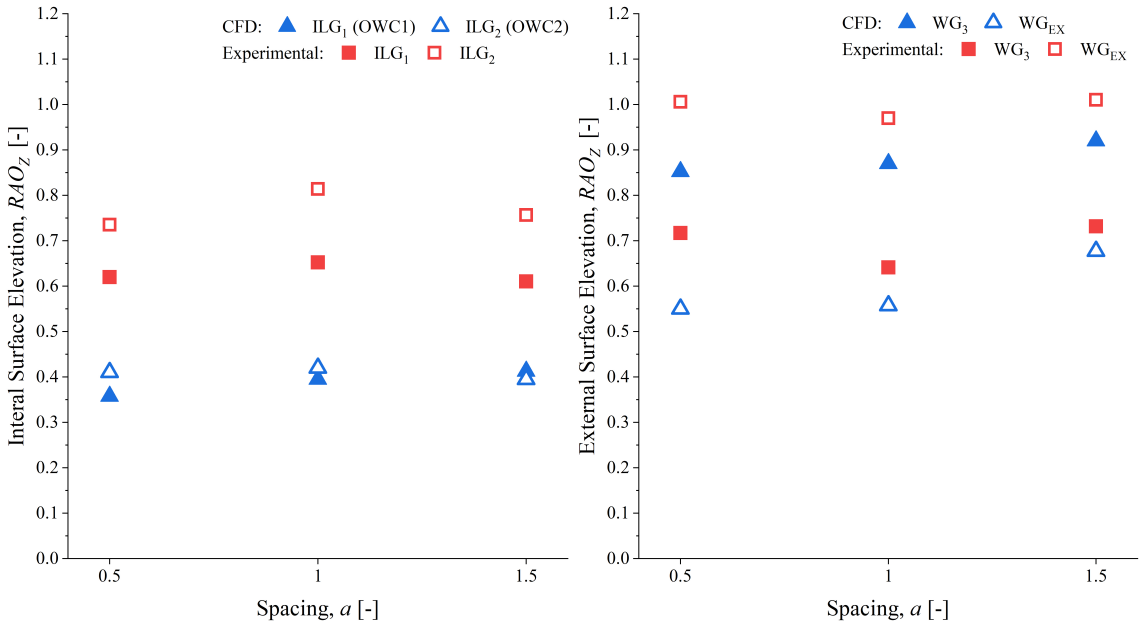


Figure 7.18: *Comparison of CFD and experimental results for Internal and external RAOs for the OWC array for chamber spacings* $a = 0.5,\ 1$ *and* 1.5*, for a representative wave frequency of* $f_{wave} = 0.88\,Hz$ *and wave height* $H_{wave} = 0.08\,m$

The same underprediction in terms of pneumatic power is evident in the simulations of the M-OWC and M-OWC breakwater (Figure 7.19). The spacing of OWCs was not altered for these models as closer agreement could not be found. The original intention of the analysis was to study the changes caused by increasing chamber spacing. Although the results of the OWC array simulations do not match experimental values perfectly, the expected trend and behaviour means that some level of qualitative analysis be carried out.

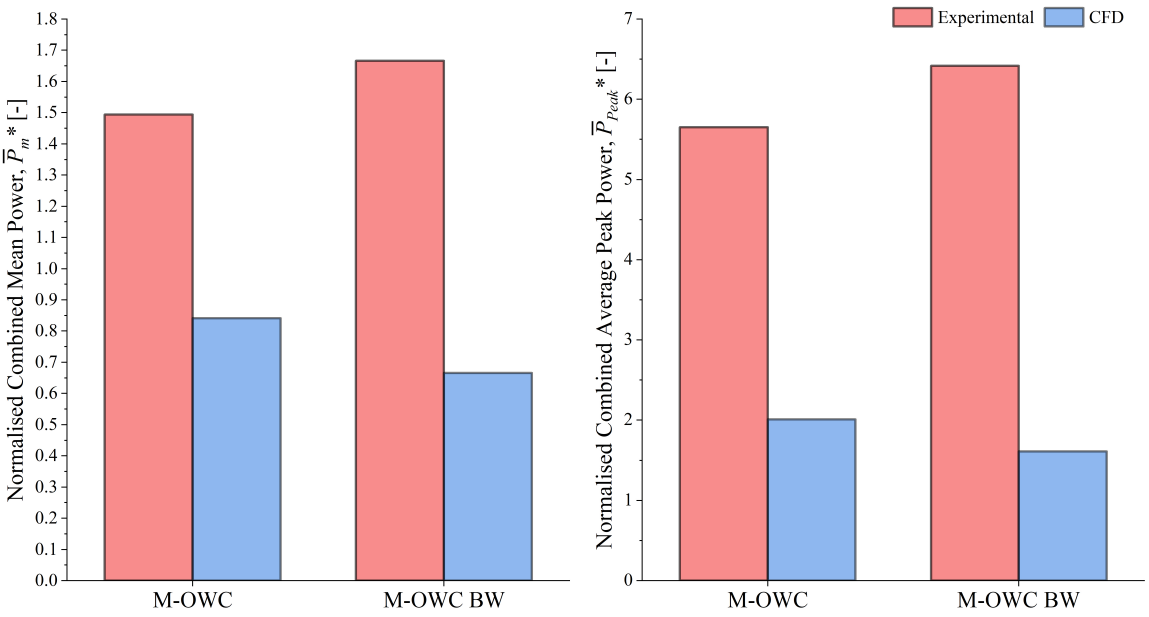


Figure 7.19: *Mean and Average Peak Power comparison between CFD and experimental results for the M-OWC bidirectional model and breakwater variation for a representative wave frequency of* $f_{wave} = 0.88\,Hz$ *and wave height* $H_{wave} = 0.08\,m$

Model Comparison

During experimental testing, it was suspected that the closer proximity of the OWC chambers in all M-OWC models made a difference to the phase of the responses from the centre (OWC1) and outer OWCs (OWC2 and 3). From literature, it is also known that phase lag can be induced with over damping [220]. In Figure 7.20, phase lag, ϕ_L is expressed as time lag, t_L for the array and M-OWC simulations and compared to the experiments. The phase difference in this case is calculated by the relative time difference between peak responses of the relevant OWCs and the external level gauge, WG_{EX} (or WG_4). On the left of Figure 7.20, the phase lag is compared for the three different chamber spacings. In general, the values show close agreement especially at $a = 1$, however the main differences are noticeable in the opposite trends at $a = 0.5$.

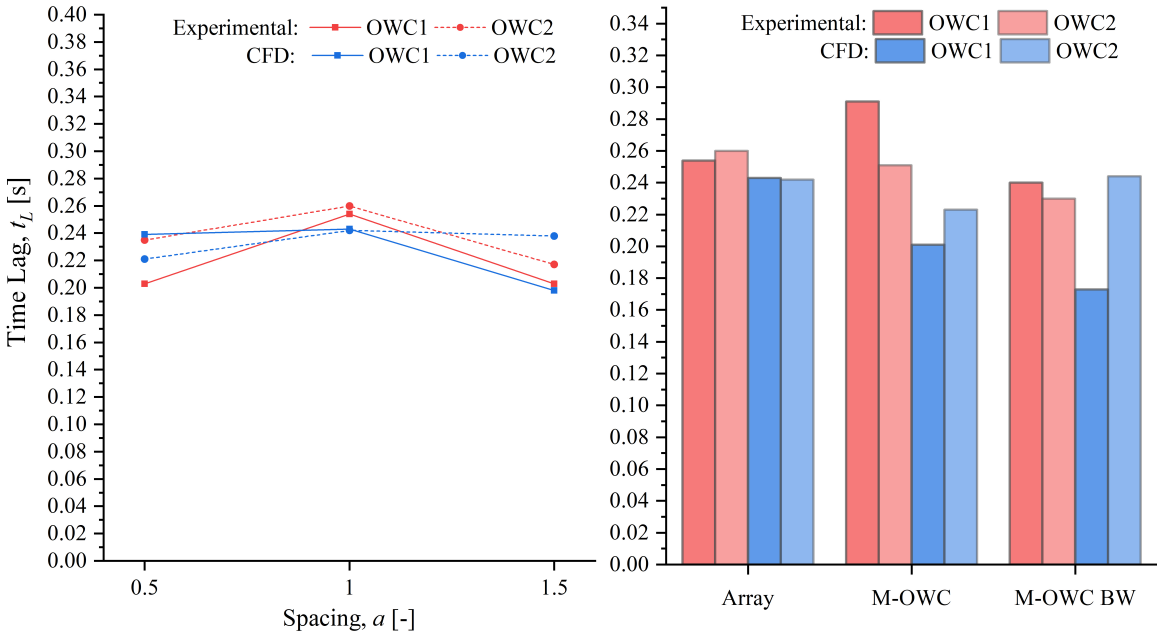


Figure 7.20: *Experimental and CFD computed time lag between external gauge WG_{EX} and IGLs for OWC1 and OWC2 for chamber spacings $a = 0.5$, 1 and 1.5 for the array simulations only(left) and for all three simulated models (right)*

The M-OWC models in the right of Figure 7.20 are results of models fixed at a spacing of $a = 1$, and therefore represent a similar under prediction to the Array model. Based on both experimental and CFD results, phase lag between the OWCs is at its minimum when $a = 1$, which yields the higher performance. The trends of the centre and outer OWCs then diverge in conflicting trends but the overall evidence points toward the greater lag found in the outer OWCs, which would be expected.

In Figure 7.21, an example time series of the internal ILG_1 and external WG_{EX} are plotted to illustrate the typical phase lag between the responses. Marked on the plot are four positions considered to be points of interest for the following analysis. Firstly, these include the maximum and minimum peaks of the external WG_{EX} response, which are labelled as phase values $\phi_{EX} = \pi/2$ and $\phi_{EX} = 3\pi/2$, respectively. These points are where the greatest potential energy is stored either in the internal or external wave. The other two points are the points in time at which this is inverted, where external and internal surfaces cross, which is arguably the peak acceleration pints of the internal OWC. Thes are labelled $\phi_{EX} = \pi$ for the ascending internal level with descending external level and $\phi_{EX} = 2\pi$ for the opposite case. Note that these

latter two labels given are not an accurate position of the phase of the wave, but serve as a useful reference to the points at which those levels cross from herein.

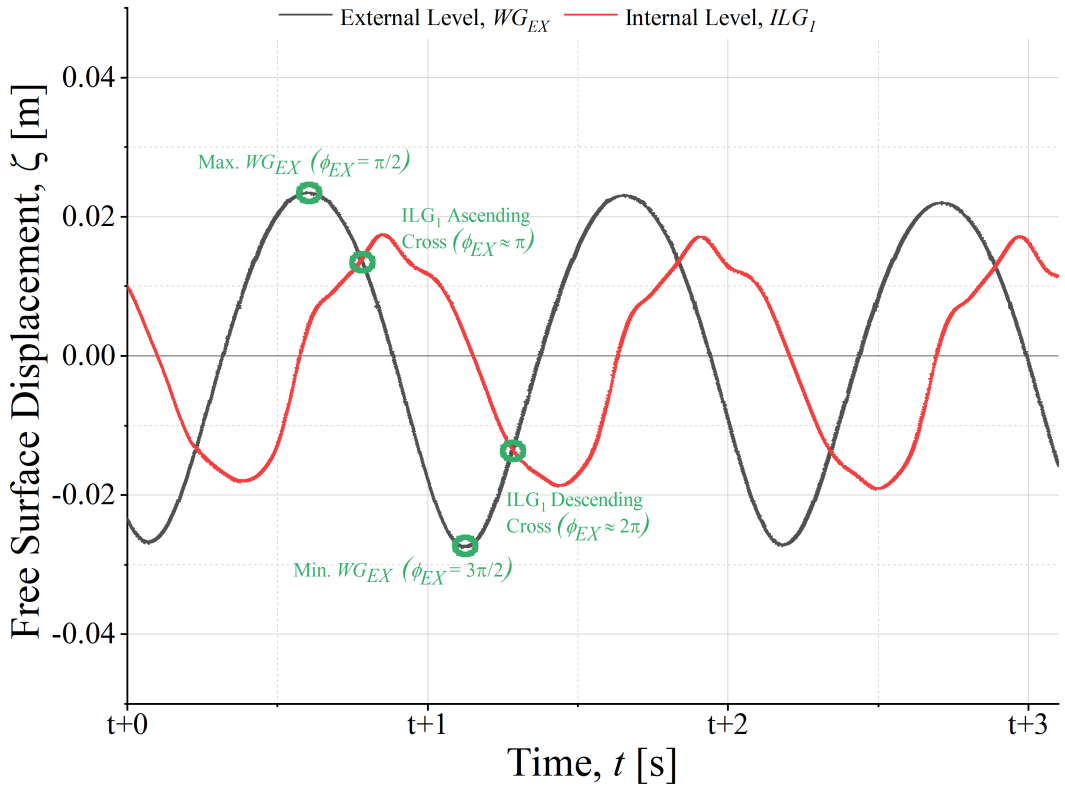


Figure 7.21: *Example plot of the external and internal level time histories with labels of points that are relevant to the following analysis*

The first plot that refers to the phase points declared above is the array of velocity magnitude contours and planar velocity vector plots in Figure 7.22 for the OWC array for the three chamber spacings. The plots are arranged left to right in order of occurrence as referenced in Figure 7.21. These contours are taken from a YZ plane positioned on the centre line of the OWC chamber. Using the velocity vectors arrows, it is helpful to see the division of energy beneath the wave across the spacings for $\phi_{EX} = \pi/2$ and the bulb-like shape that is created below each OWC. This bulb appears to overlap, especially in the smaller spacings in between the OWCs, whereas the width of this is much more visible on the outside of the outer OWC.

At point $\phi_{EX} = \pi$, the main process is noticeable as the external free surface

descends and fills in around the walls of the OWC as it rises. By the time the external level reaches its minimum level ($\phi_{EX} = 3\pi/2$), as the internal level is descending by then, the flow around the OWC walls is reversed. Interestingly, either the section of water in between the OWCs is slightly ahead in phase, and/or the descension of the internal water column is causing it to rise ahead of the external wave. This effect reduces with spacing as indicated not only by the magnitude of the velocity in this gap but also the direction since when $a = 1.5$ the magnitude and direction of the velocity matches the rest the external wave across the width of the tank. Conversely, for $a = 1.5$ and for the opposite process i.e. maximum external displacement ($\phi_{EX} = \pi/2$), the water between the OWCs is again ahead of the rest of the external, potentially due to resource from the wave being absorbed by the wider spread OWCs. For the smaller spacings, especially for $a = 0$, the water in the gap seems to behave like an additional OWC heaving between the inward facing walls of the WEC OWCs. At the phase point of $\phi_{WG5} = 2\pi$, again at the smaller spacing, the fluid is heaving ahead of the external wave and noticeably quicker than the larger spacings.

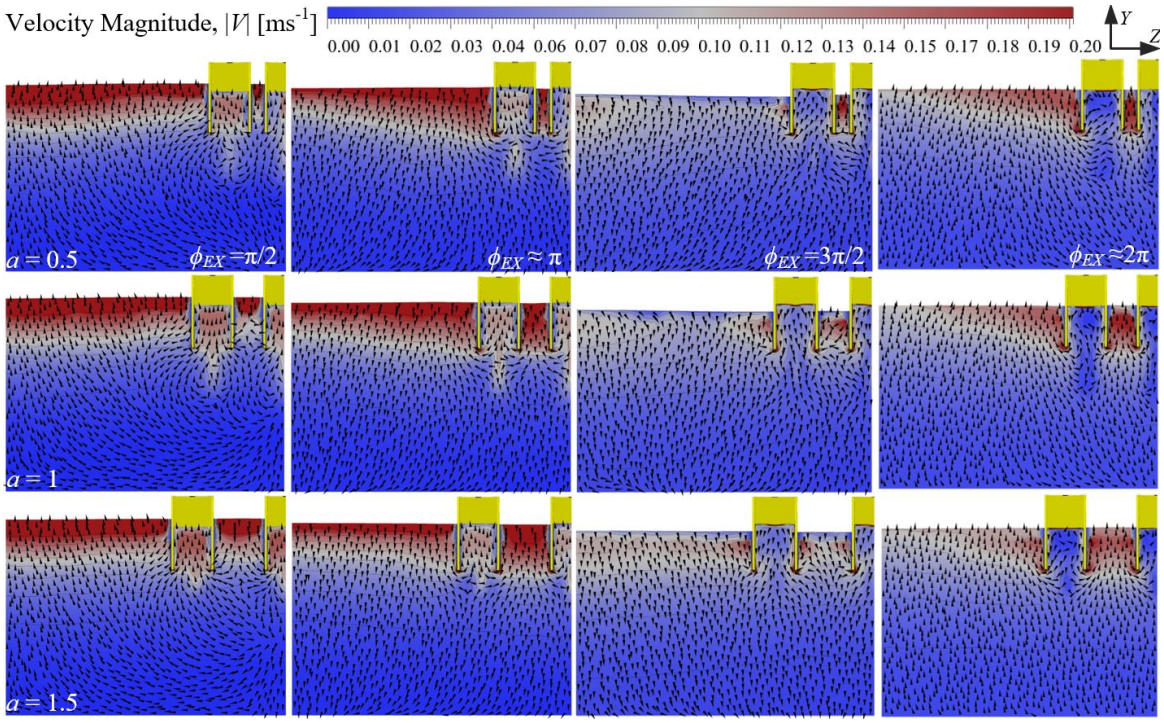


Figure 7.22: *Contour plots of velocity magnitude and vectors of velocity in the XZ plane for chamber spacings* $a = 0.5$, 1 *and* 1.5 *and the four phase points* $\phi_{EX} = \pi/2$, π, $3\pi/2$, *and* 2π

Contour plots of the velocity angle in the YZ plane in Figure 7.23 at the same position in the OWC allow for better visualisation of the phase differences at each point in the OWC cycle. This velocity angle is essentially the angle due to the Y and Z velocity components and hence is the planar or tangential component coloured as negative or positive Y components (see Figure 7.23 legend). Again, it is clear that at points $\phi_{EX} = \pi/2$ and $3\pi/2$, the water in the gap between the OWCs is affected by the operation of the OWC and as a result operating out of phase as pseudo OWC.

The interaction between the resource beneath and in close proximity of the OWCs can be seen to change with the chamber spacing. Any time water is visibly 'trapped' out of phase in between the OWCs, this can be seen to affect the operation of the OWCs, especially around the bottom edge of the walls where water is changing direction rapidly according the phase difference between the internal and external free surface elevation.

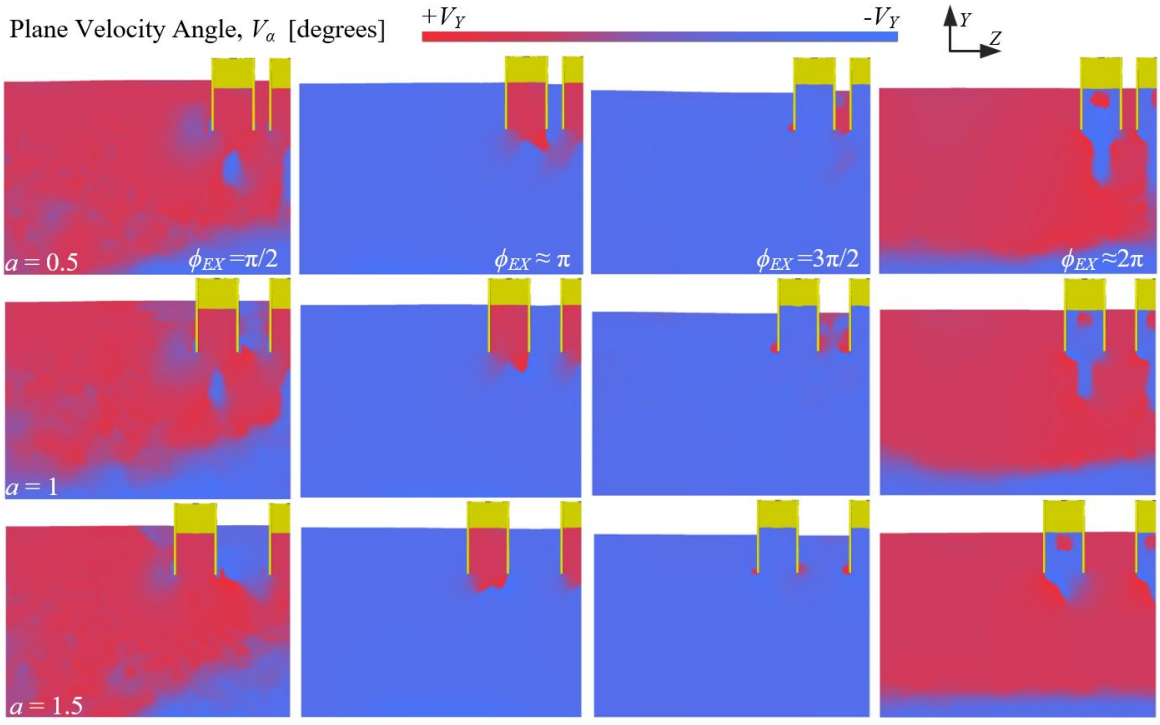


Figure 7.23: *Contour plots of velocity angle in the YZ plane (see Fig. 7.4) for chamber spacings* $a = 0.5$, 1 *and* 1.5 *and the four phase points* $\phi_{EX} = \pi/2$, π, $3\pi/2$, *and* 2π

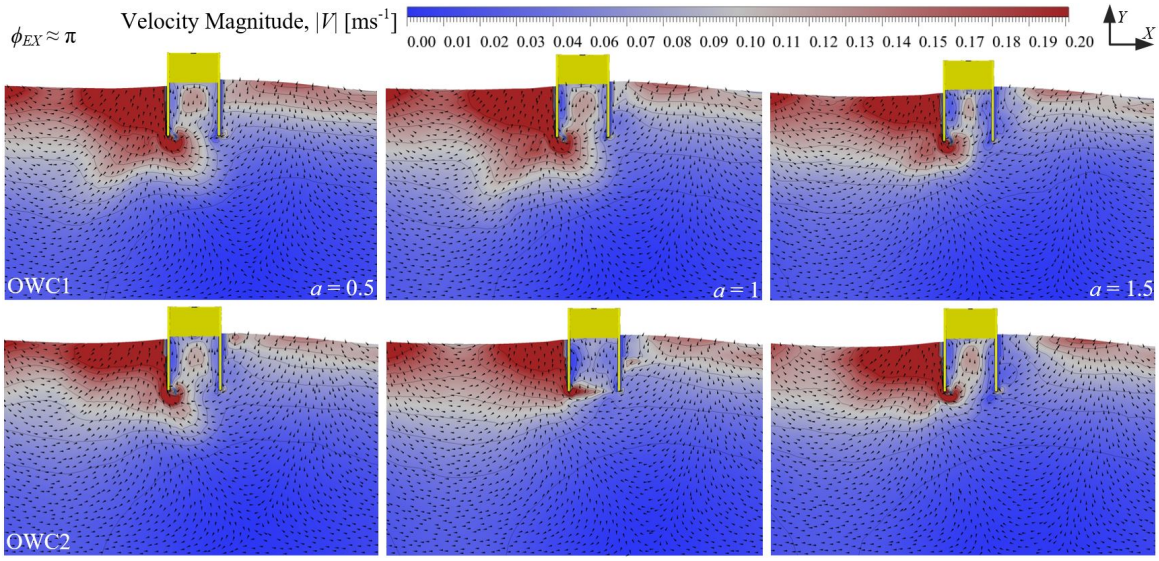


Figure 7.24: *Contour plots of velocity magnitude and vectors of velocity in the YZ plane (see Fig. 7.4) for chamber spacings* $a = 0.5$, 1 *and* 1.5 *and the phase points where the internal level crosses the external:* $\phi_{EX} = \pi$, *and* 2π

The same contour plots of velocity magnitude are implemented for the side view (in the XY plane) for both OWCs but only for phase point $\phi_{EX} = 3\pi/2$ in Figure 7.24. This phase point is of interest at this view because the internal OWC is heaving while the wave trough travels toward the front wall and hence the free surface is descending causing the increased water flow around the front wall of the OWC. Note that from the above analysis, for the CFD results only when $a = 1$ are OWC1 and OWC2 operating in phase. Here, despite being in phase with each other, they appear to be still operating differently. The level of phase lag is suspected to be caused by a combination of reflection and refraction, the latter of which can be identified in the birds-eye-view of the NWT contour plots of the free surface elevation in Figure 7.25. At smaller spacing the refraction is greatest, as one would expect from a more terminating structure with less opportunity for transmission in between the OWCs and a perhaps an OWC-like behaviour in between the actual OWC structures. At the large spacing, a sufficient width of the wave is blocked by the structure with transmission through the centre to reduce reflection and refraction.

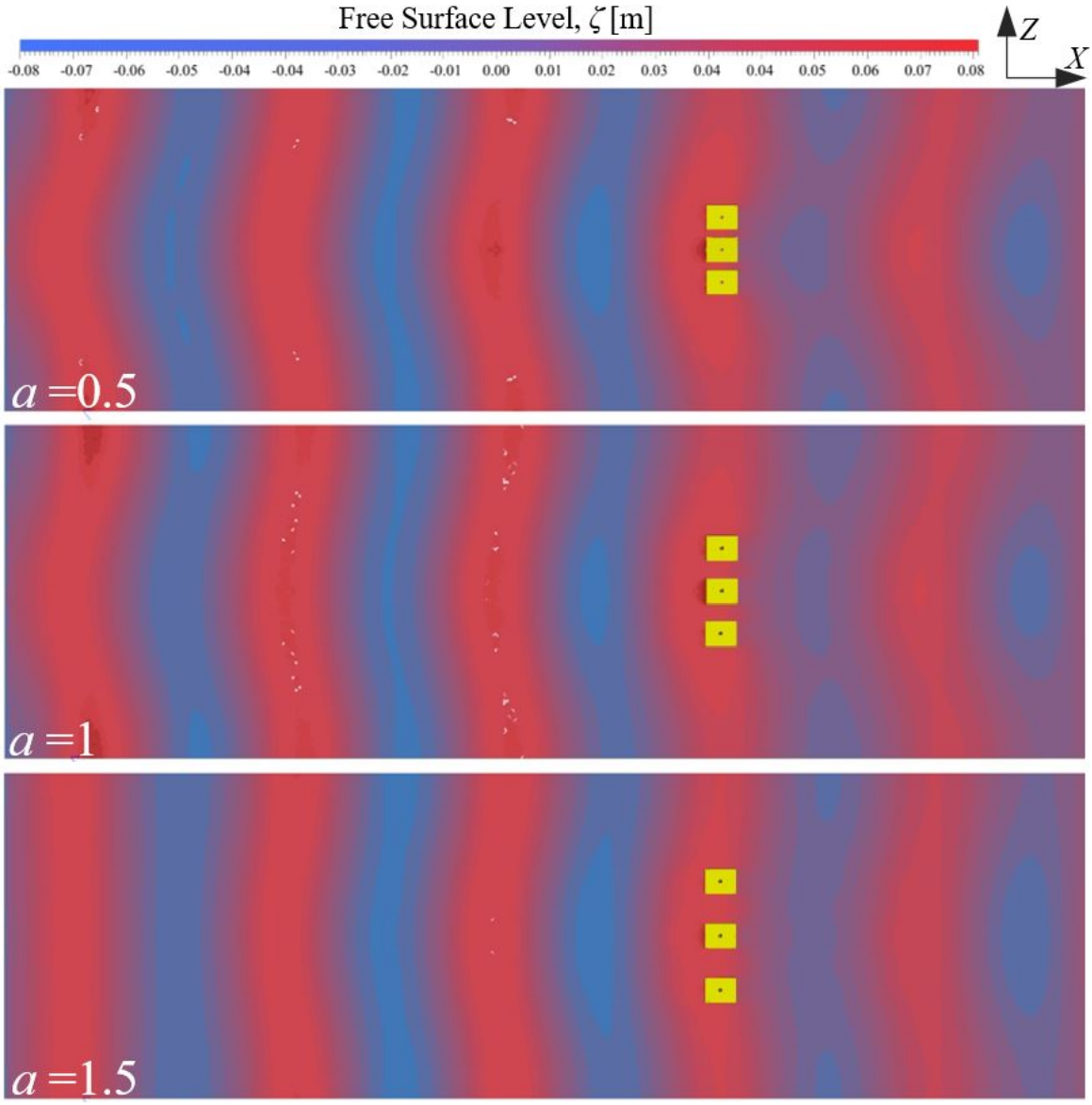


Figure 7.25: *Birds-eye view of contours of surface elevation for OWC array model and for chamber spacings* $a = 0.5,\ 1$ *and* 1.5

Although results are not strictly validated, the YZ plane contour plots for the M-OWC models at the same phase points are interesting (Figures 7.26 and 7.27). Theoretically, and ideally, because the M-OWC systems are pneumatically coupled and therefore dampened equally, this should at optimal spacing improve performance across all spacings if in fact the gap between the OWCs is affecting the performance of the individual OWCs in the array case. Referring back to the experimental results of Chapter 4, the M-OWC performed better and achieved higher capture efficiencies,

which could be due to the interaction of this heaving volume of water in between the OWCs. The breakwater M-OWC eliminates this in heaving water in the OWC gap causing either diverge or converge of flow during positive and negative displacement respectively.

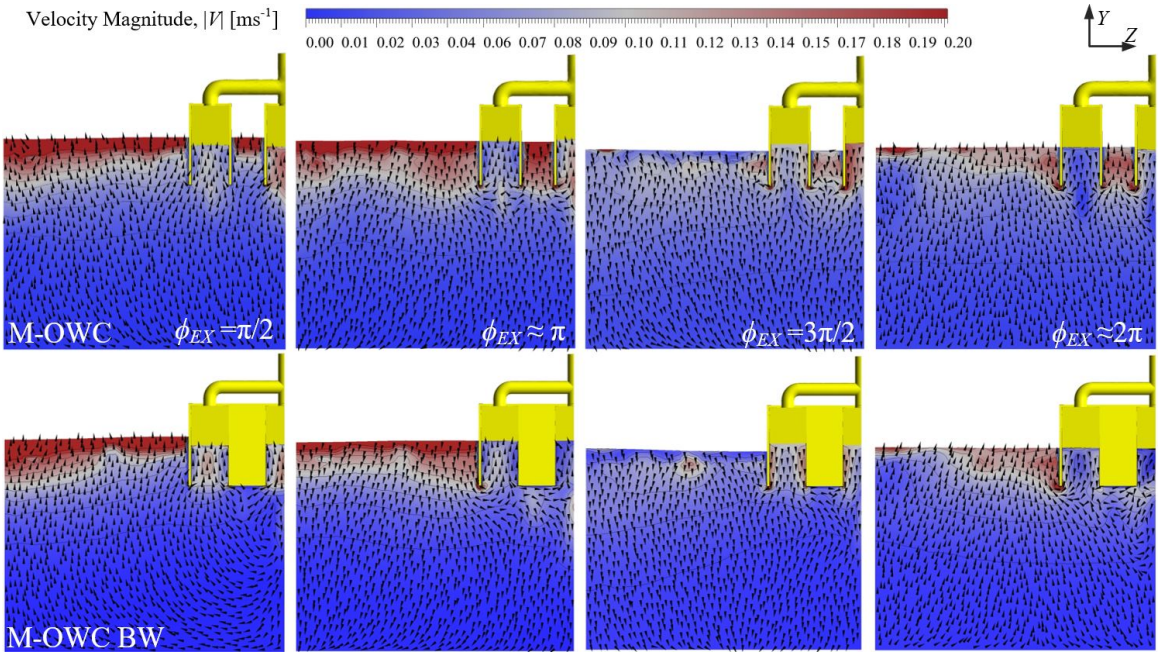


Figure 7.26: *Contour plots of velocity magnitude and vectors in the YZ plane for the M-OWC bidirectional model and breakwater variation for chamber spacing $a = 1$ and the four phase points $\phi_{EX} = \pi/2$, π, $3\pi/2$, and 2π*

The velocity angle plots of Figure 7.26 shows subtle differences due to the blocking structure preventing the rise of water in the OWC gap. The effects divergence and convergence of the water beneath the blocking structure can be seen during external wave rise in the cases of $\phi_{EX} = \pi/2$ and $\phi_{EX} = 2\pi$, respectively.

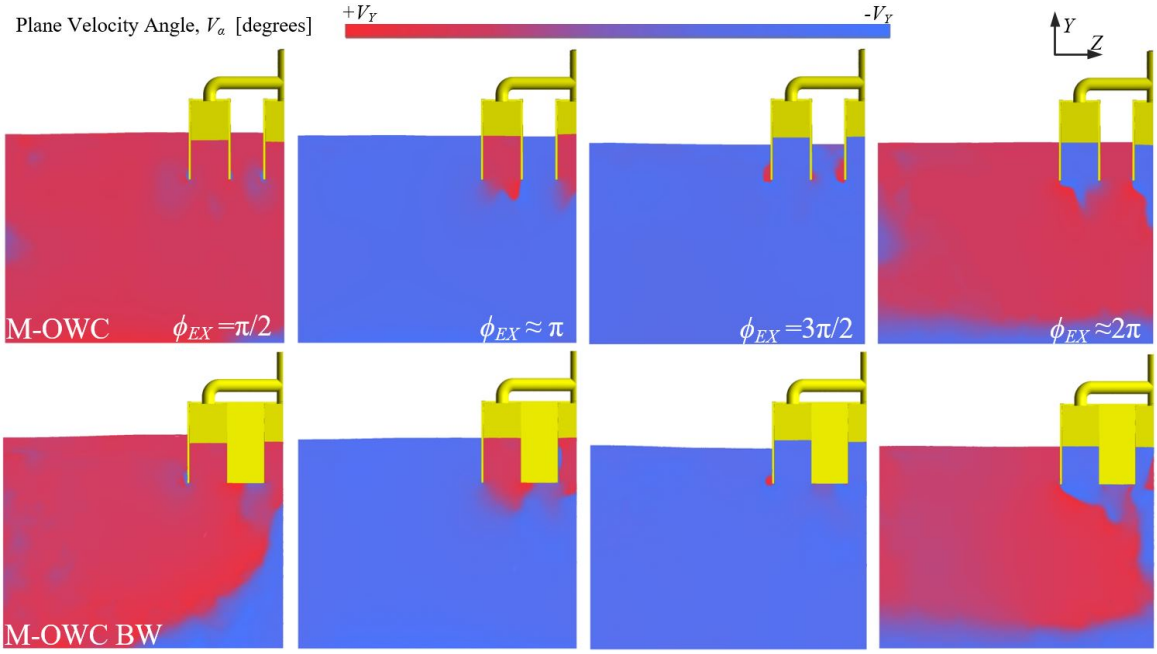


Figure 7.27: *Contour plots of velocity angle in the YZ plane for the M-OWC bidirectional model and breakwater variation for chamber spacing $a = 1$ and the four phase points $\phi_{EX} = \pi/2$, π, $3\pi/2$, and 2π*

Discussion

Pneumatic Modelling

The main purpose of the modelling of the pneumatic system was to separate the validation of the system from the full NWT model and the hydrodynamic interactions. This proved beneficial as the model could be validated, which alleviated concern from this area within the NWT simulations since the model setup and mesh refinement for the pneumatic system was kept constant across both simulation cases.

The results also shed an interesting light on the flow patterns during exhale and inhale that were otherwise unnoticeable in the experiments. While the exhale process in the manifold model works as intended, the central OWC is the direct benefactor of the inhale process at the expense of the outer OWCs. The ducted model is the opposite, working best during inhale but wasting the resource of two or more OWCs during exhale. Both models simulations have highlighting the need for further optimisation. It is clear that the there is a need for un-obstructive paths for exhale and

inhale of near equal length for all OWCs. This consideration needs to be taken in order to account for additional OWCs as the concept is scaled up.

One of the main issues with the ducted model was the close proximity of the PTO to the individual OWC outlets meaning peak flow in these areas is creating adverse pressure gradients and circulation throughout the duct.

Numerical Wave Tank Simulations

The NWT model is a large and complex model where model decisions can compound to alter final results. Being critical of this model development, as mentioned earlier in this chapter, the tuning of the generated wave could have been improved. Secondly, the repeatability of the mesh generation between wave runs could have also been improved to ensure uniform and consistent sizing of elements between runs, an extremely important but often limit control area as discussed in the literature review [216].

The NWT model proved difficult to validate against the experimental results but due to the agreement in trends and behaviour in the changing of chamber spacing with the OWC array model, the data was still analysed cautiously in a qualitative manner. This was in order to search for supporting and conclusive hypotheses as to the reasons for particular behaviour was recorded in the experimental study. This refers mainly to the changes in performance due to chamber spacing.

The results revealed that the spacing poses two causes to the change in performance. The first being the reason that was expected originally, the sharing of a smaller width of wave resource. This was mainly observable in the sub surface flow field. The second is the effect of the water column between the chambers on OWC performance. The latter was an unexpected observation found by noticing that the phase of the wave in the gap was ahead of not only the internal OWCs but the rest of the external wave. Also the effect of refraction across the tank in the changing of the OWC spacing which encouraged further phase lead. The phase lead affects performance due to the internal column and the external column in the gap travelling in opposite directions at points at which they shouldn't be. It is also suspected that

the decrease in the gap between chambers increases the free surface elevation speed in this gap.

This would give reason to the improved performance of the M-OWC bidirectional models found in the experiments, which is due to the pneumatic coupling of the chambers. Due to the damping that acts within the coupled M-OWC bidirectional pneumatic system, the effects of the out of phase water column gap has is reduced and obviously eliminated for the breakwater model. This hypothesis carries additional weight since the pneumatic system has proven to be accurately captured in the CFD simulations of the isolated pneumatic system and the experimental results prove the superiority of the M-OWC model.

Chapter 8

Conclusions and Discussion

Summary of Conclusions

The research presented in this thesis can be split into three subject areas based on the research aims outlined in Chapter 1, and the Chapter topics. The following subsections will summarise the conclusions followed by some final remarks.

Phase 1: W2W Concept Verification

The starting point of this research was defined by the stage of development of the Waves2Watts technology. On day one this technology was a concept, which like all ideas, had to be verified according to its main operating principles as claimed in the patent. This formed the primary objectives of the project and led to multiple research questions which formed the aims of this research thesis. In Chapter 4 focus was on two operating principles based on the hydrodynamics and pneumatics of the system. These points were tested individually in order to take closer look into both areas and the results reflected this attention to detail.

The hydrodynamic testing proved that there are limits to the relative wavelength, which prevents one from achieving opposite processes (exhale and inhale) in the neighbouring chambers of an attenuator M-OWC. This would require substantial spacing between the OWC chambers, something that would further prohibit the devices abil-

ity to be optimally tuned to a particular wave climate and incur significant structural costs. The smaller the relative wavelength, the worse the response of the internal free surface, to the point where sloshing results in a net zero displacement amplitude. Therefore, this ideal wavelength proposed by the W2W patent is impossible to attain while trying to also match the natural frequency of the OWC and a performance significantly greater than that of a single OWC with a significantly larger structure. Although the conclusions of this experimental study could not verify this part of the patent, the device could still theoretically operate in the intended way, just without the definitive opposite phases in the neighbouring chambers. Hence, accumulation of pressure propagating through the device could still of been a possibility at this stage.

The pneumatic experiments proved to be slightly more challenging to model at 1:50 scale due to the relatively low flow rates and the requirements of unidirectional valves to open and seal shut with these flows. Nevertheless, the effect of pneumatically coupling two chambers in attenuator formation was evident in the data and observable during the experiments. While upstream OWCs contributed high pressure peaks to the following OWC, this damping proved to be to the detriment of the performance of this OWC. Damping that is caused by the PTO, or in this case the orifice plate, would require an incredibly complex method of control in order to manage these damping levels to get the best performance out of these upstream OWCs. That being said, it was clearly evident that the wave resource available to the downstream OWC was depleted and thus optimised dynamic damping perhaps would not recover much of this lessened energy resource. The behaviour of the power outputs from the W2W concept vs a conventional single OWC revealed that the W2W generated large peaks but a very undesirable shape resulting in a lower mean output, which would require severe additional smoothing.

Due to the good approach to all experimental work and the pragmatic approach to W2W Phase 1 concept verification paid off in terms off not attempting to model both operating principles in the same physical model, which in hindsight is easy to see that it would not work and would have caused complications and delays to the project. With the conclusions of these two experimental studies not achieving the

concept verification for the W2W as originally hoped, a revisit to the W2Ws strengths determined a refreshed direction. This required incorporating the positive points of the concept into a unique application that suits W2W's characteristics and make for an attractive and viable concept with great potential.

Phase 2: W2W as a MOWC Breakwater

The change of direction brought on by the conclusions of Phase 1 ultimately led to novel research due to the unchartered territory that the device was developing into. This resulted in several novel research questions that formed that aims of Phase 2 (see Chapter 1).

It became obvious that the W2W WEC had many strengths being a larger modular M-OWC structure that could capitalise on a high OWC to turbine ratio delivering higher efficiencies with substantially lower costs, especially when integrated with another major marine structure such as a breakwater.

Investigations into how the W2W would operate as a concept was new territory and hence required a pragmatic approach in order to achieve not only concept verification. This determined the approach of the subsequent experimental testing to first understand the benefit of a M-OWC breakwater with a unidirectional PTO system. Furthermore, the requirement for certain crucial characteristics such as damping, spacing and PTO types. A summary of all the models tested and the different variables tested, and wave regimes used can be found in Table 8.1.

In the first part of these Phase 2 experiments (contents of Chapter 5), the performance between a single OWC, an OWC array as an M-OWC and the modular M-OWC were compared with changes in damping, wave runs and OWC spacings. Comparisons of chamber spacings revealed that performance is negatively affected at low spacings and above a threshold significantly improves ($a = 1$). Capture width is compared with two values that enable a fair comparison despite the inactive width in between the OWC walls. These values prove that an M-OWC at suboptimal spacing is more efficient than the OWC array and single OWC. The M-OWC also proved that it was capable of generating three times the flow rate and therefore pneumatic

power, equal to the multiple of OWCs compared to a single OWC. Hence, the M-OWC serves its purpose as a multi-chamber device multiplying power by a factor equal to the number of OWCs at minimal increase of width.

The final experimental study (Chapter 6) included the study into the inclusion of the blocking structure, which is the key transformation into a breakwater. These affects were quantified with reflection coefficients and an energy balance study through frequency domain analysis. The impact of the breakwater, as one would expect, induced a greater level of reflection and further reduced transmission slightly. The absorption of the WEC and extraction of this energy was not negatively affected, and in some cases positively affected. This fulfils the criteria of a breakwater WEC synergy – protecting downstream regions through either reflection and/or absorption.

The comparison of the PTO models were by no means a comparison of optimised models but a comparison into un-optimised types on a level playing field. The unidirectional models exhibit losses due to the rectification process, however, although this can be further optimised it will ultimately improve overall efficiency due to the inclusion of a more efficient unidirectional turbine. With the bidirectional system being the bench mark, not only in these experiments but in worldwide OWC technology, the single unidirectional model proves to be inferior primarily due to the losses incurred in the experimental modelling at this small scale. The twin system is superior due to incurring significantly fewer losses than the single system and was overall more efficient than the bidirectional both in regular and irregular sea states.

Numerical Modelling

With the path of the project ultimately involving a number of different WEC models tested experimentally, efforts where inevitably concentrated on the experimental research approach. However, at the latter stages of the project, the opportunity to use CFD as a tool to further understand some of the phenomena not observable in the experiments became apparent.

Two CFD models were successfully created and solutions verified but with only one validated against experimental results. The NWT model with less certainty in

Phase 2 Experimental Models (1:50 Scale)

	Breakwater Development			**PTO Development**		
Variables	Single OWC	OWC Array	M-OWC Bidirectaional	M-OWC Breakwater Bidirectional	M-OWC Unidirectional Single PTO	M-OWC Unidirectional Twin PTO
Wave Runs	Shorter Regime - Regular			Longer Regime - Regular and Irregular		
Damping Tests	Damping tests done are applicable to all cases					
Reflection Tests	No			Yes		
Spacing Tests	NA	Yes		No		
PTO Types	Bidirectional			Unidirectional		

Table 8.1: *Summary of all experiments carried out in Phase 2 work with details of changing variables and wave runs*

validation was still deemed appropriate for qualitative analysis only due to the agreement in trends with the change chamber spacing, which was the main curiosity that led to these investigations following the experimental work. Agreement with the experimental results could have been better and had there been more focus on numerical modelling in this research, a higher fidelity model would need to be developed. Potential reasoning behind the lack of high fidelity are reflected in the Recommendations for Future Work but mainly entail the mesh generation process, wave generation and abruption tuning and damping modelling.

It has been made more obvious through the simulations that significantly further optimisation of the pneumatic system needs to be carried out. If the device is to become scalable in terms of adding OWCs, the pneumatic system needs to converge and split flow with minimal losses during exhale and inhale, respectively, which is the essence of a modular M-OWC.

While the NWT simulations have pointed to possible areas of further investigation, it has also consolidated the conclusions made from the experimental testing. Chambers of larger spacing are not sharing resource to the same degree, are less affected by the heaving water column in between the chambers and induce less wave refraction meaning the OWCs are closer in phase. Additionally, there are clear advantages in the pneumatic coupling of the M-OWC bidirectional models operating with the same damping throughout the system. The definite causes of the changes in performance across chamber spacings and models are subject to further and more quantitative investigation but the qualitive analysis presented does not compromise the conclusions of this thesis but rather leads to additional 'academic' questions. As for the industrial style research questions that this thesis endeavoured to answer, the results are conclusive with the supporting evidence from these NWT simulations.

Discussion

Project Outcome

This project was started with the clear objectives and research aim which would help to develop the W2W from a concept stage to a higher TRL. The illustration of Figure 8.1 represents the life of this project and the development path of the device as a result.

The initial milestone was the concept verification. Giving complete benefit of doubt, these verification experiments were carried out in quest for conclusive data considering the W2W model had never been previously modelled and therefore performance was unknown.

With verification not achievable with the current concept, a loop within the TRL2/3 zone was followed whereby various solutions were considered and tested. However, following the conclusion of Phase 1 experiments it was clear that a change in direction was required. The new direction in Phase 2 provided a new path for the ongoing development, which refined the concept further, inevitably achieving a level beyond concept verification. The M-OWC breakwater with a twin unidirectional orifice system was built up from all the experimental work proving the validity of its characteristics, which makes it a device worthy of further development and investment. As an M-OWC should, capacity can be multiplied by a factor equal to the number of OWCs to ultimately reduce capital and operational costs for no trade-off in performance or annual energy production. In addition to the number of OWCs improving the components of the LCOE, the W2W M-OWC concept reduces capital and operational costs further with a lower number of turbines to OWCs and shared structural based costs. The W2W M-OWC breakwater unidirectional concept is undoubtably a concept worth of continued development as proven by the conclusions of this thesis.

Thus, this project is considered a success based on the basis of successfully achieving all original objectives and more in delivering the W2W to a higher TRL level, considered to be low TRL3 (Figure 8.1) and as a device with great potential and

contributing many learnings to the wave energy community.

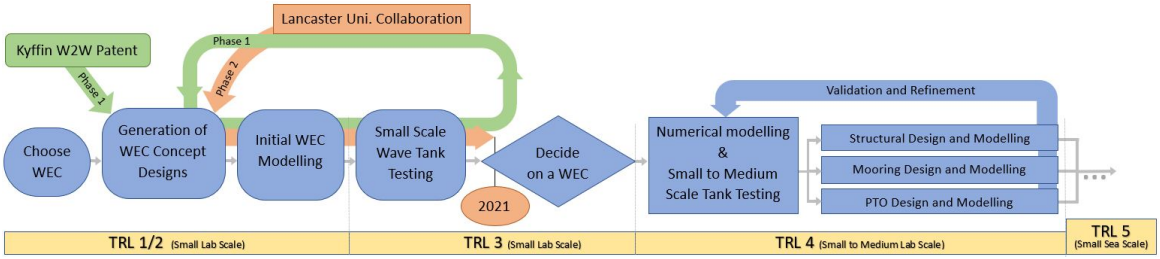


Figure 8.1: *The TRL levels for a wave energy converter with the illustration of the development path of the Waves2Watts device*

Recommendations for Future Work

As conveyed through the conclusions, it is believed that the research of this thesis proves that the W2W M-OWC breakwater unidirectional concept should be further developed. There are a few key areas in which the next stages of development should focus. It is important to note that many of the next steps depend on the choices of Waves2Watts with respect to which features of the device they wish to include moving forward. For example, if there is a willing to change certain details such as fixed vs floating, then this would change the future work path.

- Perhaps the most crucial of all recommendations is to test a floating model. Again, depending on whether having a floating model is a priority or not. The disadvantages of a floating model are mainly concerned with stability and the incurring extra costs in structure size and moorings. From a positive standpoint there has recently been work in the field with M-OWC array type breakwater models that indicate that the annual energy performance would not be negatively affected. Studies from Howe et al. [172] published after the work of this thesis reveal that the breakwater motion benefited from the inclusion of the OWCs, which caused reduction in heave and pitch motions across a range of wave runs. These conclusions are echoed in the work from Cappietti et al. [142] from more of an OWC performance perspective reinforcing the minimal impact from a fixed to a floating platform. However, limiting the affect is clearly dependent on the size of the structure. Hence, if considering a floating model, it

is recommended that potential flow numerical modelling is carried out to refine dimensions with respect to the structures response to waves with OWCs and the dimensions of the breakwater compared with the OWCs for best stability and performance. Following this an experimental model should be built, which should validate the numerical results and determine any changes in absorption, transmission, reflection and the effects of hydrodynamic characteristics such as added mass and radiation damping on WEC performance.

- Finer details of the twin unidirectional PTO system should be finalised by way of additional experimental modelling of a larger scale with larger periods to further study losses and improve efficiencies. This should begin with the operation of the rectifying valve, it's design, how it is controlled and the inclusion of venting control. Modelling at larger periods will mean that the lag of the controlled flap valve will not have such an effect on the losses. This could be done in isolation of the WEC in a specialised rig with or without turbine geometry. It is important to understand the design of PTO system and its characteristics in order to help build a reliable wave-to-wire model. The optimisation process should include determining suitable turbine scaling and appropriate manifold/ducting shape and sizing to converge the pneumatic power efficiently for the given number of chambers, which may be limited. The design of the manifold or ducting should be considered in tandem with the turbine optimisation.

- Although it is not specifically recommended, should work on the NWT simulations be continued there are some recommendations for changes to improve model fidelity. Firstly, the mesh element shapes and size relative to the wave conditions need to be consistent between different wave runs. This is difficult to be assured of with most non-manual meshing methods or at least would be very time consuming from a quality assurance point of view. Hence, a manual meshing method is recommended to irradicate uncertainty of mesh inconsistencies. The wave generation and absorption techniques also require significantly more tuning to match the experimental data and great care should be taken to

first match the incident and reflected waves in an empty NWT with those in an empty physical tank. Finally, with respect to the NWT simulation results of this thesis, it is recommended that damping values and methods are further investigated. It is true, as discussed in the literature review, that damping affects the phase of the OWC response with respect to the external free surface response [220]. Hence, it is important, once the wave generation and absorption have been validated, to then validate damping to ensure that additional phase lag is not induced and attributed to another variable or phenomena.

- Once these first recommendations are fulfilled, the overall design should be much clearer and close to being finalised, at least the large elements of the structure. With the design of the structure and moorings dependent on the hydrodynamic characteristics found in the work of the first recommendation, learnings can be taken from current floating breakwater technology to finalise the structure. Further opportunity for innovation exists at this stage in development to increase the attractiveness of the concept and ultimately its performance. For example, adding the ability to tune to the changes in the sea state at a particular site with different OWC drafts across the entire M-OWC to resonate at different wave periods making it a multi-resonant M-OWC. Currently, the design of the WEC and its structure is more conceptual and in keeping with the original shape and style of the W2W patent sketches as can be seen in the conceptual models of Figure 8.2.

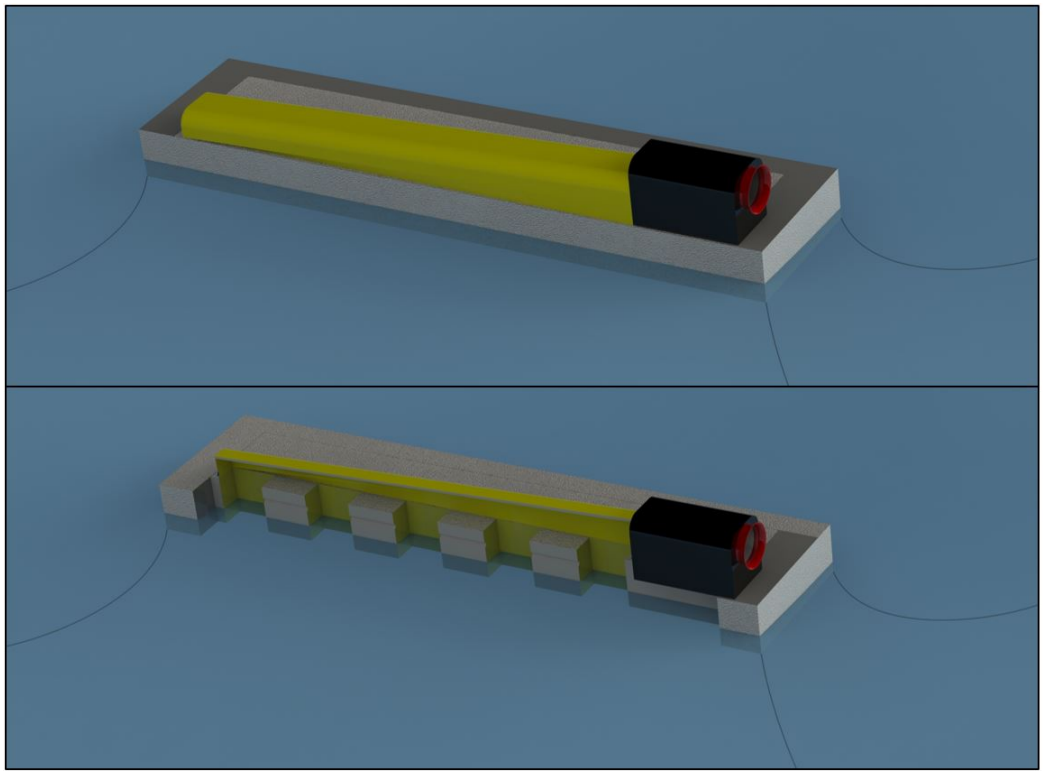


Figure 8.2: *Conceptual model of the W2W floating breakwater M-OWC in a style most similar to that of the original patent*

- With the combination of the above recommendations, a wave-to-wire mathematical model should be built to calculate energy yield for given sea states. This is dependent on the above recommendations since the model requires accurate determination of hydrodynamic characteristics through to turbine characteristics.

References

[1] International energy outlook. Report, U.S. Energy Information Administration, 2017.

[2] The outlook for energy: A view to 2040. Report, Exxon Mobil, Irving, Texas, 2016.

[3] UK Energy statistics 2019. Report, Department for Business, Energy and Industrial Strategy, 2020.

[4] S Jin and D Greaves. Wave energy in the UK: Status review and future perspectives. *Renewable and Sustainable Energy Reviews*, 143(110932):1–19, 2021.

[5] Renewables 2018: Gloabl status report. Report, REN21 Renewable Energy Policy Network for 21st Century, Paris, France, 2018.

[6] B Drew, A R Plummer, and M Sahinkaya. A review of wave energy converter technology. *Proceedings of the Institution of Mechanical Engineers Part A Journal of Power and Energy*, 2009.

[7] João Cruz. *Ocean Wave Energy: Current Status and Future Prepectives*. Springer-Verlag, Berlin , Heidelberg, Germany, 2008.

[8] Khan.N, A Kalair, N Abas, and A Haider. Review of ocean tidal, wave and thermal energy technologies. *Renewable and Sustainable Energy Reviews*, 72:590–604, 2017.

[9] A M O'Hagan, C Huertas, J O'Callaghan, and D Greaves. Wave energy in Europe: Views on experiences and progress to date. *International Journal of Marine Energy*, 14:180–197, 2016.

[10] F Neumann R Kempener. Wave energy technology brief 4. Report, IRENA - International Renewable Energy Agency, 2014.

[11] A de Andreas, A MacGillivray, O Roberts, R Guanche, and H Jeffrey. Beyond LCOE: A study of ocean energy technology development and deployment attractiveness. *Sustainable Energy Technologies and Assessments*, 19:1–16, 2017.

[12] A Pecher and J P Kofoed. *Handbook of Ocean Wave Energy*, volume 7 of *Ocean Engineering and Oceanography*. 2017.

[13] L Castro-Santos, G P Garcia, A I Estanqueiro, and P Justino. The Levelized Cost of Energy (LCOE) of wave energy using GIS based analysis: The case study of Portugal. *International Journal of Electrical Power and Energy Systems*, 65:21–25, 2015.

[14] S Astariz and G Iglesias. The economics of wave energy: A review. *Renewable and Sustainable Energy Reviews*, 45:397– 408, 2015.

[15] A S Bahaj. Generating electricity from the oceans. *Renewable and Sustainable Energy Reviews*, 15:3399–3416, 2011.

[16] M Melikoglu. Current status and future of ocean energy sources: A global review. *Ocean Engineering*, 148:563–573, 2018.

[17] R A Arinaga and K F Cheung. Atlas of global wave energy from 10 years of reanalysis and hindcast data. *Renewable Energy*, 39:49–64, 2012.

[18] S Barstow, G Mork, L Lonseth, and J P Mathisen. World wave energy resource assessments from the deep ocean to the coast. In *Proceedings of the 8th European Wave and Tidal*, 2009.

[19] M A Mustapa, O B Yaakob, Y M Ahmed, C Rheem, K K Koh, and A A Adnan. Wave energy device and breakwater integration: A review. *Renewable and Sustainable Energy Reviews*, 77:43–58, 2017.

[20] J Portilla, J Sosa, and L Cavaleri. Wave energy resources: Wave climate and exploitation. *Renewable Energy*, 57:594–605, 2013.

[21] M Folley and T J T Whittaker. Analysis of the nearshore wave energy resource. *Renewable Energy*, 34:1709–1715, 2009.

[22] C Beels, J C C Henriques, J De Rouck, M T Pontes, G De Backer, and H Verhaeghe. Wave energy resource in the North Sea. In *Proceedings of the 7th European Wave and Tidal Energy Conference*, 2007.

[23] I Fairley, H E Williams, J Horrilo-Caraballo, D Thompson, I Masters, D E Reeve, H Karunarathna, and E Faraggiana. An analysis of the wave climate in South Wales, UK. In *Proceedings of the 12th EWTEC Conference*, 2017.

[24] Fostering a blue economy: Offshore renewable energy. Report, International Renewable Energy Agency, Abu Dhabi, 2020.

[25] Lopez.I, J Andreu, C Salvador, I Martínez de Alegría, and I Kortabarria. Review of wave energy technologies. *Renewable and Sustainable Energy Reviews and The Necessary Power-equipment*, 27:413–434, 2013.

[26] A Thomas, R Mason-Jones, D Turner, P Davies, T O'Doherty, D O'Doherty, and A Mason-Jones. Tidal and marine energy in the UK - Identifying the future challenges for supply chain development. In *Proceedings of the 11th International Conference on Manufacturing Research (ICMR2013)*, 2013.

[27] Energy Department for Business and Industrial Strategy National Statistics. UK energy statistics 2019. Report, 2020.

[28] UK wave energy resource. Report, The Carbon Trust, 2012.

[29] The Crown Estate. UK wave and tidal key resource areas project. Summary report, 2012.

[30] S J Illesinghe, R Manasseh, R Dargaville, and A Ooi. Idealized design parameters of wave energy converters in a range of ocean wave climates. *International Journal of Marine Energy*, 19:55–69, 2017.

[31] D Magagna and A Uihlein. Ocean energy development in Europe: Current status and future perspectives. *International Journal of Marine Energy*, 11:81–104, 2015.

[32] Wave and tidal energy market deployment strategy for Europe. Report, SI Ocean: Strategic Initiative for Ocean Energy, 2014.

[33] Idustry vision paper. Report, Ocean Enery Europe, 2013.

[34] D Magagna, M Riccardo, and A Uihlein. JRC ocean energy status report. Report, 2016.

[35] R A Kyffin. A floating multistage air compressor with turbine - Patent: GB 2488022 A, 2012.

[36] M Attridge, D Bukauskas, H Francis, and J Harper. Design and development of the Kyffin wave energy converter - Waves2Watts. Msc thesis, 2014.

[37] J L Lye, D T Brown, and F Johnson. An investigation into the non-linear effects resulting from air cushions in the orecon oscillating water column (OWC) device. In *Proceedings of the ASME 2009 28th International Conference on Ocean, Offshore and Arctic Engineering*, 2009.

[38] D Ingram, G Smith, Claudio Bittencourt-Ferreira, and H Smith. Protocols for the equitable assessment of marine energy converters. Report, The Institute for Energy Systems, School of Engineering,The University of Edinburgh, 2011.

[39] Ocean energy: Development and evaluation protocol. Report, Marine Institute of Ireland, 2003.

[40] B Holmes and K Nielsen. Report T02-2.1: Guidelines for the development and testing of wave energy systems. Report, OES-IA Annex II Task 2.1, 2010.

[41] Offshore renewable energy. In *Proceedings of the 20th International Ship and Offshore Structures Congress (ISSC 2018)*, volume II – M.L. Kaminski and P. Rigo (Eds, 2018.

[42] P Benreguig. *Performance and power smoothing of innovative closed-circuit oscillating water column wave energy converter.* Phd thesis, 2019.

[43] D Bull, R Costello, A Babarit, K Nielsen, C B Ferreira, B Kennedy, R Malins, K Dykes, J Roberts, and J Weber. Technology Performance Level assessment methodology. Technical report, Sandia National Laboratories, Albuquerque, New Mexico, USA, 2017.

[44] J Weber, D Laird, R Costello, J Roberts, D Bull, A Babarit, K Nielsen, C B Ferreira, and B Kennedy. Cost, time, and risk assessment of different wave energy converter technology development trajectories. In *12th European Wave and Tidal Energy Conference*, 2017.

[45] Commercial readiness index assessment: Using the method as a tool in renewable energy policy design (RE-CRI). Report, IEA Renewable Energy Technology Deployment, Utrecht, Netherlands, 2017.

[46] B Kinsman. *Wind Waves: their generation and propagation on the ocean surface*. Prentice-Hall, Englewood Cliffs, New Jersey, 1965.

[47] M E McCormick. *Ocean Wave Energy Conversion*. New York, US, 2007.

[48] R G Dean and R A Dalrymple. *Water Wave Mechanics For Engineers and Scientists*, volume 2 of *Advanced Series on Ocean Engineering*. World Scientific, 1991.

[49] *Chapter 1: Water Wave Mechanics*. Coastal Engineering Manual - Part II. U.S. Army Corps of Engineers, Washington, DC, 2008.

[50] S R Massel. *Ocean Surface Waves: Their Physics and Prediction*, volume 11 of *Advanced Series of Ocean Engineering*. World Scientific, 1996.

[51] Marine energy - wave developers. URL: http://www.emec.org.uk/marine-energy/wave-developers/. Accessed: 2 Febuary 2021.

[52] A Babarit. A database of capture width ratio of wave energy converters. *Renewable Energy*, 80:610–628, 2015.

[53] J R Joubert, J L van Niekerk, J Reinecke, and I Meyer. Wave energy converters. Report, Centre for Renewable and Sustainable Energy Studies, 2013.

[54] Annual report. Technical report, Ocean Energy Systems, 2016.

[55] N Delmonte, D Barater, F Giuliani, P Cova, and G Buticchi. Oscillating water column power conversion: a technology review. *IEEE Transactions on Industrial Applications*, pages 1852–1859, 2014.

[56] A F O Falcao and J C C Henriques. Oscillating-water-column wave energy converters and air turbines: A review. *Renewable Energy*, 85:1391–1424, 2016.

[57] H Zhang and G A Aggidis. Nature rules hidden in the biomimetic wave energy converters. *Renewable and Sustainable Energy Reviews*, 97:28–37, 2018.

[58] Y Cui. Simulation of wave energy harvesting by Piezoelectric Seaweed. In *IWMSE2017 - IOP Conf. Series: Materials Science and Engineering 250 012022*, 2017.

[59] *Background Papers on Seafloor Engineering*, volume 2 of *State-of-the-art in Seafloor Engineering*. Assembly of Engineering National Research Council, 1975.

[60] Y Masuda. Wave-activated power generator - Patent: US4858434, 1989.

[61] S Lindroth and M Leijon. Offshore wave power measurements - a review. *Renewable and Sustainable Energy Reviews*, 15:4274–4285, 2011.

[62] Y Washio, H Osawa, Y Nagata, F Fujii, H Furuyama, and T Fujita. The offshore floating type wave power device "Mighty Whale": Open sea tests. In *Proceedings of the Tenth (2000) International Offshore and Polar Engineering Conference*, 2000.

[63] Y Washio, H Osawa, and T Ogata. The open sea tests of the offshore floating type wave power device "Mighty Whale" - characteristics of wave energy absorption and power generation. In *An Ocean Odyssey. Conference Proceedings (IEEE Cat. No.01CH37295)*. Japan Marine Science and Technology Center, 2001.

[64] John Brooke. *Wave Energy Conversion*, volume 6. Elsevier Science Ltd, Oxford, UK, 2003.

[65] A F O Falcao. Wave energy utilization: A review of the technologies. *Renewable and Sustainable Energy Reviews*, 14:899–918, 2010.

[66] R Badhurshah, A Samad, and T Karthikeyan. Oscillating water column wave energy system - a prospective. In *First International Conference on Automation, Control, Energy and Systems*, 2014.

[67] A F O Falcao, L M C Gato, A J N A Sarmento, and A Brtio-Melo. The Pico OWC wave power plant: Its life from conception to closure 1986–2018. In *Proceedings of the 3rd International Conference on Renewable Energies Offshore (RENEW-2018)*, 2018.

[68] T J T Whittaker, W Beattie, M Folley, C Boake, A Wright, M Osterried, and T Heath. The LIMPET wave power project - the first years of operation. *Renewable Energy*, 2004.

[69] Islay LIMPET wave power plant. Report, Queens University of Belfast, 2002.

[70] T J T Whittaker, D Langston, N Fletcher, M Shaw, and A FO Falcao. Islay LIMPET wave power plant. *The Queen's University of Belfast*, 2002.

[71] M Sutton. Court proceedings 'delay action' to remove stranded Oceanlinx wave energy generator. URL: http://www.abc.net.au/news/2017-05-17/oceanlinx-generator-stranded-as-court-proceedings-continue/8529602, 2017. Accessed: 2 April 2020.

[72] S Doyle and G A Aggidis. Development of multi-oscillating water columns as wave energy converters. *Renewable and Sustainable Energy Reviews*, 107:(75–86), 2019.

[73] V Baudry, A Babarit, and A Clement. An overview of analytical, numerical and experimental methods for modelling oscillating water columns. In *Proceedings of the 10th European Wave and Tidal Energy Conference*, 2013.

[74] E Medina-Lopez, W Allsop, A Dimakopoulos, and T Bruce. Conjectures on the failure of the OWC breakwater at Mutriku. In *Conference: Coastal Structures*, 2015.

[75] G C Nihous. Wave power extraction by arbitrary arrays of non-diffracting oscillating water columns. *Ocean Engineering*, 51:94–105, 2012.

[76] J Nader, S Zhu, P Cooper, and B Stappenbelt. A finite-element study of the efficiency of arrays of oscillating water column wave energy converters. *Ocean Engineering*, 43: 72–81, 2012.

[77] D N Konispoloatis and S A Mavrakos. Hydrodynamic analysis of an array of interacting free-floating oscillating water column (OWC's) devices. *Ocean Engineering*, 111: 179–197, 2016.

[78] L O'Boyle, B Elsaber, and T Whittaker. Experimental measurement of wave field variations around wave energy converter arrays. *Sustainablitiy*, 9(70), 2017.

[79] K Thiruvenkatasamy and S Neelamani. On the efficiency of wave energy caissons in array. *Applied Ocean Research*, 19:61–72, 1997.

[80] A Kurniawan, D Greaves, and J Chaplin. Wave energy devices with compressible volumes. In *Proceedings of the Royal Society of London A: Mathematical, Physical and Engineering Sciences*, volume 470, page 20140559. The Royal Society, 2014. ISBN 1364-5021.

[81] W Sheng, T Lewis, and R Alcorn. On wave energy extraction of oscillating water column device. In *4th International Conference on Ocean Energy*, 2012.

[82] B Wu, M Li, R Wu, T Chen, Y Zhang, and Y Ye. BBDB wave energy conversion technology and perspective in China. *Ocean Engineering*, 169:281–291, 2018.

[83] P Boccotti. On a new wave energy absorber. *Ocean Engineering*, 30:1191–1200, 2003.

[84] J Hubble. Wave power - Norway's latest export. *Electronics and Power*, pages 533–534, 1986.

[85] Wavenergy. REWEC3 - Innovative breakwaters to produce energy from ocean waves. Technical report, 2021. Accessed: 8 Feburary 2021.

[86] F Arena, A Romolo, G Malara, V Laface, E Valentino, and F Messineo. Overview on the installation of a U-OWC breakwater in the Port of Salerno. In *13th European Wave and Tidal Energy Conference*, 2019.

[87] P Benreguig, J Murphy, M Vicente, and S Crowley. Wave-to-wire model of the Tupperwave device and performance comparison with conventional OWC. In *Proceedings of the 3rd International Conference on Renewable Energies Offshore (RENEW-2018)*, 2018.

[88] P Benreguig, J Murphy, and W Sheng. Model scale testing of the Tupperwave device with comparison to a conventional OWC. In *Proceedings of the ASME 2018 International Design Engineering Technical Conferences and Computers and Information in Engineering Conference*, 2018.

[89] A Fleming, G MacFarlane, S Hunter, and T Denniss. Power performance prediciton for a vented oscillating water column wave energy converter with a unidirectional air turbine power take-off. In *Proceedings of the 12th European Wave and Tidal Energy Conference*, 2017.

[90] Annual report – an overview of ocean energy activities in 2020. Technical report, Ocean Energy Systems, 2020.

[91] A Kurniawan, J Chaplin, D Greaves, and M Hann. Wave energy absorption by a floating air bag. *Journal of Fluid Mechanics*, 812:294–320, 2017. ISSN 0022-1120.

[92] M L Jalon and F Brennan. Hydrodynamic efficiency versus structural longevity of a fixed OWC wave energy converter. *Ocean Engineering*, 206, 2020.

[93] G U Muller and T J T Whittaker. An investigation of breaking wave pressures on inclined walls. *Ocean Engineering*, 20:4:349–358, 1993.

[94] Y Kuo, C Lin, C Chung, and Y Wang. Wave loading distribution of oscillating water column caisson breakwaters under non-breaking wave forces. *Journal of Marine Science and Technology*, 23:78–87, 2015.

[95] K A Pawitan and T Bruce. Influence of power take off on front face loads on a small-scale OWC model. In *Proceedings of the Asian Wave and Tidal Energy Conference, (AWTEC2016)*, pages 486–493, 2016.

[96] J S Ashlin, V Sundar, and S A Sannasiraj. Pressures and forces on an oscillating water column type wave energy caisson breakwater. *Journal of Waterway, Port, Coastal and Ocean Engineering*, 143:5:1–18, 2017.

[97] W Allsop, T Bruce, J Alderson, V Ferrante, V Russo, D Vicinanza, and M Kudella. Large scale tests on a generalised oscillating water column wave energy converter. In *Hydralab IV Joint User Meeting, Lisbon, Portugal*, 2014.

[98] A Viviano, S Naty, E Foti, T Bruce, W Allsop, and D Vicinanza. Large-scale experiments on the behaviour of a generalised oscillating water columns under random waves. *Renewable Energy*, 99:875–887, 2016.

[99] A Viviano, R E Musumeci, D Vicinanza, and E Foti. Pressures induced by regular waves on a large scale OWC. *Coastal Engineering*, 152:1–14, 2019.

[100] K A Pawitan, A S Dimakopoulos, D Vicinanza, W Allsop, and T Bruce. A loading model for an OWC caisson based upon large-scale measurements. *Coastal Engineering*, 145:1–20, 2019.

[101] D Ning, R Wang, Q P Zou, and B Teng. An experimental investigation of hydrodynamics of a fixed OWC wave energy converter. *Applied Energy*, 168:636–648, 2016.

[102] D V Evans and R Porter. Hydrodynamic characteristics of an oscillating water column device. *Applied Ocean Research*, 17:155–164, 1995.

[103] Conghao Xu and Z Huang. Three-dimensional CFD simulation of a circular OWC with a nonlinear power-takeoff: Model validation and a discussion on resonant sloshing inside the pneumatic chamber. *Ocean Engineering*, 176:184–198, 2019.

[104] K Pawitan, W Allsop, and T Bruce. Sloshing and violent in-chamber water column movement in an OWC wave energy converter. In *Proceedings of the 4th Asian Wave and Tidal Energy Conference, (AWTEC2016), Taipei, Taiwan*, 2018.

[105] G U Muller and T J T Whittaker. Visualisation of flow conditions inside a shoreline wave power-station. *Ocean Engineering*, 22:6:629–641, 1995.

[106] I Lopez, A Castro, and G Iglesias. Hydrodynamic performance of an oscillating water column wave energy converter by means of particle imaging velocimetry. *Energy*, 83: 89–103, 2015.

[107] S Doyle and G A Aggidis. Investigation into multi-oscillating water column wave energy and a novel concept. In *Proceedings of the 3rd International Conference on Renewable Energies Offshore (RENEW-2018)*, 2018.

[108] M Shalby, D G Dorrel, and P Walker. Multi–chamber oscillating water column wave energy converters and air turbines: A review. *International Journal of Energy Research*, pages 1–16, 2018.

[109] N Delmonte, P Ruol, L Martinelli, F Giuliani, and P Cova. Multi-chamber oscillating water column device for harvesting ocean renewable energy. Report, Marine Renewables Infrastructure Network - MARINET, 2014.

[110] L Martinelli, P Ruol, E Fassina, F Giuliani, and N Delmonte. A Wave-2-Wire experimental investigation of the new "Seabreath" wave energy converter: The hydraulic response. *Coastal Engineering*, 2014.

[111] L Martinelli, P Ruol, and G Cortellazzo. On mooring design of wave energy converters: The Seabreath application. *Coastal Engineering*, 2012.

[112] I Voropaev. Wave energy converter - Patent: US20090102199A1, 2009.

[113] iVec. New technologies open new horizons. Report, 2011. Accessed: 1 August 2018.

[114] J B Thomsen. Hydrodynamic models of partner WECs. Report, Aalborg University, Aalborg, Denmark, 2018.

[115] K Nielsen, O Billeskov, and F P Jacobsen. Attenuator development phase Ib. Report, MARINET - Marine Renewables Infrastructure Network, 2015.

[116] K Nielsen and O Billeskov. Attenuator development phase Ic. Report, MARINET - Marine Renewables Infrastructure Network, 2015.

[117] K Nielsen, F P Jacobsen, M Simonson, and P Scheijgrond. Attenuator development phase I. Report, MARINET - Marine Renewables Infrastructure Network, 2013.

[118] K Nielsen. MARINET experiment KNSWING testing an I-Beam OWC attenuator. *International Journal of Marine Energy*, 12:21–34, 2015.

[119] H B Bingham, D Ducasse, K Nielsen, and R Read. Hydrodynamic analysis of oscillating water column wave energy devices. *Journal of Ocean Engineering*, 1:405–419, 2015.

[120] K D Rasmussen. Waver energy converter comprising pressure and suction pipes-Patent: WO 2007057013 A1, 2007.

[121] T Kelly, T Dooley, J Campbell, and J V Ringwood. Comparison of the experimental and numerical results of modelling a 32-oscillating water column (OWC), V-shaped floating wave energy converter. *Energies*, 6:4045–4077, 2013.

[122] P B Frigaard, J P Kofoed, and E R Beserra. Wave induced loads on the LEANCON wave energy converter. Report, Department of Civil Engineering, Aalborg University, Denmark, 2008.

[123] J P Kofoed and P B Frigaard. Hydraulic evaluation of the LEANCON wave energy converter. Report, Department of Civil Engineering, Aalborg University, Denmark, 2008.

[124] J R Joubert. *Design and Development of a Novel Wave Energy Converter*. Phd thesis, Stellenbosch University, Stellenbosch, South Africa, 2013.

[125] G de F Retief, F Muller, G Prestedge, L Geustyn, and D Swart. Detailed design of a wave energy conversion plant. *Costal Engineering*, pages 2546–2562, 1984.

[126] P H Ackerman. *Air Turbine Design Study for a Wave Energy Conversion System*. Phd thesis, Stellenbosch University, Stellenbosch, South Africa, 2009.

[127] J Fairhurst. *Modelling and Design of an Oscillating Wave Energy Converter*. PhD thesis, 2015.

[128] J Fairhurst and J L Van Niekerk. Development and application of a wave energy conversion simulation model. In *Proceedings of the 12th European Wave and Tidal Energy Conference*, 2017.

[129] J Fairhurst and J L Van Niekerk. Modelling, simulation and testing of a submerged oscillating water column. *International Journal of Marine Energy*, 16:181–195, 2016.

[130] D G Dorrell, M Hsieh, and C Lin. A multichamber oscillating water column using cascaded savonius turbines. *IEEE Transactions on Industry Applications*, 46(6):2372–2380, 2010.

[131] M Shalby, P Walker, and D G Dorrel. Modelling of the multi-chamber oscillating water column in regular waves at model scale. In *4th International Conference on Energy and Environment Research, ICEER 2017*, 2017.

[132] M Shalby, P Walker, and D G Dorrel. The investigation of a segmented Multi-Chamber Osciallting Water Column in physical scale model. In *5th International Conference on Renewable Energy Research and Applications*, 2016.

[133] Consulting Engineers Rendel Palmer and Tritton. Consultants 1981 assessment. Report, 1982.

[134] F J E Johnson. Wave energy device - Patent: US20070180823 A1, 2007.

[135] M Previsic, R Bedard, and G Hangerman. E2i EPRI Assessment: Offshore wave energy conversion. Report, 2004.

[136] Wave energy developer Orecon hits stormy waters. Technical report, Renewable Energy Focus, 2009. Accessed: 8 Febuary 2021.

[137] A Tetu. *Power Take-Off Systems for WECs.* Handbook of Ocean Wave Energy. 2017.

[138] S Takahashi, H Nakada, H Ohneda, and M Shikamori. *Wave Power Covnersion by a Prototype Wave Power Extracting Caisson in Sakata Port.* Costal Engineering. 1992.

[139] Y Torre-Enciso, I Ortubia, L I Lopez de Aguileta, and J Marques. Mutriku wave power plant: from the thinking out to the reality. In *Proceedings of the 8th European Wave and Tidal Energy Conference*, 2009.

[140] C Wan, C Yang, Q Fang, Z You, J Geng, and Y Wang. Hydrodynamic investigation of a dual-cylindrical OWC wave energy converter integrated into a fixed caisson breakwater. *Energies*, 13(896), 2020.

[141] S Zheng, A Antonini, Y Zhang, D Greaves, J Miles, and G Iglesias. Wave power extraction from multiple oscillating water columns along a straight coast. *Journal of Fluid Mechanics*, 878:445–480, 2019.

[142] L Cappietti, I Simonetti, and I Crema. Laboratory experiments on the performance of an OWC-WEC: fixed condition versus floating platform-embodied condition. In *13th European Wave and Tidal Energy Conference*, 2019.

[143] I Simonetti and L Cappietti. A CFD study on the balance of energy in a fixed bottom-detached oscillating water column wave energy converter. In *12th European Wave and Tidal Energy Conference*, 2017.

[144] A Sinha, P Mendonca, Filipe Belga, Henrique Castro, T Morais, D Clement, T Cabral, F Taveira-Pinto, P Rosa-Santos, and H G Lopes. Preliminary design of a hybrid wave energy converter integrated into a rubble mound breakwater. In *13th European Wave and Tidal Energy Conference*, 2019.

[145] M J Legaz, P Mayorga, and J Fernandez. Study of multipurpose platform. In G Soares, editor, *International Conference on Renewable Energies Offshore*, 2019.

[146] T P Mazarakos and S A Mavrakos. Second order wave drift damping of a TLP floating structure concept for combined wind and wave energy. In *Proceedings of the 3rd International Conference on Renewable Energies Offshore (RENEW-2018)*, 2018.

[147] F He, Z Huang, and A W Law. An experimental study of a floating breakwater with asymmetric pneumatic chambers for wave energy extraction. *Applied Energy*, 106: 222–231, 2013.

[148] D Howe, J Nader, and G MacFarlane. Integration of wave energy converters within floating offshore structures. In *Australasian Coasts and Ports Conference*, 2019.

[149] R Cascajo, E Garcia, E Quiles, A Correcher, and F Morant. Integration of marine wave energy converters into seaports: A cast study in the Port of Valencia. *Energies*, 12(787), 2019.

[150] F Neumann and A J N A Sarmento. An assessment of technical and economical viability of OWC integration in breakwaters.

[151] D Vicinanza, E Di Lauro, P Contestabile, C Gisonni, J L Lara, and I J Losada. Review of innovative harbor breakwaters for wave-energy conversion. *Journal of Waterway, Port, Costal, Ocean Engineering*, 145(4), 2019.

[152] X L Zhao, D Z Ning, Q P Zou, D S Qiao, and S Q Cai. Hybrid floating breakwater-WEC system: A review. *Ocean Engineering*, 186(106126), 2019.

[153] L das Neves, Z Samadov, E Di Lauro, K Delecluyse, and P Haerens. The integration of a hybrid wave energy converter in port breakwaters. In *The integration of a hybrid wave energy converter in port breakwaters*, 2019.

[154] D Z Ning, X L Zhao, L F Chen, and M Zhao. Hydrodynamic performance of an array of wave energy converters integrated with a pontoon-type breakwater. *Energies*, 11 (685), 2018.

[155] Technology: An innovative wave energy converter, the "Rho-Cee". Technical report, Float Inc. Accessed: 6 April 2020.

[156] M G Hassanabad and M Shegeft. Numerical simulation study on the offshore oscillating water column OWC integrated into a floating breakwater using CFD. In *13th European Wave and Tidal Energy Conference*, 2019.

[157] S Zheng, A Antonini, Y Zhang, J Miles, and G Iglesias. Wave power exrraction from a Multi-OWC platform. In *13th European Wave and Tidal Energy Conference*, 2019.

[158] G A Aggidis, M T Rahmati, R V Chaplin, A P McCabe, M A Bhinder, C G Mingham, and D M Causon. Optimum power capture of a new wave energy converter in irregular waves. In *Proceedings of the ASME 28th International Conference on Ocean, Offshore and Arctic Engineering*, 2009.

[159] A P McCabe and G A Aggidis. Optimum mean power output of a point-absorber wave energy converter in irregular waves. *Proc. IMechE Part A: J. Power and Energy*, 223:773–781, 2009.

[160] A P McCabe, G A Aggidis, and T J Stallard. A time-varying parameter model of a body oscillating in pitch. *Applied Ocean Research*, 28(6):359–370, 2006.

[161] A P McCabe, G A Aggidis, and M B Widden. Optimizing the shape of a surge-and-pitch wave energy collector using a genetic algorithm. *Renewable Energy*, 35(12): 2767–2775, 2010.

[162] A P McCabe, A Bradshaw, J A C Meadowcroft, and G A Aggidis. Developments in the design of the PS Frog Mk 5 wave energy converter. *Renewable Energy*, 31(2): 141–151, 2006.

[163] H Yavuz, T J Stallard, A P McCabe, and G A Aggidis. Time series analysis-based adaptive tuning techniques for a heaving wave energy converter in irregular seas. *Proc. IMechE Part A: J. Power and Energy*, 221, 2007.

[164] G A Aggidis and C J Taylor. Overview of wave energy converter devices and the development of a new multi-axis laboratory prototype. *IFAC PapersOnLine*, 50(1): 15651–15656, 2017.

[165] M A Bhinder, C G Mingham, D M Causon, M T Rahmati, G A Aggidis, and R V Chaplin. A joint numerical and experimental study of a surging point absorbing wave energy converter (WRASPA). In *Proceedings of the ASME 28th International Conference on Ocean, Offshore and Arctic Engineering*, 2009.

[166] M A Bhinder, M T Rahmati, C G Mingham, and G A Aggidis. Numerical hydrodynamic modelling of a pitching wave energy converter. *European Journal of Computational Mechanics*, 24(4):129–143, 2015.

[167] R V Chaplin and G A Aggidis. WRASPA: Wave interactions and control for pitching-surge point-absorber wave energy converters. In *7th European Wave and Tidal Energy Conference*, 2007.

[168] M T Rahmati and G A Aggidis. Numerical and experimental analysis of the power output of a point absorber wave energy converter in irregular waves. *Ocean Engineering*, 111:483–492, 2016.

[169] D Zhang, G A Aggidis, Y Wang, X Gu, W Li, and Y Chen. Wave tank experiments on the power capture of a multi-axis wave energy converter. *Journal of Marine Science and Technology*, 20:520–529, 2015.

[170] C Perez-Collazo, R Pemberton, D Greaves, and G Iglesias. Monopile-mounted wave energy converter for a hybrid wind-wave system. *Energy Conversion and Management*, 199(111971), 2019.

[171] Y Zhou, D Ning, W Shi, L Johanning, and G Iglesias. Hydrodynamic investigation on an OWC wave energy converter integrated into an offshore wind turbine monopile. *Costal Engineering*, 162, 2020.

[172] D Howe, J Nader, and G MacFarlane. Performance analysis of a floating breakwater integrated with multiple oscillating water column wave energy converters in regular and irregular seas. *Applied Ocean Research*, 99(102147), 2020.

[173] Y Zhou, D Ning, L Chen, and G Iglesias. Nonlinear hydrodynamic modelling of an offshore stationary multi-oscillating water column platform. *Ocean Engineering*, 227, 2021.

[174] E Gubesch, C Chin, N Abdussamie, and I Penesis. The hydrodynamic performance of an integrated semi-submersible platform with wave energy converters: A concept for multi-use platforms. In *Australasian Coasts and Ports*, 2019.

[175] R Ahmed, K McKee, and I Howard. Advancements of wave energy converters based on power take off (PTO) systems, a review. *Ocean Engineering*, 204(107248), 2020.

[176] T Setoguchi and M Takao. Current status of self-rectifying air turbines for wave energy conversion. *Energy Conversion and Management*, 47:2382–2396, 2006.

[177] M Takao and T Setoguchi. Air turbines for wave energy conversion. *International Journal of Rotataing Machinery*, page 10, 2012.

[178] Y Cui, Z Liu, X Zhang, and C Xu. Review of CFD studies on axial-flow self-rectifying turbines for OWC wave energy conversion. *Ocean Engineering*, 175:80–102, 2019.

[179] T H Carolus and C Moisel. Bidirectional air turbines for oscillating water column systems:fast selection applying turbomachinery scaling laws. *International Journal of Marine Energy*, 18:65–77, 2017.

[180] T K Das, P Halder, and A Samad. Optimal design of air turbines for oscillating water column wave energy systems: A review. *International Journal of Ocean and Climate Systems*, 8:37–49, 2017‘.

[181] A A Wells. Fluid drivend rotary transduce - Patent: GB1595700A, 1976.

[182] S Raghunathan. The Wells air turbine for wave energy conversion. *Aerospace Science*, 31:335–386, 1995.

[183] A F O Falcao and L M C Gato. *Air Turbines*. Comprehensive Renewable Energy. 2012.

[184] R Curran and L M C Gato. The energy covnersion performance of several types of Wells turbines designs. *Insitute of Mechanical Engineers*, 211, 1997.

[185] H Hotta, Y Washio, H Yokozawa, and T Miyazaki. RandD on waver power deivce "Mighty Whale". *Japan Marine Science and Technology Center*, 1996.

[186] M Suzuki, C Arakawa, and S Takahashi. Performance of wave power generating system installed in breakwater at Sakata Port in Japan. In *International Offshore and Polar Engineering Conference*, 2004.

[187] M Takao, R Sasaki, M Md Ashraful Alam, S Okuhara, and Y Kinoue. Development of a counter-rotating imuplse trubine for bidirectional airflow. In G Soares, editor, *Renewable Energies Offshore*, 2018.

[188] T Setoguchi, S Santhakumar, H Maeda, M Takao, and K Kaneko. A review of impulse turbines for wave energy conversion. *Renewable Energy*, 23:261–292, 2001.

[189] R Alcorn. *Wave Energy: Modern Devices*. Future Energy: Improved, Sustainable and Clean Options for our Planet. 2nd edition, 2014.

[190] R Alcorn, A Blavette, M Healy, and A Lewis. FP7 EU funded CORES wave energy project: a coordinators' perspective on the Galway Bay sea trials. *Underwater Technology*, 2014.

[191] K Mala, S N Badrinath, S Chidanand, G Kailash, and V Jayashankar. Analysis of power modules in the Indian wave energy plant. In *Annual IEEE India Conference*, 2009.

[192] A A D Carrelhas, L M C Gato, J C C Henriques, A F O Falcao, and J Varanda. Test results of a 30 kW self-rectifying biradial air turbine-generator prototype. *Renewable and Sustainable Energy Reviews*, 109:187–198, 2019.

[193] T Finnigan. Development of a 300kW ocean wave energy demonstration plant. In *Pacific 2004 International Maritime Conference*, 2004.

[194] T Finnigan and D Auld. Model testing of a variable-pitch aerodynamic turbine. In *13th International Offshore and Polar Engineering Conference*, 2003.

[195] D D Prasad, M R Ahmed, and Y-H Lee. Studies on the performance of savonius rotors in a numerical wave tank. *Ocean Engineering*, 158:29–37, 2018.

[196] S K Patel, K Ram, M R Ahmed, and Lee Y H. Performance studies on an oscillating water column employing a savonius rotor. *China Technological Sciences*, 54:1674–1679, 2011.

[197] V Jayashankar, S Anand, T Geetha, S Santhakumar, V Jagadeesh Kumer, M Ravindran, T Setoguchi, M Takao, K Toyota, and S Nagata. A twin unidirectional impulse turbine topology for OWC based wave energy plants. *Renewable Energy*, 34:692–698, 2009.

[198] K Mala, J Jayaraj, V Jayashankar, T M Muruganandam, S Santhakumar, M Ravindran, M Takao, T Setoguchi, K Toyota, and S Nagata. A twin unidirectional impulse turbine topology for OWC based wave energy plants experimental validation and scaling. *Renewable Energy*, 36:307–314, 2011.

[199] M Takao, A Takami, S Okuhara, and T Setoguchi. A twin unidirectional impulse turbine for wave energy conversion. *Journal of Thermal Science*, 20(5):394–397, 2011.

[200] S Okuhara, M Takao, A Takami, and T Setoguchi. A twin unidirectional impulse turbine for wave energy conversion — effect of guide vane solidity on the performance. *Open Journal of Fluid Dynamics*, 2:343–347, 2012.

[201] B Pereiras, P Valdez, and F Castro. Numerical analysis of a unidirectional axial turbine for twin turbine configuration. *Applied Ocean Research*, 47:1–8, 2014.

[202] Y Cui, Z Liu, and H Beom-Soo. Pneumatic performance of staggered impulse turbine for OWC wave energy converter. *Journal of Thermal Science*, 24(5):403–409, 2015.

[203] S Okuhara, M Takao, H Sato, A Takami, and T Setoguchi. A twin unidirectional impulse turbine for wave energy conversion—effect of fluidic diode on the performance. *Open Journal of Fluid Dynamics*, 4:433–439, 2014.

[204] P V Dudhgaonkar, V Jayashankar, P Jalihal, S Kedarnath, T Setoguchi, M Takao, S Nagata, and K Toyota. Fluidic components for oscillating water column based wave energy plants. In *ASME-JSME-KSME Joint Fluids Engineering Conference*, 2011.

[205] M Takao, S Fukuma, M M A Alam, S Okuhara, Y Kinoue, and S Nagata. A dual-turbine system for wave energy conversion. In *12th European Wave and Tidal Energy Conference*, 2017.

[206] N Ansarifard, A Fleming, A Henderson, S S Kianejad, S Chai, and J Orphin. Comparison of inflow and outflow radial air turbines in vented and bidirectional OWC wave energy converters. *Energy*, 182:159–176, 2019.

[207] J R Joubert and J L Van Niekerk. Recent developments in wave energy along the coast of Southern Africa. In *8th European Wave and Tidal Energy Conference*, 2009.

[208] A El Marjani, F Castro Ruiz, M A Rodriguez, and M T Parra Santos. Numerical modelling in wave energy conversion systems. *Energy*, 33:1246– 1253, 2008.

[209] Y Masuda and M E McCormick. *Experiences in Pneumatic Wave Energy Conversion in Japan*. Utilization of Ocean Waves—Wave to Energy Conversion. 1987.

[210] C Windt, J Davidson, and J V Ringwood. High-fidelity numerical modelling of ocean wave energy systems: A review of computational fluid dynamics-based numerical wave tanks. *Renewable and Sustainable Energy Reviews*, 93:610–630, 2018.

[211] J Tannehill, D Anderson, and R Pletcher. *Computational Fluid Mechanics and Heat Transfer*, volume Second Edition. Taylor and Francis, Washington, DC, 1997.

[212] F M White. *Fluid Mechanics (4th Edition)*. University of Rhode Island, 1998.

[213] *ANSYS Fluent Theory Guide*. Canonsburg, Pennsylvania, US, 2017.

[214] *ANSYS Fluent User's Guide*. Canonsburg, Pennsylvania, US, 2017.

[215] T Vyzikas, S Deshoulieres, O Giroux, M Barton, and D Greaves. Numerical study of fixed oscillating water column with rans-type two-phase CFD model. *Renewable Energy*, 102:294–305, 2017.

[216] Saishuai Dai, S Day, Z Yuan, and H Wang. Investigation on the hydrodynamic scaling effect of an OWC type wave energy device using experiment and CFD simulation. *Journal of Renewable Energy*, 142:184–194, 2019.

[217] F Scarpetta, G Martina, M Torresi, and S M Camporeale. A CFD simulation of a full-scale U-OWC breakwater. In *Proceedings of the 12th European Wave and Tidal Energy Conference 27th Aug – 1st Sept 2017, Cork, Ireland*, 2017.

[218] F Scarpetta, G Martina, M Torresi, and S M Camporeale. CFD analysis of the wave interaction with both a submerged impermeable breakwater and one embedding an OWC device. In *Proceedings of the 11th European Wave and Tidal Energy Conference 6-11th Sept 2015, Nantes, France*, 2015.

[219] A Fleming, I Penesis, G Macfarlane, N Bose, and T Dennis. Energy balance analysis for an oscillating water column wave energy converter. *Ocean Engineering*, 2012: 26–33, 54-1.

[220] A Elhanafi, A Fleming, G Macfarlane, and Z Leong. Numerical energy balance analysis for an onshore oscillating water column wave energy converter. *Journal of Energy*, 116:539–557, 2016.

[221] A Elhanafi, A Fleming, G Macfarlane, and Z Leong. Underwater geometrical impact on the hydrodynamic performance of an offshore oscillating water column wave energy converter. *Journal of Renewable Energy*, 105:209–231, 2017.

[222] A Elhanafi, A Fleming, G Macfarlane, and Z Leong. Numerical hydrodynamic analysis of an offshore stationary floating oscillating water column wave energy converter using CFD. *Journal of Naval Architecture and Ocean Engineering*, 9:77–99, 2017.

[223] A Elhanafi, G Macfarlane, A Fleming, and Z Leong. Investigations on 3d effects and correlation between wave height and lip submergence of an offshore stationary OWC wave energy converter. *Journal of Applied Ocean Research*, 64:203–216, 2017.

[224] A Elhanafi, G Macfarlane, A Fleming, and Z Leong. Experimental and numerical measurements of wave forces on a 3d offshore stationary OWC wave energy converter. *Journal of Ocean Engineering*, 144:98–117, 2017.

[225] A Elhanafi, G Macfarlane, A Fleming, and Z Leong. Experimental and numerical investigations on the intact and damage survivability of a floating–moored oscillating water column device. *Journal of Applied Ocean Research*, 68:276–292, 2017.

[226] A Kammath, H Bihs, and O A Arntsen. Numerical investigations of the hydrodynamics of an oscillating water column device. *Ocean Engineering*, 102:40–50, 2015.

[227] A Kammath, H Bihs, and O A Arntsen. Numerical modelling of power take-off damping in an oscillating water column device. *International Journal of Marine Energy*, 10:1–16, 2015.

[228] A Celik and A Altunkaynak. Determination of hydrodynamic parameters of a fixed OWC by performing experimental and numerical free decay tests. *Ocean Engineering*, 204, 2020.

[229] A Elhanafi, G Macfarlane, and D Ning. Hydrodynamic performance of single–chamber and dual–chamber offshore–stationary oscillating water column devices using CFD. *Applied Energy*, 228:82–96, 2018.

[230] M Shalby, A Elhanafi, P Walker, and D G Dorrel. CFD modelling of a small-scale fixed multi-chamber OWC device. *Applied Ocean Research*, 88:37–47, 2019.

[231] E Medina-Lopez, W Allsop, A Dimakopoulos, and T Bruce. Damage to the Mutriku OWC breakwater – some lessons from further analysis. In *Coasts, Marine Structures and Breakwaters*, 2017.

[232] E Otaola, A J Garrido, J Lekube, and I Garrido. A comparative analysis of self-rectifying turbines for the Mutriku oscillating water column plant. *Wiley - Hindawi*, 2019:14, 2019.

[233] F Fay, J C Henriques, J Kelly, M Mueller, M Abusara, W Sheng, and M Marcos. Comparative assessment of contol strategies for the biradial turbine in the Mutriku OWC plant. *Renewable Energy*, 146:2766–2784, 2020.

[234] Wave Power Engineering. The Wave Mill: Efficient wave energy converter. Report, 8 Febuary 2021 2021. URL `https://wavepowerengineering.com/home/projects`.

[235] S Doyle and G A Aggidis. Advancement of oscillating water column wave energy technologies through integrated applications and alternative systems. *Journal of Energy and Power Engineering*, 14(12):401–412, 2020.

[236] S Doyle and G A Aggidis. Experimental investigation and performance comparison of a single OWC, array and M-OWC. *Renewable Energy (Accepted, In Press)*, 2020.

[237] M Shalby, P Walker, and D G Dorrel. The characteristics of the small segment Multi-Chamber Oscillating Water Column. In *3rd AWTEC (Asian Wave and Tidal Energy Conference Series)*, 2016.

[238] Edinburgh Designs. Wave maker. Manual. URL `http://www4.edesign.co.uk/`.

[239] *Tank Testing of Wave Energy Conversion Systems*. Marine Renewable Energy Guides. The European Marine Energy Centre Ltd, 2009.

[240] I Lopez, B Pereiras, F Castro, and G Iglesias. Optimisation of turbine-induced damping for an OWC wave energy converter using a RANS-VOF numerical model. *Applied Energy*, 127:105–114, 2014.

[241] Measurement of fluid flow by means of pressure differential devices — guidelines for specification of nozzles and orifice plates beyond the scope of ISO 5167-1. Report, British Standards Institution, 1998.

[242] M Vicente, P Benreguig, S Crowley, and J Murphy. Tupperwave - preliminary numerical modelling of a floating OWC equipped with a unidirectional turbine. In *12th European Wave and Tidal Energy Conference*, 2017.

[243] P Gaillard, M Gauthier, and F Holly. Method of analysis of random wave experiments with reflecting coastal structures. *Coastal Engineering*, pages 204–220, 1980.

[244] J Weber. Representation of non-linear aero-thermodynamic effects during small scale physical modelling of OWC WECs. In *7th European Wave and Tidal Energy Conference*, 2007.

[245] W Sheng, R Alcorn, and T Lewis. Hydrodynamics of oscillating water column wave energy converters. In *1st International Conference on Renewable Energies Offshore*, 2014.

[246] P J Roache. Quantification of uncertainty in computational fluid dynamics. *Fluid Mechanics*, 29, 1997.

Appendix A

Methodology Support

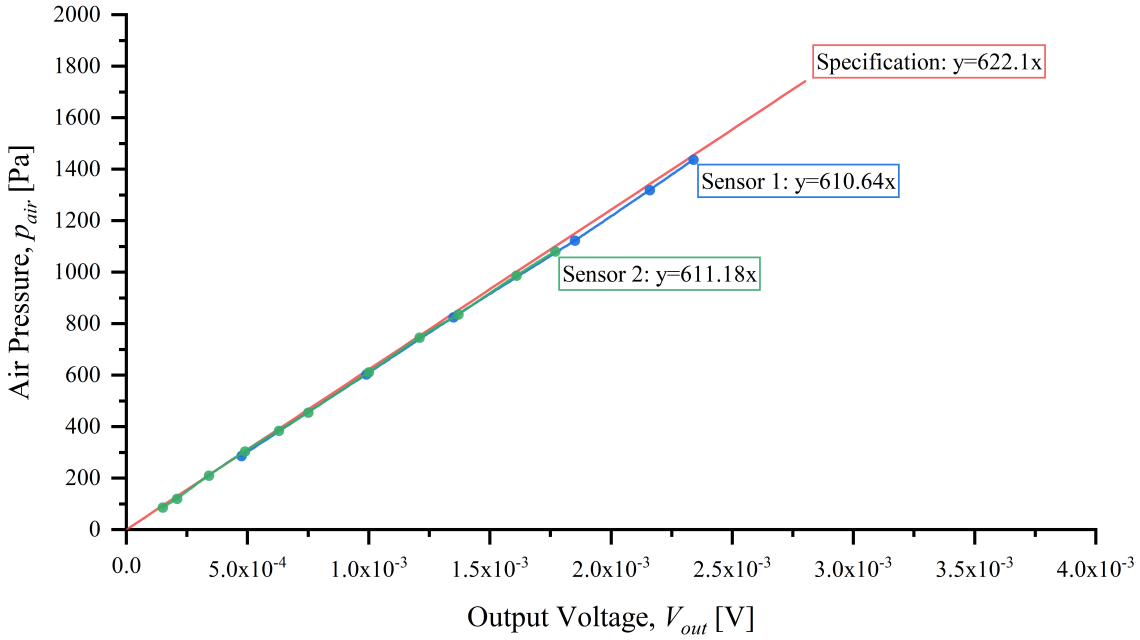


Figure A.1: *Differential pressure sensor calibration test results*

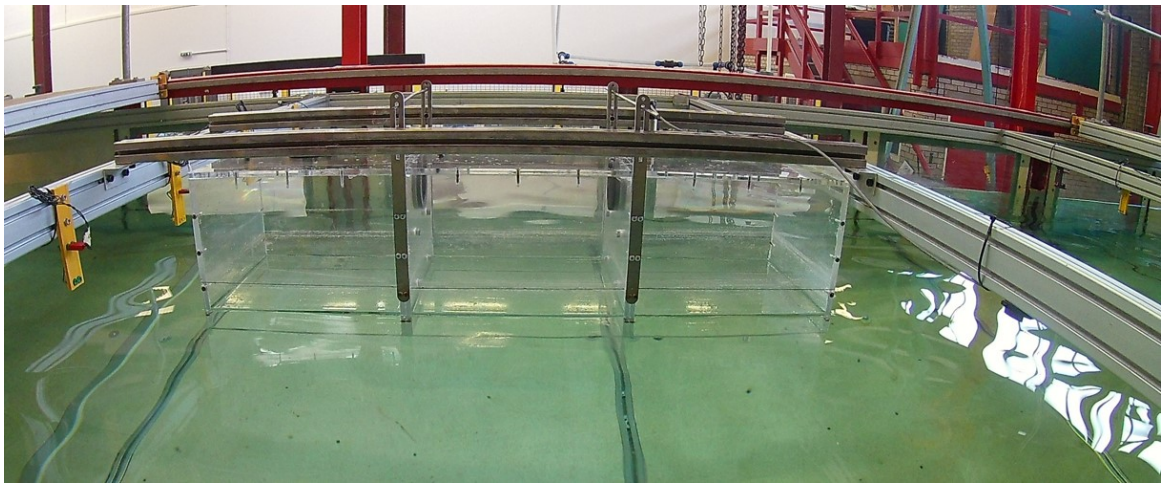


Figure A.2: *Picture of Phase 1 experimental set-up for hydrodynamic tests*



Figure A.3: *Phase 1 W2W M-OWC skeleton with calibrated copper strip ILGs out of tank close-up*

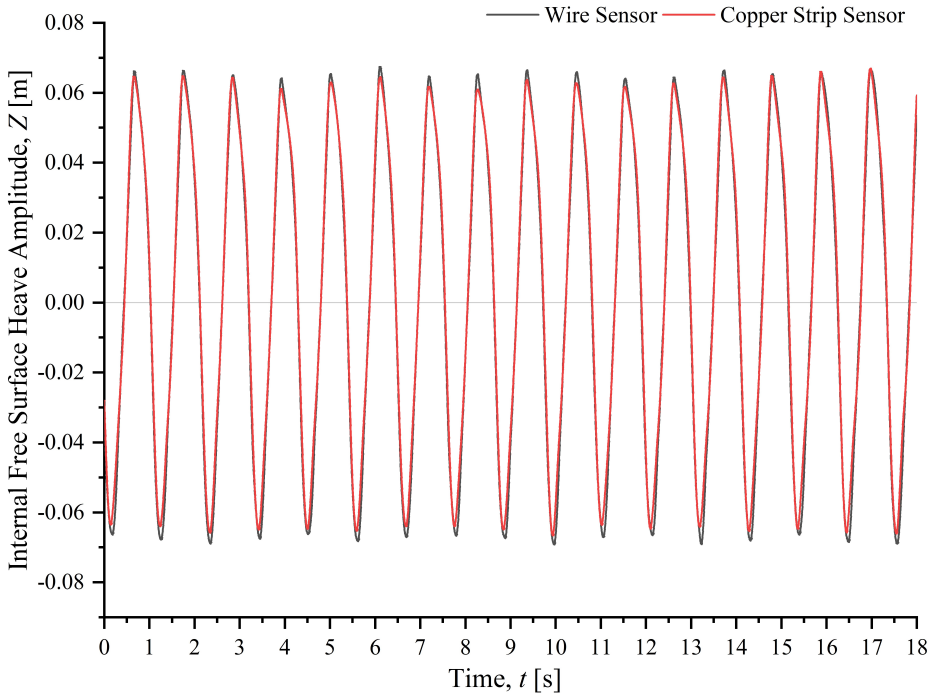


Figure A.4: *Internal heave amplitude sensor calibration test*



Figure A.5: *Phase 1 W2W M-OWC skeleton with copper strip ILGs installed in the wave tank for calibration tests*



Figure A.6: *Render of Phase 1 pneumatic experimental model intermediate one-way valve with incline for transfer between 1^{st} and 2^{nd} stage*

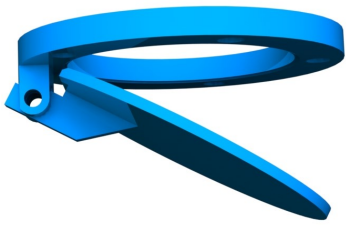


Figure A.7: *Render of Phase 1 pneumatic experimental model inlet one-way valve with for 1^{st} stage*

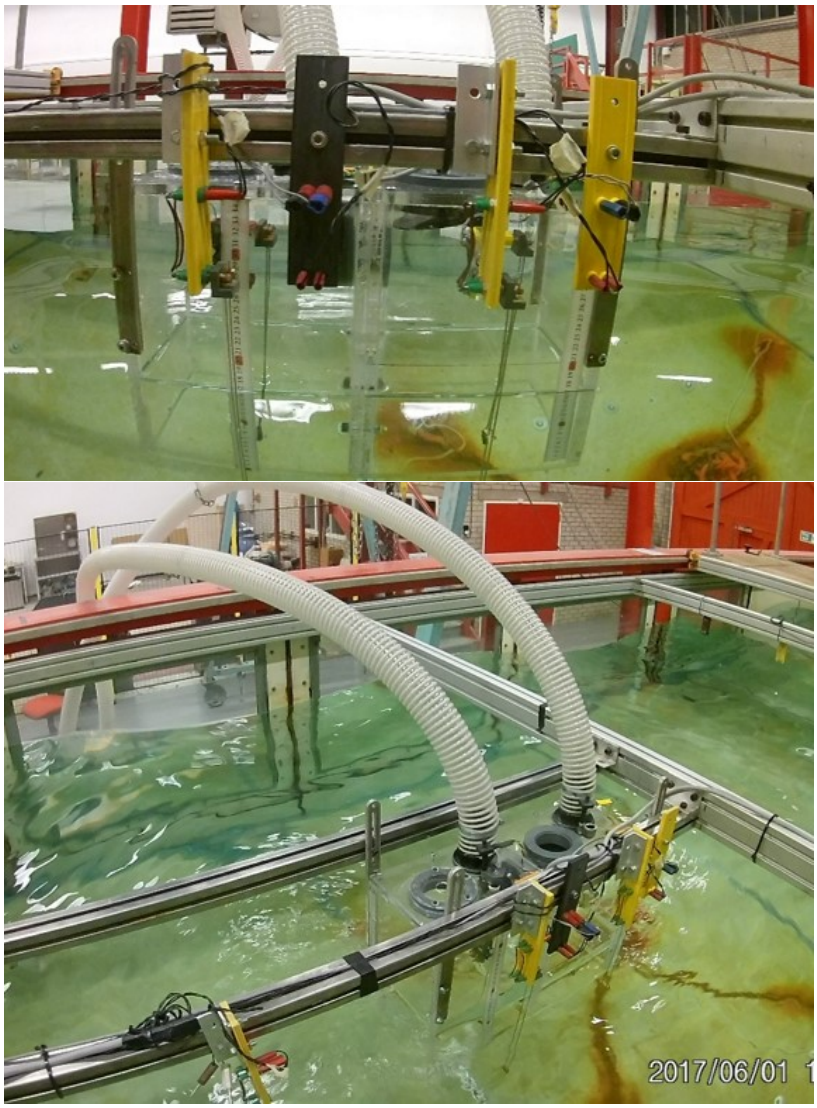


Figure A.8: *Phase 1 W2W conept M-OWC model installed in wave tank for pneumatic tests*

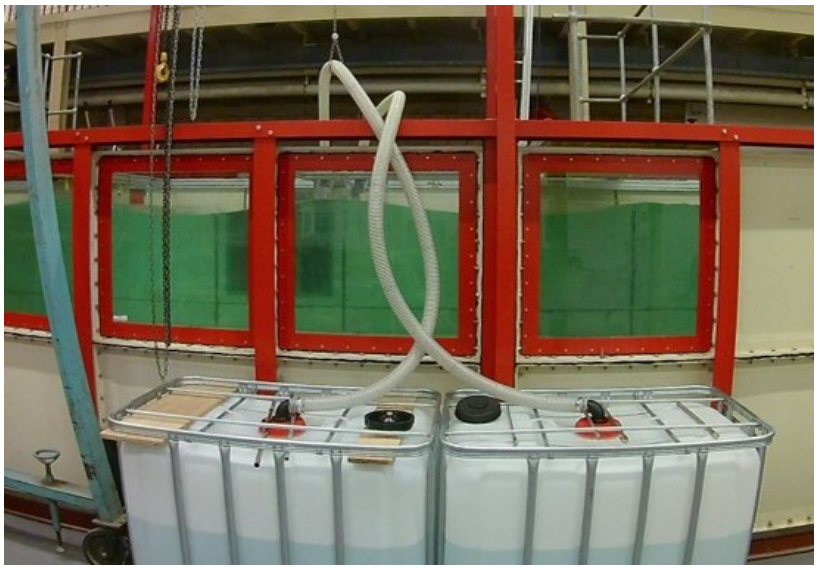


Figure A.9: *Phase 1 W2W Conept M-OWC model auxiliary air volume tanks and connecting hoses installed in wave tank for pneumatic tests*

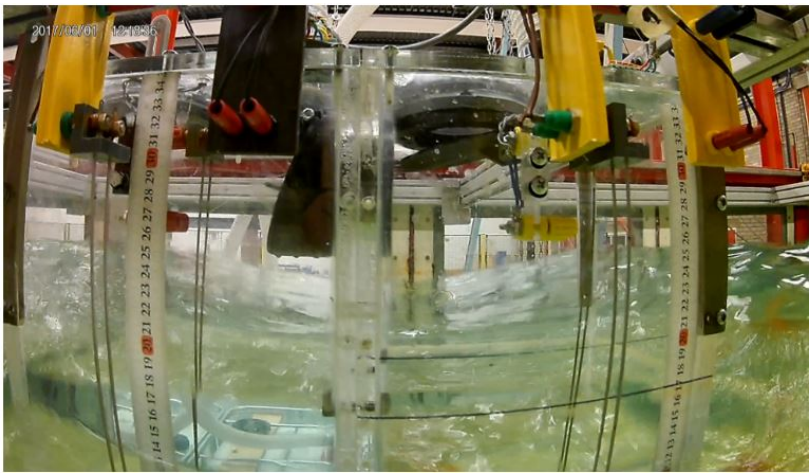


Figure A.10: *Live snapshot of inhale process during pneumatic testing of the Phase 1 W2W conept M-OWC*

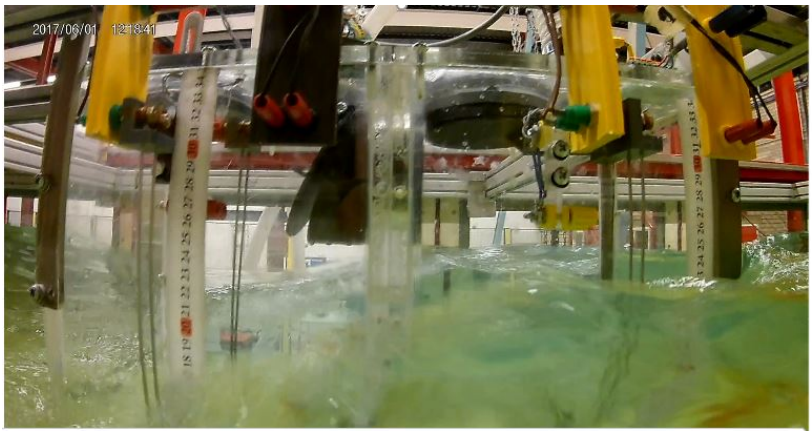


Figure A.11: *Live snapshot of Exhale process during pneumatic testing of the Phase 1 W2W conept M-OWC*

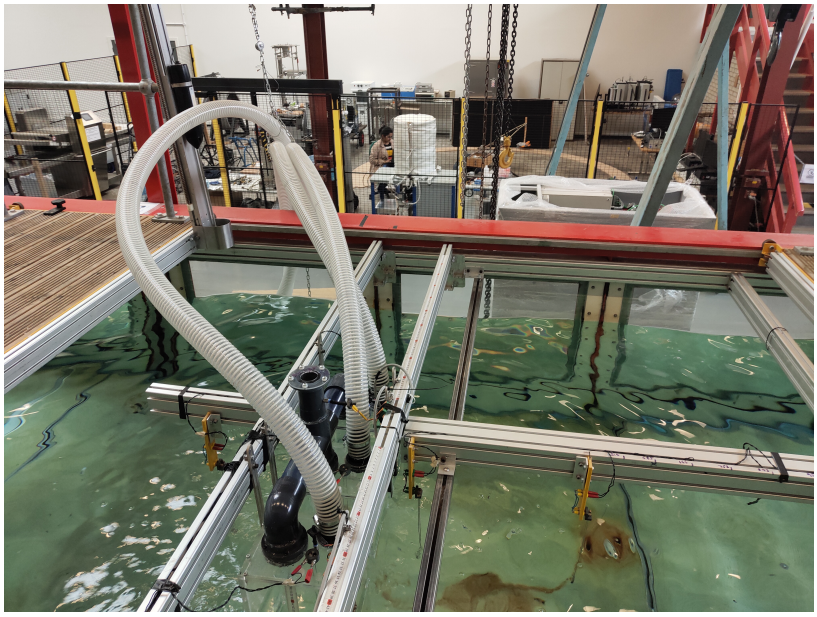


Figure A.12: *Phase 2 M-OWC bidirectional manifold model installed in the tank*

Appendix B

EMEC Wave Data and Runs



Figure B.1: *Location of EMEC Billia Croo test site and wave data source site*

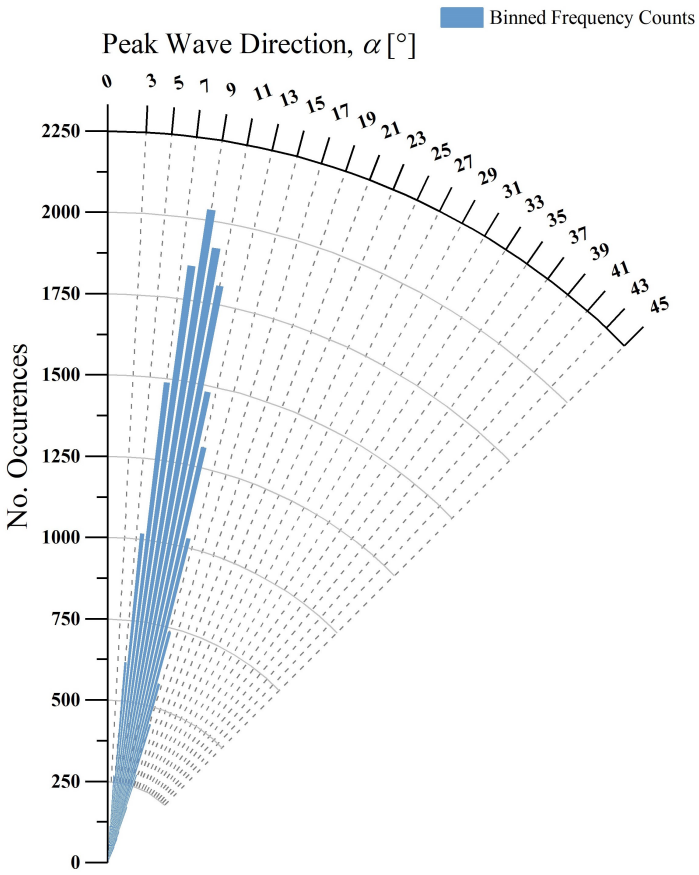


Figure B.2: *Polar histogram plot for the wave direction at the EMEC Billia Croo test site*

Run No.	f^m_{wave}	λ^m	H^m	a^m_{wave}	dx_{12}	dx_{23}
1.1	1.01	1.53	0.050	0.025	0.510	1.020
1.2	1.01	1.53	0.060	0.030	0.510	1.020
1.3	1.01	1.53	0.070	0.035	0.510	1.020
2.1	0.94	1.76	0.050	0.025	0.585	1.171
2.2	0.94	1.76	0.060	0.030	0.585	1.171
2.3	0.94	1.76	0.070	0.035	0.585	1.171
2.4	0.94	1.76	0.080	0.040	0.585	1.171
3.1	0.88	2.00	0.050	0.025	0.666	1.332
3.2	0.88	2.00	0.060	0.030	0.666	1.332
3.3	0.88	2.00	0.070	0.035	0.666	1.332
3.4	0.88	2.00	0.080	0.040	0.666	1.332
4.1	0.83	2.26	0.05	0.025	0.752	1.504
4.2	0.83	2.26	0.06	0.030	0.752	1.504
4.3	0.83	2.26	0.07	0.035	0.752	1.504
4.4	0.83	2.26	0.08	0.040	0.752	1.504
4.5	0.83	2.26	0.09	0.045	0.752	1.504
5.1	0.79	2.53	0.05	0.025	0.843	1.686
5.2	0.79	2.53	0.06	0.030	0.843	1.686
5.3	0.79	2.53	0.07	0.035	0.843	1.686
5.4	0.79	2.53	0.08	0.040	0.843	1.686
5.5	0.79	2.53	0.09	0.045	0.843	1.686
5.6	0.79	2.53	0.10	0.050	0.843	1.686
6.1	0.74	2.82	0.05	0.025	0.939	1.879
6.2	0.74	2.82	0.06	0.030	0.939	1.879
6.3	0.74	2.82	0.07	0.035	0.939	1.879
6.4	0.74	2.82	0.08	0.040	0.939	1.879
6.5	0.74	2.82	0.09	0.045	0.939	1.879
6.6	0.74	2.82	0.10	0.050	0.939	1.879

Table B.1: *Full wave run for use in experiments, filtered and selected regular waves range runs from EMEC data*

Appendix C

Tank Reflection Characteristics

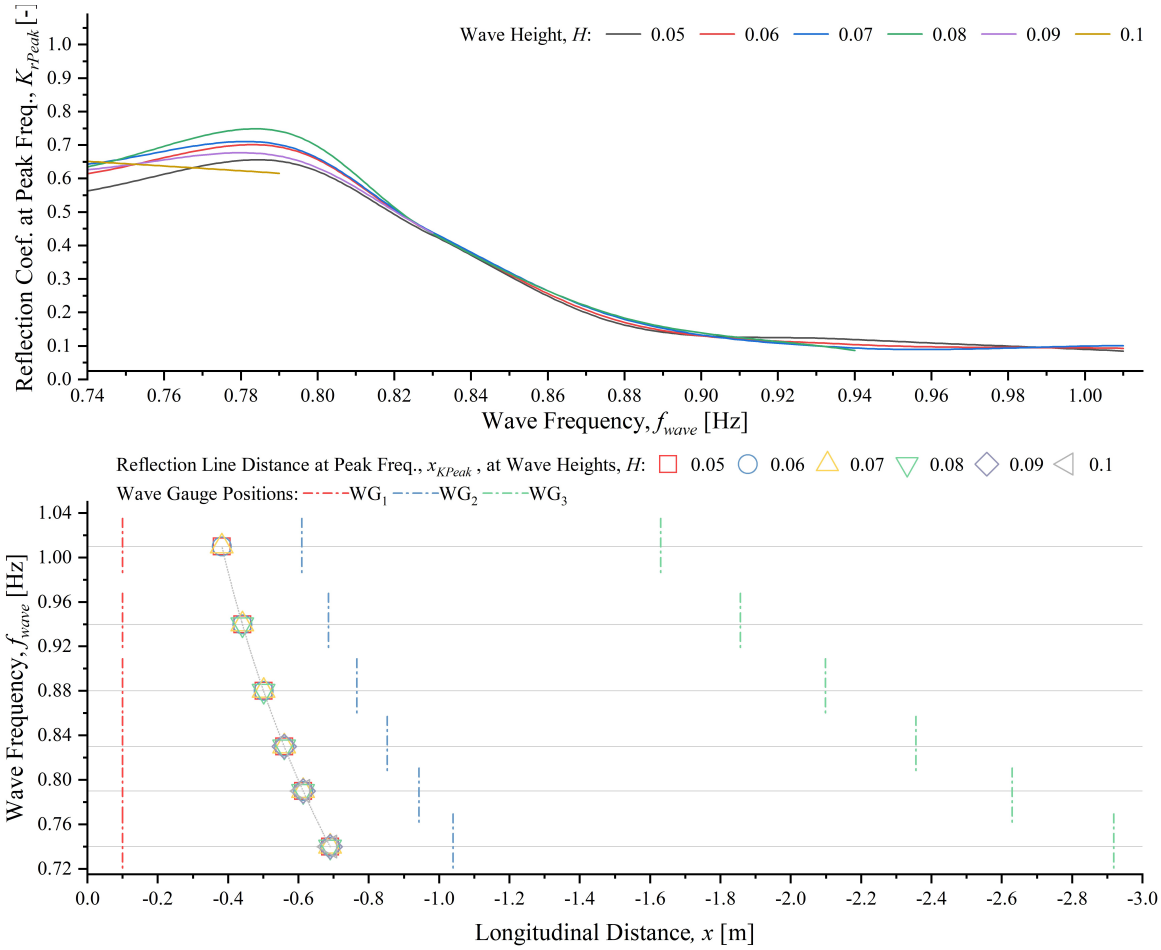


Figure C.1: *Reflection coefficient (top) and reflection line distance (bottom) results in empty tank reflection tests*

Appendix D

Phase 2 Model Reflection Full Results

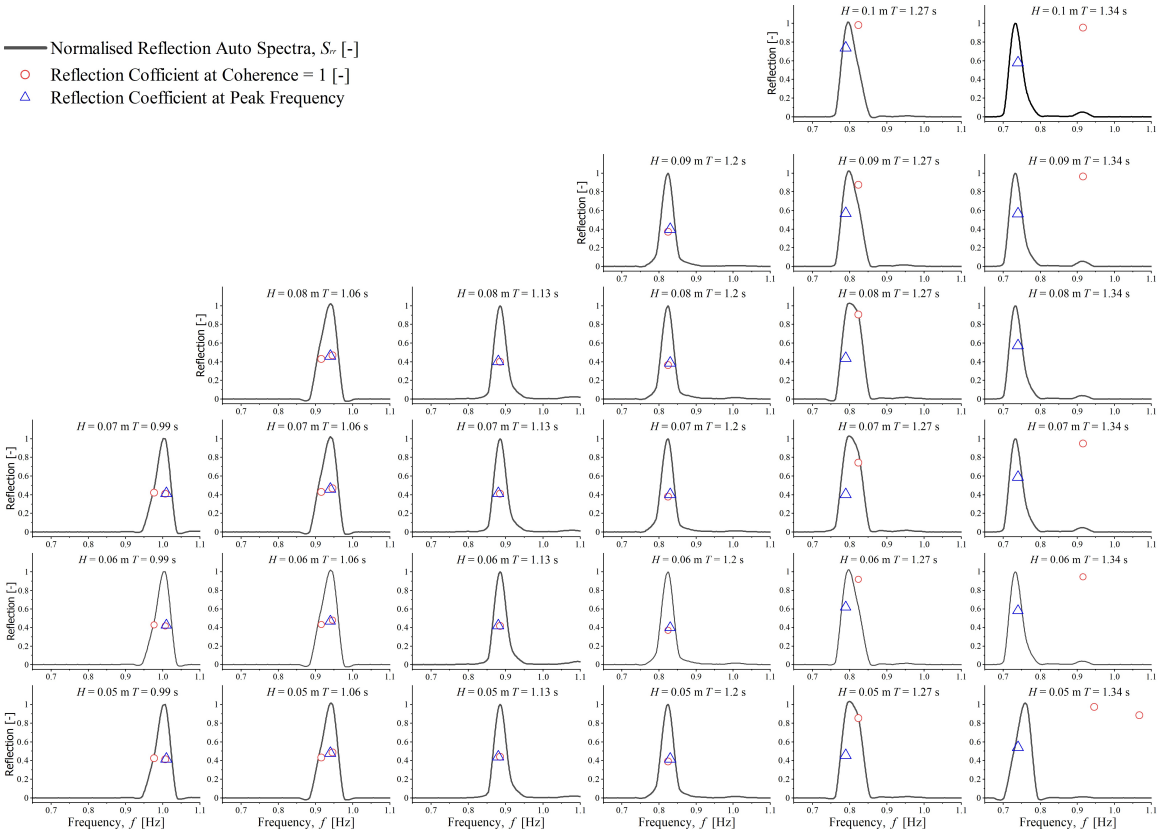


Figure D.1: *Phase 2 M-OWC Bidirectional Model Full Reflection Results*

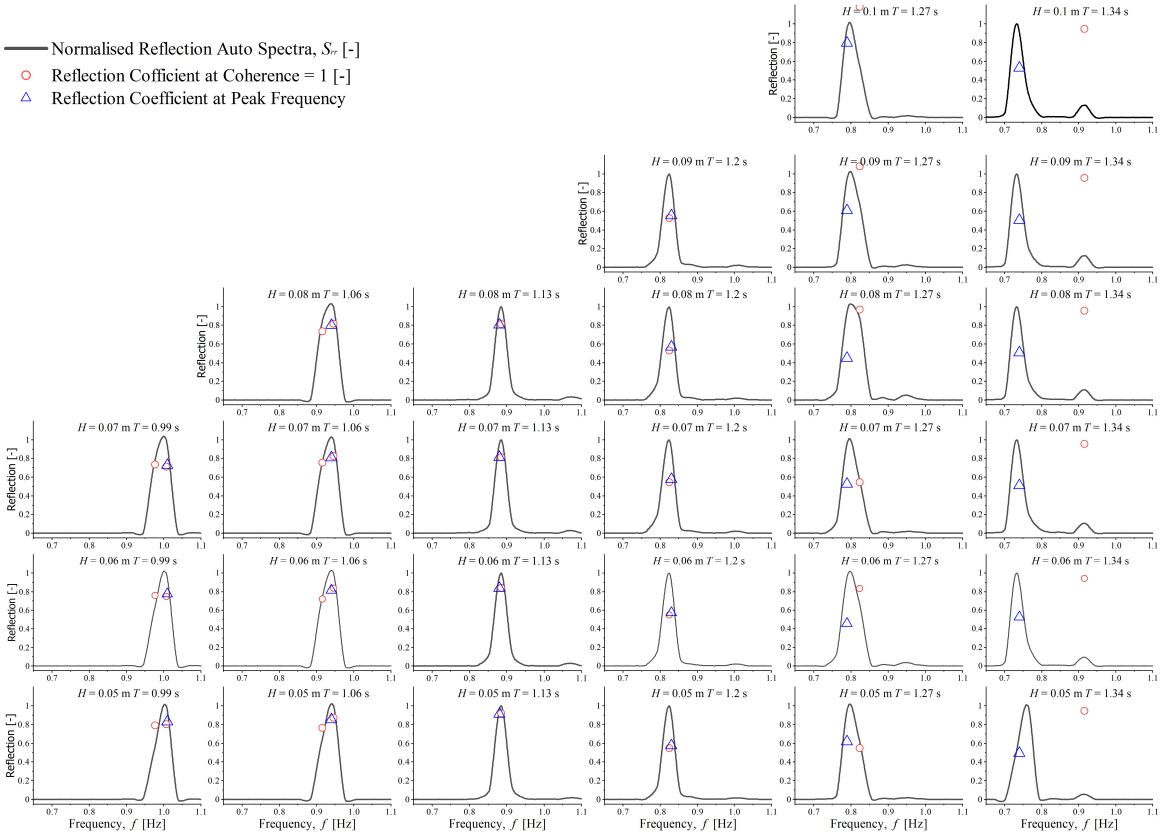


Figure D.2: *Phase 2 M-OWC Bidirectional Breakwater Model Full Reflection Results*

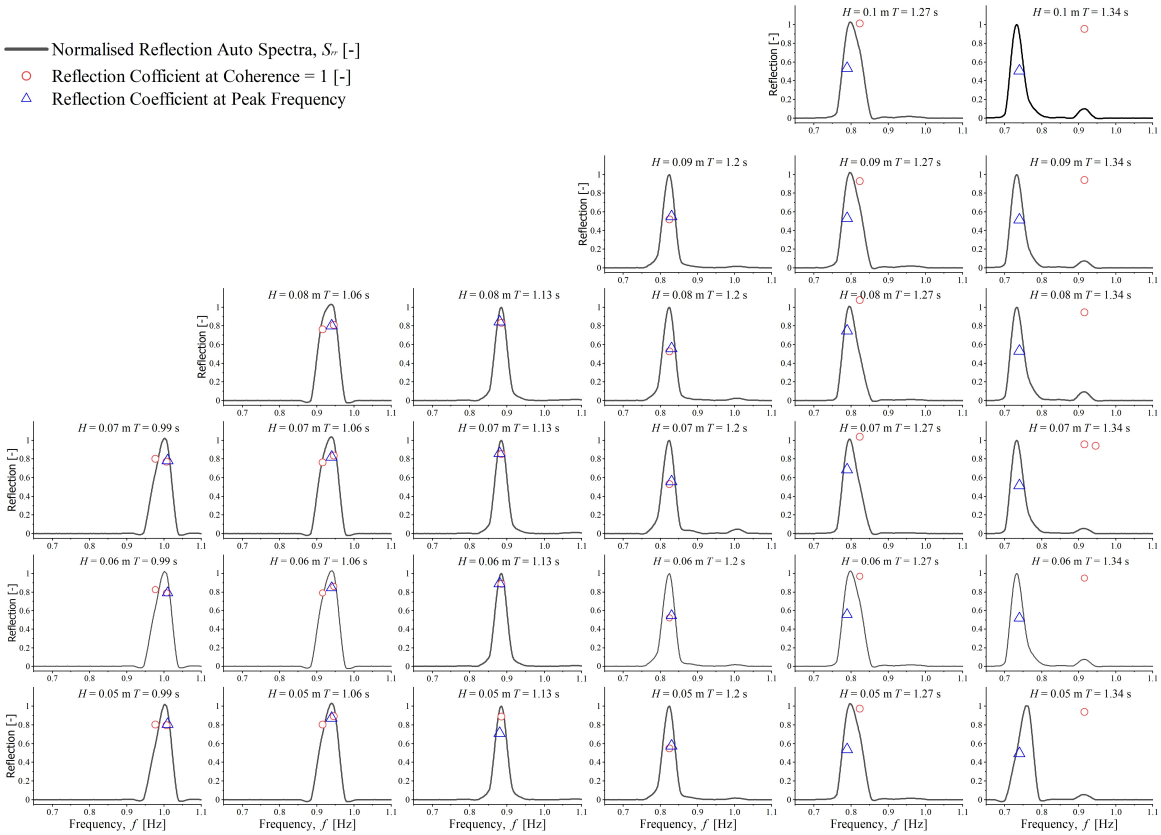


Figure D.3: *Phase 2 M-OWC Unidirectional Single Model Full Reflection Results*

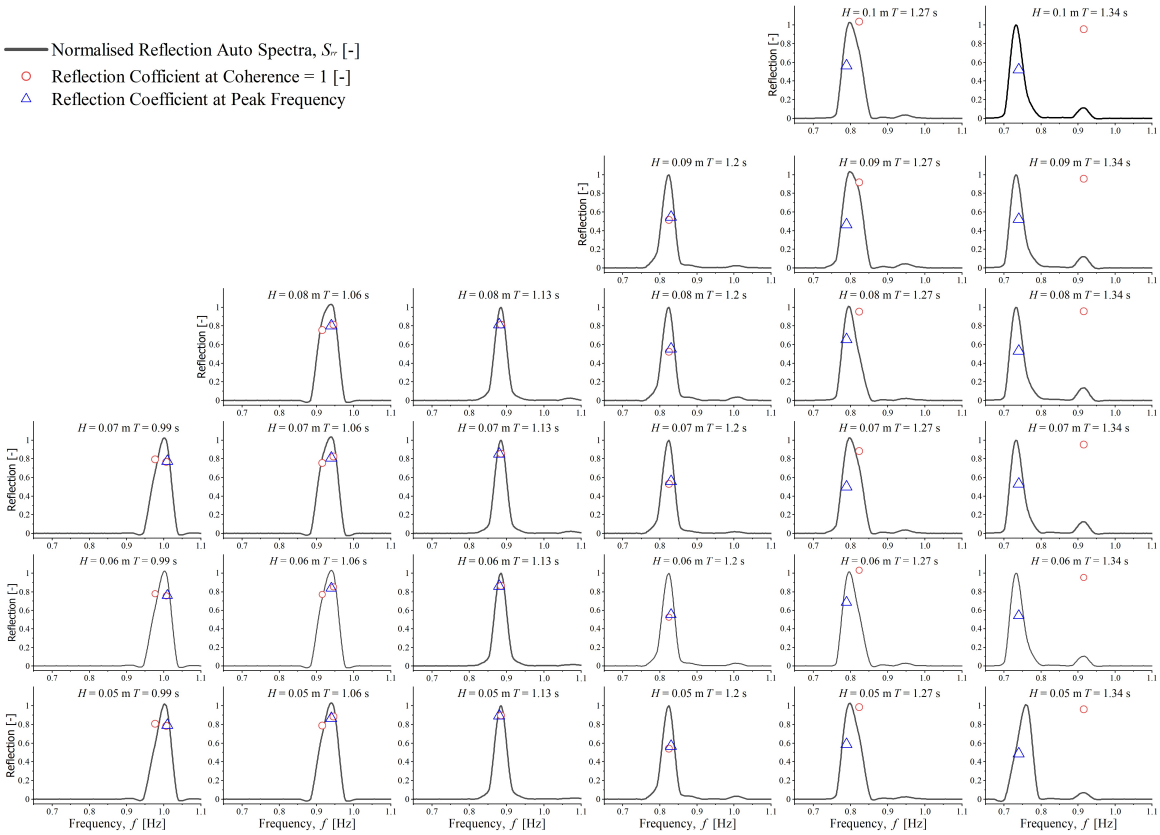


Figure D.4: *Phase 2 M-OWC Unidirectional Twin Model Full Reflection Results*

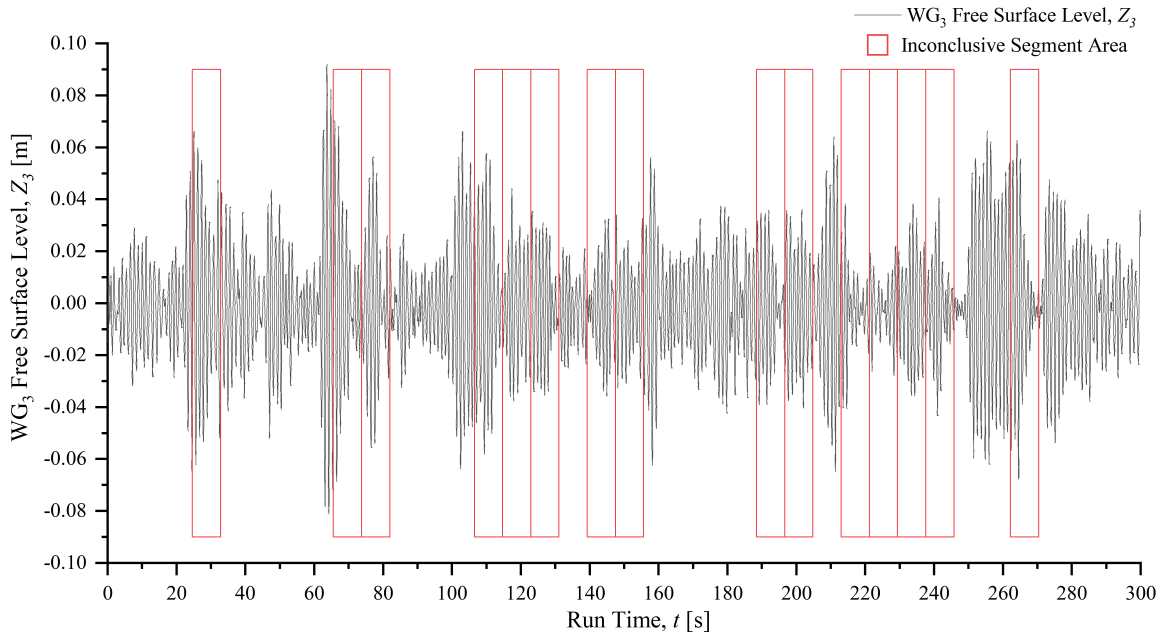


Figure D.5: *Segments of the irregular time series generated incident wave that frequently yielded bad results across all models and wave runs*

Appendix E

Irregular Wave Generation

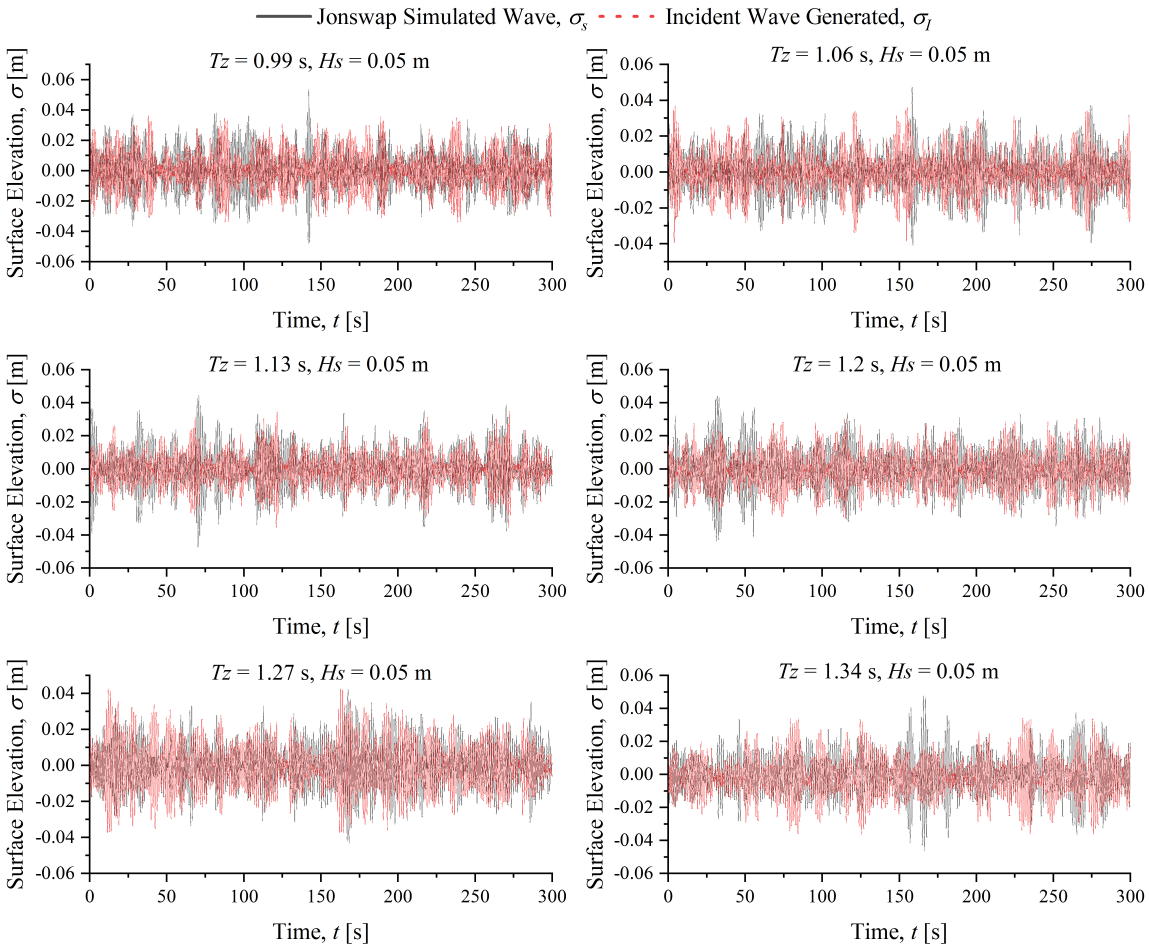


Figure E.1: *Time series of generated compared with recorded incident wave in empty tank*

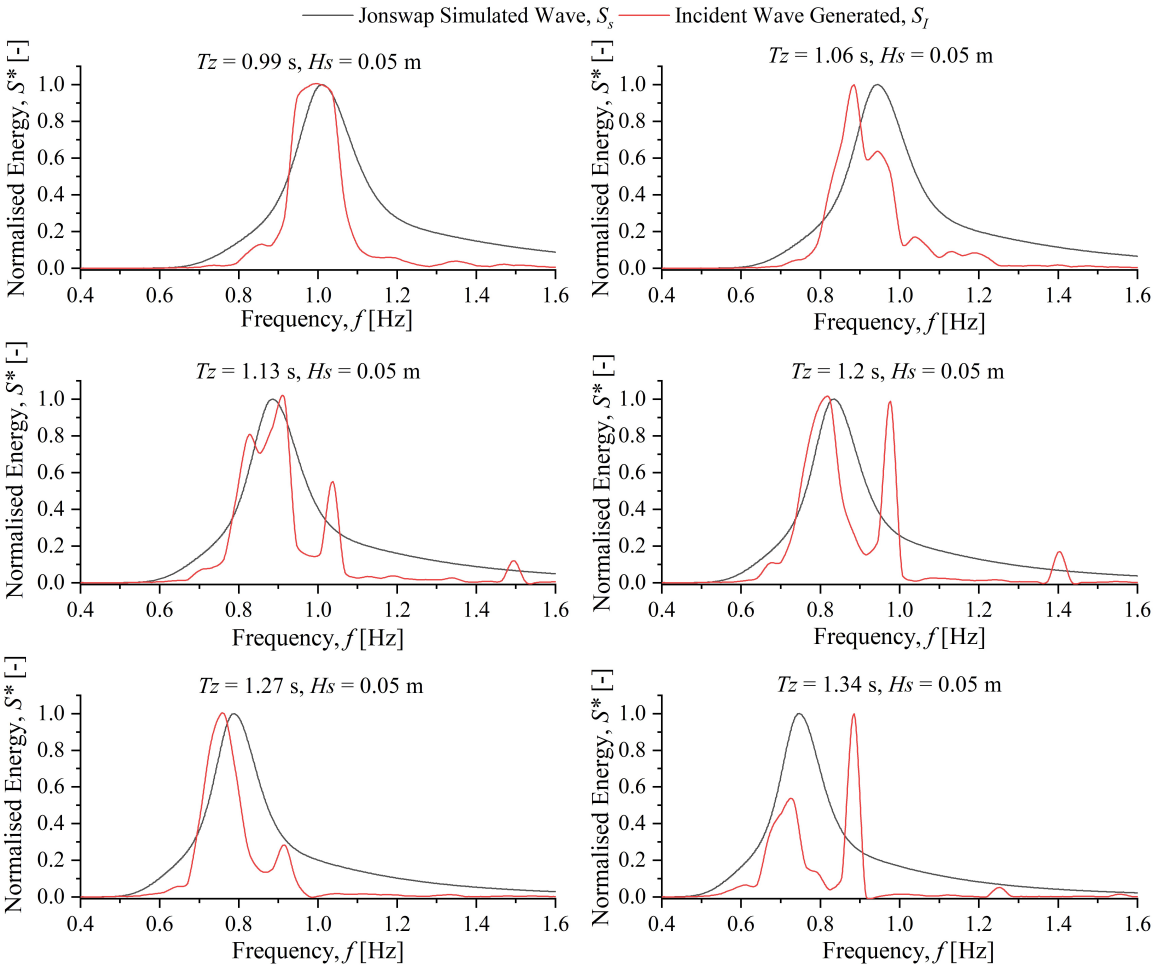


Figure E.2: *Jonswap spectra generated compared with recorded incident wave in empty tank*